Growth, single-particle, and ensemble X-ray diffraction from model catalysts under operando reaction conditions

Dissertation

zur Erlangung des Doktorgrades an der Fakultät für Mathematik,
Informatik und Naturwissenschaften

Fachbereich Physik
der Universität Hamburg

vorgelegt von

Henning Runge

Hamburg

2021

Gutachter/in der Dissertation:	Prof. Dr. Andreas Stierle Dr. Ivan Vartaniants
Zusammensetzung der Prüfungskommission:	Prof. Dr. Andreas Stierle Prof. Dr. Daniela Pfannkuche Prof. Dr. Wolfgang Hansen Dr. habil. Thomas Keller Dr. Ivan Vartaniants
Vorsitzende der Prüfungskommission:	Prof. Dr. Daniela Pfannkuche
Datum der Disputation:	29.10.2021
Vorsitzender des Fach-Promotionsausschusses PHYSIK:	Prof. Dr. Wolfgang Hansen
Leiter des Fachbereichs PHYSIK:	Prof. Dr. Günther Sigl
Dekan der Fakultät MIN:	Prof. Dr. Heinrich Graener

Eidesstattliche Versicherung / Declaration on oath

Hiermit versichere ich an Eides statt, die vorliegende Dissertationsschrift selbst verfasst und keine anderen als die angegebenen Hilfsmittel und Quellen benutzt zu haben.

_____

Unterschrift der Doktorandin / des Doktoranden

Abstract

This thesis provides a growth study of α-Al_2O_3(0001) supported Pt particles and subsequent structure monitoring using ensemble and single-particle X-ray diffraction (XRD) during catalytically driven CO oxidation on PtRh particles.

The growth study provided two different particle morphologies dependent on the type of annealing after epitaxial growth at 830 °C using molecular beam epitaxy (MBE) in ultra high vacuum (UHV): annealing of particles at 1100 °C in UHV yielded (111)-oriented, flat particles with a height of about 4 nm and an average diameter of about 20 nm (surface coverage about 40 %). In turn, exposure to air at 1200 °C, the nanoparticles undergo a redistribution of the deposited material with the coverage significantly decreased to 7 %, likely via the formation of metastable PtO_x species. The transformation results in a broad height and diameter distribution with particles covering sizes from few nanometers to diameters of above 100 nm. These particles do not exhibit a flat morphology, instead they are closer to their equilibrium shape. Monitoring a sample with particles of flat morphology using ensemble XRD during catalytically enhanced, CO oxidation detected no shape changes at a temperature of 370 °C with a stoichiometric ratio of oxygen and carbon monoxide near ambient pressure. However, at 450 °C and over-stoichiometric ratio of oxygen to carbon monoxide, the flat particles were subject to non-reversible intra-particle mass transport increasing height while decreasing diameter of the particles which was pronounced for larger particles. The formation of a superficial rhodium oxide layer and Ostwald-rippening were not detected.

A single-particle XRD study was carried out at the synchrotron end station ESRF ID01 on a single, $SrTiO_3$-supported $Pt_{60}Rh_{40}$ particle with (111)-orientation, a height of 55 nm, and a diameter of about 120 nm. Exposure to catalytically enhanced CO oxidation (stoichiometric ratio of O_2 and CO) at 425 °C did not inflict significant shape changes of the particle. Differences in the diffraction patterns for different gas dosing steps indicate partially reversible changes in surface strain fields. Analysis of the particle's diffraction signal indicates outward displacement of the topmost 4-5 atomic layers caused by an expansion of the fourth or fifth layer of at least 9 % under Argon dosing, contrary to findings reported by other researchers. Again, no rhodium oxide layers were detected under oxidizing conditions.

Zusammenfassung

Die vorliegende Arbeit präsentiert auf Basis einer Wachstumsstudie von Platin Nanopartikeln auf α-Al_2O_3 katalytisch beschleunigte CO-Oxidationsexperimente an PtRh-Ensemblepartikeln und an einem PtRh-Einzelpartikel, während deren die Morphologie der jeweiligen Partikel mittels Röntgendiffraktion (XRD) beobachtet wird.
Die durchgeführte Wachstumsstudie lieferte zwei Partikelmorphologien des bei 830 °C im Ultrahochvakuum (UHV) mittels Molekularstrahlepitaxie (MBE) deponierten Materials in Abhängigkeit von einer darauffolgend durchgeführten Wärmebehandlung. Tempern bei 1100 °C in UHV führte zu weitestgehend uniformen, flachen Partikeln (Höhe ca. 4 nm, Durchmesser ca. 20 nm) bei einer mittleren Bedeckung der Probe von knapp 40 %. Anschließendes Erhitzen der Probe bei 1200 °C in Luft hingegen führte zu einer totalen Umverteilung des Platins auf der Substratoberfläche mit nunmehr drastisch verringerter Bedeckung von 7 %, breiter Höhen- und Durchmesserverteilung der Partikel, mit sowohl kleinen Partikeln der Größe weniger Nanometer, als auch großen Partikel mit Höhen und Durchmessern mehrerer hundert Nanometer. Womöglich wird die Transformation getragen von volatilen, metastabilen Platinoxiden.
Die Überwachung der Partikelgrößen mittels XRD während katalytisch beschleunigter CO Oxidation nahe Umgebungsdruck zeigte keine signifikanten Änderungen von Partikeln flacher Morphologie bei 370 °C und einem stöchiometrischen Verhältnis von O_2 zu CO. Bei 450 °C und überstöchiometrischem Verhältnis jedoch sorgte ein Massentransportmechanismus innerhalb der Partikel für ein nicht reversibles Höhenwachstum bei gleichzeitiger Verringerung des Durchmessers der Partikel, besonders bei Partikeln großer Durchmesser. Die Entstehung einer Rhodiumoxidschicht an der Oberfläche der Partikel unter oxidierenden Bedingungen wurde nicht nachgewiesen.
Das katalytisch beschleunigte Einzelpartikel-Streuexperiment wurde bei ESRF ID01 an einem (111)-orientierten $Pt_{60}Rh_{40}$-Partikel (55 nm hoch, ca. 120 nm Durchmesser) auf einem $SrTiO_3$ (STO) Substrat durchgeführt. Oxidierende Bedingunen bei 425 °C Substrattemperatur und stöchiometrisches Verhältnis von O_2 zu CO hatten keine signifikanten Formänderungen des Partikels zur Folge. Unterschiedliche Streubilder des Partikels für die einzelnen Reaktionsschritte deuten auf teilreversible Veränderungen der Oberflächenverspannung hin. Vergleich zwischen berechneten Strukturfaktoren und den Streudaten in Argon-Atmosphäre zeigten einen Versatz der Oberfläche durch

Expansion der vierten oder fünften Lage um mindestens 9 %, im Widerspruch zu Ergebnissen anderer Forscher. Wieder wurde das Entstehen einer Rhodiumoxidschicht im Experiment nicht beobachtet.

Contents

Chapter 1.

Introduction

Catalysis is a vital part of our daily life. Exemplarily, in our body cells enzymes are of utmost importance for metabolism processes in our body. Additionally, the genetic information (e.g. deoxyribonucleic acid, DNA) is reproduced catalytically [1]. As first described by chemist Elizabeth Fulhame in 1794, a catalyst increases a reaction rate by either promoting certain educts and/or lowering the activation energy of a reaction without being consumed in the process [2]. The crucial role of catalysts not only in small cells, but on large scale in industrial applications is underlined by the fact that about 20-30 % of the global GDP are directly or indirectly accounted by catalytic processes, and about 85 % of today's chemical products are produced using catalytic processes [3]. As of 2019, the size of the global catalyst market was valued at about 34 billion USD [4]. Well-known applications of catalysts cover cleaning of exhaust gases by cars or by large-scale facilities, petrochemical refinement (e.g. cracking and naphtha reforming), and the production of ammonia. Generally, the most relevant parameters concerning the catalyst itself are activity (turnover frequency), selectivity (sensitivity of a catalyst material towards a certain species), and lifetime (degeneration of a catalyst material). Although the concept of catalysis is known for more than 200 years, the exact mechanisms of catalytic activity are still under debate for many materials. Mostly, this is due to a complicated correlation of the activity with the respective atomic structure of the catalyst. Not only is the activity of a catalyst strongly dependent on environmental conditions (i.e. temperature, total pressure, stoichiometry of specimen), it is further altered for different surface terminations or vicinal surfaces [5], and (metastable) surface oxides or reconstructions may further increase or decrease the turnover frequency of a reaction [6–8]. Further, a catalyst's activity is different for single crystals and nanoparticles, where additionally a size effect is observed. A change in a catalyst's activity due to different sizes of the nanoparticles is not solely due to the accompanying change in total surface

area, it is also due to smaller particles being easier to oxidize [9], accompanied by a change of the atoms' coordination numbers, as in the limit for very small particles well-defined facets are vanishing. An increasing influence by short-range interaction forces additionally alters the surface energy of catalytic nanoparticles [10]. From an industrial perspective, not only the catalytically increased reaction speed for a certain type of reaction is relevant. A typical catalyst's activity decreases over time, exemplarily in the case of car exhaust catalysts due to sintering of nanoparticles [11, 12]. To countervail deactivation mechanisms, a thorough understanding of the correlation between the catalyst's atomic structure and the activation or deactivation mechanisms upon reaction conditions is necessary. Other deactivation mechanisms may include surface poisoning by adhesion of reactants, formation of superficial oxides, and segregation effects in bimetallic nanoparticles (among others) [13].
In the near future, the impact of catalysis will increase further, as it will play a vital role in the reformation of humanity's energy supply towards renewable sources and will impose further challenges in the operation and properties of modern catalysts [13]. Exemplarily, the renewable-driven electrocatalytic decomposition of water or carbon dioxide into reactive species and their further catalytically enhanced conversion in batteries, fuel cells, or even combustion engines is inherently of dynamic nature, as renewable energies naturally offer a supply with electricity (e.g.) that fluctuates over time [13].
The proper operation of catalytically enhanced reactions under either static or dynamic conditions strongly relies on suitable, tailored catalysts which in turn presupposes in-depth understanding of the catalyst itself. Typical instruments for corresponding surface studies are electron-based analytical methods as X-ray photoelectron spectroscopy (XPS), transmission electron microscopy (TEM), or scanning electron microscopy which are perfectly suitable for vacuum conditions, but usually cannot bridge the so-called *pressure gap* caused by the low mean free path of electrons under near-ambient conditions [13, 14]. Additionally, it is usually not possible to extrapolate from experimental results obtained from studies performed under vacuum conditions [15]. Hence, the operando investigation of catalysts is closely related to advances of surface science instruments which provide suitable probing capabilities when applying desired ambient conditions. Examples are ambient pressure XPS (APXPS), low-energy ion scattering (LEIS), polarization modulation infrared reflection absorption spectroscopy (PM-IRAS), or modern near-edge X-ray absorption fine structure (NEXAFS/XANES) [15]. Typically, these measurements are supported by theoretical studies (e.g. density functional theory, DFT) to gain

insight in reaction kinetics or intermediate species. However, spectroscopy-based methods usually lack insight in the direct determination of the surface structure. The development of extremely brilliant synchrotron light sources enabled the exact measurement of surface structures down to atomically precise levels and below [15], as will be further promoted in this work.

This work contributes to the ongoing development of heterogeneous catalysis by promoting the role of X-rays in both in-situ and operando studies revealing the nature of catalytic reactions and accompanying effects induced to the catalyst. More precisely, the feasibility and power of coherent X-ray diffraction imaging (CXDI) are demonstrated by performing X-ray diffraction on a single $Pt_{60}Rh_{40}$ particle upon exposure to well-defined carbon monoxide oxidation reactions at near-ambient pressures. As a first step, Chapter 3 characterizes two different particle morphologies to be applied for further catalytic studies in this thesis. The first type of particles exhibits a flat morphology with a height to diameter ratio of about 1:5 making these particles suitable for studies covering surface effects especially on the (111)-type top facet of the particles. Particles of the second type of morphology exhibit a three-dimensional shape close to the Wulff shape in thermodynamic equilibrium. As second step, Chapter 4 demonstrates a catalytic study on particles with flat morphology. Well-defined environmental conditions are established by using a catalysis reactor with a gas flow setup and a mass spectrometer installed downstream to the reactor. The reactor is equipped with a beryllium dome transparent to X-rays, making it possible to monitor shape transitions of the particles during the catalytic reaction. Subsequently, a single-particle catalytic experiment using the same equipment used for the study on flat particles is presented in Chapter 5, on a particle with 3D shape and suitable size necessary for CXDI. Before presenting the growth study in Chapter 3, terms and physical concepts constituting the basis of this work together with the setups employed are introduced in the following Chapter 2. Finally, the conclusions and results achieved in this work are summarized in Chapter 6.

Chapter 2.

Theoretical background

This chapter is dedicated to the introduction of physical quantities, phenomena, and measurement techniques employed in this work. Firstly, keywords, important physical quantities and underlying mechanisms determining the chemical and physical properties will be described. Section 2.1 introduces surfaces and related terms like thermodynamic potentials and strain, followed by an introduction into the growth of supported particles in Section 2.2 with different growth techniques and the material systems used for this work. Afterwards, concepts of catalysis will be briefly discussed in Section 2.3, followed by a discussion of the measurement techniques and instruments used, see Sections 2.4 and 2.5.

2.1. Surfaces of solids

The key towards the underlying mechanisms and driving forces of catalytically enhanced CO oxidation on noble metal nanoparticles lies in the comprehension of the surfaces involved. Developing a fundamental idea of the physical properties of which will be the starting point of this chapter, accordingly. Surfaces in general are a concept as intuitive as self-evident in daily life. Still, the presence of surfaces may alter physical (bulk) properties, symmetries, and the behaviour of the overall system and constituents involved. Many properties of surfaces are closely related to (breaking) the electronic structure and thus, many macroscopic characteristics can be derived from these features. The basics of crystal structures and corresponding concepts will not be introduced here, though. For these it shall be referred to common literature [16–21], physical constants and values of physical properties can be found in [22]. The presented description of the fundamental entities is mainly based on [19], further references to literature will be given throughout the chapter.

2.1.1. Physical description of surfaces

In the case of solids, a surface represents a violation of the otherwise periodic bulk lattice structure. It leads to a variation of the electronic structure at the surface compared to the bulk as chemical bonds are rearranging due to the absence of bonding mates. For simplicity, surfaces are considered to be adjacent to vacuum in the following – if not specified differently. The situation is similar for interfaces, compare Sections 2.2.5, 2.1.3, and 2.1.4. Thermodynamically spoken, the *specific free energy of a surface*[1] γ represents the reversible work per unit area needed to create a surface, hence increasing the total internal energy U of a system in thermodynamical equilibrium. The increase is proportional to the area of the surface, thus leading to [23]

$$U(S, V, N) = TS - pV + \mu N + \gamma A, \tag{2.1}$$

where U – again – is the total internal energy of a system, T the temperature, S the entropy, μ the chemical potential, N the number of particles, γ the specific free surface energy, and A the area of the surface. The increase γA of the internal energy is positive since the crystal system does not gain energy upon establishing a surface – which in turn would imply instability of surfaces in general [24]. Note that in literature γ sometimes is referred to as the *surface tension*, compare [19, 23, 25]. The latter term will be avoided in this work, though. More details on the thermodynamics of surfaces can be reviewed in [26].
Generally, the thermodynamic quantities applied in solid state physics are temperature and pressure, since they can be determined comparably easy. Consequently, the thermodynamic potential of interest is the *Gibbs free energy*[2] [28]

$$G(N, T, p) = U - TS + pV, \tag{2.2}$$

From equation 2.1 it is clear, that any solid will tend to minimize both its surface area and free surface energy to minimize the Gibbs free energy. In the frame of this work, following mechanisms minimizing the contribution introduced by additional free surface energy are to be considered:

1. Restructuring the surface by displacement of atoms, i.e. atoms shifting inwardly or outwardly (see following Sections),

[1] In the following, it will be referred to as *free surface energy*.
[2] The Legendre transform allows for to derive all thermodynamical potentials from the total internal energy. It represents a change of the set of variables, here $U(V, S, N) \rightarrow G(p, T, N)$. Compare [27].

2. constituting a surface reconstruction by recombination of otherwise dangling bonds (see Section 2.1.3),

3. adsorption of external species via physisorption or chemisorption (see Section 2.1.5 and 4.1),

4. diffusion of heterogeneous species within the bulk-surface system, thus introducing a segregation profile (compare Sections 2.2.4 and 4.1). This is applicable if the crystal is built up out of two or more constituents, see Chapter 5.

Something not being discussed within the frame of this thesis is the impact of surface vibrations on the atomic structure of surfaces, as this effect does not significantly influence the systems studied, here. Instead, it is referred to [21] and especially within the scope of elastic surface properties [29].

2.1.2. Surface stress and surface strain

As mentioned above, the rearrangement of bonds upon establishment of a surface or interface might be accompanied by a change of the positions of the atoms close to the truncation, thus introducing positive or negative surface stress to the system. Accordingly, from a very fundamental, macroscopic point of view, it is not only the free specific energy of a surface, but also intrinsic, elastic effects such as *surface stress* and *strain* which determine the formation and therefore morphology and structure of a surface. The term *elastic* implies that a solid will reacquire its original shape after external forces are removed. Originally, the description of surface energy and surface modification is based on the work of J. W. Gibbs where interfaces between gases and solids are developed from a thermodynamical approach [19, 30]. Especially in the case of non-coherent epitaxial growth[3] of a crystalline material A on another crystalline material B, a certain amount of energy is stored in the interface [29]. In the following, we assume the crystal distortions to be small, i.e. few percent of the lattice constant.
Here, surface stress is represented by an elastic stress tensor $\tau_{ij} = \partial f_i / \partial a_j$, compare [19, 31]. It describes the change of the force $\mathrm{d}f$ in direction i with respect to the areal element $\mathrm{d}a$ with orientation j. For a 3D solid, the tensor describing the stress

[3] Here, non-coherent means, that the two crystalline materials exhibit different lattice constants, $a_A \neq a_B$.

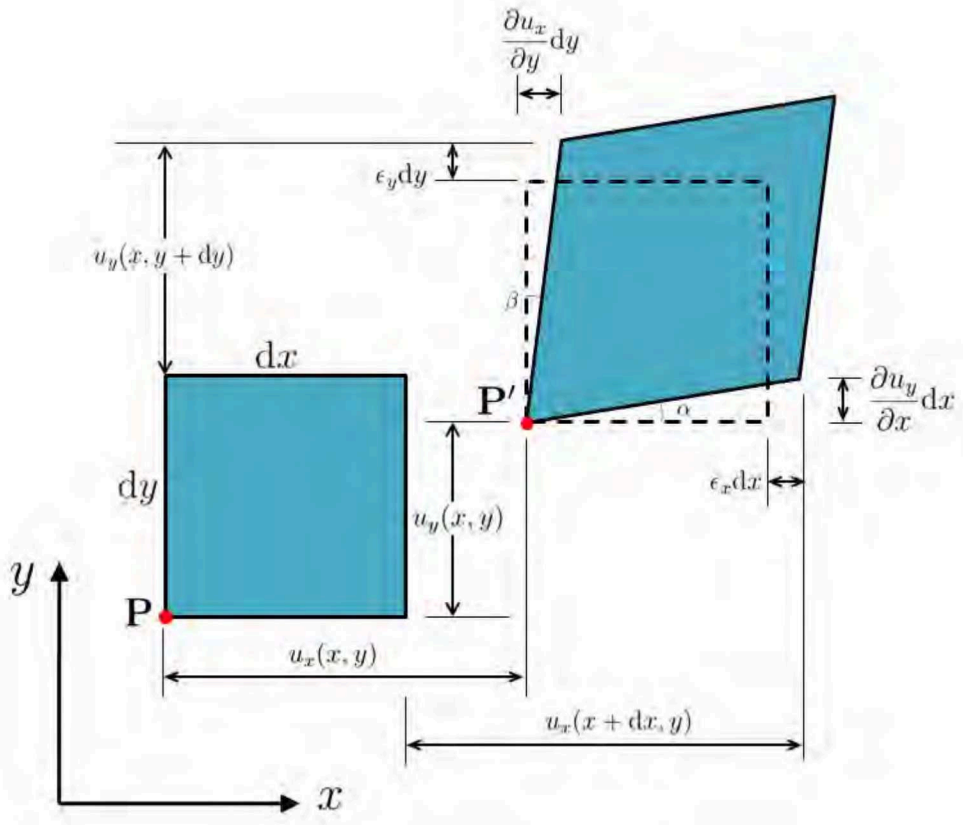

Figure 2.1.: Illustration of strain deforming a 2D shape. Originally, the figure positioned at **P** has the size $\mathrm{d}x \cdot \mathrm{d}y$. The transform initiated by strain includes the displacement from **P** to **P′**, both positions are marked with a red dot. The dashed square represents the original shape, translated by displacement **u**(x,y). The resulting shape is deformed with normal strain components $\varepsilon_{x,y}$ and shear strain, represented with angles α and β. Adapted from [32].

state at all points will exhibit following form [32]:

$$\boldsymbol{\tau} = \begin{pmatrix} \tau_{xx} & \tau_{xy} & \tau_{xz} \\ \tau_{yx} & \tau_{yy} & \tau_{yz} \\ \tau_{zx} & \tau_{zy} & \tau_{zz} \end{pmatrix}. \tag{2.3}$$

The components $\tau_{i=j}$ of $\boldsymbol{\tau}$ are called *normal stress*, whereas components $\tau_{i\neq j}$ are referred to as *shear stress*. The definition is such that τ_{xx} is perpendicular to the yz-plane, and components τ_{xy} and τ_{xz} lay within this face.
Similarly, the strain tensor ε can be defined as the change of the length of a volume element $\mathrm{d}u$ (called *displacement field*) due to a change in the position $\mathrm{d}x$ [32]:

$$\boldsymbol{\epsilon} = \begin{pmatrix} \varepsilon_{xx} & \varepsilon_{xy} & \varepsilon_{xz} \\ \varepsilon_{yx} & \varepsilon_{yy} & \varepsilon_{yz} \\ \varepsilon_{zx} & \varepsilon_{zy} & \varepsilon_{zz} \end{pmatrix}. \tag{2.4}$$

Again, the diagonal elements $\varepsilon_{i=j}$ denote *normal strain* and components $\varepsilon_{i\neq j}$ shear strain. Figure 2.1 illustrates how strain components and displacement field act on an exemplary 2D shape. The strain components can be written as [29]

$$\epsilon_{ij} = \frac{1}{2}\left(\frac{\partial u_i}{\partial x_j} + \frac{\partial u_j}{\partial x_i}\right), \tag{2.5}$$

u_i being the components of the displacement field and x_i denoting the three dimensions of space. The displacement field $\boldsymbol{u}(\boldsymbol{r})$ describes the translation of a point $\boldsymbol{P}$ at position $\boldsymbol{r}$ to point $\boldsymbol{P'}$ at position $\mathbf{r}'$. Strain and stress tensor are connected via the generalized *Hooke's law* in Einstein notation [33]

$$\tau_{ij} = C_{ijkl}\epsilon_{kl} \tag{2.6}$$

$$\varepsilon_{ij} = S_{ijkl}\tau_{kl}, \tag{2.7}$$

with

$$\mathbf{CS} = \mathbb{1}. \tag{2.8}$$

$\mathbf{C}$ is called *stiffness tensor* or stiffness constant and $\mathbf{S}$ *compliance tensor* or compliance constant.

In the macroscopic picture of a surface, the surface stress tensor $\tau_{ij}^{(s)}$ varies along the surface normal z, and can be expressed by [17, 19, 24]

$$\tau_{ij}^{(s)} = \int_{-\infty}^{\infty} \mathrm{d}z[\tau_{ij}(z) - \tau_{ij}^{(b)}], \tag{2.9}$$

where $\tau_{ij}^{(b)}$ denotes the stress tensor deep inside the bulk and $\tau_{ij}(z)$ describes the spatial variation of tension along z. Within this frame, i and j correspond to x and y, respectively, and z points away from the surface for values larger than zero. Note that generally $\mathrm{d}f$ cannot be formulated explicitly anymore, if all possible elastic influences occurring at surfaces in mechanical and thermodynamic equilibrium are to be considered, see [29]. This impedes e.g. the exact calculation of equilibrium shapes (see below).
For sufficient large z, $\tau_{ij}(z)$ equals the bulk stress tensor and the corresponding

components of $\tau_{ij}^{(s)}$ vanish. Only for a narrow region at the surface, equation 2.9 has non-vanishing elements. Basically, the surface stress is the reversible force per area to compress or stretch the surface (relaxation of the topmost layers). Further details on the thermodynamical interpretation can be found in [24]. Details on the mathematical description on surface stress and surface strain can be reviewed in [33–36] – ordered from rather basic to very in-depth. Additionally, details on the stiffness and compliance tensors, especially in anisotropic cases (orthorhombic crystal structures e.g.) can be found in [32].
The surface stress is linked to surface free energy via the *Shuttleworth equation*

$$\tau_{ij}^{(s)} = \gamma\delta_{ij} + \frac{\partial\gamma}{\partial\epsilon_{ij}}, \tag{2.10}$$

where δ_{ij} denotes the Kronecker Delta. Details on the mathematical derivation are omitted here, but can be reviewed in [17, 19, 24, 37].

2.1.3. Restructuring of surfaces

Forming any surface will increase the total internal energy U while keeping temperature, particle number, and total volume constant (equation 2.1). Additionally, establishing surfaces likely also includes the formation of surface defects such as steps and surface reconstructions or super structures. The latter two denote a (crystalline) surface where due to rearrangement of bonds the superficial (crystal) structure is different from the bulk structure[4]. In Figure 2.2 examples of surface reconstructions are depicted, 2.2(b) applies for the Pt(110) surface under certain conditions [39]. Generally, in surface reconstructions the unpaired bonds form a highly strained surface lattice depending on details of the electronic structure and the environmental conditions (i.e. the adjacent medium, temperature etc.). Figure 2.3 represents a top view of a surface lattice (blue-greyish circles) on a bulk structure (red circles) and indicates the nomenclature of surface lattices. In this figure, a_1 and a_2 denote the unit vectors of the 2D bulk unit cell whereas c_1 and c_2 represent the unit vectors of the surface lattice. The unit cell of the surface lattice is described by [16]:

$$\left(\frac{c_1}{a_1} \times \frac{c_2}{a_2}\right) R\alpha, \tag{2.11}$$

[4]The term *superstructure* is especially used for heterogeneous material systems, e.g. graphene clusters on metal surfaces [38].

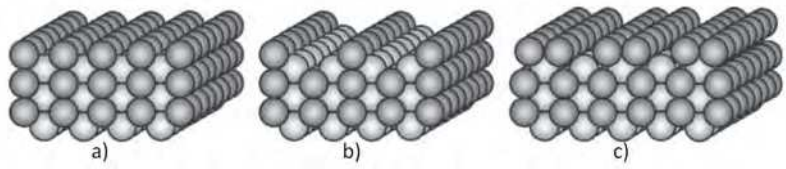

Figure 2.2.: Possible reconstructions of face-centered cubic (110) crystal surfaces: a) unreconstructed, b) missing row (MR) reconstructed, c) pairing row (PR) reconstructed. Taken from [37] and modified.

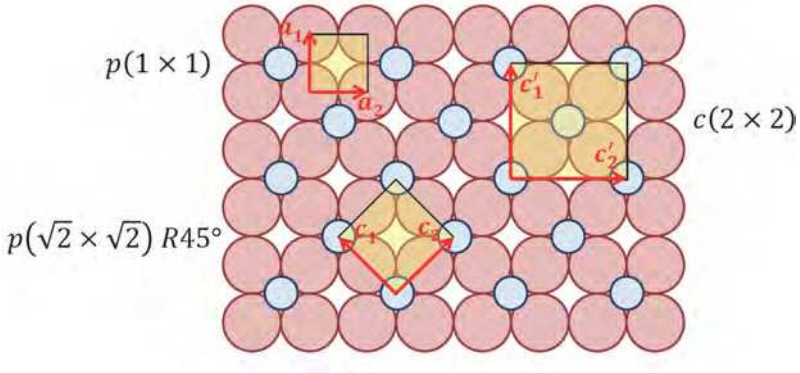

Figure 2.3.: Nomenclature of surface reconstructions according to [40]. Taken from [16].

where $R\alpha$ indicates that the surface unit cell might be rotated around the surface normal $\boldsymbol{n}$ with respect to the lattice unit cell. This is the case for the example in Figure 2.3, where the primitive cell of the surface lattice $p(\sqrt{2} \times \sqrt{2})R\alpha$ is stretched by a factor of $\sqrt{2}$ and rotated by 45 ° around $\boldsymbol{n}$. p and c additionally indicate whether the surface lattice is primitive or centred. Compare $p(\sqrt{2} \times \sqrt{2})R45\,^\circ$ and the non-primitive but centred $c(2 \times 2)$. Some lattices cannot be described using this notation and a matrix notation has to be utilized. Additional details on this can be found in [19].

Note that in addition to relaxation and surface reconstruction (or superlattices), many other violations or variations of the crystal structure and its surfaces are possible, that blur the image of an idealized surface. These surface defects cover both atomistic and macroscopic length scales: dislocations, kinks, ledges, terraces, (foreign) adatoms, and adsorbates – just to name some (see [19]). In Figure 2.4, potential inner-particle and interfactial defects (particle-particle or particle-substrate) are depicted.

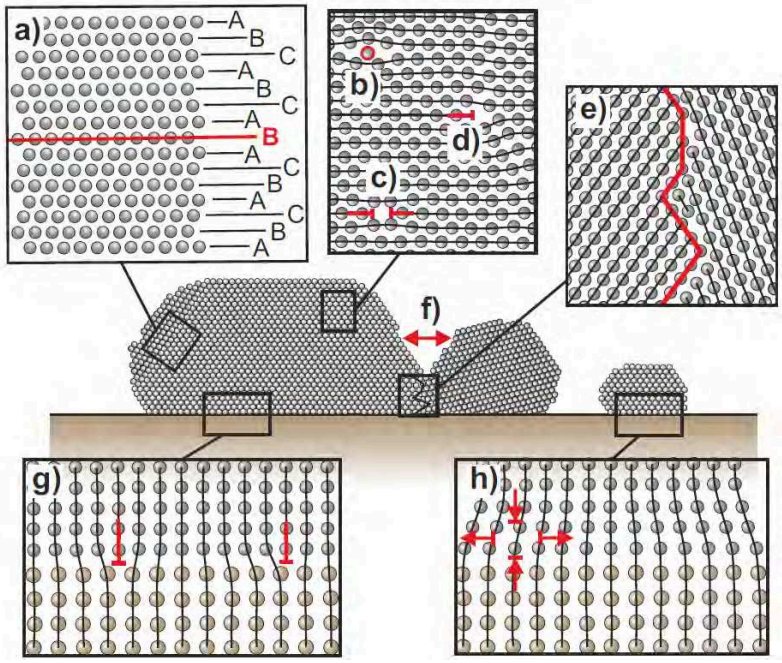

Figure 2.4.: Different types of epitaxial defects: a) internal twinning, b) interstitial atom, c) vacancy, d) inner-particle dislocation, e) grain boundary – here as a consequence of f) particle coalescence, g) interfacial dislocations, and h) interfacial strain. Taken from [41].

2.1.4. Shape of supported particles

What additionally determines the macroscopic shape of a crystal is the fact that for solids with a crystal structure γ depends on the orientation $\boldsymbol{n_i}$ of the respective face with respect to the bulk structure, i.e. $\gamma = \gamma(\boldsymbol{n_i}) = \gamma(hkl)$, compare [19]. Here, (hkl) denote the *Miller indices*. The macroscopic shape of a crystal in thermodynamic equilibrium is then determined by the requirement to minimize the free energy $\int_A \gamma(\boldsymbol{n_i})\mathrm{d}A$.

Nevertheless, determining the surface energy parameters proves difficult for solid surfaces as probing appears challenging and solid surfaces are often not in equilibrium, inhomogeneous and contaminated [37]. Examples for experiments conducted are shown in [43–45]. It turns out that one consequence of γ depending on the orientation $\boldsymbol{n_i}$ of each face is faceting, i.e. formation of a geometrical shape with only few different, lowest-energy facet types occurring – e.g. {111} and {100}. Furthermore, examples of calculated surface energies and surface stress can be found in [37, 46], especially for the case of Pt and Rh see [39].

The minimization requirement allows for the macroscopic equilibrium shape of a crystal to be estimated using the *Wulff's theorem* or *Gibbs-Curie-Wulff's theorem* [18, 47]:

$$\frac{\gamma_i}{h_i} = const, \tag{2.12}$$

where index i represents a set of Miller-indices (hkl) and h_i is the distance between a crystal's centre and the corresponding (hkl)-plane. Basically, equation 2.12 states that in equilibrium the distances between the crystal's centre and its facets are proportional to the corresponding specific free surface energies [18]. A theoretical approach of how to obtain the crystal shapes is presented in [28]. Note, that the Wulff's theorem and the prediction of surface energies rely on the assumption of thermodynamical equilibrium at zero Kelvin. The influence of temperature on the shape of crystalline particles will be discussed in 2.1.5.

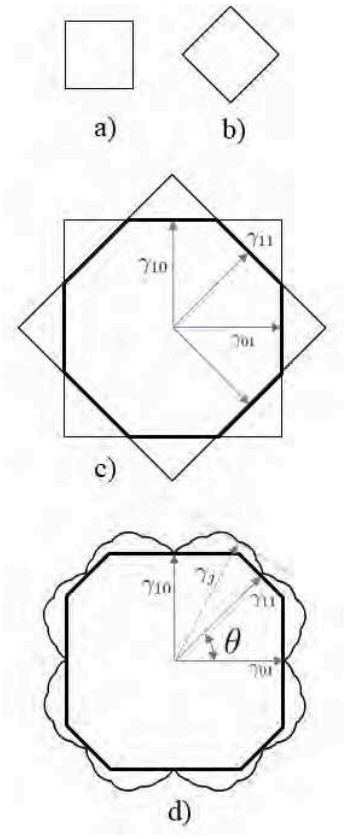

Figure 2.5.: Determining the 2D geometry of a crystal: a) planes with (01) type, b) planes with (11) type, and c) an overlay of a) and b). The inner envelope (thick, black line) of the overlaying faces in c) is the resulting macroscopic shape of the crystal. In d) a full polar plot of $\gamma_i(\theta)$ is shown (thin line), where the tangents to the smallest h_i yield the inner envelope (thick line) and reflect the crystal's shape. Figures a)-c) adapted from [31, 42] and d) adapted from [19].

Practically, one obtains the macroscopic shape of a crystal and the corresponding facets by converting equation 2.12 into a polar plot, the so-called *Wulff-plot*. Figure 2.5 depicts qualitatively the principle of how to yield the equilibrium shape. Here, we assume that $\gamma_{01} = \gamma_{10}$ and γ_{11} are the lowest specific free surfaces energies of a crystal[5]. Figure 2.5 a) and b) show the planes built up by the normals to h_{01} and h_{11}, respectively. The inner envelope of the overlay of a) and b) (see Figure 2.5 c), thick line) represents the resulting equilibrium shape of the crystal. When considering all possible planes i.e. plotting γ_i in polar coordinates one yields a geometry as depicted in Figure 2.5 d). The inner envelope of all normals to h_i

[5]Note that for convenience in Figure 2.5 the free surface energies are indicated. Correctly, one would assign distances h_i to the arrows. The scale of the distances h_i are normalized with the energy – see equation 2.12.

results in the equilibrium shape of the considered solid. A plane excluded from the equilibrium shape is indicated by γ_j. Its corresponding distance h_j from the centre is too far to be considered within the inner envelope.
Examples of the free equilibrium shapes of monometallic Pt, Rh, and the bimetallic PtRh-alloy crystals are shown in [41]. The very basic though helpful concept of the Wulff-plot gives a first impression of what to expect when trying to describe free crystals and their surfaces. In reality, shapes of crystals or crystalline particles will differ from ideal theory, as will be discussed in the following.

The exact description of the equilibrium shape of crystals experiences limitations in the cases of either the transition towards very small particles (clusters) or crystals grown on supports. As the Wulff's theorem does not account for higher order interactions e.g. between edges of facets or steps, the equilibrium shape will vary in the case of small particles where second or higher order interactions will attribute to the surface free energy as undercoordinated atoms on spatially seperated faces will start to interact, if the cluster's size is small enough, see [48–52].
More important for this work in particular is that the interaction between a crystal or nanoparticle with its support will modify Wulff plots. For supported particles, the original free equilibrium shape is truncated, see Figure 2.6 for a qualitative example. A highly truncated Wulff shape determined from high resolution transmission electron microscopy (HRTEM) measurements and theoretical surface energies is shown in Figure 2.7 [53]. An example of platinum particles on γ-Al_2O_3 can be found in [54]. The determination of the particle's shape follows the *Wulff-Kaishew theorem* [18],

$$\frac{\Delta h}{h_i} = \frac{E_{adh}}{\gamma_i}, \tag{2.13}$$

or

$$\frac{h_m}{h_i} = \frac{\gamma_m - E_{adh}}{\gamma_i} \tag{2.14}$$

where Δh is the truncation of the particle along the surface normal $\boldsymbol{n}$ (the corresponding surface energy and distance are γ_m and h_m) at the interface and E_{adh} the adhesion energy which in turn scales the truncation Δh. E_{adh} on the other hand can be determined via the relation of *Dupré* [18],

$$E_{adh} = \gamma_{metal} + \gamma_{oxide} - \gamma_{interface}. \tag{2.15}$$

Here, γ_{metal} and γ_{oxide} together form the energy gained by forming the interface

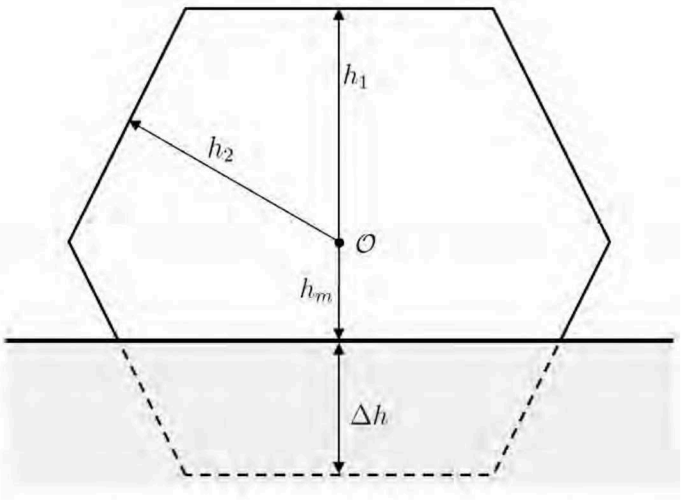

Figure 2.6.: Truncated Wulff shape of a crystalline particle on a foreign substrate. The particle's centre is indicated by $\mathcal{O}$. h_1 and h_2 point to free surfaces that have the same distance from the centre as in the case of a free crystal. The dashed line indicates the shape of a free particle according to equation 2.12, the greyish area adumbrates the substrate.

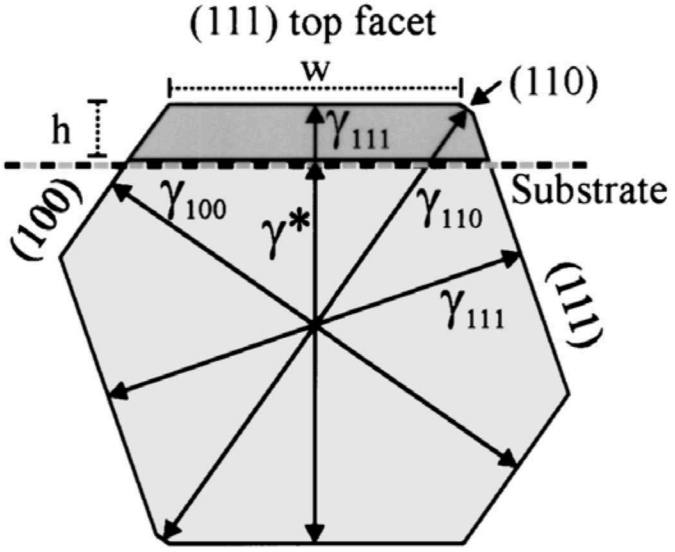

Figure 2.7.: Cross-section through a Pd cluster with calculated surface energies taken from [55]. Image taken from [53].

as the total surface area of the system decreases and $\gamma_{interface}$ denotes the energy required to build up the interface itself. In the non-wetting case of $\gamma_{interface} = 0$ the original Wulff shape according to equation 2.12 is regained [18].
Relation 2.15 may become arbitrarily complicated, when considering additional effects such as strain and dislocations. See [56] and [29] for elaborate discussions of these effects. In particular, for a discussion of dislocations see [57]. Generally, $\gamma_{interface}$ decreases with increasing number of defects at the interface between particle and substrate. It also decreases with increasing size of the particle or cluster [58].

2.1.5. Influence of gas atmosphere and temperature on equilibrium shape

Two more remarks towards the equilibrium shape of crystals will be discussed in this section. The equilibrium shape will vary upon changing the thermodynamical conditions, namely temperature and adjacent medium. Generally, acquiring the equilibrium shape can be hindered by kinetic limitations like diffusion barriers, such that some Wulff-shapes and surface reconstructions become accessible for the crystal at elevated temperatures only. Likewise, adsorbates from the adjacent medium (air e.g.) may stabilize metastable structures or modify the energetic most favourable equilibrium shape. These effects play an important role in Chapters 3 and 4 and will be further discussed there.

In general, crystals obtain the highest anisotropy ratio between different free surface energies γ_i at zero Kelvin [59]. With increasing temperature, the crystal may transit through various metastable shapes upon establishing side facets and decreasing the anisotropy, finally resulting in a round shape with isotropic surface energy [60, 61].

Especially when studying catalytic phenomenons, the effect of physisorbed or chemisorbed species on the surface must be regarded. Particularly upon chemisorption, establishing or braking bonds may involve energies of as much as several eV [21]. Thus, it is possible for adsorbates to induce the formation of a surface relaxation or reconstruction, or to remove it – as in the case of oxygen adsorbed on the Pt(110) surface [21]. Further details are discussed in [31, 57, 62]. More details on the interplay between superficial atomic structure and adsorption properties – and the closely related catalytic activity – will be given in Section 2.3.

2.1.6. Influence of growth technique on particle shape and facet growth speed

The samples used in the frame of this thesis were grown via molecular beam epitaxy, see Section 2.2.2. Generally, techniques utilizing molecular or atomic ion beams may have an impact on the growth and epitaxy of particles or thin films, because the ion beam has a direction and a penetration depth. In sputtering techniques, the employed beam does not consist of single atoms, but clusters or grains with a certain velocity. The causes can be manifold – depending on the respective properties of the techniques [57, 63]. If growth is kinetically limited[6], deposition via grains of a material – as in sputter deposition – will lead to a broad distribution of grains, grain boundaries, internal twinning, and an overall defect-rich structure with decreasing long-range order. If the velocity of specimen in beam-employing deposition techniques is too high, diffusion into the substrate is possible thus creating a rough, less well-defined interface and introducing defects.
Generally, the growth speed varies for different facets. Since non-equal crystal facets exhibit different superficial particle densities, their growth speed upon a constant impinging adatom rate will differ [57]. In beam-employing deposition techniques the impinging rate itself is strongly dependent on the geometry of the setup, as usually the beam will be approximately unidirectional and perpendicular to the substrate's surface and thus to top-facets of particles or islands. Consequently, the setup influences the growth speed of respective facets and thus the particle shape itself [61]. Figure 2.8 indicates eventually developing particle shapes for metals with fcc crystal structure upon different ratios of growth speeds between the respective facets. Modifying facet growth speeds thus implies huge impact on the particle's morphology, see [64] for further reading and examples.

2.2. Growth of supported particles

Now that surfaces of crystals have been discussed in general, let us have a closer look on the growth of the samples examined within this work, again starting with a brief discussion of the fundamental energetics leading to the principles of nucleation. Subsequently, different modes of growth and the underlying processes will be examined briefly.

[6] This means that surface diffusion of the deposited clusters or atoms is hindered.

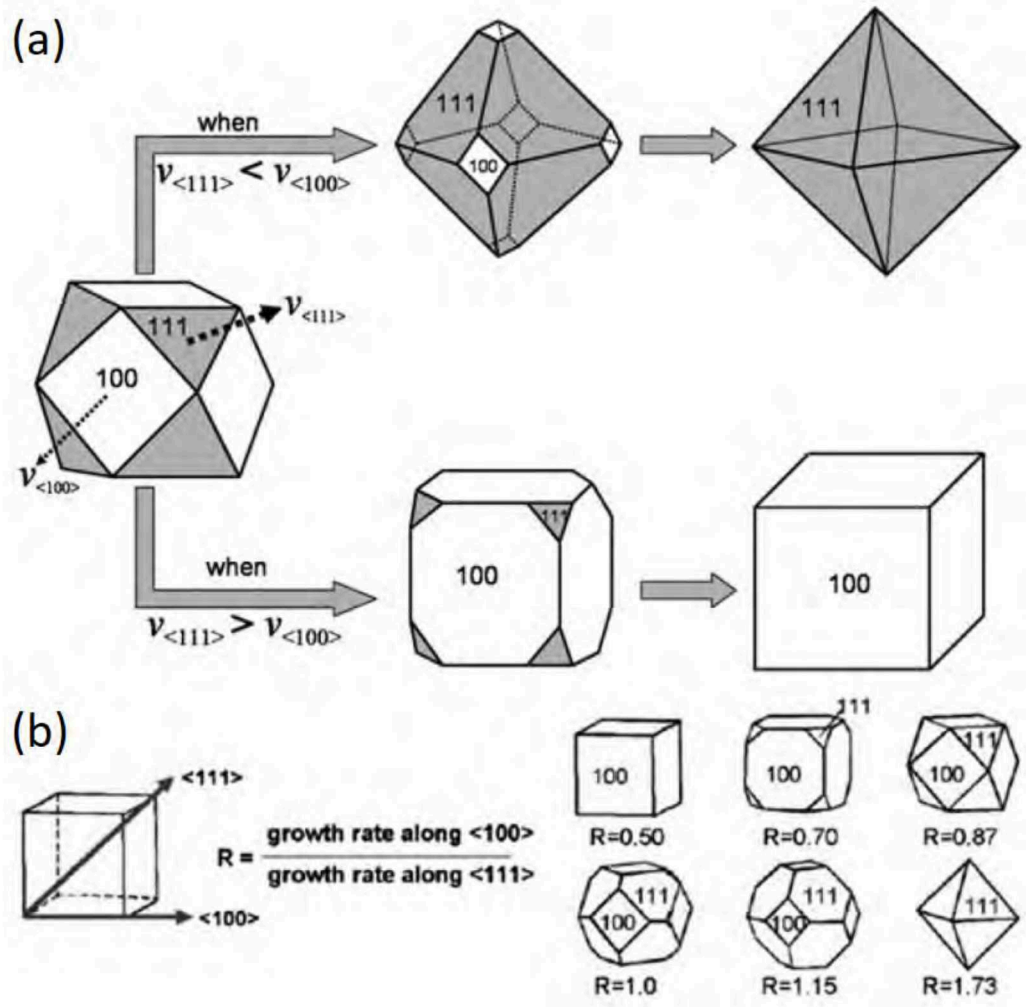

Figure 2.8.: Schematics of the morphology of a cubic crystal upon varying the velocity $\nu_{<xyz>}$ of growth perpendicular to the {xyz} face. (a) eventually forming particle shapes indicating shrinking and growing faces if growth rates significantly differ from each other. (b) indicates different crystal shapes for different ratios of growth rates. Taken from [61] and modified, original from [64].

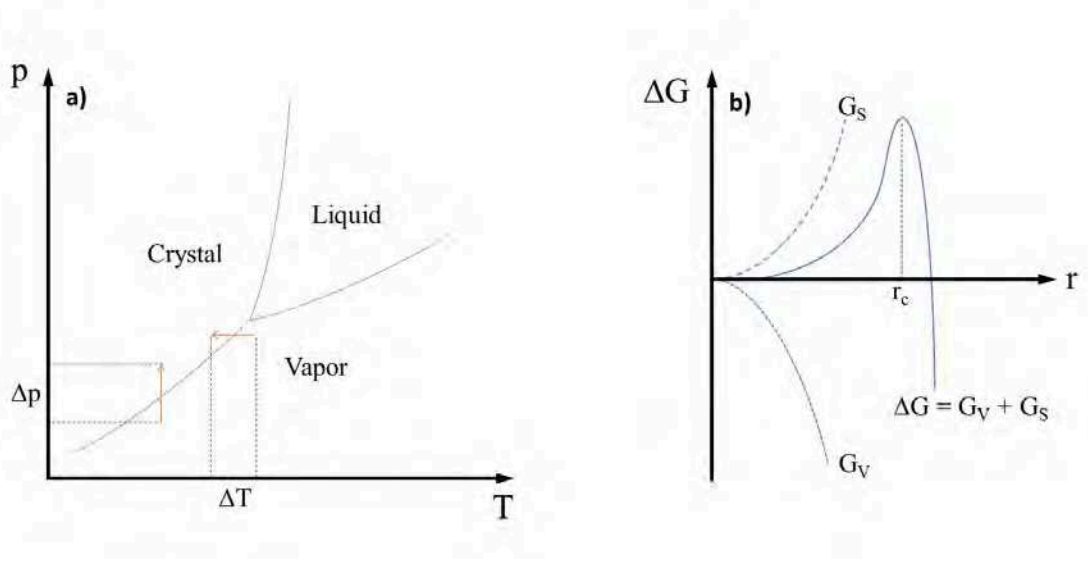

Figure 2.9.: a) p-T phase diagram of a system constituting of one component. Orange arrows indicate exemplarily phase transitions via undercooling (horizontal arrow, ΔT) and supersaturation (vertical arrow, Δp), compare [18]. b) ΔG as a function of nucleus' radius r. The overall change in ΔG (solid line) is the sum of both the surface and volume contribution G_S (dashed line) and G_V (dotted line), compare [31].

2.2.1. Mechanisms of nucleation and epitaxial growth

As a starting point, a system in thermodynamical equilibrium is regarded, consisting of one element only. Again, the *Gibbs free energy G(T,p,N)* is considered, compare equation 2.2. Analogous to Section 2.1.1, the system will converge towards the minimum of G. The existence of separated phases in equilibrium is allowed under the assumption of an infinitely large, flat boundary dividing the phases. Additionally, temperatures, pressures, and chemical potentials within the phases have to equal the respective variable in the other phase [18]. Such a system is depicted in Figure 2.9 a), where the blue lines indicate the points where the system meets the conditions aforementioned – coexistence of two or three phases. Deviating from these states of equilibrium by changing either pressure or temperature – leaving the other constant – will stabilize one phase. This implies a change of the chemical potential, which in general is a function of both temperature and pressure. This difference drives the transition towards another phase [31]. If the transition from gas phase to crystalline phase is driven by a difference in temperature, it is called *undercooling*; if it is driven by pressure (or concentration C), it is called *supersaturation* – see Figure 2.9 a). Nucleation will appear spontaneously if the difference in the chemical potentials (and thus Gibbs free energy) is negative. Generally, this difference in $\Delta\mu$ or ΔG follows

following behaviour [31]:

$$\Delta\mu \propto \Delta G \propto \ln\left(\frac{C}{C_0}\right) \propto \ln\left(\frac{p}{p_0}\right). \tag{2.16}$$

Here, p_0 and C_0 are the pressure and concentration in equilibrium. This nucleation mechanism is called *homogeneous nucleation*. In other words, homogeneous nucleation is the direct condensation of nuclei out of the gas phase and does not involve any kind of substrate surface in the first place[7]. In fact, the formation of growth nuclei does not imply formation of a stable solid phase. On the one hand, this is due to dissolving atoms or nuclei, if nucleation itself is a equilibrium process. On the other hand, forming a solid does include developing a surface with positive surface energy, see Section 2.1.1. Hence, the nuclei might dissolve back right away into the gas phase, again. In these terms, the change in Gibbs free energy ΔG can be written as the sum of the two opposing contributions of surface and volume, G_S and G_V – see Figure 2.9 b). Referring to these two contributions, newly formed nuclei are stable, if a critical radius r_c is overcome. Intuitively, the latter increases with increasing temperature, hence impeding condensation of the solid phase at too high temperatures [31]. Further, r_c decreases with increasing supersaturation [57].

If in turn nucleation does involve a foreign substrate surface, it is called *heterogeneous nucleation* [57]. If the substrate exhibits different lattice parameters, it is called *heteroepitaxy*. Generally, there are three relevant modes of heteroepitaxial (and homoepitaxial) growth [65]:

1. layer-by-layer growth (Frank-van der Merwe)

2. 3D/island growth (Volmer-Weber)

3. layer + island growth (Stranski-Krastanov).

These three rather general modes of epitaxial growth are, essentially, independent on the growth technique. They are presented more extensively in [29] including an extensive discussion of the influence of strain on these growth models. Mixed growth models and their variations are presented in [57]. Macroscopically, the growth of a crystal phase on a substrate can be described using surface free energies. Referring again to the examination of surface energies in equation 2.15 in Section 2.1.4, wetting

[7] The term *homogeneous growth* in turn refers to growth of a species on a substrate of the same material.

of metal particles on an oxide support is not expected if the energy required to constitute and maintain the metal-substrate interface is higher then the sum of both surface free energies of the metal and the substrate surface: $\gamma_{interface} > (\gamma_{metal}+\gamma_{oxide})$. Contrary, complete wetting is expected in the case of $\gamma_{oxide} > (\gamma_{metal} + \gamma_{interface})$, see [57]. Some authors refer to the *Bauer criterion* [66], which states 3D growth mode in the case [67]:

$$\gamma_{interface} + \gamma_{metal} > \gamma_{oxide}. \tag{2.17}$$

The correlation of this macroscopic, energetic perspective with above atomistic modes of epitaxial growth is not necessarily straight-forward. Exemplarily, the formation of islands can be more favourable even under complete wetting conditions if the layers are highly strained – see elaborate discussion in [57]. Growth mechanisms will be discussed more specifically in terms of molecular beam epitaxy in Section 2.2.3, after introducing the technique itself.

2.2.2. Molecular beam epitaxy

To realize well-defined growth of supported nanoparticles, molecular beam epitaxy (**MBE**) was applied in this work. In MBE, a molecular or mono-atomic beam from a source of a certain material or composition is facilitated to grow epitaxial thin films or islands on a substrate. Usually, MBE is facilitated at elevated temperatures to enable surface diffusion of the material to be deposited. Typical growth rates can be in the order of monolayers per second, which is slow enough to allow arriving atoms to migrate on the substrate without being hindered by subsequently impinging atoms [68, 69]. The MBE system is embedded in an ultra-high vacuum (**UHV**) vessel, where a pressure of below 10^{-9} mbar on the one hand allows for mean free paths of the atomic beam to be in the order of kilometres, allowing the atoms to arrive on the substrate collision free. On the other hand, this pressure regime ensures that the surfaces are as free of unwanted adsorbates from air as possible and the thin films or islands grow without contamination or incorporation of foreign species. Facilitating UHV has another advantage, as various probing techniques can be applied during growth, such as AES (Auger electron spectroscopy), RHEED (reflection high energy electron diffraction), ellipsometry, and laser interferrometry among others [68]. Typically, a mechanical beam shutter is used for abrupt control of the beam. Together with the stable flux, this well-defined growth environment is an additional unique feature of MBE-vessels. The sample environments used for the samples investigated in this thesis, are presented in Section 2.5.1. MBE-technique

and related vessels in general are discussed more extensively in [68].

2.2.3. Growth mechanisms in molecular beam epitaxy

The requirements for actual crystal growth differ from the prerequisites of e.g. homogeneous nucleation as one finds that, in fact, growth of a (supported) film or particle is a strongly non-equilibrium process [19, 70] – concerning the molecular beam epitaxy technique applied for the samples for this thesis[8]. This is determined by the nature of the underlying, opposing processes. In equilibrium, the rate of impinging, condensing atoms forming layers and islands, and the rate of atoms re-evaporating from the substrate or decaying islands must match. Thus, there would be no net crystal growth after a certain time. To understand the effects driving exactly this formation of either particles or layers, a change from the macroscopic picture towards an atomic perspective is necessary. Figure 2.10 the stages occurring on the atomic level during growth, they will be discussed now in the context of MBE. The atoms to be deposited on the substrate are adsorbed on the surface with a sticking probability of nearly unity [66, 71, 72]. Being adsorbed, the metal atoms may move on the substrate surface via surface diffusion, Figure 2.10 c). Surface diffusion is strongly depended on the local surface potential and especially temperature, indicated by the *Arrhenius law* [73]:

$$N = \omega_D \exp\left(-\frac{E_0}{k_B T}\right), \tag{2.18}$$

where N is the average number of atomic jumps per unit time, ω_D is the Debye-frequency of the atomic species, E_0 the energetic diffusion barrier (typical 0.1 to 1 eV), k_B Boltzmann constant, and T the temperature. Average surface diffusion lengths in a certain time interval can already differ by a factor in the order of 10^3 when comparing paths at 300 K and 400 K, respectively [73]. Consequently, the crystal structure and roughness of deposited material are strongly dependent on the temperature and not only the local energetic structure of the surface. If the temperature is sufficiently high, atoms diffusing on the surface will likely adsorb at positions of minimal local potential, such as kinks, steps , vacancies, point defects, and adatoms – see Figure 2.10 i)-iv). Depending on the local binding energies and temperature, diffusion onto already formed islands d) or from islands towards the substrate e) is possible, thus affecting the growth mechanism. Atoms may also desorb again after some time, if the activation energy is overcome. Further growth of islands

[8] Other epitaxial techniques such as vapour phase epitaxy or liquid phase epitaxy approximately maintain equilibrium conditions during growth [68].

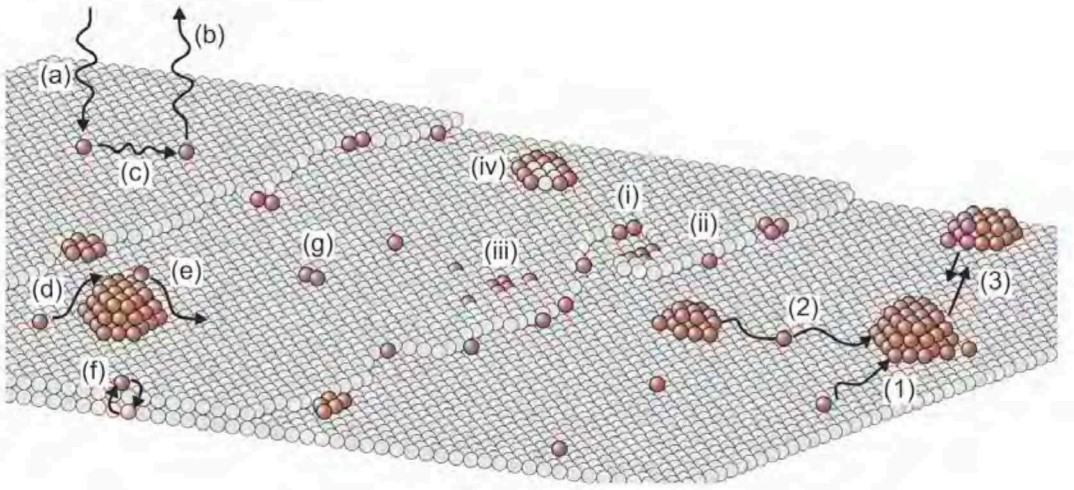

Figure 2.10.: Overview of processes on microscopic level during growth: a) adsorption, b) desorption c) surface diffusion, d) on-step diffusion, e) down-step diffusion, f) inter-diffusion, g) nucleation; arriving atoms preferably condense on: i) kinks, ii) steps, iii) vacancies and point defects, and iv) adatoms; stable nuclei form bigger particles via 1) trapping of diffusing atoms, 2) inter-particle diffusion or Ostwald-ripening, and 3) particle coalescence. Figure taken from [41].

or even layers continues by agglomerating diffusing atoms 1), inter-particle diffusion 2) or coalescence 3). From this atomic perspective, it is clear that surface diffusion – hence diffusion barriers and temperature – is the main driving force determining the growth mechanism together with the deposition rate [73], neglecting desorption for the moment. If diffusion is kinetically limited due to low temperature, the diffusion barriers will prevent adsorbing atoms from moving on the surface and eventually the deposited material will adopt an amorphous structure.

In a general approach, a growth equation describing the local height $h(x,t)$ incorporating surface diffusion may adapt the form [73]

$$\frac{\partial h(x,t)}{\partial t} = -\nabla^4 h(x,t) + F(x,t) + \eta(x,t), \tag{2.19}$$

where $F(x,t)$ represents the (homogeneous) atomic flux impinging the surface and $\eta(x,t)$ the uncorrelated, statistical fluctuation on the atomic flux[9]. This equation accounts for the fundamental driving forces in MBE and reflects roughly the growth process at large length scales far from interatomic distances. When accounting for

[9]The formula arrises from the continuum equation $\frac{\partial h}{\partial t} = F(h,x,t)$ whereas diffusion is incorporated by another continuity equation $\frac{\partial h}{\partial t} = -\nabla \cdot \boldsymbol{j}(x,t)$, which connects the local height with an atomic flux $j \propto \Delta\mu$ parallel to the surface.

desorption, surface tension etc., it becomes more complicated, evolving nonlinear terms which hinder correct scaling behaviour when predicting the outcome of the growth process. Further details can be found in [73]. A deviation of rate equations can be found in [18]. For more models describing MBE growth (esp. for group III-V semiconductors) it is referred to [57, 70, 74–77].

2.2.4. Pt, Rh, and alloyed nanoparticles

With the principles of growth and nucleation introduced, this chapter now focusses on the materials and measurement techniques employed. For the studies conducted in this thesis, two different nanoparticle compositions emplyoing two different elements were chosen. These are pure platinum particles and bimetallic platinum rhodium particles with two different supports (see next section). Apart from famous applications as coin metals e.g., both platinum and rhodium have an even larger impact on catalytic applications due to their catalytic activity and their selectivity to different gases [78]. This aspect is discussed more in detail in Section 2.3.
Both platinum and rhodium crystallize in face-centred cubic lattices, with lattice parameters of $a_{Rh} = 3.804\,\text{Å}$ [79] and $a_{Pt} = 3.923\,\text{Å}$ [80]. The miscibility of platinum-rhodium alloys was subject to discussions in the past. Whereas *Moffat et al.* reported a miscibility gap of the alloy across a broad range of temperature [81], *Maisel et al.* reported homogeneous alloying without formation of separated phases [82], where the average lattice constant can be determined according to *Vegard's law* $a_{\text{alloy}} = x \cdot a_{Pt} + (1 - x) \cdot a_{Rh}$, with x denoting the ratio of platinum [83, 84]. The results of this thesis are in line with the assumption of homogeneous miscibility of the binary alloy for bulk material. However, due to different free surface energies of platinum and rhodium, elemental segregation occurs at the interface and surface of the studied nanoparticles [85, 86]. This is additionally modulated during catalytic experiments due to the different affinity of platinum and rhodium towards oxygen, resulting in a temperature and gas atmosphere dependent agglomeration of either platinum or rhodium at the surface of nanoparticles, see especially Sections 4.4 and 5.4.1. Phenomena related to supported particle growth, sintering, segregation, and exposure to gases are discussed in the following chapters.

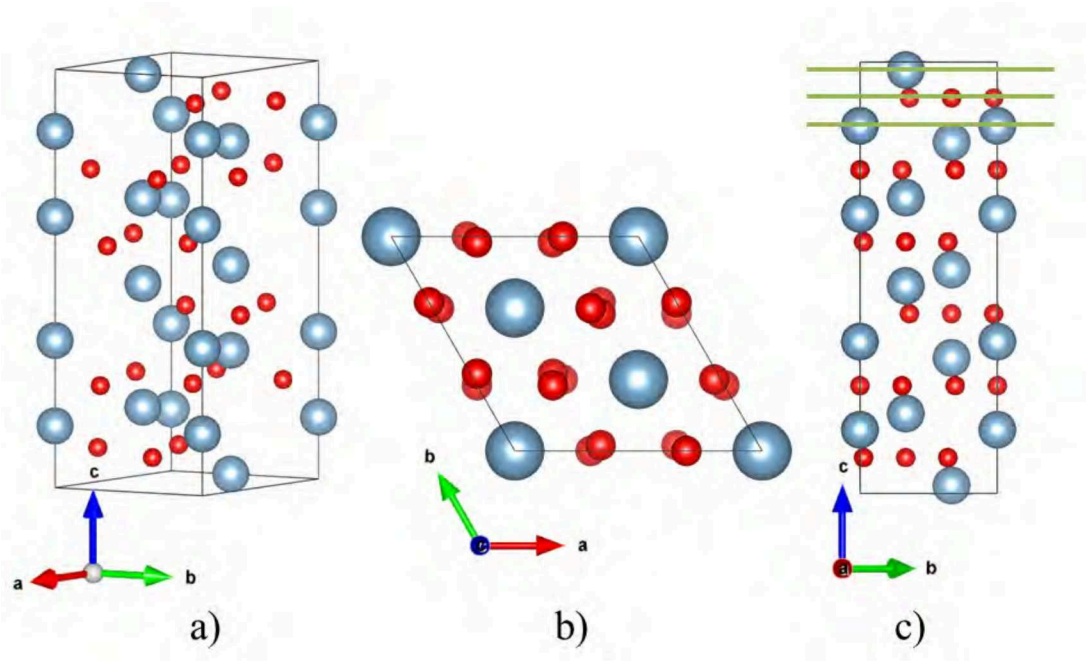

Figure 2.11.: Unit cell of α-Al_2O_3. Blue spheres represent Al-atoms, red spheres oxygen. Here, a) represents a 3D-side view, b) a top-view with the c-axis pointing towards the spectator, indicating a hexagonal-type structure, and c) a pure side view with a pointing towards the spectator. Thick, green lines in c) indicate the three different possibilities of surface terminations along the c-axis. Crystallographic axes are indicated in the bottom left, respectively. Generated with [87].

Termination	Surface treatment	Surface structure	Technique, reference
O layer	Heating in O_2 plasma, 850 °C	$T < 750$ °C: (1×1); $T < 1000$ °C: $(\sqrt{3} \times \sqrt{3})R30°$; $T > 1100$ °C: $(\sqrt{31} \times \sqrt{31})R \pm 9°$; Mixed Al- and O terminated domains	LEED supported by AES [88]
Single Al layer	UHV, RT	(1×1)	TOF-SARS, LEED [89]
	UHV annealing to 1100 °C	(1×1); 63% inward relaxation of top Al layer; H presence even at 1100 °C	
	Annealing in air at 1500 °C for 2 h, annealing in O_2 at 10^{-5} Torr 900 °C for 20 min	unreconstructed, 51% inward relaxation of top Al layer	GIXS [90]
	Annealing at 1425 °C in air for 12 h; heating at 650 °C using atomic deuterium beam plasma discharge; then turn of deuterium and annealing in $5 \cdot 10^{-5}$ Torr O_2	(1×1); 51% inward relaxation of top Al layer	LEED [91]
	Heating 760 Torr O_2 at 1300 °C for 10 h, followed by UHV annealing at 600 °C for 10 min	(1×1)	CAICISS, RHEED [92]
Double Al layer	UHV, 1250 °C for 20 min	$(3\sqrt{3} \times 3\sqrt{3})R30°$	GIXD [93]
	Annealing in air at 1500 °C for 3 h; UHV, 1350 °C for 20 min	$(\sqrt{31} \times \sqrt{31})R \pm 9°$	GIXD [94]
	Annealing in air at 1500 °C for 3 h; UHV, 1350 °C for 20 min	$(\sqrt{31} \times \sqrt{31})R \pm 9°$	GIXD,LEED,XAS [95]
	Etched crystal; Heating in O_2 plasma at 850 °C; UHV annealing at 1300 °C	$(\sqrt{31} \times \sqrt{31})R \pm 9°$	SFM [96]
OH layer	Exposure to 10^{-4} Pa H_2O	Formation of surface OH	HREELS, XPS [97, 98]
	Exposure to H_2O	(1×1); Chemisorption of H_2O	LITO,TPD,LEED [99, 100]
	Surface in ambient conditions	Fully hydrated surface with O termination; 2.3 Å up disordered O layer form adsorbed water	CTR diffraction [101]
	Exposure of Al-terminated surface to > 1 Torr water followed by oxygen plasma treatment at RT	1 ML coverage of surface OH	XPS [102]
	Exposure of clean surface to water drops followed by oxygen plasma treatment at RT	0.5 ML coverage of surface OH	XPS [103]
	Exposure to water vapor	Formation of surface OH	XPS [104–106]
Other surface terminations	Etched crystal; UHV heating, O_2 annealing, Al deposition, or Si etching	UHV, $T > 1250$ °C: transition from (1×1) to $\sqrt{3} \times \sqrt{3}$ and finally to $(\sqrt{31} \times \sqrt{31})R \pm 9°$; Al deposition at 800 °C: $(\sqrt{31} \times \sqrt{31})R \pm 9°$; O_2 annealing at $1000 - 1200$ °C: (1×1)	LEED [107]
	1 keV Ar bombardment	3 nm $\gamma - Al_2O_3$ layer with high density defects	TEM [108]
	Annealing in air at 900 or 1500 °C. UHV heating or ion sputtering	Surface Al-rich phases; 1000 °C: (1×1); 1100 °C: $(2\sqrt{3} \times 2\sqrt{3})R30°$; 1250 °C: $(3\sqrt{3} \times 3\sqrt{3})R30°$; 1350 °C: $(\sqrt{31} \times \sqrt{31})R \pm 9°$	LEED, XPS, EELS [95, 109]
	Annealing in UHV at 1000 °C for few minutes; Al deposition	$(\sqrt{31} \times \sqrt{31})R \pm 9°$: Al-rich surface phases	LEED, EELS, AES [110, 111]
	Annealing in air, 1500 °C, 3 h, subsequent UHV annealing	single Al termination (1×1) with large inward relaxation (see [90]) below 1000 °C; $(\sqrt{3} \times \sqrt{3})R30°$ at 1100-1150 °C; $(3\sqrt{3} \times 3\sqrt{3})R30°$ at 1250 °C; $(\sqrt{31} \times \sqrt{31})R \pm 9°$ at 1350 °C	CTR diffraction [112]

Table 2.1.: Surface terminations of $Al_2O_3(0001)$ by means of different preparation procedures. Table taken from [113], corrected for errors, and complemented with additional information.

2.2.5. Oxide supports

Oxide supports fulfil a crucial part in forming a model system. On the one hand, they heavily influence the epitaxy and growth mechanism of the deposited material, due to their own crystal structure, lattice mismatch, and possible adsorbates – as already discussed above. On the other hand, their physical properties do not only influence the ability of probing with methods that involve interaction of electrons with the surface (like AES, LEED, SEM, e.g.), but may also influence the catalytic behaviour of the noble metal nanoparticles [71, 114–118], see Section 2.3. Accordingly, the oxide supports utilized in the frame of this thesis, namely α-$Al_2O_3(0001)$ and $SrTiO_3(100)$, will be discussed in the following. Special attention will be given to alumina as it plays the major role as a substrate in the present work. All rather general properties of aluminium oxides, hydroxides, and oxide-hydroxides can be found in [119].

Single-crystalline phases of **alumina** condense in many, mostly metastable crystal structures, most importantly the cubic phase γ-Al_2O_3 and the only thermodynamically stable, corundum phase α-Al_2O_3 [113, 120, 121]. Especially in its amorphous, ceramic phase, alumina has a wide variety of applications. Due to its ceramic characteristics such as high melting point, hardness, and electrical isolation, it is commonly used as thermal or corrosion protective coating and in the production of aluminium and other metals. Technologically relevant applications cover its use in microelectric devices and as a support in catalysis e.g. [122–124] or even rocket motors [99, 100]. In this work, α-Al_2O_3 with (0001)-axis normal to the surface was used as a support for the metal nanoparticles.

Figure 2.11 the unit cell of α-Al_2O_3 containing six formula units of Al_2O_3, with the lattice parameters of $a = b = 4.7591\,\text{Å}$, $c = 12.9894\,\text{Å}$, $\alpha = \beta = 90\,^\circ$, and $\gamma = 120\,^\circ$ [22]. The top-view in Figure 2.11 b) indicates the six-fold symmetry of the hexagonal-type lattice.

Apart from the pure crystallographic parameters, the surface structure and termination will have striking impact on the morphology of the interface with metal particles deposited on the Al_2O_3-substrate. Taking a look at Figure 2.11 c), the α-Al_2O_3 crystal structure unit cell along the c-axis consists out of six layers of hexagonal close-packed oxygen layers. Between these oxygen layers are aluminium atoms which are not coplanar but buckled layers. Along the c-axis, this results in a $R{-}AlAlO_3{-}R$ sequence, R being the continuation of the periodically, quasi-infinite crystal structure. Consequently, for a clean bulk-truncated model there exist three possible surface terminations, not considering further surface reconstructions. These are indicated in Figure 2.11 c) with green lines: O termination $O_3AlAl{-}R$, single Al termination

$AlO_3Al{-}R$, and double Al termination $AlAlO_3{-}R$ [113]. Intuitively, these three terminations exhibit different surface energies and thus stabilities, with the oxygen termination being the most unstable in UHV and at room temperature, because of its high dipole moment [113, 122]. In turn, the single Al termination is predicted to be the most stable termination, as it exhibits no dipole moment at the surface due to a large inward relaxation resulting in the Al atom being almost coplanar (sp^3 hybridized [125]) with the sub-surface oxygen layer [112, 125–128].
In addition to these three purely geometrical terminations, many surface reconstructions and relaxed surfaces are reported in literature, many of which strongly depend on both the pre-treatment of the crystal and conditions during the determination of the surface structure. Table 2.1 connects terminations and reconstructions experimentally observed with the respect preparation of the surface. In UHV at room temperature, the clean surface is reported to be unreconstructed and single-Al terminated, i.e. (1×1) [89, 93, 94, 113]. Upon annealing temperatures above 1000-1100°C in UHV, several reconstructions are reported: $(\sqrt{3} \times \sqrt{3})R30\,^\circ$, $(2\sqrt{3} \times 2\sqrt{3})R30\,^\circ$, $(3\sqrt{3} \times 3\sqrt{3})R30\,^\circ$, and $(\sqrt{31} \times \sqrt{31})R \pm \arctan(\frac{\sqrt{3}}{11})$ [88, 95, 129]. These reconstructions exhibit an Al-rich surface due to oxygen deficiency caused by oxygen atoms evaporating from the crystal at high temperatures in UHV [92, 94, 107]. A (2×2) termination was shown to originate due to Ca incorporation [95, 109]. The $(\sqrt{13} \times \sqrt{13})R \pm 9\,^\circ$ termination reported in [113] turns out to be an error in the publication.

If exposed to water or air, however, this stable but highly reactive [96] surface will be OH terminated, as studies on monocrystalline alumina surfaces [96, 99–101, 103, 130, 131], nanocrystals [121, 132], and alumina powders [106] (and references therein; additional info is given in Table 2.1 and references therein) have shown. The adsorption of water on the surface is reported to be primarily dissociative [96, 97], as the molecularly adsorbed water molecules adopt a metastable state on the surface regardless of defects [130]. Further, the molecules' reaction pathways are preferred to be

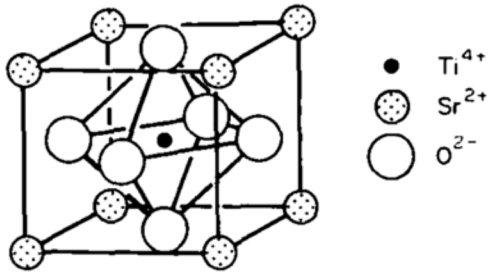

Figure 2.12.: Unit cell of strontium titanate. Taken from [135] and modified.

kinetic [130]; studies with different pressures of H_2O suggest collisionally activated type of adsorption [100], where the sticking probability increases with increasing water pressure and decreases with coverage. The dissociation gives rise to two possible types of superficial OH-groups: either directly via dissociation or by binding of the remaining H-atom to near-surface oxygen atoms [130]. These two distinct types of surface hydroxyl groups differ in their electronic and vibrational properties, as the oxygen atom of the hydroxyl group is either adsorbed on the surface or already strongly bound to the surface lattice as part of the original Al_2O_3 surface structure [130]. The structure of the hydrated surface itself remains subject to debates. Similar to experiments on alumina powder, where exposure to water results in 1 monolayer coverage with OH and the formation of both gibbsite (γ-$Al(OH)_3$) and bayerite (α-$Al(OH)_3$) [106, 133, 134], a study proposes intermediate superficial structures between gibbsite and α-Al_2O_3 with OAlAl-termination and superficial, semiordered water layer [101]. *Liu et al.* measured and calculated the threshold water pressure where the transition from basal alumina towards gibbsite occurs [106]. Above this pressure of about 1 Torr, complete hydroxylation of the surface would occur, whereas below the threshold pressure dissociative hydroxylation would be carried out only at defect sites. Nonetheless, binding energies of the superficial OH-groups occupy a wide energetic spectrum [131] and consequently, kinetically driven desorption of any superficial OH-groups will occur in a broad range of temperatures [99]. Additionally, it was reported that AES and LEED measurements or similar treatment with electron beams are sufficient to dehydroxylate a partially hydroxylated surface [100, 136, 137]. The hydroxyl coverage rapidly decreases upon annealing above 300 K [99], becoming negligible at temperatures of about 230 °C [99] to 500-600 °C [103, 131]. Other authors claim that even UHV annealing at 1200 K is insufficient to remove all hydroxyl groups from Al_2O_3 surfaces [98]. Complete desorption of hydroxyl groups results in a single Al-terminated (1×1) surface [103]. *Wang et al.* calculated that hydrogen remains strongly stabilize unfavourable surface terminations like $O_3AlAl{-}R$ [125]. Further, partial desorption of oxygen from the latter termination would lead to increasing stability of the surface, giving rise to $O_2AlAl{-}R$ and $OAlAl{-}R$ terminations. These calculations have not been supported with experimental data, however.

Strontium titanate ($SrTiO_3$ or short STO) is a compound material with a cubic perovskite crystal structure (see Figure 2.12) with a lattice parameter of 3.905 Å [138]. Generally, for the (001)-oriented crystal two surface terminations are possible with either Sr-O or O-Ti-O in the topmost layer [135]. Other crystalline orientations

like (110) a.o. can be generated with sputtering and reducing cycles [139, 140]. For the TiO_2 terminated surface, different surface reconstructions have been discussed in literature [135, 141, 142]. Main applications of $SrTiO_3$ are optics and usage as a substrate for growth of superconductors [143]. More info on $SrTiO_3$ can be found in [129].

2.2.6. Sample preparation

Now that alumina and STO have been discussed in general, the sample preparation in terms of the present work will be focussed on more in detail. A complete sample list can be found in Appendix A in Table A.1. Info on the UHV system used is given in Section 2.5.

Alumina:
The alumina substrates were bought either from *CrysTec GmbH*[10], *CRYSTAL GmbH*[11], or *SurfaceNet GmbH*[12]. The crystal phase was α-Al_2O_3 with the (0001) crystallographic axis perpendicular to the flat surface. Both round and square – edge orientation (1120) – shaped substrates were used, thicknesses were 0.5 or 1 mm, diameters 1 cm (round), 1 cm × 1 cm (square), or 1 cm × 0.5 cm (square). The miscut between the surface normal and (0001) direction was specified by the companies to be smaller than 0.1 °.

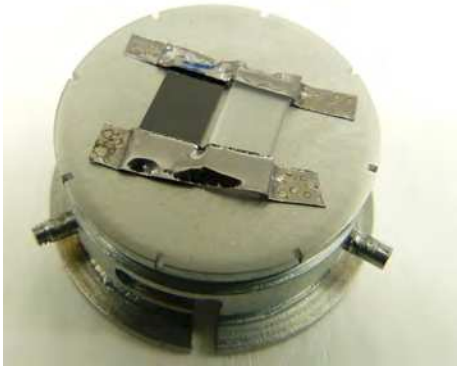

Figure 2.13.: A typical, black Nb-doted STO substrate and a transparent alumina substrate, both spot-welded with tantalum clips to a molybdenum sample holder prior to annealing in UHV.

Before transferring to the UHV system, the alumina substrates underwent a pretreatment. They were kept for 10-15 min in acetone and afterwards isopropanol or ethanol in an ultrasonic bath, respectively. After dry-blowing with nitrogen gas, the substrates were spot-welded with tantalum clips onto a molybdenum sample holder, see Figure 2.13. The tip of the spot welder was made out of copper, which sometimes left small residuals on the tantalum clips after spot-welding. Copper contaminations were not detected on the substrates with AES, though (measurements

[10] CrysTec GmbH, Köpenicer Straße 325, D-12555 Berlin.
[11] CRYSTAL GmbH, Ostendstraße 25, D-12459 Berlin.
[12] SurfaceNet GmbH, Oskar-Schindler-Ring 7, D-48432 Rheine

not shown here).
After mounting, the alumina substrates were inserted into the UHV system. Within the MBE vessel, they were annealed at 500 °C for 2-12 h at a base pressure of 10^{-10}-10^{-9} mbar. To remove any carbon contaminates, the sample surfaces were cleaned with a OAR TC50 oxygen cracker for 90-120 min at 300 °C and an oxygen back pressure of 10^{-7} mbar. Few substrates were annealed in an oxygen atmosphere of 10^{-6}-10^{-5} mbar at 500 °C for at least 2 h, without applying thermal cracking. Figure 2.14 typical AES spectra that were taken of the respective crystals to verify the purity of the surfaces. Here, three measurements were taken on the same, bare alumina substrate before, right after, and 15 after the cleaning procedure (i.e. annealing and thermal cracking with oxygen). Usually, traces of calcium are detected (around 290 eV) which could not be removed by the cleaning procedure. The peak occurs in all three scans in Figure 2.14. For carbon though, the cleaning is effective - judged from these AES measurements, as the signal at 271 eV arising due to carbon contaminates is damped in both black and blue curves (i.e. measurements after cleaning procedure) compared to the red curve before applying cleaning procedures. LEED measurements for the purpose of cross-checking the quality of the surface structure could not be undertaken due to surface charging.

STO:

The $SrTiO_3$ substrates were either ordered from *Crystec GmbH* (see footnote 10) or *SurfaceNet GmbH* (see footnote 12) where they were grown applying the Verneuil method with Nb-doting (0.7 wt% Nb) [144, 145]. They were further treated by Thomas F. Keller or Satishkumar Kulkarni from DESY FS-NL by cleaning in dry air, soaking in high-purity water for 10 min in an ultrasonic bath, dipping into ammoniumfluoride-buffered hydrofluoric acid for 30 s and rinsing with high-purity water. Subsequently, the crystals were heated in air to 1223 K for 1 h (see supporting material to [146]). This procedure results in well-defined surfaces with titanium oxide termination [147] with the surface normal parallel to the (001) axis and a miscut between these axes of below 0.1 °. The edge orientation was (100). For transferring the substrates to UHV, spot-welding as in the case for alumina was used, see Figure 2.13.

Deposition of noble metals:

For the creation of noble metal nanoparticles with well defined shapes different approaches were chosen depending on the substrate and the scientific purpose of the

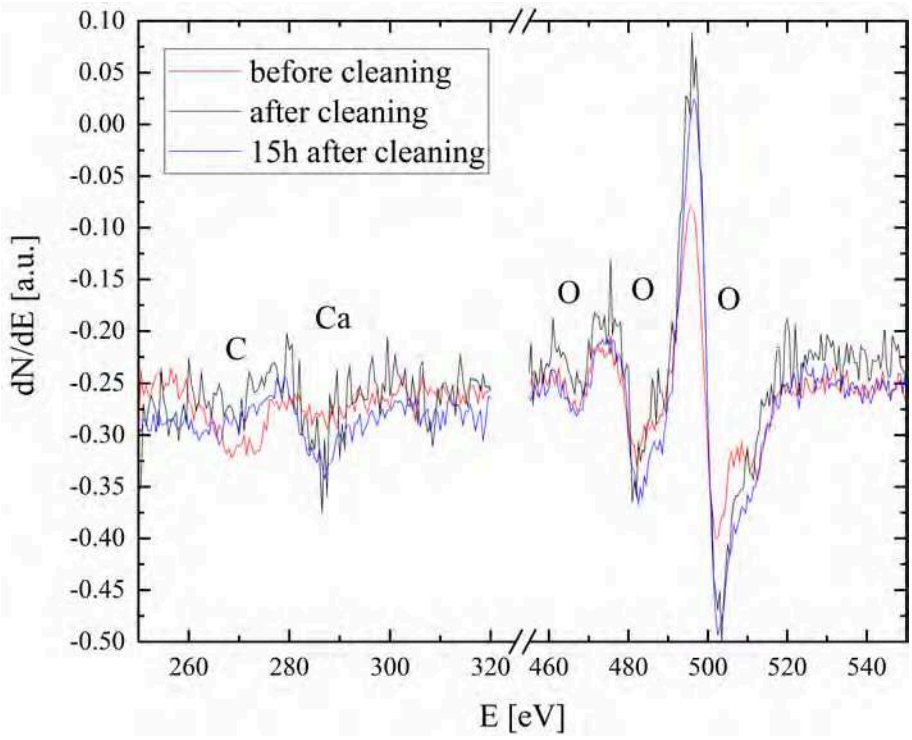

Figure 2.14.: Auger electron spectra of a bare α-alumina substrate before any cleaning procedure in UHV (red), right after annealing and treatment with the oxygen cracker (black), and 15 h after cleaning procedure (blue). The position of possible Auger peaks are indicated for carbon, calcium, and oxygen.

sample. Generally, platinum was deposited either using the Focus EFM3T triple evaporator or a SPECS EBE-1 single evaporator. Rhodium was deposited utilizing the triple evaporator. The substrate temperature during deposition was set between RT and 830 °C. For some samples, subsequent postannealing was applied, either in vacuum at temperatures between 1100 and 1300 °C for 10-150 min or a tube furnace Thermoconcept ROC 50/250/15[13] at temperatures between 1000 and 1200 °C for a few seconds to 10 min. Details can be reviewed in the Appendix in Section A where a list of the relevant samples for this thesis is given with additional info on the samples.

2.3. Heterogeneous catalysis

This section gives a brief overview of heterogeneous catalysis. As this huge field cannot be displayed elaborately here, further references to literature will be given throughout this section.
Generally, a catalyst is a material which speeds up a chemical reaction without being consumed in this process. This material is called a heterogeneous catalyst, if it is a different phase or material compared to the reactants. As already mentioned in Chapter 1, catalysis has a huge impact on every kind of industry related to the production of chemicals and conversion of exhaust gases. Additionally, catalysts play an important role in renewable energies, as the fluctuating character of the energy conversion requires an infrastructure capable of responding adequately to these dynamic demands (see Chapter 1).
The overall performance of a catalyst is driven by its activity, selectivity to specific reactants, and its degradation or lifetime. Generally, the correlation of the performance of a catalytically active material to either its environment or its microscopic structure is challenging as the identification of active sites is not straight-forward – especially under steady-state operation conditions [148]. Consequently, in this thesis the main approach is to study a small model system under operando conditions.
A catalyst increases reaction speed (often expressed through the turnover frequency TOF) by circumventing the high potential to break the molecular bonds via adsorption and desorption of the specimen, thus decreasing the potential barrier to be overcome. Based on this principle, three main reaction types can be identified, here for the reaction path of $2CO + O_2 \rightarrow 2\ CO_2$:

1. Langmuir-Hinshelwood mechanism [149] – see Figure 2.15: both CO and O_2 are

[13] Thermoconcept Dr. Fischer GmbH & Co KG, Friedrich-List-Straße 17, D-28309 Bremen.

adsorbed[14] on the catalyst's surface and the O_2 molecule is dissociated. The reactants may diffuse along the surface. Eventually, if the necessary activation energy E^*_{act} is overcome, reactants form a weakly bound CO_2 molecule which in turn desorbs from the surface[15]. As can be seen in Figure 2.15, the overall change in potential energy ΔH is the same for both the reaction paths with catalyst and without. Hence, involvement of a catalyst does not change thermodynamics of a reaction, but its kinetics.

2. Eley-Rideal mechanism [155]: only one species is chemisorbed on the catalyst's surface (here: O_2) and the other reactant (CO) remains either in gaseous phase or is weakly adsorbed on the surface, enabling the reaction of the molecules. The reaction product (CO_2) directly desorbs from the surface.

3. Mars-van-Krevelen mechanism [156]: one of the reactants forms a compound with the catalyst, here platinum oxide. Upon adsorption of the second species (CO), the reaction product is formed. The oxygen vacancies are constantly refilled from the gas phase.

Further details on these mechanisms can be reviewed in [150, 157–159]. The actual reaction pathway strongly depends on the reaction environment, i.e. temperature, pressure, and catalyst material, as these parameters strongly influence adsorption and diffusion properties of the catalyst's surface. Here, adsorption plays a key role, as a reactant could possibly block all adsorption sites for the second reactant and hence hindering the reaction, if the adsorption would be too strong. Further, if the reaction product does not desorb easily, the overall activity is damped, too. In turn, if adsorption of the reactants is too weak, the time of interaction between the reactants might be too short to allow for a reaction to happen. This is described by the *Sabatier principle* [160], stating that a reaction is effectively catalytically enhanced, if adsorption of both reactants and reaction products is neither too weak or too strong. A graphical visualization of this principle are the so-called *volcano curves* or *volcano surfaces*, see reference [161, 162].
The dependency of the reaction path on the respective reaction conditions leads to the so-called *pressure gap*, which indicates the inability to transfer reaction mechanisms verified for a certain range of pressure to other pressure regimes [163–165]. For catalysts from the platinum-group metals, the Langmuir-Hinshelwood reaction path

[14] In this case, the adsorption mechanism for both molecules is chemisorption. The strong bond to the catalyst results in dissociation of the O_2 molecule. The CO molecule stays intact, see [150–152].
[15] See [153] on adsorption properties of CO_2. Adsorption in general is presented in [154].

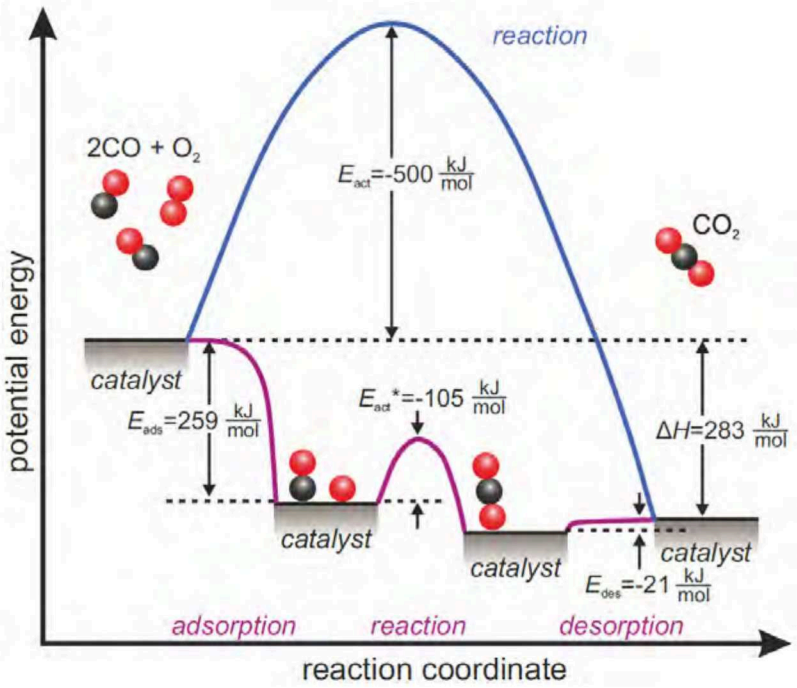

Figure 2.15.: Reaction pathways for CO oxidation. The blue curve displays the potential barrier for CO oxidation in absence of a catalytically active surface. The purple curve displays the Langmuir-Hinshelwood mechanism on a catalytically active Pt(111) surface (low surface coverages are assumed). Taken from [41, 157].

for CO oxidation was found to be dominating the pressure regime below 10^{-6} mbar [150, 166, 167]. Further, studies found the CO molecules to be migrating upon adsorption, indicating a collision-limited rate of reaction [168, 169]. Exemplarily, for platinum catalysts it was shown that upon CO rich conditions, oxygen adsorption – and hence dissociation – is prevented, as adsorption sites are already blocked by CO molecules [118, 170, 171]. It was demonstrated though, that the resulting low activity can be overcome by increasing the O_2 partial pressure towards oxygen-rich conditions [167].

In the near-ambient pressure regime however, the exact reaction mechanics and additionally the presence and role of any surface oxides are still under debate[16]. Several studies conducted at near-ambient oxygen pressure found surface oxides at elevated temperatures on Pt(110) [180, 181] and Pt(111) [182–184]. For the latter, formation of surface oxides is observed upon a threshold pressure (10-20 mbar at 640 K), proceeding from chemisorbed oxygen atoms via a quasi Pt-O like oxide to a α-PtO_2, eventually forming the bulk oxide [184]. Formation of platinum oxides on

[16]The discussion includes the exact adsorption mechanims, adsorption sites and surface aggregates, see [171–179].

γ-Al_2O_3 supported platinum crystallites has been studied depending on the sample temperature [185]. Reduction of these surface oxides was demonstrated already at low dosages (10 % total ratio) of CO [184] or H_2 [183]. On rhodium, a close-packed O-Rh-O trilayer was found on all low-index surfaces, an overview is given in [41]. The respective reaction pathway depends on the temperature regime. At near-ambient pressure, the turn-over frequency is greatly enhanced above a certain ignition temperature T_i of the catalyst. Below T_i, CO oxidation is dominated by the Langmuir-Hinshelwood mechanism on both platinum [166, 167, 186] and rhodium [5, 187, 188]. Do to the relatively high adsorption energy of CO on the surfaces of both rhodium and platinum, this temperature regime is characterized by CO-molecules blocking possible adsorption sites for oxygen, hence resulting in a collision-limited reaction. At $T > T_i$, CO-adsorption is decreased and the Sabatier principle is fulfilled, resulting in a mass-transfer limited reaction rate. This rate is then restricted by both the rates at which the catalyst's surface is supplied with CO and O_2, and at which CO_2 desorbs into the gas phase [166].

In addition, for rhodium the formation of an oxide trilayer and a bulk oxide (see below) in the regime of high activity ($T > T_i$, near-ambient pressure) are reported [189–191]. Accordingly, if the reaction mechanism itself involves solely a surface oxide, a Mars-van-Krevelen would be dominating. It is still unclear, if only one of the mechanisms mentioned or even a synergetic mechanism is dominating the temperature regime above ignition temperature at near-ambient pressure. Synergetic effects might involve e.g. formation of surface oxide islands, surface reconstructions, and adsorption sites on any edges of these islands or nanoparticles in general, see references [7, 189, 190, 192, 193]. Eventually, the exact role of rhodium oxide phases in the catalytic reaction is unclear [5, 41, 190, 194]. For platinum no clear evidence for the formation of any surface oxides under CO oxidation condition at both elevated temperatures and near-ambient pressure and the nature of its impact on the catalytic reaction is given, see references [6, 7, 165, 167, 193, 195] and discussion therein[17].

Comparing the various catalysis related studies on platinum-group metals with experiments on single-crystals, thin-films, and nanoparticles made so far, it is evident that catalytic activity is strongly correlated to the atomic structure of the catalyst, as any modulation of the atomic structure might (locally) effect adsorption of the reac-

[17] Other authors claim the existence of platinum surface oxides for NO_2 dissociation over Pt nanoparticles on Al_2O_3 [196] and for CO oxidation over PdPt nanoparticles on Al_2O_3 [197].

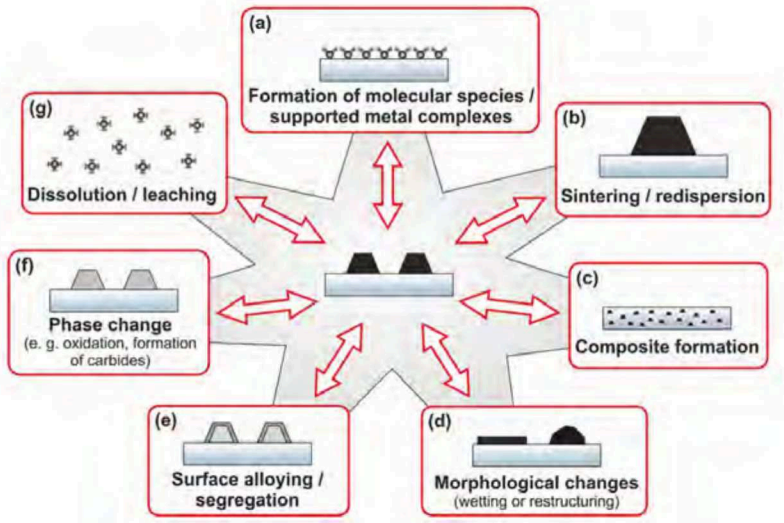

Figure 2.16.: Possible changes of the morphology or composition of the surface of supported metal (alloy) nanoparticles induced by the surrounding local environment. Image taken from [13].

tion products and educts. Accordingly, adhesion might occur specific to atomic sites, especially step edges, edges and corners of nanoparicles, or interfaces/boundaries between oxide phases, pure metals, and the support [118, 179, 198, 199]. Additionally, lattice strain further impacts adsorption properties of especially supported thin films and nanoparticles [31, 62, 114, 200].

Oxide supported nanoparticles in comparison to single-crystal surfaces offer the advantage of an increased surface area. At the same time, the utilized amount of catalytically active material – usually expensive noble metals – is greatly decreased which is relevant for any industrial application [118, 201]. The effect of the nanoparticles' size on the catalytic reaction was studied exemplarily in [8, 202].

In turn, it is well known that a catalyst's ability to increase the turn-over rate of a reaction decreases with total reaction time or the number of catalytic reaction cycles [13, 157]. As the nanoparticles' structure strongly influences the catalytic activity, the hence induced deactivation of the catalyst might be correlated to changes in the catalyst's structure. Note, that the correlation of the microscopic structure of any catalyst with its catalytic activity is not straight-forward [13]. Apart, Figure 2.16 examples of different possible structural changes of supported metal (alloy) nanoparticles. A more detailed explanation including examples from literature is given in reference [13]. This work primarily focusses on the observation of (b) sintering, (d) morphological changes induced by wetting, (e) segregation effects at the surface of alloy nanoparticles, and (f) possible formation of surface oxides – see experimental

Chapters 3, 4, and 5. Naturally, observed effects might not be distinct and somewhat involve other structural effects.
In the case of CO oxidation upon small supported platinum nanoparticles (diameter of few nanometers), sintering via e.g. non-classical Ostwald-ripening induced by additional heat from the exothermal reaction is expected to be a main cause of deactivation [41, 203]. In some cases, sintering processes can be hindered by adding a second metal to the nanoparticles[18] – here: adding rhodium to platinum – see references [41, 203, 204]. Though increasing the stability of the catalyst, alloy nanoparticles make the identification of correlations between the catalyst's structural properties and the catalytic activity even more challenging by adding more parameters to the overall system to be characterized. As now not only size effects influence the model system, but also concentration and possible miscibility effects leading to local (de-)alloying and segregation and phase changes, a valid structural characterization becomes even more crucial - see Chapters 4 and 5.
For more information on heterogeneous catalysis and its correlation to structural properties of the respective catalysts it is referred to [13, 118, 157].

2.4. X-ray diffraction methods

This section will give a brief overview about the most important measurement method applied in this work, namely X-ray diffraction (XRD). In the present study it offers many advantages compared to typical direct imaging methods as SEM or AFM. On the one hand, X-rays can be regarded as a non-destructive measuring method. This means that with a photon energy of 8-9 keV applied, X-rays leave the noble metal nanoparticles intact and have no further impact on the basic physical properties or catalytic behaviour to be determined. Equally important, X-rays with aforementioned energy are capable of penetrating light elements as beryllium with only a small loss in intensity, allowing for enclosed sample environments with varying gas compositions and temperatures to be applied. Further, depending on the measurement technique applied, X-rays deliver precise in-depth information of the nanoparticles or the structural formation of surfaces, as the scattering process is extremely sensitive to atomic positions – as will be discussed below. The basics of X-rays and their propagation in space or media will not be discussed in the frame of

[18] Generally, sintering is caused by the system trying to minimize the total surface energy. Hence, the surface energy of the respective constituents themselves plays a role for the energy minimization, but is only a part of the overall driving forces. In total, a complete energetic analysis is necessary to yield the sintering behaviour of a system [203].

this thesis. Accordingly, for further reading it is referred to [205–207].
The instrumentation used for the implementation of X-ray diffractive methods is presented in Section 2.5.3.

2.4.1. Kinematic scattering of X-rays

In the following section, X-ray scattering on systems at different scales will be discussed briefly, eventually yielding the description of scattering on crystal surfaces. The brief discussion here follows the introduction into X-ray scattering concepts presented by [205]. Further, assumptions made are covered by the *kinematic approximation*, thus excluding any absorption effects and re-scattering of a scattered wave. Additionally, crystals are assumed to be perfect and incident beams to be monochromatic. Dynamical diffraction theory will not be discussed in the frame of this thesis. Again, it is referred to [205] for further reading.
To introduce the concept of X-ray scattering on matter, a basic problem will be discussed: Let us consider a monochromatic plane wave propagating with its electric field component $\boldsymbol{E}$ along $\boldsymbol{r}$

$$\boldsymbol{E}(\boldsymbol{r},t) = E_0\ \hat{\boldsymbol{\epsilon}}\mathrm{e}^{\mathrm{i}(\boldsymbol{k}\cdot\boldsymbol{r}-\omega t)}, \tag{2.20}$$

where E_0 is the amplitude of the plane wave, ω the wave frequency, $\boldsymbol{k}$ the wave vector, and $\hat{\boldsymbol{\epsilon}}$ the polarization unit vector with $\hat{\boldsymbol{\epsilon}} \cdot \boldsymbol{k} = 0$ [205]. Now, let us consider elastic scattering of such a wave on a single, free electron[19]. Fundamentally, this scattering process is described via a differential scattering cross-section $\mathrm{d}\sigma/\mathrm{d}\Omega$ with

$$\frac{\mathrm{d}\sigma}{\mathrm{d}\Omega} = \frac{I_{sc}}{\Phi_0 \Delta\Omega} = \frac{|\boldsymbol{E}_{rad}|^2 \boldsymbol{R}^2}{|\boldsymbol{E}_{in}|^2}, \tag{2.21}$$

where Φ_0 is the flux of the incident number of photons per unit area per second, I_{sc} the number of recorded photons per second at a detector covering a solid angle $\Delta\Omega$ at a distance $\boldsymbol{R}$ [205]. $\boldsymbol{E}_{in}$ and $\boldsymbol{E}_{rad}$ are the electric fields of the incident and radiated wave, respectively. The differential cross-section is a measure of the efficiency of the scattering process itself. From the classical point of view, the incident wave forces the electron to vibrate. The latter then acts as a point source and in turn emits a

[19] If not stated differently, elastic scattering will be regarded as dominating scattering process throughout this thesis, as it sufficiently describes the physical process of scattering from a macroscopic point of view. Neither classical, inelastic scattering (Compton scattering), nor quantum mechanical treatment of scattering which necessarily implies inelastic scattering will be treated here.

spherical wave with $\boldsymbol{E}_{rad} \propto \hat{\boldsymbol{\epsilon}}' \mathrm{e}^{\mathrm{i}kR}/R$, $\hat{\boldsymbol{\epsilon}}'$ being the polarization vector of the emitted (scattered) wave. Eventually, one finds that the scattering cross-section for a plane wave scattering at a free electron can be expressed through the polarization vectors and the fundamental Thomson scattering length – or classical radius of the electron – r_0[205]:

$$\frac{\mathrm{d}\sigma}{\mathrm{d}\Omega} = r_0^2 |\hat{\boldsymbol{\epsilon}} \cdot \hat{\boldsymbol{\epsilon}}'|^2. \tag{2.22}$$

This has important consequences for the chosen geometry at the particular experiment, as according to equation 2.22 the measured intensity depends on the polarization state of both incident and scattered wave. This allows for the polarization factor P to be defined [205]:

$$P = |\hat{\boldsymbol{\epsilon}} \cdot \hat{\boldsymbol{\epsilon}}'|^2 = \begin{cases} 1 & \text{synchrotron: vertical scattering plane} \\ \cos^2\psi & \text{synchrotron: horizontal scattering plane} \\ \frac{1}{2}\left(1 + \cos^2\psi\right) & \text{unpolarized source} \end{cases} \tag{2.23}$$

Here, ψ is the angle between the propagation direction of the incident wave and the position of the detector $\boldsymbol{R}$. Notably, the differential cross-section does not depend on the energy of the incident wave. This allows for the description of the scattering process to be applied to more complicated systems as atoms or crystals, as for X-ray energies the approximation of free electrons holds, too – as long as the energy is far from absorption edges [205], as will be discussed below.

The next system to be discussed is scattering of X-rays on an atom. Instead of a single electron, an atom consisting of Z electrons represented by a charge distribution $\rho(\boldsymbol{r})$ will be regarded. Accordingly, the scattered wave will be a superposition of different wave components from scattering on volume elements of the charge distribution [205]. The difference in phase of the incident wave and a wave around the origin in the centre of the radial symmetric charge distribution (see Figure 2.17 (a)) is $\boldsymbol{k} \cdot \boldsymbol{r}$. Similarly, the phase difference between a wave at origin and a scattered wave is equal to $-\boldsymbol{k}' \cdot \boldsymbol{r}$. Thus, the resulting phase difference between incident and scattered wave is [205]

$$\Delta\phi(\boldsymbol{r}) = (\boldsymbol{k} - \boldsymbol{k}') \cdot \boldsymbol{r} = \boldsymbol{Q} \cdot \boldsymbol{r}, \tag{2.24}$$

where we defined the momentum transfer or *scattering vector* $\boldsymbol{Q} = (\boldsymbol{k} - \boldsymbol{k}')$. Again, elastic scattering is assumed, where the condition $|\boldsymbol{Q}| = 2|\boldsymbol{k}| \sin\theta = \frac{4\pi}{\lambda} \sin\theta$ holds

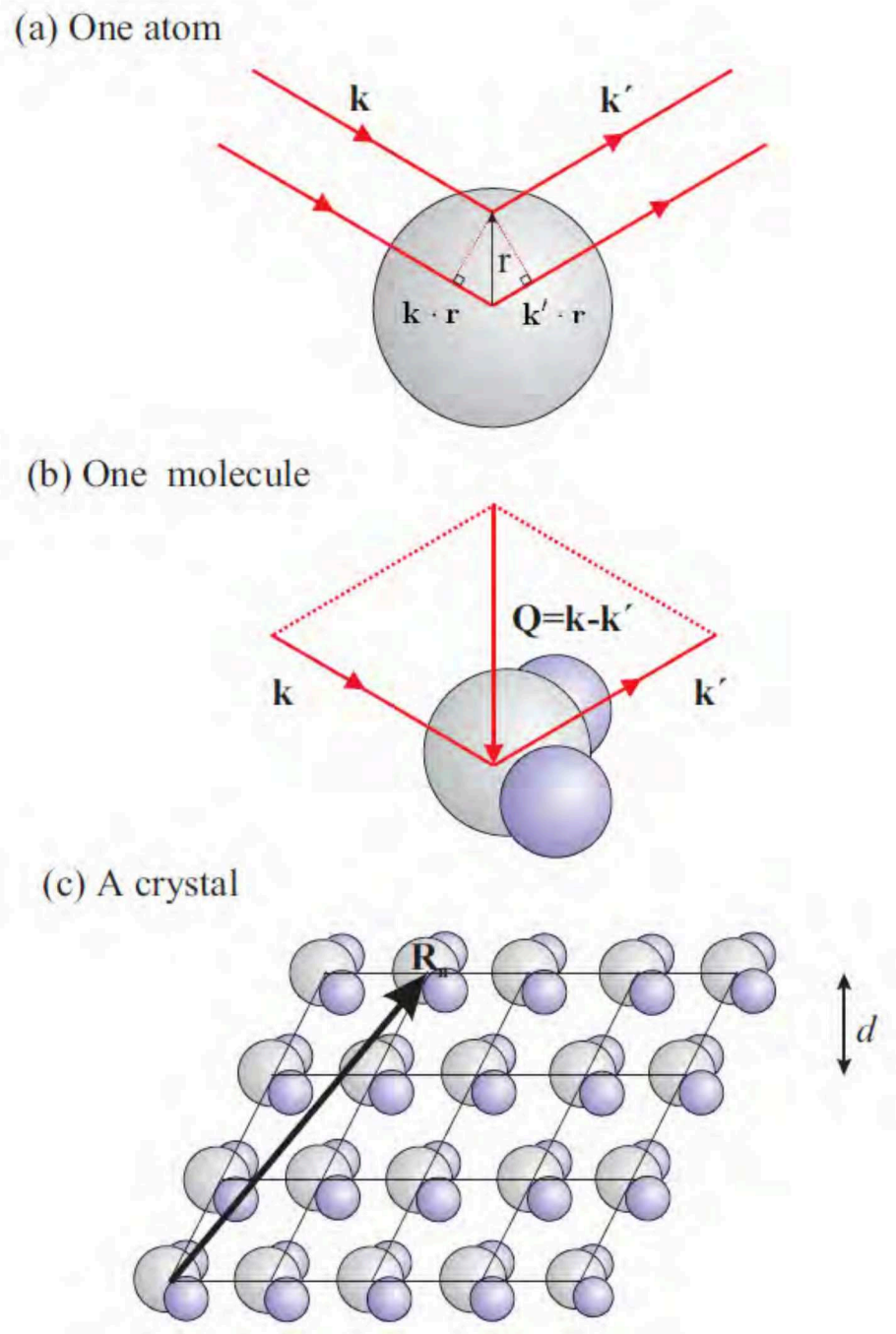

Figure 2.17.: Scattering scheme with objects on different length scales relating $\boldsymbol{Q}$, $\boldsymbol{k}$, and $\boldsymbol{k}'$: (a) single atom, (b) a molecule, and (c) a crystal composed of molecules at positions $\boldsymbol{R}_n$. The lattice spacing of the crystal is d. Figure taken from [205].

[205]. Eventually, one finds that each element $\mathrm{d}\boldsymbol{r}$ at position $\boldsymbol{r}$ contributes $-r_0\rho(\boldsymbol{r})\mathrm{d}\boldsymbol{r}$ to the total scattered field with a phase factor $\mathrm{e}^{\mathrm{i}\boldsymbol{Q}\cdot\boldsymbol{r}}$, yielding [205]

$$-r_0 f^0(\boldsymbol{Q}) = -r_0 \int \rho(\boldsymbol{r})\mathrm{e}^{\mathrm{i}\boldsymbol{Q}\cdot\boldsymbol{r}}\mathrm{d}\boldsymbol{r}. \tag{2.25}$$

Here, f^0 denotes the *atomic form factor*. The integral on the right hand side of equation 2.25 resembles the form of a Fourier transform, which implies important consequences for the determination of the scattering cross-section from the electron density of a sample, as will be discussed later in this chapter. In the case of perfect forward scattering, i.e. $\boldsymbol{Q} \to 0$, elements $\mathrm{d}\boldsymbol{r}$ scatter in phase and f^0 takes the value of the number of electrons in the atom, $f^0(\boldsymbol{Q} = \boldsymbol{0}) = Z$. Contrary, for increasing momentum transfer, elements $\mathrm{d}\boldsymbol{r}$ scatter out of phase and thus $f^0(\boldsymbol{Q} \to \infty) = 0$. Using this definition, the scattering cross-section can be formulated in analogy to equation 2.22 as [205]

$$\frac{\mathrm{d}\sigma}{\mathrm{d}\Omega} = r_0^2|\hat{\boldsymbol{\epsilon}} \cdot \hat{\boldsymbol{\epsilon}}'|^2|f^0(\boldsymbol{Q})|^2. \tag{2.26}$$

As mentioned above, it is assumed that upon scattering of X-rays on electrons the energy of these X-rays is far from absorption edges of the discrete electronic levels - generally much larger. In reality, the scattering process is altered by the more or less bound state of the electrons. This leads to dispersion corrections to the atomic form factor:

$$f(\boldsymbol{Q}, \hbar\omega) = f^0(\boldsymbol{Q}) + f'(\hbar\omega) + \mathrm{i}f''(\hbar\omega). \tag{2.27}$$

$f'(\hbar\omega)$ arises due to the sole fact, that the electrons will respond less to the external driving force by the incident electromagnetic wave, if their binding energy is not negligible compared to the incident wave. Hence, the scattering cross-section will be significantly damped. Additionally $f''(\hbar\omega)$ introduces absorption to the form factor. In the notation given, it is negative and becomes extremal at absorption edges. Again, both $f'(\hbar\omega)$ and $f''(\hbar\omega)$ are negligible, if the photon energy is far from absorption edges [205].

The transition towards scattering by a crystalline system is done by summation over all scattering contributions. For this, the intrinsic properties of crystals are used. On the one hand, crystals are periodic structures. On the other hand, the element being periodic is a single or multi-atomic base. Consequently, the crystals

form factor factorize into a product of two contributing sums [205]

$$F^{crystal}(\boldsymbol{Q}) = -r_0 P \underbrace{\sum_j f_j(\boldsymbol{Q}) \mathrm{e}^{\mathrm{i}\boldsymbol{Q}\cdot\boldsymbol{r}_j}}_{\text{Unit cell structure factor}} \underbrace{\sum_n \mathrm{e}^{\mathrm{i}\boldsymbol{Q}\cdot\boldsymbol{R}_n}}_{\text{Lattice sum}}. \tag{2.28}$$

The corresponding scattered intensity of an infinite crystal reads [205]

$$I^{crystal}(\boldsymbol{Q}) = |F^{crystal}(\boldsymbol{Q})|^2 = |r_0 P F_N(\boldsymbol{Q}) S_N(\boldsymbol{Q})|^2, \tag{2.29}$$

where F_N and S_N denote the unit cell structure factor and the lattice sum, respectively. The unit cell structure factor sums over all atomic form factors $f_j(\boldsymbol{Q})$ at positions $\boldsymbol{r}_j$, whereas the lattice sum accounts for all lattice points $\boldsymbol{R}_n$ – see Figure 2.17(c). Consequently, the positions of all atoms in the lattice structure are given by $\boldsymbol{r}_j + \boldsymbol{R}_n$. Mathematically spoken, the lattice sum is a phase factor with order of unity. If however

$$\boldsymbol{Q} \cdot \boldsymbol{R}_n = 2\pi m, m \in \mathbb{N} \tag{2.30}$$

is fulfilled, the sum takes the value of the total number of unit cells. $\boldsymbol{R}_n$ can be expressed through basis vectors $\boldsymbol{a}_i$ in the form $\boldsymbol{R}_n = n_1\boldsymbol{a}_1 + n_2\boldsymbol{a}_2 + n_3\boldsymbol{a}_3$ with $n_1, n_2, n_3 \in \mathbb{N}$. Another way to fulfil equation 2.30 is by introducing the concept of a *reciprocal lattice* in momentum space. The reciprocal space basis vectors are defined by

$$\begin{aligned}
\boldsymbol{a}_1^* &= 2\pi \frac{\boldsymbol{a}_2 \times \boldsymbol{a}_3}{\boldsymbol{a}_1 \cdot (\boldsymbol{a}_2 \times \boldsymbol{a}_3)} \\
\boldsymbol{a}_2^* &= 2\pi \frac{\boldsymbol{a}_3 \times \boldsymbol{a}_1}{\boldsymbol{a}_1 \cdot (\boldsymbol{a}_2 \times \boldsymbol{a}_3)} \\
\boldsymbol{a}_3^* &= 2\pi \frac{\boldsymbol{a}_1 \times \boldsymbol{a}_2}{\boldsymbol{a}_1 \cdot (\boldsymbol{a}_2 \times \boldsymbol{a}_3)}
\end{aligned} \tag{2.31}$$

and consequently, all reciprocal lattice sites are described by

$$\boldsymbol{G} = h\boldsymbol{a}_1^* + k\boldsymbol{a}_2^* + l\boldsymbol{a}_3^*, \text{with } h, k, l \in \mathbb{N}. \tag{2.32}$$

Hence, $\boldsymbol{G} \cdot \boldsymbol{R}_n = 2\pi(hn_1 + kn_2 + ln_3)$ is a solution to equation 2.30. Accordingly, equation 2.30 is fulfilled if the so-called *Laue condition*

$$\boldsymbol{Q} = \boldsymbol{G} \tag{2.33}$$

holds[20] [205]. This condition is equivalent to *Bragg's law* for constructive interference of scattering of X-rays on atomic layers [205]

$$\lambda = 2d_{hkl} \sin\theta, \tag{2.34}$$

which links the distance of atomic layers d_{hkl} with the angular position θ of constructively interfering waves of wavelength λ. A derivation of the formula is given in [205]. If the crystal's unit cell is determined with $a_1 = a_2 = a_3$ and $\boldsymbol{a}_i \cdot \boldsymbol{a}_j = \delta_{ij}$ (δ_{ij} being the Kronecker Delta and $i, j \in [1; 2; 3]$), d_{hkl} is given by the relation

$$d_{hkl} = \frac{a_{bulk}}{\sqrt{h^2 + k^2 + l^2}}, \tag{2.35}$$

which holds for both platinum and rhodium.

It is convenient when performing surface X-ray scattering to define a *surface lattice* $\boldsymbol{a}_S$, $\boldsymbol{b}_S$, and $\boldsymbol{c}_S$. In the frame of this work, surface coordinates are used to describe diffraction patterns of Pt- and PtRh nanoparticles, which are mostly (111)-oriented, hence they exhibit a hexagonal surface cell. The convention for the construction of the surface cell is such that $\boldsymbol{c}_S$ always defines the coordinate corresponding to the direction perpendicular to the surface. $\boldsymbol{a}_S$ and $\boldsymbol{b}_S$ define the in-plane components of the unit cell laying in the surface. The system of surface vectors can be constructed from the fcc-real space lattice (compare Figure 2.18) by:

$$\begin{aligned} \boldsymbol{a}_S &= \frac{1}{2}(\boldsymbol{a}_1 - \boldsymbol{a}_3) \\ \boldsymbol{b}_S &= \frac{1}{2}(\boldsymbol{a}_2 - \boldsymbol{a}_3) \\ \boldsymbol{c}_S &= \boldsymbol{a}_1 + \boldsymbol{a}_2 + \boldsymbol{a}_3. \end{aligned} \tag{2.36}$$

This leads to a hexagonal surface cell as depicted in Figure 2.19. Here, the surface plane is shown, $\boldsymbol{c}_S$ and $\boldsymbol{c}_S^*$ are pointing perpendicular out of the plane depicted. The bulk Miller-indices are exchanged for a set of surface coordinates $(H_S\, K_S\, L_S)^{\mathrm{T}}$. The

[20] Note that with the definition of $\boldsymbol{Q} = \boldsymbol{k} - \boldsymbol{k}'$ given above $\mathbf{Q}$ is pointing towards origin in reciprocal space. Hence, the Laue condition should read $\boldsymbol{Q} = -\boldsymbol{G}$. Nonetheless, the change in sign does not have any impact on the formulas derived from this condition.

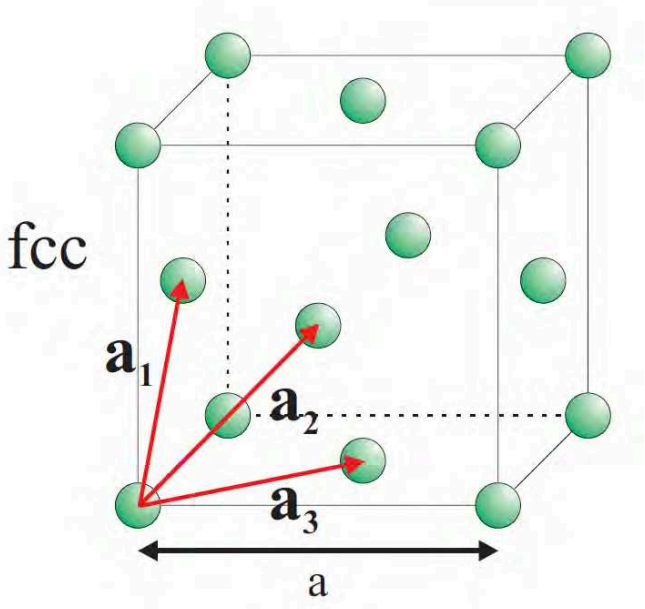

Figure 2.18.: Real space lattice vectors for a fcc crystal with lattice constant a. Taken from [205].

conversion from surface coordinates to bulk coordinates is done via [208]

$$\begin{pmatrix} h \\ k \\ l \end{pmatrix} = \frac{1}{3} \begin{pmatrix} 2 & -2 & 1 \\ 2 & 4 & 1 \\ -4 & -2 & 1 \end{pmatrix} \cdot \begin{pmatrix} H_S \\ K_S \\ L_S \end{pmatrix}. \tag{2.37}$$

Note that throughout this thesis phrases like "the intensity along L_S" will be used as shortened version of "the intensity along $L_S \boldsymbol{c_S^*}$.

In equation 2.28, the unit cell structure factor determines how strong elements in the crystal scatter, whereas the lattice sum $S_N(\boldsymbol{Q})$ indicates the positions of the scattered, interfering signals. Using the mathematical definition of the geometric series it can be reformulated yielding the *Laue equation*

$$|S_N|^2 = \prod_{m=1}^{3} \frac{\sin^2\left(\frac{1}{2} N_m \boldsymbol{a_m} \cdot \boldsymbol{Q}\right)}{\sin^2\left(\frac{1}{2} \boldsymbol{a_m} \cdot \boldsymbol{Q}\right)}, \tag{2.38}$$

where m refers to the respective dimension and N_m is the number of unit cells in dimension m. The Laue function itself is an inadequate measure to display the lattice sum of a crystal, since the number of unit cells will be large and generally unknown. Despite, it provides insight in thin-layer or nanoparticle systems. Figure 2.20 displays

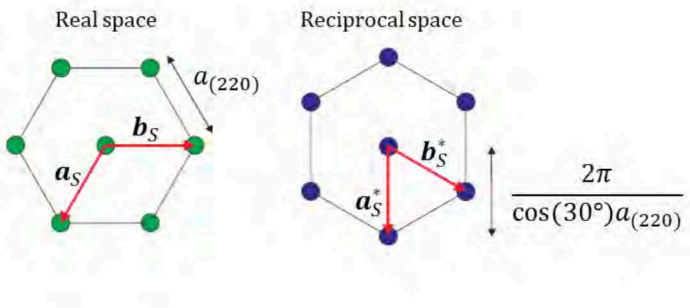

Figure 2.19.: Transformation of the real space surface cell (left) to the reciprocal surface cell (right). Note that in this case $a_{(220)} = a_{Pt}/\sqrt{2}$. $\boldsymbol{c}_S$ and $\boldsymbol{c}_S^*$ are pointing perpendicular out of the plane shown. Image taken from [205] and modified.

an one-dimensional example for $|S_N(\boldsymbol{Q} \cdot \boldsymbol{a}_1)|^2$ with $N_1 = 4$ (dashed, red line) and $N_1 = 8$ (solid, black line). Main maxima occur at multiples of 2π – as required by the Laue condition – with $N_1 - 2$ side maxima (so-called *Laue-fringes*). The height of the main maxima is $|S_N(2n\pi)|^2 = N_1^2$ and the height of the side maxima is determined by the envelope, the so-called crystal truncation rod which will be discussed further below. The distance between two side minima ΔQ corresponds to the number of scattering planes of the respective object along the corresponding dimension, $\Delta x = \frac{2\pi}{N_1}$. If plotted as a function of the momentum transfer $\boldsymbol{Q}$, it provides a direct measure to determine e.g. the particle size or layer thickness D along $\boldsymbol{a}_1$: $\Delta Q = \frac{2\pi}{D}$. The fact that the height of the main maxima corresponds to N_1^2 has important consequences for nanoparticles, as accordingly here the scattered intensity will be proportional to the $N_1^2 N_2^2 N_3^2$, hence $I \propto N^6$. On the one hand, this how weak the scattered intensity of a single nanoparticle will be – compare equation 2.29. On the other hand, if performing X-ray scattering on an ensemble of nanoparticles with a size distribution, the mean size of these particles will be strongly dominated by large particles – already 20 % larger particles exhibit three times more intensity. However, for crystals with quasi-infinite size it is more convenient to reformulate the Laue equation 2.38. Using the Dirac delta function $\delta(x)$, it can be rewritten in the limit of infinite cells ($N \to \infty$) as [205]

$$|S_N(\boldsymbol{Q})|^2 \to N v_c^* \sum_{\boldsymbol{G}} \delta(\boldsymbol{Q} - \boldsymbol{G}), \tag{2.39}$$

where N is the total number of unit cells and v_c^* the volume of the unit cell in

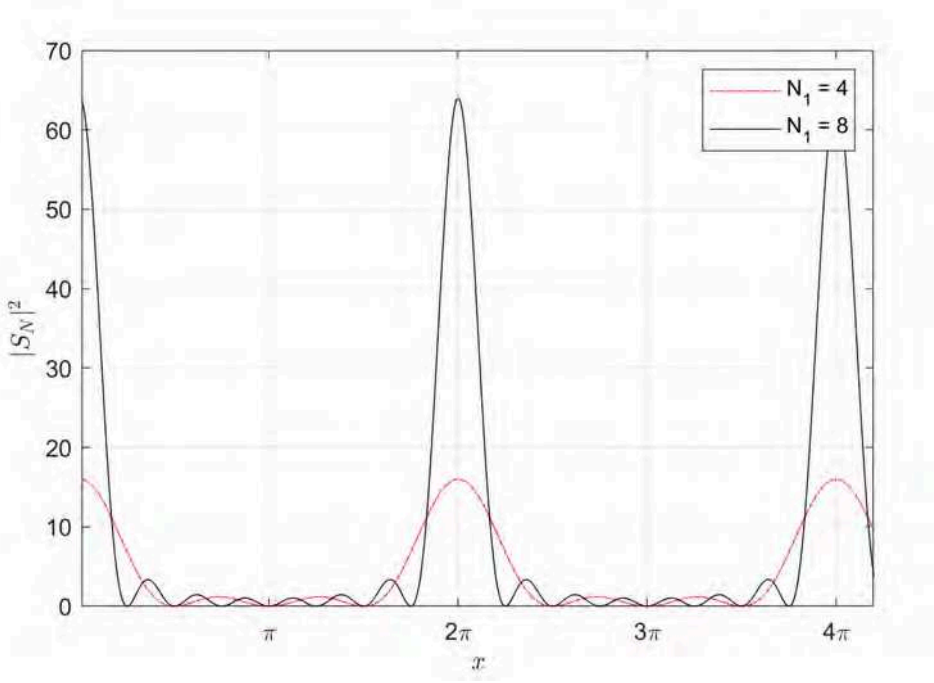

Figure 2.20.: 1-dim Laue function – see equation 2.38 – with $x = \boldsymbol{Q} \cdot \boldsymbol{a}_1$ for $|S_N|^2$ with $N_1 = 4$ (dashed, red line) and $N_1 = 8$ (solid, black line).

reciprocal space[21]. This relation basically that the scattered signal of an (infinite) crystal will comprise distinct, sharp Bragg peaks. This is indicated in Figure 2.21 through blue dots.

2.4.2. Surface X-ray diffraction

However, real crystals have a finite size and consequently, they exhibit surfaces. To describe the effect of introducing surfaces a semi-infinite crystal will be regarded, which exhibits a truncation only perpendicular to $\boldsymbol{a}_3$. Hence, the lattice sum in this dimension will read $\sum_n \mathrm{e}^{2\pi i n l} = \frac{1}{1-\exp(-2\pi i l)}$ (excluding absorption effects). Thus, the scattered intensity will be of the form [205]

$$I_{sc} \propto |F_N(\boldsymbol{Q})|^2 \delta(\boldsymbol{Q}_\parallel - \boldsymbol{G}_\parallel) \frac{1}{4\sin^2(\pi l)}. \tag{2.40}$$

Here, $F_n(\boldsymbol{Q})$ denotes the unit cell structure factor and l denotes a continuous variable instead of a natural number, as this allows for describing points in reciprocal space in between spots originating from constructive interference from scattering

[21] Here, it was used that $\lim_{N\to\infty} \frac{\sin^2(Nx)}{\sin^2(x)} = \delta(x)$.

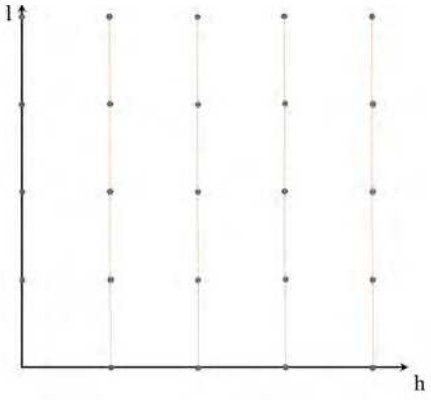

Figure 2.21.: Sketch of a reciprocal space map in the h-l plane of an infinite cubic crystal (blue) and a semi-infinite crystal cut parallel to the $\boldsymbol{a}_1$-$\boldsymbol{a}_2$ plane (orange).

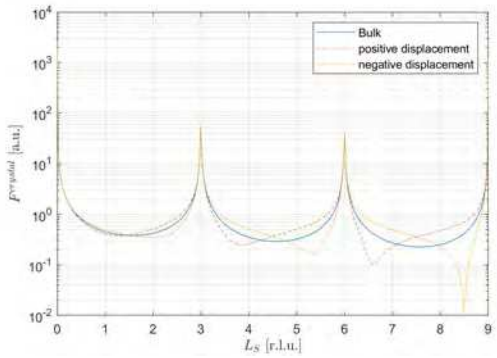

Figure 2.22.: Crystal truncation rod of a semi-infinite platinum crystal: $F^{crystal}$ as a function of L_S for the bulk system (blue, solid line), the topmost layer displaced outwardly (red, dashed line), and the topmost layer contracted (yellow, dash-dotted line). Further info is given in the text.

on atomic planes. Further, $\delta(\boldsymbol{Q}_\parallel - \boldsymbol{G}_\parallel)$ indicates that the reciprocal lattice parallel (thus $\boldsymbol{Q}_\parallel$ and $\boldsymbol{G}_\parallel$) to the surface will still comprise distinct points. Along l however, there will be non-vanishing intensity even for points not fulfilling the Laue condition (so-called asymptotic scattering), as now wave components are missing that would annihilate the amplitude in the case of an infinite crystal – see orange rods along l in Figure 2.21. The intensity along such a crystal truncation rod perpendicular to the surface is depicted in Figure 2.22. Here, $F^{crystal}$ becomes extremal at points fulfilling the Laue condition – as for a perfect, infinite crystal. But aside these points, $F^{crystal}$ does not become zero. In fact, in between the Bragg peaks (which are at $L_S = 3, 6, 9, ...$ in this case), $F^{crystal}$ is highly influenced by the geometry of the established surface. To indicate this behaviour, apart from the crystalline form factor for a perfect, truncated, semi-infinite platinum crystal (blue, solid) in (111)-orientation two modified models are shown[22]: one semi-infinite crystal as before, but with the topmost layer displaced outwardly by 4 % of the bulk lattice constant a_{Pt} (red, dashed line), and the topmost layer contracted by 4 % of a_{Pt} (yellow, dash-dotted line). Hence, recording such crystal truncation rods provides insight of the atomic structure of both the bulk system and surface. What makes these CTRs relevant for this work, is that CTRs appear for every surface. Accordingly, in single-particle diffraction any CTRs and their direction to one another will give

[22]The CTRs have been calculated using the program *Rod*. See reference [209] and Chapter 5 for further info.

insight about the corresponding facets of the nanoparticle – see Chapter 5.

Another probing technique sensitive to the structure of the surface is grazing incidence diffraction (GID). It will discussed here mere briefly. For further reading it is referred to [210–212]. Furthermore, the proper physical description of GID requires concepts beyond kinematic approximation – as dynamical diffraction theory. The overall starting point is a macroscopic view of diffraction on a surface. The geometry is depicted in Figure 2.23. A wavefront $\boldsymbol{k}_i$ incident with an angle $\alpha_i \leq \alpha_c$ scatters at atomic planes which are tilted in the surface plane by θ with respect to the plane of the incident wave. The momentum transfer $\boldsymbol{Q}$ exhibits in-plane and out-of plane components and hence $\boldsymbol{k}_f$ points of-specular. It is a unique feature of X-rays that, if $\alpha_i \leq \alpha_c$ is fulfilled, X-rays undergo total external reflection and the out-of plane component of the wave vector of the transmitted wave $k_{f,\parallel}$ is complex for $\alpha_i < \alpha_c$. The result is a near-surface evanescent wave, propagating almost parallel to the surface and decaying exponentially towards the bulk (along the negative surface normal $-\boldsymbol{n}$). The existence of an evanescent wave basically is enabled by the index of refraction

$$n = 1 - \delta + \mathrm{i}\beta \tag{2.41}$$

being below one for about all materials in the X-ray regime [205]. In equation 2.41, $\delta = \frac{2\pi\rho r_0}{\boldsymbol{k}^2}$ sometimes is referred to as *electron density*, so throughout this work the term *electron density* will be accompanied by the proper physical quantity to avoid confusion. This description of the refractive index does also account for absorption in the material via β. The latter is linked to the absorption correction f'' of the atomic form factor $f(\boldsymbol{Q})$ or the absorption coefficient[23] μ_m via $\beta = -\frac{2\pi\rho_{at} r_0}{\boldsymbol{k}^2} f'' = \frac{\mu_m}{2|\boldsymbol{k}|}$, respectively. The phenomenon of evanescent waves upon total external reflection allows for gathering structural information of the surface despite the fact that the X-rays are totally reflected at the surface. The evanescent wave scatters on atomic layers laying in the surface plane. Accordingly, if $\boldsymbol{Q}_\parallel$ fulfils the Laue condition $\boldsymbol{G}_\parallel = \boldsymbol{K}_\parallel$, in-plane Bragg peaks can be observed under a glancing angle 2θ – in a scattering geometry depicted in 2.23. For angles below the critical angle, the penetration depth of the evanescent wave can be several tens of nanometres [205]. The overall scattered intensity is linked to the transmission function $T = 4\frac{\alpha^2}{\alpha_c^2}$, thus offering maximum intensity.

[23] A characteristic physical property of materials. It denotes after which length z the intensity is attenuated by a factor of $\frac{1}{\mathrm{e}}$. In other words: after travelling a distance z, the intensity is attenuated by a factor of $\mathrm{e}^{-\mu_m z}$.

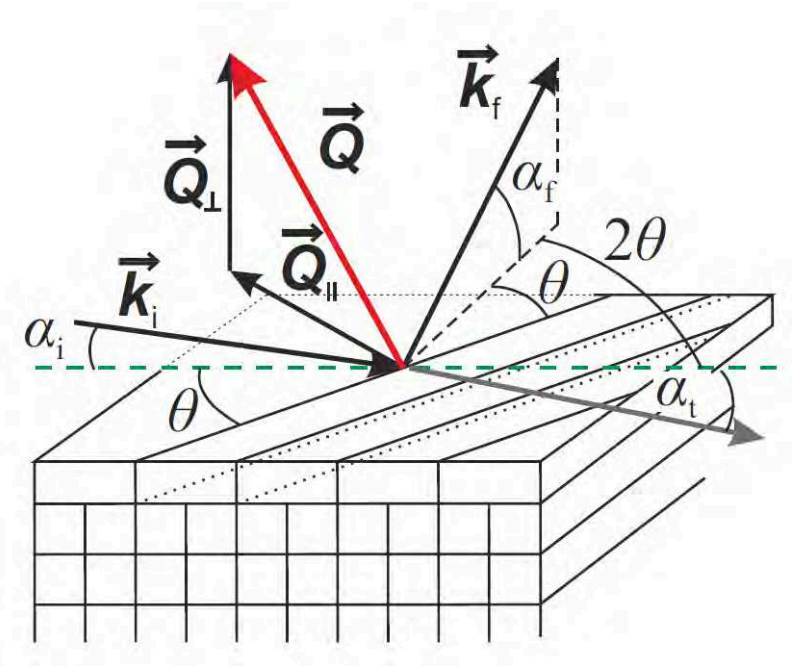

Figure 2.23.: Geometry of grazing incidence diffraction (GID).

$$I \propto |T(\alpha_i)|^2 I_{\mathrm{sc}}(\boldsymbol{Q}_\parallel)|T(\alpha_f)|^2, \tag{2.42}$$

compare equation 2.40 and references [41, 210]. The transmission function becomes extremal for $\alpha = \alpha_c$. Note that in reality there are many more factors influencing the intensity and intensity profile being measured in a diffraction experiment – see [205, 213]:

- Since crystals and scattering objects always exhibit a temperature $> 0\,\mathrm{K}$, more exact treatments of X-ray diffraction must account for thermal corrections, implemented via the Debye-Waller factor.
- Intensity profiles in experiments are always a convolution of the physically given profile and an inherent profile by the measurement instrument. Slits or the sample itself may be blocking beam pathways. Beams are neither monochromatic, nor are they unidirectional; beam divergence is always limiting the resolution of the diffracted image.
- Samples always exhibit a finite size and crystals are composed of crystallites. Thus, the Laue condition is smeared out, broadening the Bragg-peaks. The intensity is further modified, described by the *Lorentz-factor* (see [205]).
- Especially nanoparticles may exhibit in-plane rotations or tilts with respect to

the surface normal or with respect to other nanoparticles. Consequently, in an ensemble diffraction experiment, resulting ensemble Bragg peaks will be broadened.

- Diffuse scattering and detector noise give rise to a background overlaying the calculated intensity distribution.

2.4.3. X-ray reflectivity

X-ray reflectivity (XRR) is another physical mechanism important in the frame of this work for it allows to determine the thicknesses of thin layers or layer thicknesses in multilayer systems. In contrast to X-ray diffraction discussed above it does not rely on the microscopic quality of a crystalline system, as not the constructively interfering scattered waves by atomic planes are considered, but interfering scattered waves by boundary layers and interfaces between media. Since the technique is sensitive to the electron density of the layers – via the refractive index n of the respective layer –, it also allows for the determination of particle coverage if the material and composition is known. Details on physical details, derivation of formula, and the technique itself can be reviewed in [205, 213, 214].
The measurement geometry is a specular geometry. The momentum transfer vector $\boldsymbol{Q} = \boldsymbol{Q}_z$ is always perpendicular to the surface normal $\boldsymbol{n}$. Hence, the angles of incident and glancing beam θ with respect to the surface plane are always equal and gradually increased. At every boundary layer (surface, interfaces) the X-rays will be reflected and refracted if $\theta_i > \alpha_c$.
The intensity reflectivity R and transmissivity T are governed by the *Fresnel equations* [214]

$$R = \frac{I_r}{I_i} = \frac{(\theta_i - A^2)^2 + B^2}{(\theta_i + A^2)^2 + B^2} \tag{2.43}$$

$$T = \frac{I_t}{I_i} = \frac{4\theta_i^2}{(\theta_i + A^2)^2 + B^2}, \tag{2.44}$$

where indices i, r, and t refer to the incident, refractive and transmitted quantities, respectively. Furthermore, A and B are introduced as:

$$A = \frac{1}{\sqrt{2}} \left([(\theta_i^2 - \alpha_c^2)^2 + 4\beta^2]^{\frac{1}{2}} + (\theta_i^2 - \alpha_c^2) \right)^{\frac{1}{2}} \tag{2.45}$$

$$B = \frac{1}{\sqrt{2}} \left([(\theta_i^2 - \alpha_c^2)^2 + 4\beta^2]^{\frac{1}{2}} - (\theta_i^2 - \alpha_c^2) \right)^{\frac{1}{2}}. \tag{2.46}$$

For $\theta_i \leq \alpha_c$ will be 1 (for negligible absorption β), and for $\theta_i > \alpha_c$ R will be proportional to $\frac{1}{\boldsymbol{Q}_z^4}$.
In the case of multilayers, the *Parrat formalism* [214] allows for an exact description of the reflected intensity. The formalism itself is a recursively performed summation over the reflectivity contributions and phase factors of the respective layers – see [205, 214] for more details.
Since in reality layers will not be atomically flat, a roughness parameter is introduced. Here, the roughness of the surface/interface of layer j is implemented as a Gaussian distributed height variation [41, 215]

$$g(z) = \frac{1}{\sqrt{2\pi\sigma_j}} \exp\left(\frac{(z-d_j)^2}{2\sigma_j^2}\right), \tag{2.47}$$

where σ_j is the standard deviation from the ideal layer thickness d_j of layer j. This deviation causes a diffusive background, as now scattered waves will exhibit off-specular components.
In the frame of this thesis, reflectivity curves and related parameters like d_j, σ_j, δ_j, and β_j among others are determined by fitting through the program *Fewlay* [216]. Figure 2.24 illustrates how these parameters effect the XRR-curves. Here, δ_{th} denotes the theoretical electron density δ for a certain element. For this thesis, case III is relevant and further modified, here. To construct a more precise model for nanoparticles with an inherent height distribution, several slabs with different respective heights and electron densities are the basis of the fitting model. The normalized electron density $\frac{\delta}{\delta_{th}}$ can be regarded as a superficial coverage.

2.5. Instrumentation supporting operando, in-situ studies

In this section, the instrumentation and setups used to both fabricate and characterize the samples will be briefly introduced.

2.5.1. UHV preparation system

The fabrication of well-defined model systems is crucial for the studies conducted throughout this thesis. To establish a controlled and stable growth environment and to gain samples with as little contamination as possible, two UHV vessels have been used. One of these systems is depicted in Figure 2.25. The layout of the

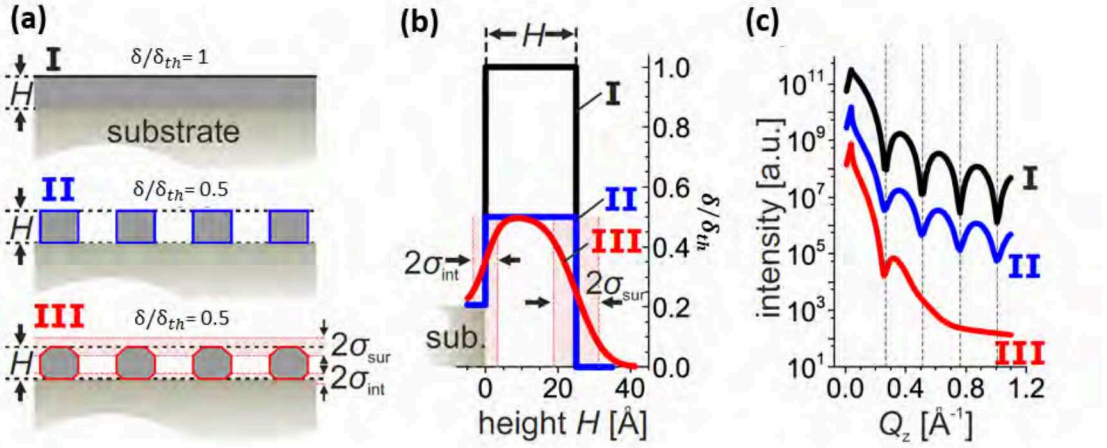

Figure 2.24.: Impact of different physical parameters on XRR-curves: (a) profile sketches of three single-layer systems with (I) a perfectly closed layer with a normalized electron density $\frac{\delta}{\delta_{th}}$, (II) homogeneously distributed, perfect cubic particles, and (III) homogeneously distributed particles with both the particles and the substrate exhibiting height fluctuations. The two latter systems feature half the normalized electron density compared to the perfectly closed layer (I). (b) the corresponding normalized electron density profile, whereas (c) XRR-curves simulated in *Fewlay* (here: $Pt/MgAl_2O_4(0001)$, data are offset for illustration purposes; see [41]). Figures taken from [41] and modified.

second UHV vessel resembles that of the vessel shown. It comprises 1) a manipulator which enables horizontal rotation and positioning of the sample in x,y,z, 2) a sputter gun with Argon supply gas line (not used for this work), 3) FOCUS EFM3T triple evaporator[24], 4) sample heating stage mounted on the manipulator, 5) pressure gauge to monitor the pressure inside the vessel, 6) OAR TC50 thermal gas cracker[25] with oxygen supply gas line, 7) FOCUS EFM3 single-pocket evaporator, 8) turbo pump, and 9) titanium sublimation pump and ion pump. The second UHV chamber features a SPECS EBE-1 single-pocket evaporator[26]. Both UHV vessels additionally have a LEED/AES system installed (not shown in the figure). The base pressure of both chambers is 10^{-11}–10^{-10} mbar. The detailed sample preparation is described in Section 2.2.6.

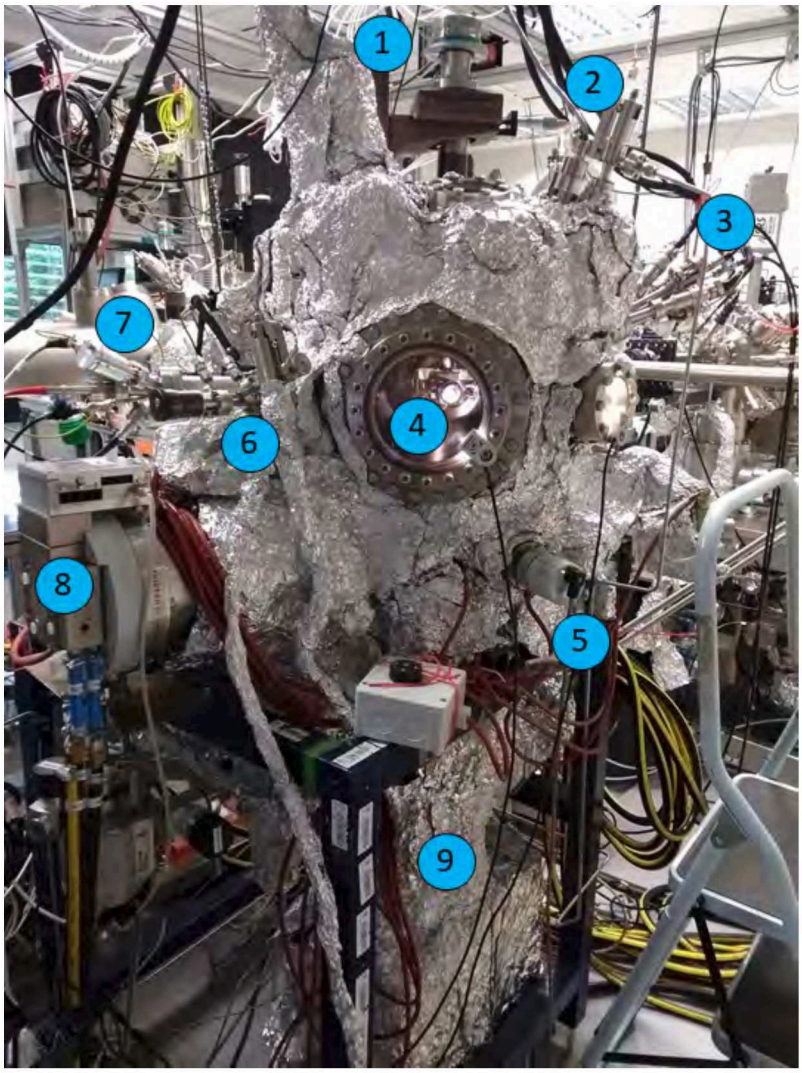

Figure 2.25.: UHV sample preparation vessel equipped with 1) manipulator, 2) sputter gun with Argon supply gas line, 3) triple evaporator, 4) sample heating stage, 5) pressure gauge, 6) thermal gas cracker with oxygen supply gas line, 7) single-pocket evaporator, 8) turbo pump, and 9) sublimation pump and ion pump. On the back of the vessel, an AES/LEED system is installed.

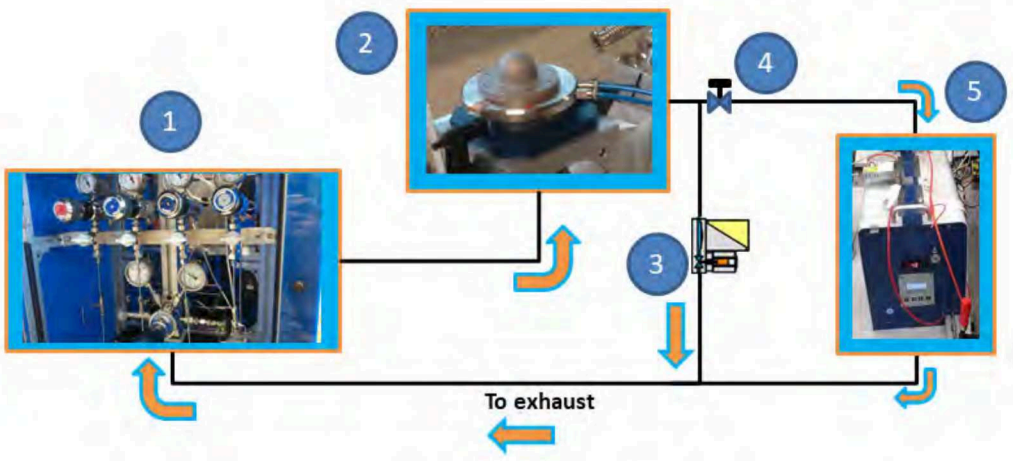

Figure 2.26.: Schematic of the gas supply setup used for operando measurements employing the small catalysis reactor: 1) mobile gas flow cabinet, 2) catalysis chamber, 3) back pressure controller, 4) needle valve, 5) residual gas analyser. More info given in text.

2.5.2. Versatile gas supply system with in-situ SXRD reactor

To allow for in-situ XRD measurements on nanoparticles during a catalytic reaction a comprehensive gas supply setup and corresponding reactor is necessary. The general layout of the system is depicted in Figure 2.26. Heart of the gas system is a mobile gas flow cabinet 1) manufactured by LPM[27]. This cabinet is connected to the laboratory's gas infrastructure and provides a stable, monitored gas flow of 1–100 $\frac{\text{ml}}{\text{min}}$ for a gas mix of up to 5 different gases (see Figure C.10 and additional info in the Appendix C.4). Argon was used as a carrier gas throughout the studies in this work. The gas cabinet provides the LPM SXRD catalytic reactor (catalysis chamber) 2) with a well-defined flow of mixed gases. The accessible pressure range is between few mbar and 1.2 bar (limited by the Viton gasket and the beryllium dome of the chamber). The pressure is controlled by a back pressure controller 3) in the exhaust gas line downstream the catalysis reactor. A parallel connection to the back pressure controller allows for the gas composition to be analysed via a needle valve 4) and a gas analysing system 5). The latter is a LPM T100 residual gas analyser (RGA) which is a stand-alone vacuum system comprised of a rough pump, a turbo pump, a small vacuum chamber and a mass spectrometer, and a temperature controller enabling degassing the vacuum chamber at up to 70 °C. The needle valve allows to

[24]FOCUS electronics GmbH, Naumburger Straße 28, D-04229 Leipzig.
[25]Oxford Applied Research Ltd, Nursery Road, North Leigh Business Park, Witney, Oxfordshire, United Kingdom, OX29 6SN.
[26]SPECS surface Nano Analysis GmbH, Voltastraße 5, D-13355 Berlin.
[27]Leiden Probe Microscopy, Kenauweg 21, 2331 BA Leiden, the Netherlands.

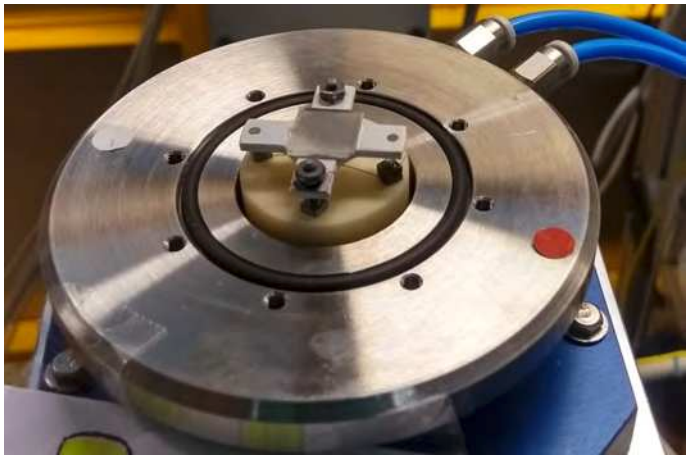

Figure 2.27.: A sample mounted on the ceramic heating stage of the catalysis reactor with its beryllium dome removed.

control the amount of bypassing gas entering the vacuum chamber. The residual gas analyser is typically operated at 10^{-7} mbar pressure inside its vacuum chamber. Thus, the amount of bypassing gas is small compared to the gas going through the back pressure controller.

The catalysis chamber is a small, lightweight ($m < 1\,\mathrm{kg}$) reactor to be mounted on typical diffractometer (piezo) stages. It comes equipped with two gas connectors and feed throughs for a thermocouple and heating current connection for a ceramic heating stage[28] operational up to 500 °C. Water cooling ensures a stable temperature. To provide a decent thermal contact, samples are glued on top of the ceramic heater using boron nitride, see Figure 2.27. The beryllium dome is nearly transparent for X-rays of about 8–10 keV energy, thus providing a controlled environment for the reaction and allowing penetration by X-rays at the same time. In a test experiment, the temperature, where the CO_2 production of CO oxidation upon alumina supported PtRh particles has the best trade-of towards careful treatment of the equipment, was determined – see Figure C.12 and associated information given in Section C.4 and Section C.5 in the Appendix. Prior to any experiments, gas lines from the local gas infrastructure of the respective laboratory towards the mobile gas flow cabinet are degassed using attached heating tapes while flowing gas and pumping down the gas lines. Additionally, a LPM carbonyl trap CT2.0 is installed in the CO supply line, to clean the gas from remaining carbonyls. All valves and gas lines are flushed and pumped down several times to ensure clean gas supply. Despite all the cleaning measures, a (usually decreasing) water signal is still detectable by the

[28] The temperature of the heating stage is set via an external current supply. Temperature monitoring via a thermocouple is optional. See Section C.4 for info on the temperature calibration.

mass spectrometer in all measurements. The origin of the signal could either be originating due to leaks or be correlated to water remains in the gas supply (remains in the gas line of the laboratory infrastructure or the gas itself).

2.5.3. X-ray diffraction instruments

In this work, X-rays are the primary tool to obtain size information of the nanoparticles investigated. All measurements employing X-rays except for the experiment presented in Chapter 5, which was conducted using synchrotron radiation, were done at DESY NanoLab with the six-circle diffractometer[29] depicted in Figure 2.28. The diffractometer consists of a detector (1), which is mounted together with two sets of detector slits (2) on the diffractometer arm, the diffractometer cradles with the sample stage (3), and the X-ray source (4). The sample stage enables translation of the sample both horizontally and vertically, and rotation of the sample around the surface normal and along two horizontal, perpendicular axes for sample alignment. Additionally, the angle of incidence is adjustable. The detector arm can be moved both horizontally and vertically, thus enabling to record a large area in reciprocal space. On the picture, a point detector is mounted, the measurements presented in this thesis were conducted with 2D detectors. The X-ray source *Incoatec*[30] $I\mu S$ emits Cu Kα_1 radiation with $\lambda = 0.154\,\mathrm{nm}$ with $9 \cdot 10^8\ \frac{\mathrm{photons}}{\mathrm{s}}$ (right behind the optics) and a divergence of 5 mrad. The beam is focussed to a spot size of $(250 \times 250)\,\mu\mathrm{m}^2$.

2.5.4. Direct imaging methods

To additionally support the X-ray measurements conducted in this thesis with complementary information about the spatial dimensions of the nanoparticles both Scanning Electron Microscopy (SEM) and Atomic Force Microscopy (AFM) were conducted. All SEM and AFM measurements in this work were conducted by M. Abuìn, S. Kulkarni, or A. Jeromin[31].

SEM is a versatile tool, providing a quick direct image of a sample's surface. In SEM, the sample's surface is scanned with a collimated electron beam with energies between hundreds of eV and tens of keV with a diameter of down to 0.5 nm [218]. The corresponding resolution of the image depends on the imaging method and can be of the same order of magnitude. The imaging process is based on the interaction

[29] See [217] for further information on six-circle diffractometers.
[30] Incoatec GmbH, Max-Planck Straße 2, 21502 Geesthacht.
[31] Deutsches Elektronen-Synchrotron, Notkestraße 85, 22607 Hamburg.

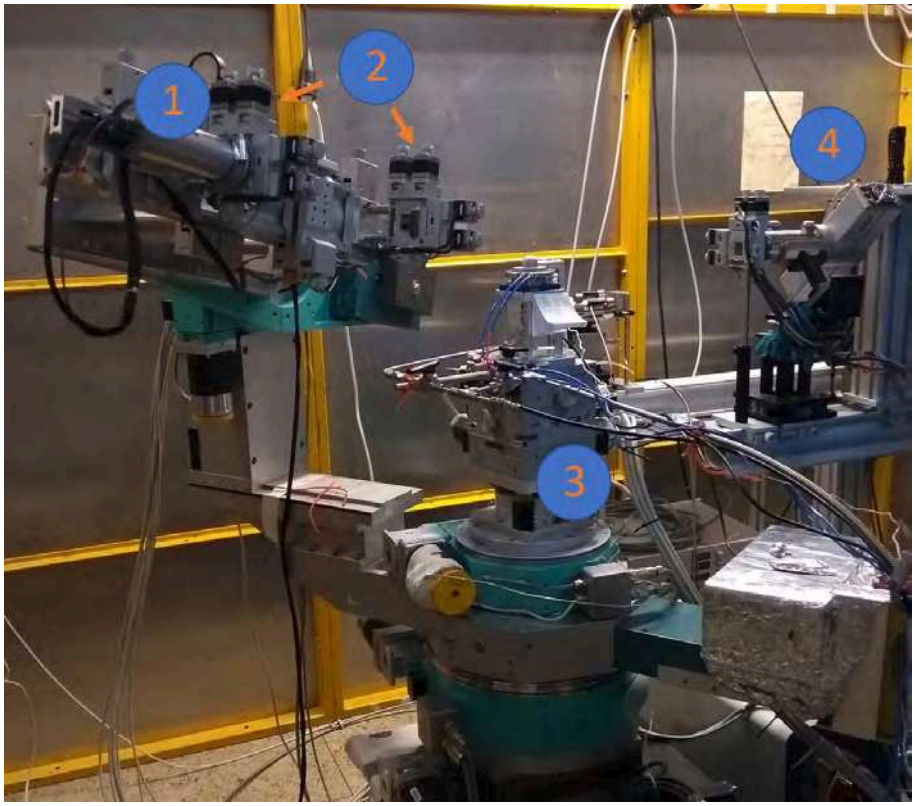

Figure 2.28.: Six-circle diffractometer at DESY NanoLab. (1) detector, (2) two sets of detector slits, (3) diffractometer cradles and sample stage (here with catalysis reactor mounted), and (4) X-ray source.

of electrons with the surface of the imaged specimen, hence different types of signals are possible:

- Secondary electrons are generated by inelastic scattering of the primary electron beam in the interaction volume in the sample. Typically, their energy is in the range of few ten eV, hence only secondary electrons from the surface reach the detector. Consequently, the secondary electron signal is very sensitive to the topology of the sample's surface.

- Backscattered electrons originate from elastic scattering on atomic shells in the interaction volume. As the scattering probability increases with atomic number, this signal is sensitive to the chemical composition of the sample. Additionally, electron backscatter diffraction (EBSD) may be used to determine the crystallographic structure of the sample.

- Inelastic scattering of the primary beam on atomic shells additionally produces X-rays as bremsstrahlung. If electrons from the primary beam happen to expel electrons from inner shells of the atoms, recombination of the unoccupied states generates characteristic X-rays. These are elemental specific and can be used to determine the elemental composition of the sample (energy dispersive X-ray analysis, i.e. EDX).

Further signals may include Auger electrons, luminescence, and induced electron current. See [219] for further information.

AFM is a direct imaging method which offers precise height information on studied specimen on the sub-nanometer scale. The measurement method is based on a well-defined tip mounted on a cantilever and the interaction between the tip and the surface of the specimen to be imaged. Typically, the position of the cantilever is monitored optically (e.g. LASER beam) to precisely detect any movement of the tip while it interacts with the surface. The tip can be in direct contact to the surface of the sample or be in a non-contact mode, including the tapping mode where the cantilever is forced to oscillate close to its resonance frequency. Thus, changes in the probed topography induced by a varying interaction between tip and surface cause a change in either frequency, amplitude, or phase, which in turn can be monitored. The tapping usually comes to use if measuring under ambient conditions. The dominating interactions between tip and surface depend on the measuring mode applied. Generally, interaction forces include Van der Waals forces, electrostatic

forces, dipole-dipole interactions, capillary forces, among others. Though directly imaging a surface, the lateral topography recorded is the actual topography of the surface folded with the shape and lateral size of the tip. Consequently, lateral information (e.g. diameter of nanoparticles) has to be treated with care. For further info on the AFM technique, it is referred to [220].

Chapter 3.

Growth of 3D shaped Pt particles on alumina

As a first step towards a deeper understanding of the dynamic morphology of nanoparticles upon catalytic reactions, the model system itself is to be characterized. The overall aim is to find growth parameters suitable for well-defined growth of particles with dimensions of about 100 nm in both height and diameter to allow for single particle X-ray diffraction imaging to be applied. The need for a particle size of about 100 nm in both diameter and height will be further discussed in Chapter 5. As a starting point, this chapter will give insight in studies undertaken by other research groups or researchers so far (first two sections) and findings obtained from own experimental studies done using different gas environments (Section 3.3). Eventually, in Section 3.4 boundary conditions and driving forces limiting and determining the morphology of platinum particles on alumina support will be illuminated again (compare Section 2.2) in the frame of the experiments undertaken. A well-motivated suggestion for the underlying process causing a drastic change of the particles' morphology will be given.

3.1. Morphology of platinum microstructures on alumina

Extensive studies were undertaken on thin film Pt/Al_2O_3 systems, grown via MBE [221, 222], sputter deposition [223–226], evaporation [227–229], or metal-organic chemical vapor deposition (MOCVD) [230]. Prior to deposition of platinum, the alumina substrates were exposed to annealing at minimum 500 °C in either high vacuum or UHV throughout all studies mentioned. Key findings of platinum thin films on substrate orientation (0001) are:

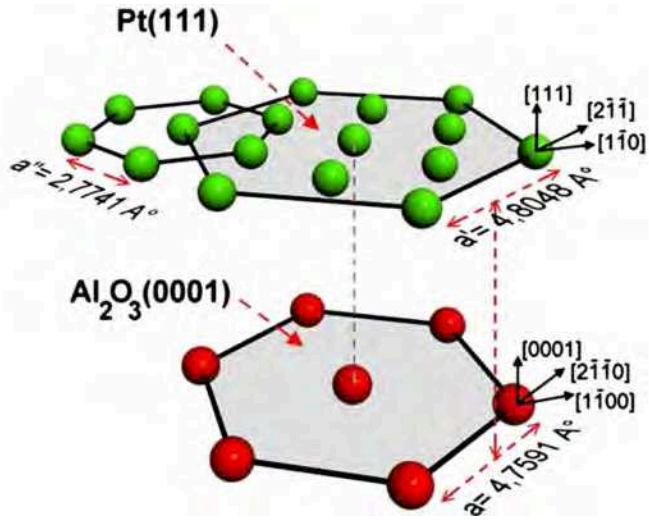

Figure 3.1.: Sketch of the α-$Al_2O_3(0001)$ superficial plane in Al-termination (in red; compare [101] and Section 2.2.5) and Pt(111) plane (in green). Taken from [67] and modified.

- Upon deposition far below 500 °C, platinum films will grow in macroscopically flat and smooth, though disordered layers with random epitaxial relationship towards the substrate.

- At temperatures roughly between 500 to 650 °C the platinum atoms are mobile and may diffuse along the surface, thus initiating epitaxy. Macroscopic roughness of the films increases with temperature as the growth mode is of Volmer-Weber type and platinum atoms will arrange in islands, first. The higher the temperature, the more pronounced these findings are.

- The epitaxial relationship of platinum and Al_2O_3 at elevated temperatures are: $Pt[111]||Al_2O_3[0001]$ and $Pt[2\bar{1}\bar{1}]||Al_2O_3[10\bar{1}0]$.

The latter configuration is sketched in Figure 3.1 and exhibits the smallest possible lattice mismatch of about 0.96 %:

$$misfit = \left(a_{Pt} \frac{\sqrt{3}}{\sqrt{2}} - a_{Al_2O_3} \right) / a_{Al_2O_3}, \tag{3.1}$$

with $a_{Pt} = 3.923\,\text{Å}$ and $a_{Al_2O_3} = 4.759\,\text{nm}$. Furthermore, *Nefedov et al.* found platinum films to be growing in [111] direction on $(11\bar{2}0)$-alumina [231].

Despite the variety of thin films studies, few information is available on the epitaxial relationship between platinum and alumina in regard of small nanostructures. *Benamara et al.* investigated the growth of ultrathin Pt films on alumina by means

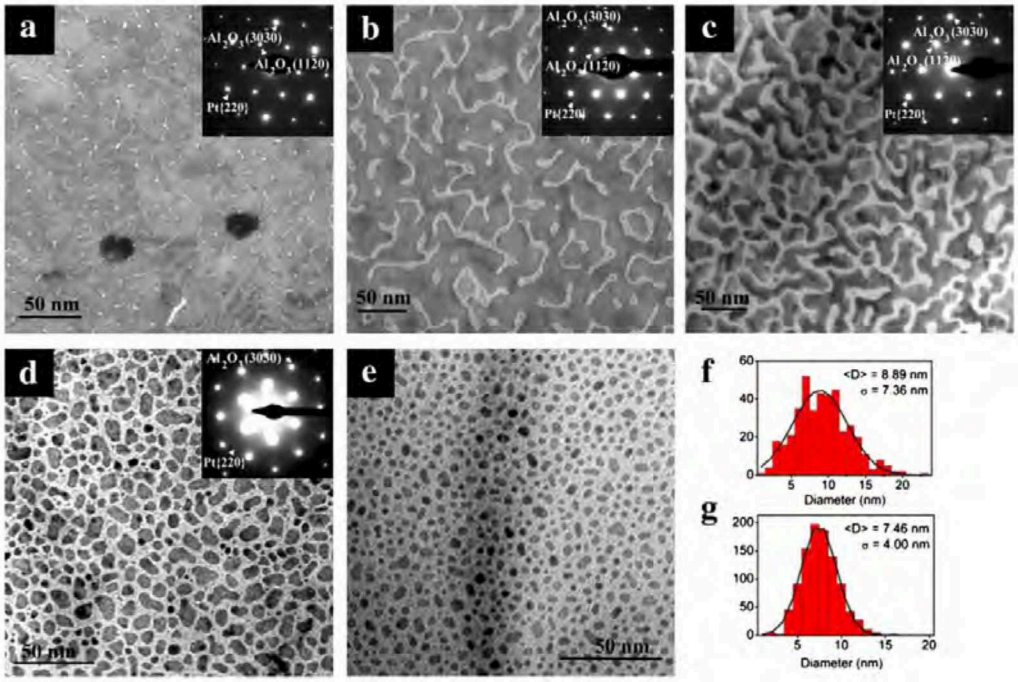

Figure 3.2.: TEM micrographs of platinum thin films grown on Al_2 $O_3(0001)$ at 650°C with deposited thicknesses 10 nm, 4 nm, 2 nm, 1 nm, and 0.5 nm, (a)-(e) respectively. Insets - if any - show corresponding SAED images. Grain size distributions are given for 1 nm and 0.5 nm in (f) and (g). Taken from [67].

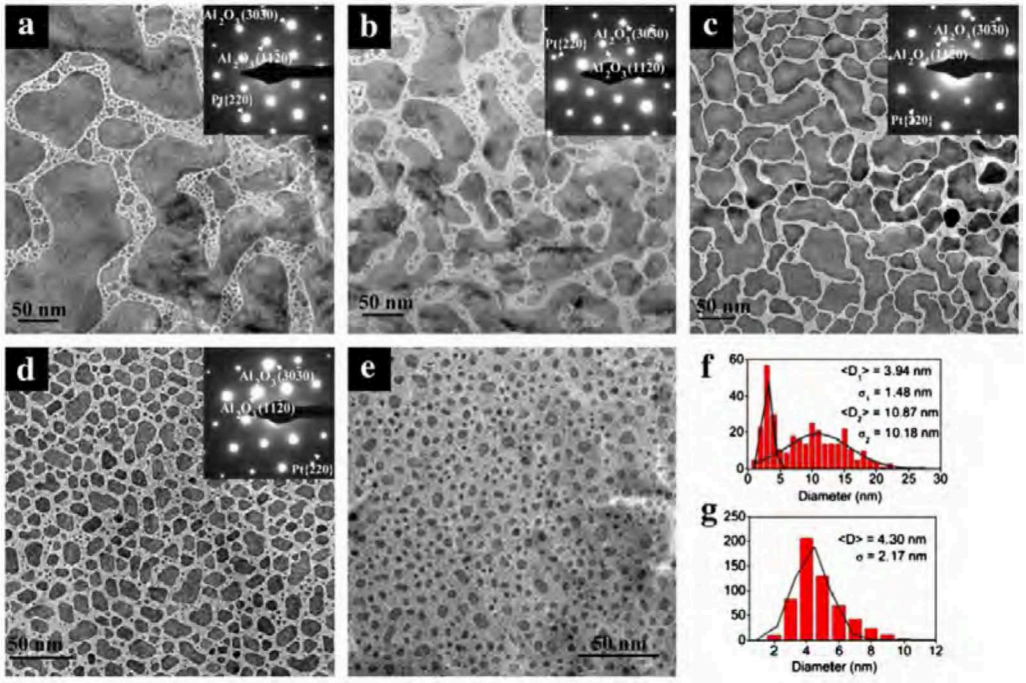

Figure 3.3.: TEM micrographs of platinum thin films grown on Al_2 $O_3(0001)$ at 750°C with deposited thicknesses 10 nm, 4 nm, 2 nm, 1 nm, and 0.5 nm, (a)-(e) respectively. Insets - if any - show corresponding SAED images. Grain size distributions are given for 1 nm and 0.5 nm in (f) and (g). Taken from [67].

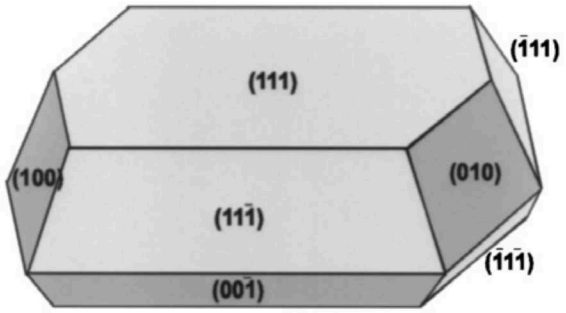

Figure 3.4.: Estimated morphology of a platinum particle grown at elevated temperatures as proposed by [67]. Taken from [232].

of varying nominal film thicknesses and temperature during growth [67], see Figures 3.2 and 3.3. Two series of samples with well-defined thicknesses between 0.5 and 10 nm were grown at two temperatures, respectively – 650 and 750 °C. This work confirms the findings of the studies above and emphasizes the two main driving forces determining the morphology and epitaxy of the platinum particles on alumina: temperature and amount of deposited material. At 650 °C deposition temperature, they report a rather static (diffusion limited) growth of rather smooth thin films and islands, which grow laterally, quasi-linearly with increasing amount of deposited material. At 750 °C, dynamic growth with pronounced island formation is reported and especially in the limit of few material deposited, the Volmer-Weber growth mode is accompanied by coalescence and Ostwald-ripening, leading towards a bimodal particle diameter distribution – see Figure 3.3(f) for the example of 1 nm deposited material: contrary to growth at at 650 °C, for all varying thicknesses there is one small pronounced particle diameter of about 4 nm observable together with a second diameter peak increasing with the amount of deposited material (not shown here). Qualitatively, the overall morphology of forming platinum islands is flat with a low height to diameter ratio. By means of surface energy arguments, they introduce a morphology model – see Figure 3.4 – as proposed by *Gatel et al.* who studied the growth of platinum islands on MgO [232]. On the one hand, the Bauer criterion – see equation 2.17 in Section 2.2.1 – would predict 3D growth for low nominal layer thicknesses. On the other hand, surface energy calculations of the respective low-index planes of platinum state $\gamma_{\{111\}} < \gamma_{\{100\}} < \gamma_{\{110\}}$, thus favouring the proposed model[1]. *Benamara et al.* did not quantitatively determine the thicknesses of the

[1]Calculated surface energies for metals and respective experimental values have been published by *Vitos et al.* [233]. Surface energies of the interface, the alumina phase, and the platinum phase can be found in publications [121, 234, 235], respectively. Applying these to the relation of Dupré 2.15 and the Wulff-Kaishev theorem 2.13 allows for the particle morphology to be

formed platinum islands or films dependent on the amount of deposited material for the two temperatures, thicknesses were qualitatively shown in TEM cross-sections. Accordingly, the predicted morphology model remains qualitative.
A recent publication by *Sui et al.* investigated the effects governing the morphology of alumina supported platinum nanostructures by another approach. They did not choose a bottom-up approach as in the studies mentioned above, but deposited platinum films first and exposed them to a post-growth annealing at different temperature and varying time of annealing [236]. By these means they created nanostructures via dewetting of the original platinum thin film. For similar amount of deposited material and similar applied temperature of the system, their AFM study resembles the work of *Benamara et al.* above. Above 750 °C, enhanced surface diffusion and Ostwald-rippening are reported for initial film thicknesses of 10 nm and below. For an initial film thickness of 20 nm, wiggly nanostructures instead of islands are formed upon annealing which are said to be due to pronounced coalescence and Rayleigh instability.

3.2. Morphology of platinum nanoparticles on alumina

As one of the major aims in the present work was to generate alumina supported platinum particles with a well-defined 3D geometry and preferably isolated from other particles in order to pursue single-particle X-ray diffraction imaging, further studies were undertaken in our group. To further investigate the epitaxial relationship of Pt deposited on α-Al_2O_3(0001) in the regime of few monolayers deposited, Jan-Christian Schober from DESY Nanolab characterized Pt particles deposited at different temperatures [237]. Pt was deposited on α-Al_2O_3(0001) at RT, 330 °C, 530 °C, 630 °C, and 830 °C – samples 1-5, see Table A.1 in Appendix A. The samples were generated in the manner described in Section 2.2.6 and characterized employing XRD, XRR, and SEM. No postannealing has been undertaken on these samples. The nominal deposited amount of material is depicted in Figure 3.5 (b) and was between 3 and 5 monolayers of platinum. Figure 3.5 (a) shows the average coverage on the samples determined with XRR, following a trend indicated already in the work of *Benamara et al.*, where, too, the average coverage on the samples decreases slightly with temperature. They correlate the decreasing coverage with more and more pronounced formation of geometrical shaped islands via Vollmer-Weber growth and surface diffusion enabled at elevated temperatures. Analogously to studies performed on platinum thin films,

estimated.

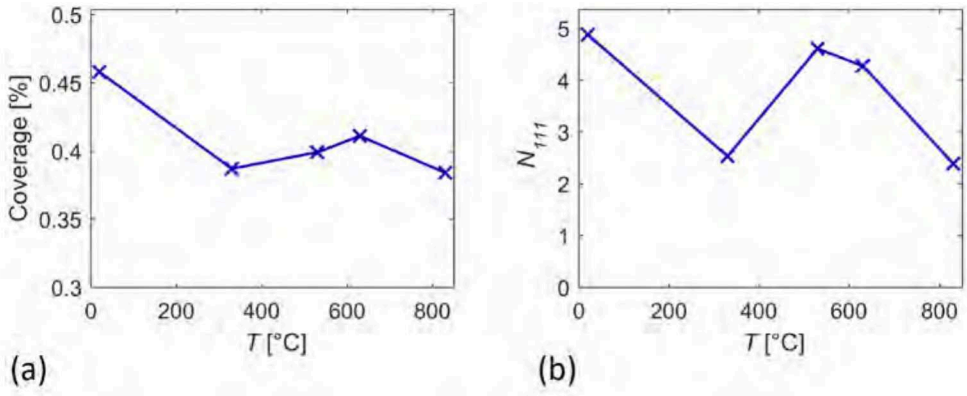

Figure 3.5.: Coverage (left) and number of nominal deposited (111)-oriented atomic layers (rigth) of Pt overlayers deposited at different temperatures on alumina substrates. Taken from [237].

XRD measurements confirm a disordered structure of the platinum deposited at RT. With increasing temperature – here already starting at 330 °C –, particles are epitaxially growing with their [110] or [111]-axis aligned with the substrate's surface normal. The XRD measurements suggest that the (110)-orientation becomes more and more unfavourable with increasing temperature. Particles with (110)-orientation were not detectable in XRD measurements performed on platinum particles grown at 830 °C, as demonstrated in Figure 3.6, which shows an intensity map in surface coordinates of (111)-oriented particles. (110)-oriented particles would be detectable via a reflection at roughly $H_S = 2.25$ r.l.u. and $L_S = 0.86$ r.l.u. in Figure 3.6 (a). At 530 and 630 °C, (111)-oriented particles are present in rotations with 0 and 30 ° with respect to the surface normal[2] and both in ABC and CBA stacking. Particles rotated with 30° are less pronounced on the sample generated at 830 °C, as indicated in Figure 3.6 (a) and (b). An overall correlation of the height of the particles determined via XRD line scans and particle diameter determined from both XRD line scans and SEM images led to the finding that the ratio of height to diameter is decreasing from about 0.33 at 330 °C to about 0.1 at 830 °C, with the height slightly increasing from about 6 nm to 9 nm and the diameter increasing at the same time from about 10 nm to 80 nm. Further, the height was found to be strongly dependent on the amount of deposited material.

[2]The publication referred to here states particles with twists of 60°, which does not fit the measurement results given in the publication.

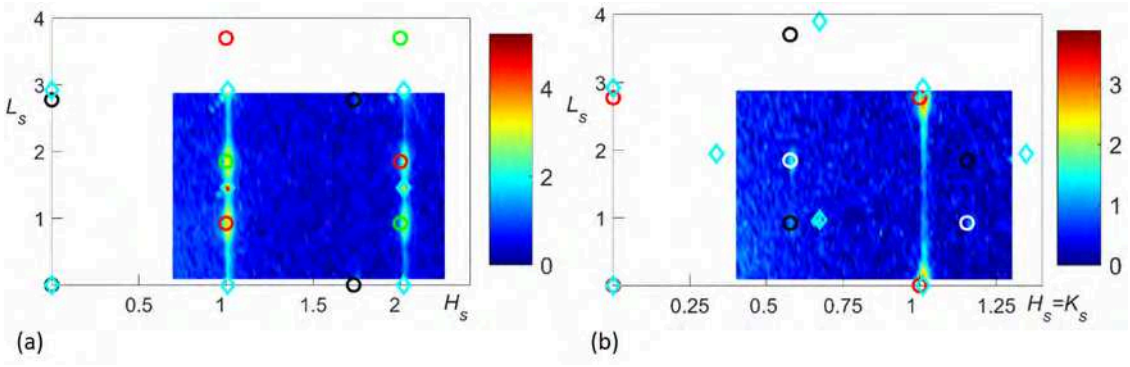

Figure 3.6.: 2D XRD maps in (a) $H_S, K_S = 0, L_S$ and (b) $H_S = K_S, L_S$. Scans were taken with an integration time of 5 s. Calculated positions are indicated for α-Al_2O_3 bulk (cyan diamonds), (111)-oriented Pt with ABC and CBA stacking (red and green circles, respectively), (111)-oriented Pt with 30 ° rotation with respect to the surface normal (black and white respectively). Taken from [237].

3.3. Growth of platinum particles upon annealing in different environments

Again, if single particle XRD is to be applied on such a system, the platinum particles need to be significantly larger – see Chapter 5. Consequently, the amount of deposited material and the temperature had to be increased in the present study following previous findings mentioned above, in order to on the one hand provide sufficient amounts of material for 3D particle formation and on the other hand allow for platinum adatoms to overcome kinetic diffusion barriers over steps of platinum islands.

Two different treatments were applied to the deposited platinum, resulting in two opposing particle morphologies. First, UHV-annealing was applied. Subsequently, the sample was annealed in air. Prior to the annealing in air and after the treatment, the particles were characterized with SEM, AFM, XRD, and XRR, as described in the following. Please note, that physical errors on the quantities determined will not be stated here, as the quantification of these errors was not possible within the frame of this thesis for the techniques applied. Sources of errors and their estimated impact on the measurements will be discussed qualitatively, though.

3.3.1. 2D particles through annealing in UHV

To study the morphology of platinum particles in the aforementioned frame, sample 26 (see Section A.1) was generated by depositing 1 nm (nominal) of platinum on

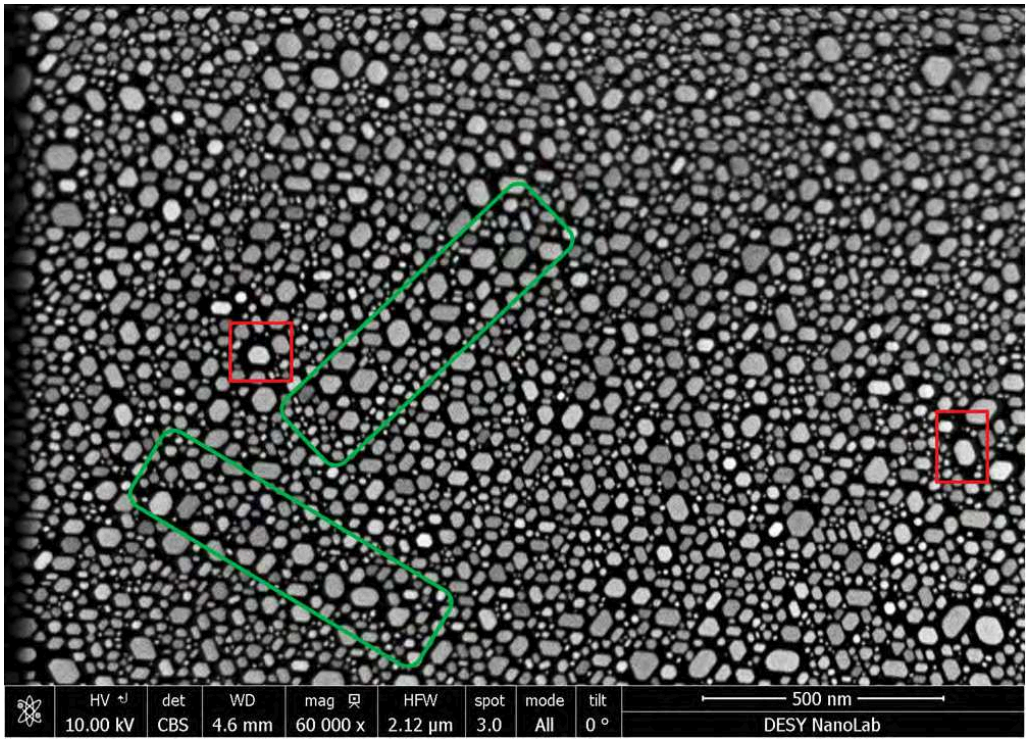

Figure 3.7.: SEM image of sample 26 before annealing in air. Dark areas correspond to the substrate and bright areas to platinum islands. The image is representative for the sample surface.

a pretreated alumina substrate as described in Section 2.2.6. Figure 3.7 shows an SEM image after deposition of platinum and annealing in UHV at 1100 °C for 10 min. Dark areas correspond to the alumina substrate, whereas the bright spots are the platinum particles. It is representative for the whole sample surface and, to some extent, resembles the results of *Benamara et al.* discussed above for samples with low amounts of platinum deposited – compare Figure 3.3 (d) and (e). Main differences are that in the present study the particles tend to be closer to a Wulff-like and hexagonal shape[3]. Similar to Figure 3.3 (d), in-plane alignment with the hexagonal surface is favoured. Another finding is, that the spatial arrangement of larger and smaller particles is not arbitrary – particles seem to align in lines on the substrate, most likely due to steps on the surface as exemplarily indicated by green markers in Figure 3.7. Further, the average inter-particle distance is larger for large particles compared to small particles, especially for particles with higher contrast in the image (brighter particles correspond to higher particles due to more intense back scattering). Examples for these areas are marked with red boxes and indicate the presence of

[3]As already stated in Section 3.1 above, qualitatively spoken, the (111)-oriented particles will adopt a hexagonal, flat shape.

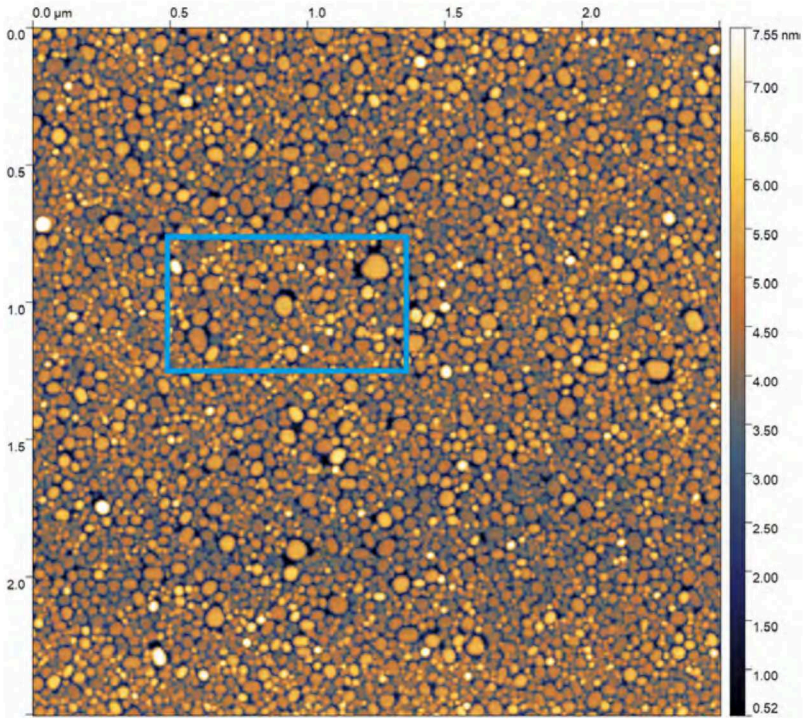

Figure 3.8.: AFM micrograph of a preselected area on sample 26 after annealing in UHV, but before annealing in the tube furnace. Three larger particles are highlighted in blue to correlated the area with Figure 3.8 below. The whitish particles exhibit heights of 10-16 nm. Yet, the maximum of the colour scale has been set to about 8 nm, to allow for a more distinct discrimination of the particles' height.

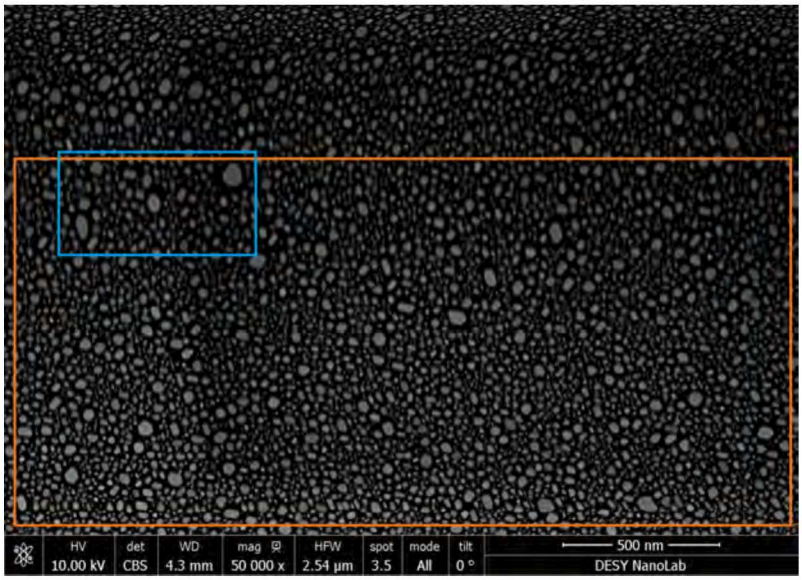

Figure 3.9.: SEM image of the same preselected area as in Figure 3.8 on sample 26 – compare particles highlighted by a blue framed box. Image was taken after annealing in UHV, but before annealing in the tube furnace. Due to superficial charging, the contrast varies a lot and the image becomes blurry. The orange rectangle represents the area, where particle statistics was evaluated.

diffusion mechanisms like Ostwald ripening or particle coalescence – see Section 2.1.3 and Figure 2.4 therein. In Figure 3.7, the overall coverage of platinum particles on the alumina substrate is about 41 % and the average size about 297 nm^2; both values may differ on other surface areas due to the platinum beam being not perfectly unidirectional and homogenous during the evaporation process. The average size of the particles corresponds to an average diameter of about 20 nm. Both average size and coverage are considerably higher compared to the study by Jan-Christian Schober above due to the increased amount of deposited material. The estimated diameter is twice as high compared to Figure 3.3 (f). Information on the image analysis for both SEM and AFM-images can be reviewed in Section B.2 in the Appendix.

To compare the morphology of the particles before and after annealing in air, an area of interest was chosen, as depicted in Figures 3.8 and 3.9. The region of interest could be tracked back by making use of macroscopic inhomogeneities on the sample surface, compare Figure B.1 in Appendix B.1. Figure 3.8 shows an AFM micrograph in the area of interest. The total area here is (2.5 µm× 2.5 µm) and the colour coding corresponds to the height of the particles with a maximum of 7.55 nm. The analysis of this area yields an average particle height of around 4 nm – compare the height distribution in Figure 3.14. The latter will be discussed in the following section. Figure 3.9 shows a SEM-image of the respective area of interest. Statistics derived from the orange area in SEM image 3.9 yield similar values as stated above, roughly 42 % coverage and an average particle size of about 325 nm^2. Because of superficial charging and – caused by this – fluctuations in the contrast of the image, only area surrounded by an orange box in Figure 3.9 was chosen to be evaluated. Still, the values are not as precise as for image 3.7. The rectangular area with contrast arose due to long exposure to the electron beam for images taken before.

The average height of the platinum particles was confirmed using XRR, which yielded an average height of about 4.7 nm compared to 4.1 nm by AFM. Details on XRD and XRR measurements will be given in the following section dealing with sample 26 after annealing in air. Deviations between XRR and AFM measurements arise due to the difference in investigated area of the sample as the X-ray footprint was about the size of the sample and the AFM region of interest only 6.25 $µm^2$.

3.3.2. 3D particles through annealing in air

From the sections above, it is clear that platinum particles grown on α-alumina with (0001)-orientation will adopt a flat morphology if exposed to temperatures above

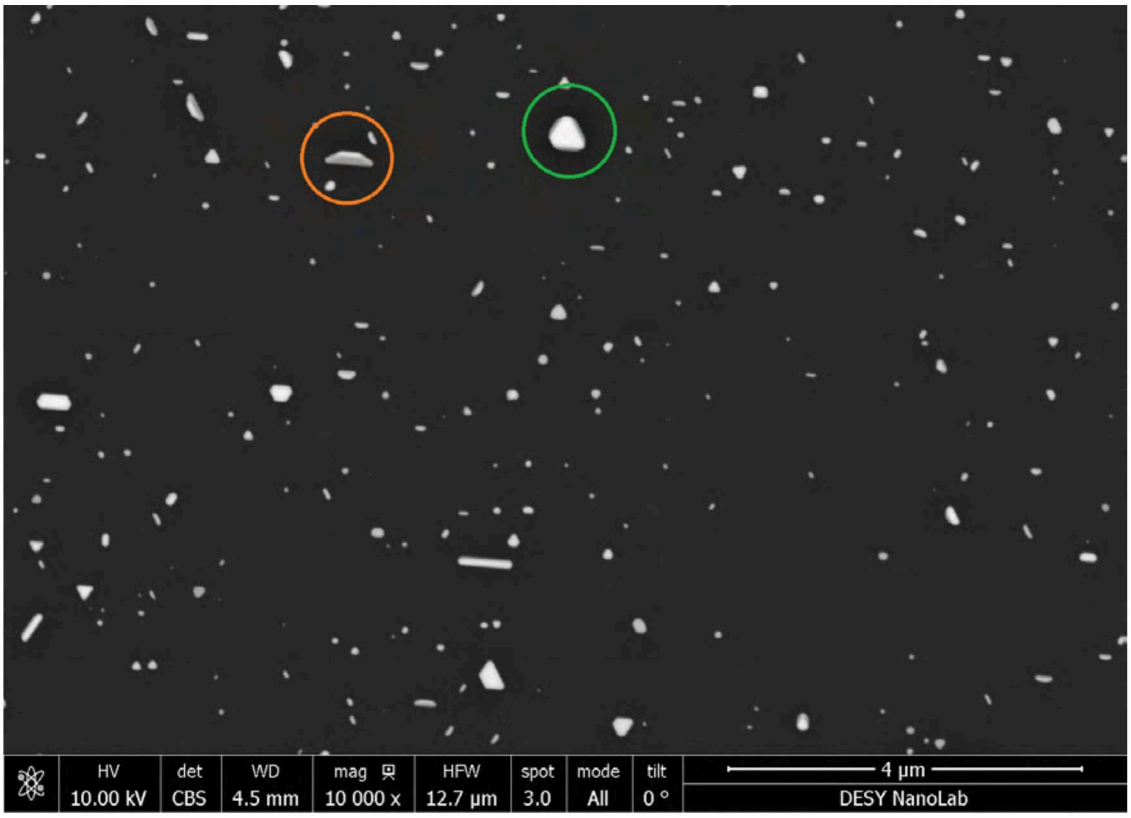

Figure 3.10.: SEM image of sample 26 after annealing in air – here an arbitrarily chosen position on the sample. The orange and green marking highlight most pronounced particle morphologies.

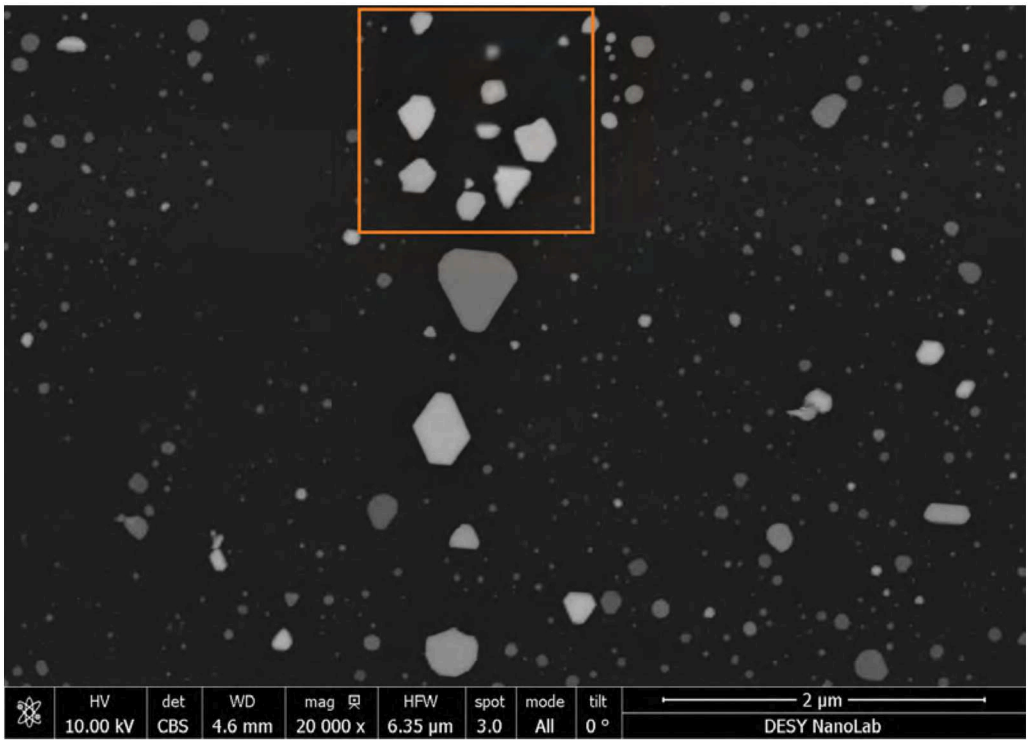

Figure 3.11.: SEM image of sample 26 after annealing in air in the same preselected area of interest as in Figures 3.8 and 3.9. The orange area highlights a former inhomogeneity on the substrate and is excluded from particle distribution statistics.

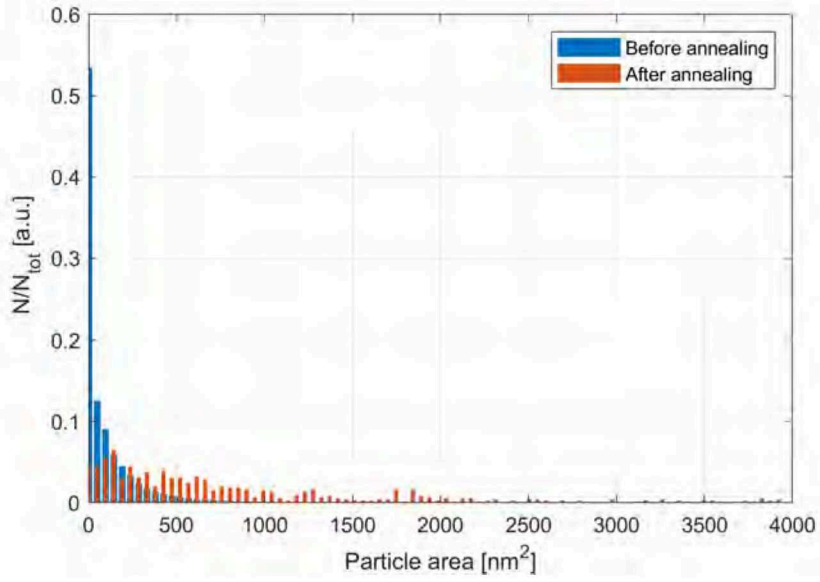

Figure 3.12.: Size distribution of particles on sample 26 before (broad, blue bars) and after annealing (thin, orange bars). See text for further info.

650 °C under UHV-conditions either during the evaporation process or afterwards. In turn, the picture changes drastically upon annealing in air, as will be further emphasized in the following.

After undertaking measurements revealing the morphology of the platinum particles annealed in UHV (see previous section), sample 26 was transferred to a tube furnace and annealed in air at 1200 °C for few seconds – see Sections A.1 and 2.2.6 for details. Figure 3.10 shows a SEM-image of a randomly picked area on the sample's surface after annealing in air. Judged only by eye, the overall density of platinum particles (bright, distinct areas) on the alumina surface is far lower than before annealing in air and particles are larger on average with a far broader diameter distribution. Further, the particles still tend to adapt certain in-plane orientations to the surface, though their overall morphology has changed. In Figure 3.7, hexagonal particles before annealing are rather close to a roundish shape in the plane parallel to the surface, as faces have roughly the same distance from the respective particles' centres. In contrast, after annealing in air, particles may adopt a more triangular shape in the surface plane, i.e. three pronounced large faces and three small faces (see green marking in Figure 3.10), or even a very elongated, almost rod-like geometry. For the former, the bright faces correspond the top-facets surrounded by less bright side facets. Further, particles may acquire upright hexagonal or triangular disc-like morphologies. The orange circle in Figure 3.10 highlights such a particle which most likely has an elongated interface with the alumina substrate, but adopts a 3D-shape as indicated by the different contrast: again, the bright area corresponds to the facet parallel to the surface and the less bright face has a certain tilt with respect to the top-facet. Possibly, the particle has a truncated tile-like shape. In this SEM-image, the average particle size in the projection towards the surface plane is around 9000 nm^2 and the coverage is around 2 %. These values are a very rough estimate, since at this magnification small particles either cannot be resolved or are neglected in the image analysis due to their contrast being too low.

To get an overview and a direct comparison, Figure B.2 in the Appendix shows SEM-images of the same area on the sample before and after annealing in air. The area could be tracked back via the large inhomogeneity marked in orange. The image clearly underlines the observations made above. Close-ups of the same surface area before and after annealing in air are given by Figures 3.9 and 3.11. In the latter, the area marked with the orange box is excluded from further analysis, because

this is the position of the not further identified, macroscopic particle marked in orange in Figure B.2. Most likely, it is a contamination with some platinum particles inside[4]. It allows for the area of interest to be tracked back, though - see also Section B.1. A direct comparison of this area of interest before and after annealing in air shows that it is not possible to track single nanoparticles before and after annealing in air, as it seems that all the platinum on the alumina has been rearranged into different morphologies. The particle size distributions for Figures 3.9 and 3.11 is given in Figure 3.12. Further info on the image analysis is given in Section B.2 in the Appendix. Before annealing in air, platinum particles will predominantly acquire a small lateral size, with their overal sharp distribution exhibiting a dominant peak below 50 nm^2 and rapidly decreasing with increasing size[5]. Contrary particles after annealing in air: generally, the distribution function is broad, slowly decreasing with increasing size and additional small peaks at around 1300 nm^2, 1700 nm^2, and 1800 nm^2. The average sizes are given in Table 3.3, namely 325 nm^2 before annealing in air and 2266 nm^2 afterwards. The x-scale for the particle distribution function was cut at 4000 nm^2, because only for the condition after annealing particles adopt even larger sizes and their number is too low to be visible in the diagram.

Height information, again, is gained via AFM-measurements. If not specified any further, diameters refer to the particle diameters gained from the AFM-image[6]. Figure 3.13 shows the surface of sample 26 in the aforementioned region of interest (compare Figure 3.11). The AFM-image indicates that both the size and height of platinum particles exhibit a broad distribution. Particles with diameters of 10-50 nm exhibit heights of 3-8 nm, height correlating with diameter. Although this indicates some kind of scaling behaviour, the AFM-measurement does not imply a clear correlation between lateral size and height for particles with a diameter larger than 50 nm. At least no correlation such that a larger diameter always corresponds to a higher particle. Though, all particles with a height of at least 20 nm exhibit diameters of at least 80 nm for the image taken. A comparison with the same area before annealing

[4]This assumption is supported by AFM-images of this area, like in Figure 3.13. Here, on the top of the image, the same area is depicted as the orange marked area in SEM-image 3.11. From the AFM-image it is clear that there is still surrounding material which most likely has a far lower electron density, as this remaining material can only be guessed from the darker contrast in the corresponding SEM-image's area.

[5]The bins of the particle area have a size of around 48 nm^2. The y-scale represents the number of particles per bin N divided by the number of particles in the total area N_{tot} for the two conditions, respectively.

[6]Note that in AFM-images, the shape information is a convolution of the actual particle shape and the tip shape. Thus, the determined height of any particles and islands will be rather precise, but any lateral information will be overestimated in the resulting image. The overestimated difference in diameter compared to SEM is about +30 nm for particles with about 100 nm height.

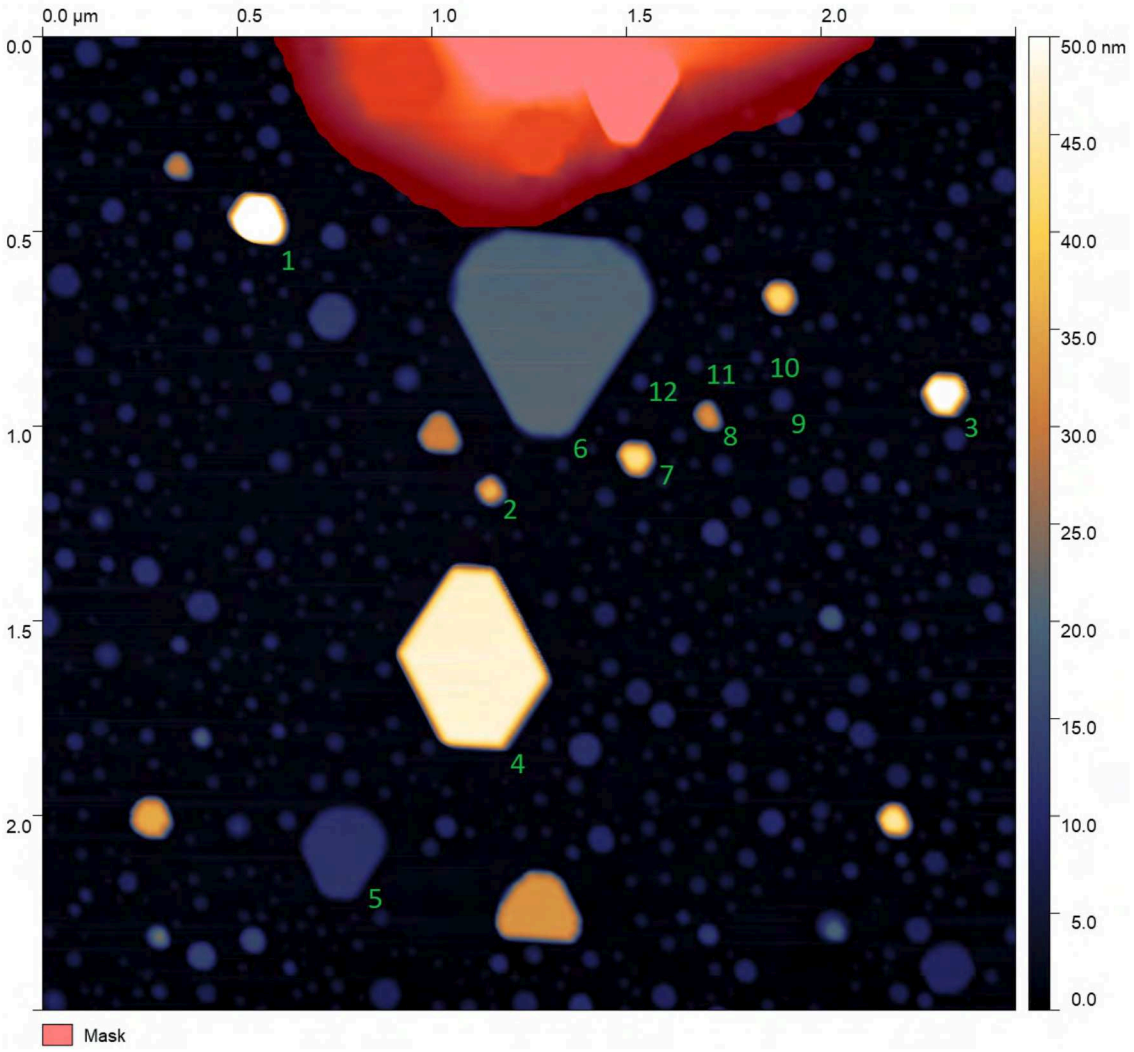

Figure 3.13.: Close-up AFM-micrograph of the area of interest on sample 26 after annealing in air. The area marked in red is excluded from particle statistics. The maximum of the colour scale is set to 50 nm, but the actual height maximum outside the red area is the particle in the top left with 76 nm. As particles with a height of 4 nm and less are hard to see with this colour scale, the same image with another colour scale can be found in Figure B.4 in the Appendix. For numbered particles, the height to diameter ratio has been calculated (see text). Numbers are at the bottom left of the particles, respectively.

in air – see Figure 3.8 – fits the observations made in SEM-measurements. Before annealing in air, the platinum particles exhibit a rather homogenous distribution in both lateral size and height with few deviations from the predominant morphology. However, after annealing in air, there are many small, flat particles, and some laterally large particles with considerable height. Figure 3.14 shows the height distribution in the region of interest on sample 26 before and after annealing in air. For the analysis, aforementioned AFM-images in Figures 3.8 and 3.13 have been employed. Here, ρ is the non-cumulative density per automatically chosen bin. ρ is normalized by means of $\int_{-\infty}^{\infty} \rho(h)\mathrm{d}h = 1$, with h being the height (and so, dh the size of the bin). Note that the average height does not refer to the average particle height. Instead, the hole image (except marked region) is spatially subdivided into a grid of few pixels and the respective height information then counted as a density $\rho(h)$ for the corresponding height bin dh. Generally, the particle distribution functions support the observations made above. Before annealing in air, the particle height distribution exhibits an almost Gaussian-like, rather narrow distribution with its maximum around 4.23 nm. After annealing in air, the overall distribution is broad. Here, the sharp, intense peak at around 1 nm height is mostly caused by artefacts in the fast-scanning direction (x-axis), which could not be properly corrected for – see Section B.2. Due to the colour scale in Figure 3.13, these strip-like features are not visible, compare Figures B.4 and B.5 in the Appendix, instead. The sharp peak at 1 nm features a shoulder at around 1.6 nm, which can be mostly attributed to borders of nanoparticles with low diameter (about 20-30 nm) and to surface roughness. This dominant maximum overlays a broad, less high distribution with a peak at around 3 nm, which corresponds to small particles that exhibit diameters of below 20-30 nm. Peaks at about 20 nm and 47 nm correspond to the two top facets of larger particles. The plot is cut at 50 nm, though there are small densities observable for even higher particles. For further statistics, particles were marked using a height threshold of 3 nm. This allows for fast-scanning features to be ignored, but naturally implies the drawback that particles with heights below 3 nm are not considered in the analysis. Images of particle mask and the resulting particle height distribution can be found in the Appendix, see Figures B.6 and B.8. The resulting average height with height threshold applied is 13.8 nm.

In Figure 3.13, 12 particles are marked with numbers. For these particles, the height-to-diameter ratio is given in Table 3.1. Here, the diameter values are taken from SEM-image 3.11. Particles 10-12 are at the lower detection limit in the SEM-image, so no smaller particles could be considered. The ratios cover a broad range and –

Number	Height [nm]	Diameter [nm]	H/D
1	78	94	0.83
2	31	68	0.46
3	54	80	0.68
4	48	299	0.16
5	12	187	0.06
6	21	447	0.05
7	43	53	0.81
8	32	39	0.82
9	10	27	0.37
10	8	13	0.61
11	8	15	0.53
12	10	19	0.53

Table 3.1.: Height to diameter ratios for numbered particles in Figure 3.13 – an AFM measurement on sample 26 after annealing in air. For the ratios. height was determined using AFM, diameter was gained from SEM-measurements.

as stated already above – disclose no clear relation between height and diameter. One observation is, that the particles with highest diameter feature the lowest H/D. Particles with a H/D close to 1 are the highest particles, too. The smallest particles visible to SEM are found to have a H/D close to 0.5. Before annealing in air, the average H/D is about 0.2, as obtained for the chosen area of interest mentioned above.

To support the direct imaging measurements with complementary methods, X-ray reflectivity measurements were conducted on sample 26 before and after annealing in air. Due to the large footprint of the beam, results of course might deviate from the outcome of the analysis made above. Figure 3.15 shows respective XRR-curves, data points are marked with crosses (blue: before annealing in air, orange: after annealing in air). For both curves, the peak around zero corresponds to the direct beam and the peak around 0.54 ° to the critical angle of platinum. Further oscillations arise due to constructive interference of the nanoparticles interfaces along the scattering vector Q_z – see Section 2.4.3 for a more elaborate discussion. For the curve taken after annealing in air, the position of the critical angle is shifted by about 0.08 ° towards higher angles which might be due to misalignment of the measurement setup. For low coverage with platinum, a shift towards lower angles would be expected, since the critical angle is proportional to the square root of the electron density, which is lower for alumina. Both curves were fitted using the software *Fewlay* [216], the respective fits for the two conditions are displayed by the straight lines in yellow and purple. As described in Section 2.4.3, the respective fit models in both cases

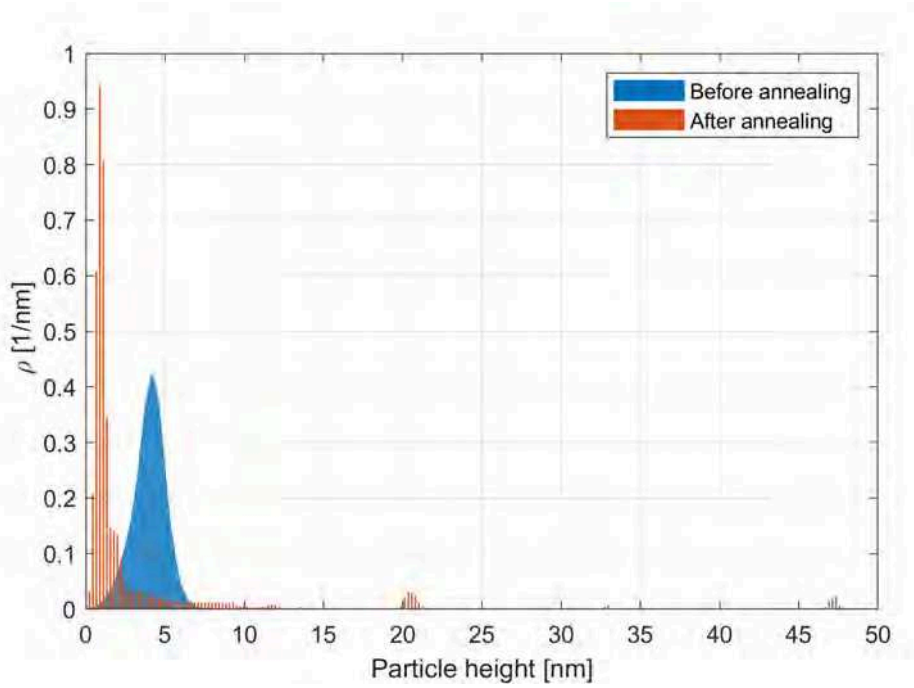

Figure 3.14.: Height distribution ρ (see text) on sample 26 before (blue bars) and after (orange bars) annealing in air.

were semi-infinitely thick substrates (fitting parameter: only roughness) and two layers (fitting parameters: thicknesses d_1 and d_2, roughness for both layers, electron densities δ_1 and δ_2 and absorptions for both layers). Indices 1 and 2 refer to these two layers, 1 referring to the topmost. The models obtained a fitting quality of normalized χ^2 of about 0.05 (before annealing in air) and 0.11 (afterwards), aberrations manly arising at low angles – likely related to the setup. In Figure 3.16, the resulting electron density profiles for the fitting parameters obtained are depicted, again, the condition before annealing in air coloured blue and after annealing in air in orange. The electron density profile before annealing in air resembles the outcome of the AFM-measurements. Overall, the effective thickness of the platinum layers $d_{\text{eff}} = d_1\delta_1 + d_2\delta_2$ of 2.5 nm ($d_1 + d_2 = 4.8\,\text{nm}$) fits the average particle height of about 4.0 nm determined via AFM, as the effective layer thickness represents a weighted thickness of the overall layer and is not probing sole particles. The pseudo-coverage $\bar{\delta} = \frac{d_1\delta_1 + d_2\delta_2}{d_1 + d_2}$ is considerably higher (about 52 %) than the value determined from the SEM-measurements (42 %). This abbreviation is related to the fact that the XRR geometry does not directly yield the coverage, but a ratio of electron density values $\bar{\delta}$. The fitting parameters themselves are summed up in Table 3.2. The electron density profile of the XRR-measurement after annealing in air qualitatively fits the findings made so far: it consists of a 1 nm thin layer (d_2) with a pseudo-coverage

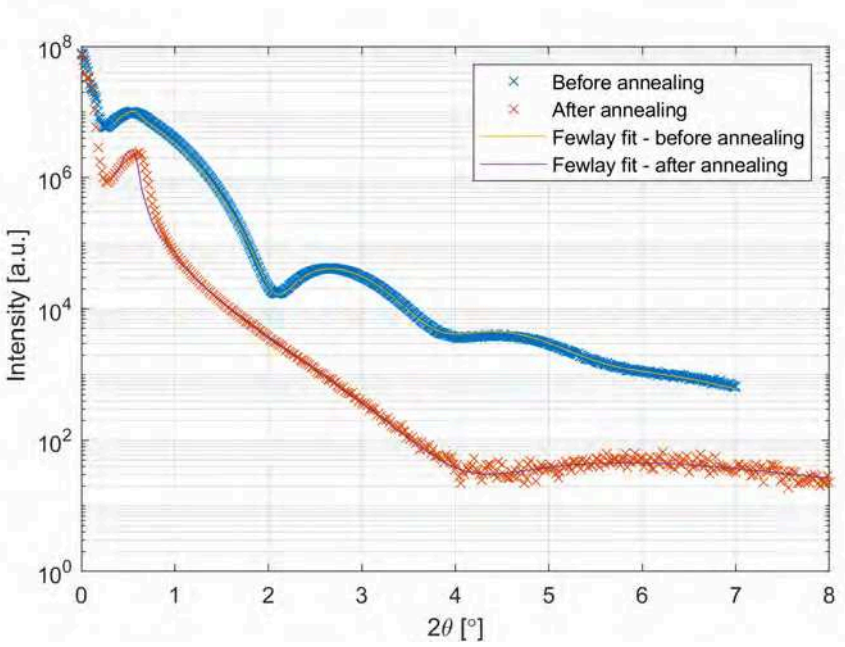

Figure 3.15.: X-ray reflectivity curves measured on sample 26, before and after annealing in air. Original data is marked with crosses (blue: before annealing in air, orange: after annealing in air), fits created with *Fewlay* are marked with straight lines (yellow: before annealing in air, purple: after annealing in air).

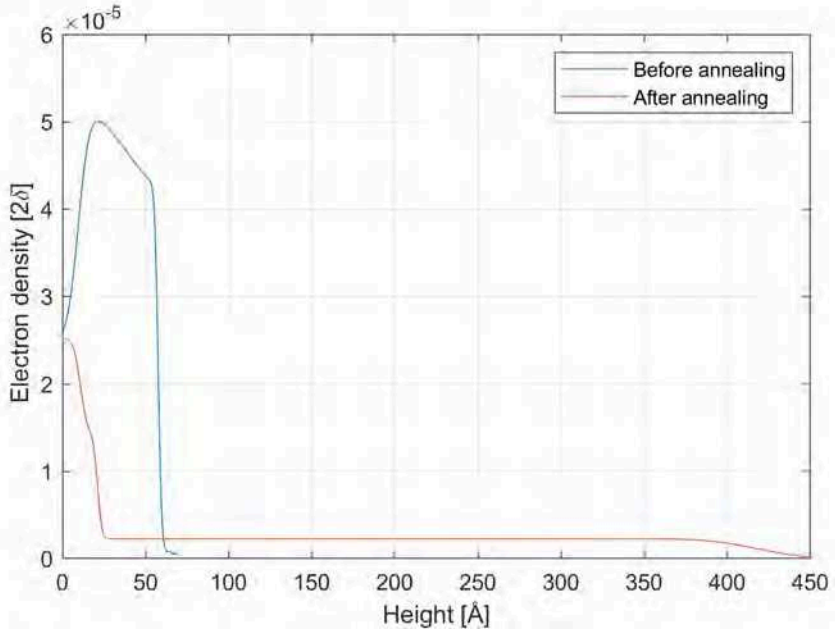

Figure 3.16.: Electron density profiles gained through fitting of XRR-curves measured on sample 26 before and after annealing in air. Respective XRR-curves are depicted above in Figure 3.15. On the x-scale, zero corresponds to the substrate's surface and increasing values correspond to distance along the surface normal.

δ_2/δ_{th} of about 14%. The topmost layer is fitted to be about 40 nm, with a very low pseudo-coverage (3 %) and relatively high roughness parameter σ (about 2.4 nm). The error on this layer is very high, though, as it does only have a minor influence on the fitting due to the very low pseudo-coverage and thus low average electron density. However, qualitatively spoken the results fit the overall picture. Additional wide-angle XRR scans can be found in Figure C.7 in the Appendix. Due to the configuration of the setup used, only peaks up to a 2θ-value of about 43 ° could be investigated. Additionally, for both measurements the setup was aligned on the alumina (0006) substrate peak – a systematic error, because with such a setup the momentum transfer will be aligned to atomic layers perpendicular to the substrate orientation rather than the surface normal itself. Though, the Figure basically confirms the (0001)-orientation of the substrate through strong peaks at about 41.6 ° – alumina (0006) – for both the sample before and after annealing in air. For both curves shown, a platinum (111)-peak is found at about 39.8 °. Here, the two curves deviate from each other, as the curve recorded before annealing in air features a broad peak accompanied by Laue oscillations[7] towards decreasing angles. This indicates platinum islands with low height. From the distance between two minima, an average height of about 4.4 nm can be estimated, which fits the value determined by XRR and AFM (2.5 nm and 4.0 nm, respectively – see below). The average particle height determined from the FWHM of the Bragg peak is about 5.3 nm. The deviation between the heights determined could be due to the intrinsic height distribution, which favours higher particles due to the dependence on the scattering atoms of N^6 – see Section 2.4.1 – or the misalignment of the surface normal. The Pt(111)-peak of the sample after annealing in air is almost as narrow as the alumina substrate peak[8], thus indicating scattering by high particles. The particle height corresponding to the FWHM of the platinum Bragg peak is about 32 nm, the pseudo height determined from the alumina Bragg peak is about 40 nm, the latter being a rough estimate due to the substrate peak featuring a bimodal peak shape. Likely, the platinum Bragg peak width is limited by the resolution of the instrument. The absence of distinct, accompanying Laue oscillations are manifold. The oscillations could be too narrow if the particles are too high. Further, if the size distribution was too broad, fringes would be overlaying each other and eventually be washing out. From AFM and XRR it is already clear that the size distribution is very broad and not systematic.

[7] See end of Section 2.4.1.

[8] The peak width is limited due to the resolution of the setup. The peak width is proportional to the width of the beam profile of the setup (including beam divergence and angular resolution introduced by the detector) folded with the scattered signal from the sample.

	Before annealing in air	after annealing in air
d_1 [Å]	13.31	396.83
d_2 [Å]	34.67	10.30
$d_1 + d_2$ [Å]	47.98	407.12
δ_1/δ_{th} [%]	44.87	2.2
δ_2/δ_{th} [%]	55.0	13.67
$\bar{\delta}$ [%]	52.2	2.5
d_{eff} [Å]	25.04	10.14

Table 3.2.: Most relevant fitting parameters, gained from *Fewlay*-fits depicted in Figure 3.15. For each condition, a two-layer model with varying coverage of platinum was assumed, supported by an alumina substrate. Indices 1 and 2 refer to these two platinum layers, with 1 being the topmost. Accordingly, d and δ are the corresponding electron densities in the complex refractive index (δ_{th} being the literature value and $\bar{\delta}$ the pseudo-coverage, see text).

Consequently, the particle size determined here will be severely dominated by few very large particles due to the N^6 dependency, mentioned above.
Table 3.3 summarizes coverage, average particle size, and average height for the two annealing conditions. The two former were determined by image analysis of SEM-images, the later parameter was determined via analysis of AFM-micrographs that have not been further processed apart from levelling, see Figures 3.8 and 3.13. Additionally, values derived from XRR-measurements are given. Although coverage and average particle size reproduce observations made by eye, the effective height d_{eff} is decreased after annealing in air. This is partly caused by the height distribution for the condition after annealing in air being dominant at below 2 nm, on the one hand due to artefacts from the AFM-measurement, on the other hand there are small particles with heights of about 1.6-2 nm. The value for the particle height determined from (111) specular platinum Bragg peaks d_{Bragg} resembles the values determined from XRR and AFM quite well for the condition before annealing in air. After annealing in air, the value strongly deviates, as the FWHM of the (ensemble) Bragg peak is dominated by large particles ($I_{\text{Bragg}} \propto N^6$). In turn, this resembles the overall broad size distribution of the platinum particles after annealing in air. Again, many of these parameters have to be thought of rather qualitatively due to systematic errors either during measurement (e.g. XRR and AFM-measurements) or analysis (e.g. SEM-measurements).

Additionally to the measurements mentioned so far, X-ray diffraction was applied to get more crystallographic information and the exact epitaxial relation from the

	Before annealing in air	after annealing in air
Coverage [%]	41.8	6.9
Average particle size [nm^2]	325	2266
d_{AFM} [nm]	4.0	4.1
d_{eff} [nm]	2.5	1.14
$\bar{\delta}$ [%]	52.2	2.5
d_{Bragg} [nm]	5.3	32

Table 3.3.: Particle statistics in the preselected area on sample 26 before annealing in air and afterwards. Coverage and average particle size were determined using SEM-images and evaluation via *imageJ*. Average particle height d_{AFM} was determined via measurement with AFM and evaluation with *Gwyddion*. The effective layer thickness d_{eff} was determined using XRR and *Fewlay*. d_{eff} and $\bar{\delta}$ are taken from Table 3.2. d_{Bragg} was calculated from the FWHM of platinum (111) specular Bragg peaks.

nanoparticles before and after annealing in air. Figures 3.17, 3.18, and 3.19 show the measured intensity during in-plane rocking scans around the surface normal for Pt(200), Pt(220), and Pt(111) reflections before annealing in air (blue) and afterwards (red), respectively. As described in Section 2.4.2, these scans are sensitive to atomic planes with their crystallographic axis in the surface plane. Crystallographic information can be gained from the symmetry of occurring peaks or even the absence of peaks. For the three aforementioned figures, offsets in the ω-position between peaks at different conditions occur due to slightly different mountings of the sample on the diffractometer. The integration time was 5 s for the condition before annealing in air and 10 s for the condition afterwards. The curves are not shifted in intensity with respect to each other. The different background of the measurements arises due to a different setting of the energy threshold of the detector.

Geometrically spoken, for (111)-oriented particles (220)-type in-plane reflections must be observed. Figure 3.17 shows the scan for corresponding in-plane reflections[9]. Here, the intensity is plotted in logarithmic scale due to the broad range of intensity values. The very intense peaks with sixfold symmetry correspond to bulk reflections from the alumina substrate. They overlay with less intense Pt(220)-type peaks which occur every 30 °. Differences in intensity of peaks of the same type might arise either due to slight misalignment or due to the macroscopic geometry of the sample[10]. Since particles with either (110)- or (100)-orientation would also show Pt(220)-type reflections, in-plane rocking scans for the corresponding occurring in-plane reflections

[9]For Figures 3.17, 3.18, and 3.19, the background for the conditions before and after annealing in air differs, because before the measurements done on sample 26 after annealing in air, the detector threshold was set to a higher energy value.

[10]The overall shape of sample 26 is rectangular.

have to be considered. Figure 3.18 shows on linear scale the intensity versus in-plane rocking angle for Pt(200)-type reflections. They appear every 30 °, which proves the occurrence of either (110)- or (100)-oriented particles which possibly adopt in-plane rotations towards the alumina substrate with at least 0, 30, or 60 °. Additionally, there are weak peaks with an offset of 15 ° towards the more intense peaks after annealing in air. Additionally, peaks are sharper after annealing in air. Since in Figure 3.19 the sharp peaks are actually noise (peaks only include one datapoint, which is not possible for peaks originating due to Bragg-peaks with the setup used), only (100)- and (111)-orientations can be demonstrated with the data, as the absence of (111)-type in-plane peaks excludes particles in (110)-orientation.

To support the crystallographic information gained so far, intensity maps were recorded before and after annealing in air. Figures 3.20 and 3.21 show such maps in reciprocal surface coordinates for platinum[11], here: H_S and L_S (recorded at $K_S = 0$, integration time: 10 s). Further, Figures 3.22 and 3.23 show intensity maps for $H_S = K_S$ versus L_S, the integration time is 5 s, respectively. These maps show a small part of the reciprocal space of sample 26. Additionally, theoretical positions of Bragg peaks originating due to presence of (111) platinum particles in either ABC- or CBA-stacking (green circles), (001) platinum particles (blue circle), and the alumina substrate (white diamonds) are indicated. The intensity was recorded using a certain region of interest (*lmbdROI3*) of the 2D detector used, see Section C.2. In general, the maps for the same coordinates do not deviate much from each other comparing the condition before and after annealing in air. In both H_S-L_S maps, the brightest and most narrow peaks correspond to alumina substrate peaks. Small, stripe-like features pointing towards $H_S = L_S = 0$ (especially in Figure 3.21) are probably features from the beam, as all these features are pointing towards the origin, rather than to other Bragg peaks. Furthermore, Bragg peaks from (111)- and (001)-oriented platinum particles appear, the latter being less intense. The peaks can be attributed to a certain particle orientation by comparing their in-plane and out-of plane momentum transfer to the ratio expected from certain particle orientations. Notably, (001)-oriented particles have not been demonstrated in the study by Jan-Christian Schober for a sample identical to sample 26, but with less platinum deposited and without any further annealing after deposition[12] (see Section

[11] See Section 2.4.1.

[12] Neither have these particles been demonstrated in literature. The deviation could be explained by the different thermodynamical conditions in the study presented here, as the temperature was considerably higher than in any other study mentioned in Section 3.2. Furthermore, these particles could not be demonstrated on a sample identical to the condition before annealing in air, where instead of pure platinum, a 85:15 ratio of platinum and rhodium has been deposited –

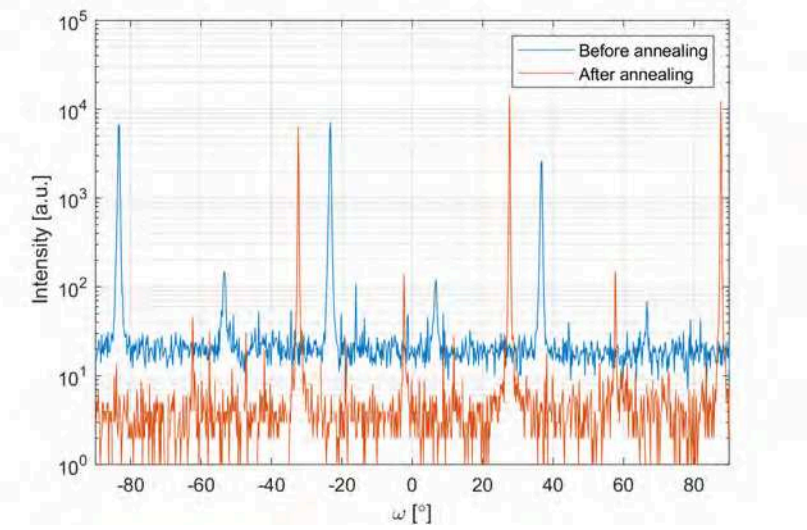

Figure 3.17.: XRD rocking scan for Pt(220) in-plane peaks.

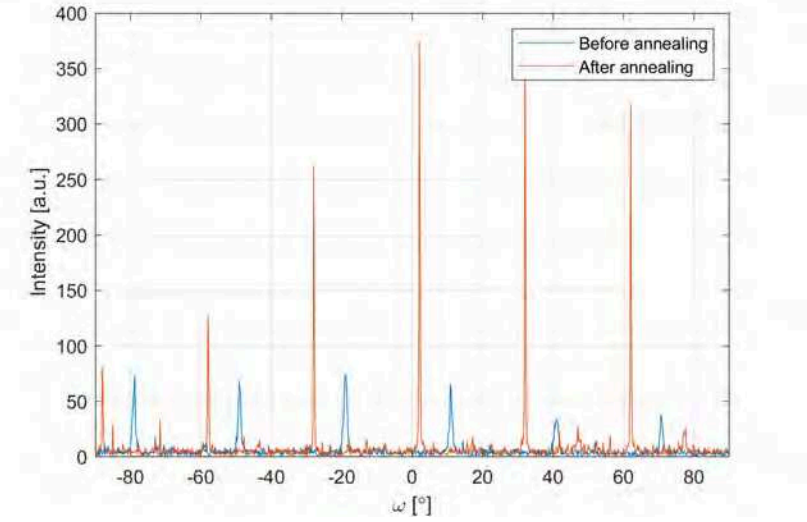

Figure 3.18.: XRD rocking scan for Pt(200) in-plane peaks.

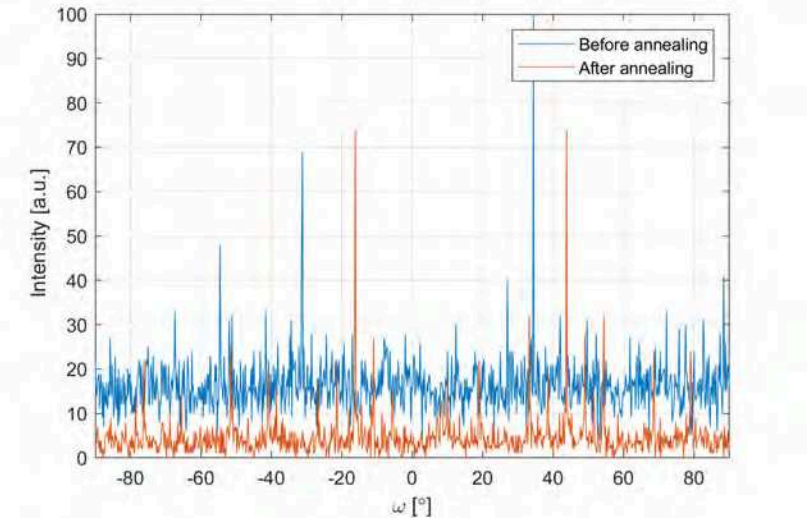

Figure 3.19.: XRD rocking scan for Pt(111) in-plane peaks.

3.2; compare also sample 4 in Table A.1). Crystal truncation rods along L_S most likely belong to flat platinum particles, as these maps are slightly misaligned and the in-plane momentum transfer is not exactly aligned with the $[1\bar{2}10]$-axis of the alumina substrate. Alignment was an even bigger issue for the $H_S = K_S$-L_S plane, where Bragg peaks for platinum are barely visible at all at the calculated positions. Though, the maps are sufficient to correlate the crystallographic axes of (0001)-alumina and platinum particles. For both the sample before and after annealing, (001)- and (111)-oriented platinum particles have their [110]-axis aligned with the substrate's $[10\bar{1}0]$- or $[3\bar{2}\bar{1}0]$-axis, the latter in the case of particles rotated by 30 ° around the surface normal. Both types of (111)-oriented platinum particles appear in ABC- and CBA-stacking order. Apart from the crystallographic relationship, the maps comprise more information. In Figures 3.20 and 3.21, the platinum Bragg peaks with same index are at about the same intensity before and after annealing in air. Less intense crystal truncation rods could indicate a broad height distribution for the sample after annealing in air. Further, the Bragg peak originating by (001)-particles seems to be smeared out along the corresponding momentum transfer – almost like a section of a powder ring. Accordingly, tilted particles could be present on the surface.

In conclusion, the diverse measurements above have shown that upon annealing in air at elevated temperatures platinum particles on α-alumina (0001) undergo a massive transformation from an overall flat and rather hexagonal morphology with narrow height- and diameter distribution towards particles that underwent a complete redistribution of platinum on the substrate resulting in both very small nanoparticles and comparably large islands with a broad distribution of both height and diameter. Further, the relation between height and diameter turns out to be not straight-forward, but complex. Suggestions for the underlying process will be given in the following section.

3.4. Driving forces enabling 3D platinum particles

Generally, the macroscopic morphology of a specimen on a substrate is a matter of surface free energies, as already discussed in Section 2.2.1. In the frame of the observations made above, the question is, what energy change enables such a drastic redistribution of deposited material. The measurements above were conducted on the same sample, first after annealing in UHV, then after a second annealing air.

see sample 6 in Table A.1.

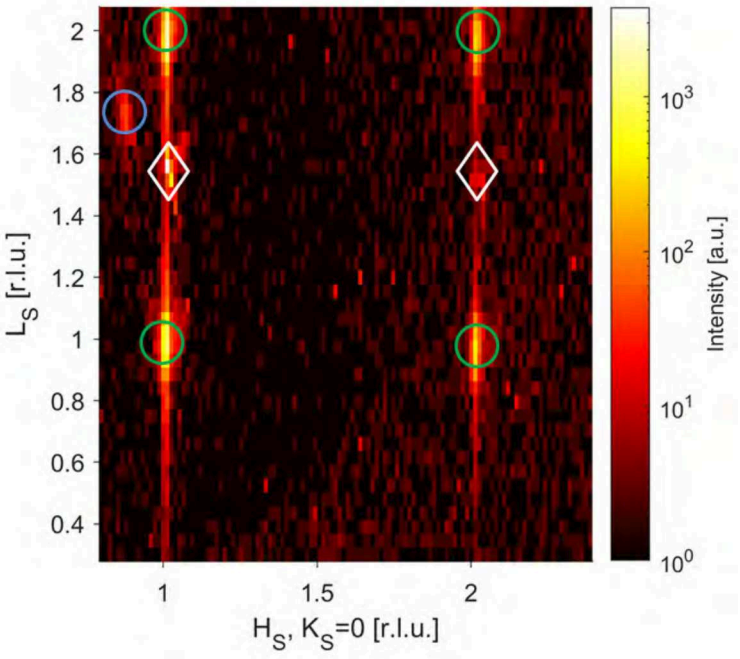

Figure 3.20.: Colour-coded intensity map in reciprocal surface coordinates of platinum L_S and $H_S = K_S$. Measured with SXRD on sample 26 before annealing in air. Theoretical positions of Bragg peaks are marked for (111)-oriented platinum particles in either ABC- or CBA-stacking (green circles), (001)-oriented platinum particles (blue circles), and alumina substrate peaks (white diamonds).

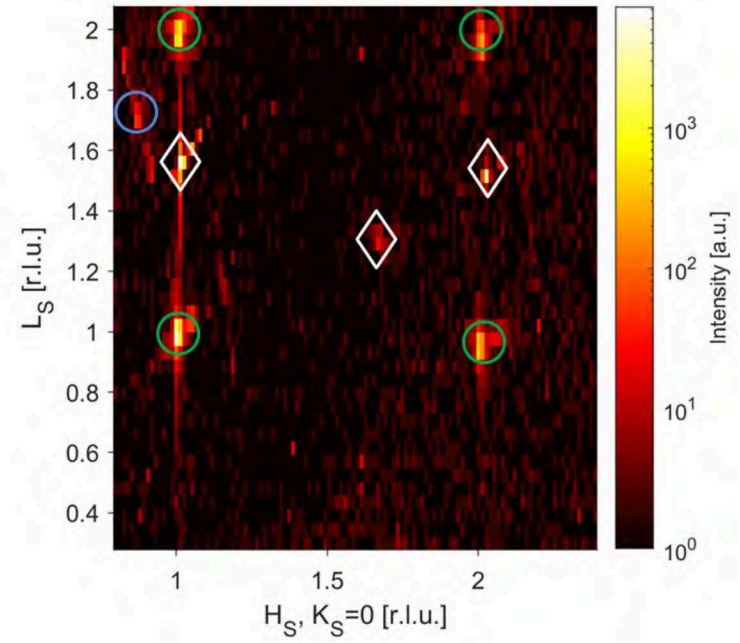

Figure 3.21.: Colour-coded intensity map in reciprocal surface coordinates of platinum L_S and $H_S = K_S$. Measured with SXRD on sample 26 after annealing in air. Theoretical positions of Bragg peaks are marked for (111)-oriented platinum particles in either ABC- or CBA-stacking (green circles), (001)-oriented platinum particles (blue circles), and alumina substrate peaks (white diamonds).

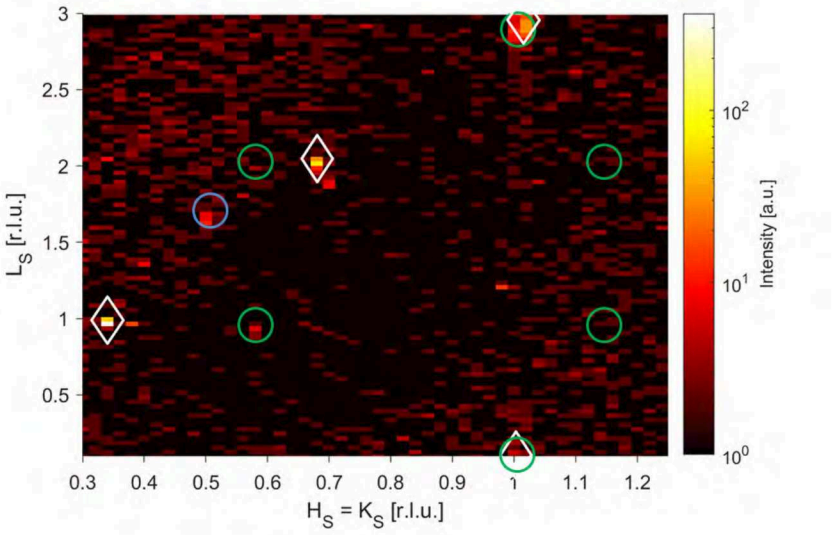

Figure 3.22.: Colour-coded intensity map in reciprocal surface coordinates of platinum L_S and H_S at $K_S = 0$. Measured with SXRD on sample 26 before annealing in air. Theoretical positions of Bragg peaks are marked for (111)-oriented platinum particles in either ABC- or CBA-stacking (green circles), (001)-oriented platinum particles (blue circles), and alumina substrate peaks (white diamonds).

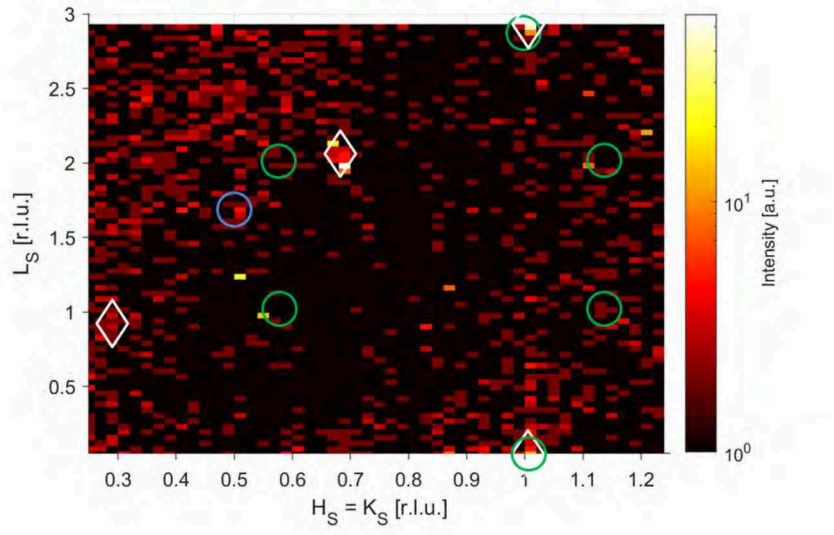

Figure 3.23.: Colour-coded intensity map in reciprocal surface coordinates of platinum L_S and H_S at $K_S = 0$. Measured with SXRD on sample 26 after annealing in air. Theoretical positions of Bragg peaks are marked for (111)-oriented platinum particles in either ABC- or CBA-stacking (green circles), (001)-oriented platinum particles (blue circles), and alumina substrate peaks (white diamonds).

Since for both annealing steps the temperature was about the same, the answer to the question will be linked to the oxygen partial pressure (and hence its chemical potential) during annealing.
If the oxygen partial pressure influences the morphology of the particles, there are some options, what the underlying effect is:

- The interfacial energy and/or the substrate's surface energy is modified due to a change of the substrate's surface termination,
- the interfacial energy is modified due to an induced change in the interface stoichiometry by unconsidered adsorbates, or
- the surface free energy of platinum is modified or the morphology transition is driven by formation of meta stable transition states.

These points will be briefly discussed in the following. Note that the impact of defects and impurities on the growth of platinum particles cannot be properly addressed here[13].
The substrate directly influences if and how particles form on a surface. Consequently, possible phase transitions or induced changes in substrate surface termination will be illuminated in the following.
The experiments and studies presented in this chapter so far have revealed an overall flat morphology of platinum particles over a broad range of temperature in UHV. If annealed in UHV at temperatures of 1200-1300 °C, particles remain flat, too. From the Wulff-Kaishev theorem 2.13 it is clear that stronger work of adhesion will lead to a flatter particle shape as the truncation gets larger[14].
XPS studies and DFT-calculations of the Pt/Al_2O_3 interface have shown that binding of platinum atoms is preferred via oxygen atoms [244–246]. Additionally, an EELS-study on the Pt/γ-Al_2O_3 system showed similar conclusions [247]. This is also true for the (relaxed) Al-terminated surface [245], as the Al-atoms are relaxed towards the oxygen layer beneath and thus, oxygen atoms are very close to the surface [90, 101]. It has been shown that upon annealing in UHV α-alumina(0001) will undergo a surface reconstruction towards an Al-rich and oxygen deficient surface termination at about 1250 °C – which is very close to the UHV-annealing temperature of sample 26 (and definitely within the uncertainty of temperature of the setup used) – see references in Table 2.1. This could explain the findings of Jan Schober, that upon

[13] Defects in the Al_2O_3 and the Pt/Al_2O_3 systems are partly addressed in [238–242]. The impact on the growth of platinum particles is unclear.
[14] Exemplary, the metal support interactions are demonstrated in [243] for the Pt/γ-Al_2O_3 system.

increasing temperature the particle height increases as the work of adhesion decreases for this surface termination. It cannot explain the results of the present study, as this surface termination is also found to be reversible upon excess to oxygen. At 1200 °C and oxygen pressure of at least 10^{-4} mbar the original (1×1) Al-terminated surface will be re-established [107].

Theoretically, the alumina surface could be covered with water or hydroxyl groups. What makes a hydroxylated alumina surface relevant to discuss in the frame of this thesis is its reactivity, which is damped towards water, but highly enhanced towards metals [101]. Experiments with cobalt, rhodium, and copper grown on alumina substrates have shown that metal adatoms strongly bind to superficial oxygen atoms or that OH-remains on alumina may induce a strong (ionic-like) bond of metal adatoms to the substrate [102, 104, 105, 113, 248, 249]. Further, it was predicted that for Al, Hf, and Y charge transfer would initiate ionic bonds towards superficial oxygen atoms [245]. However, charge transfer and ionic character of the bonds of the metal/Al_2O_3-interface are found to scale with the oxygen affinity, which is relatively low for platinum in comparison to the metals mentioned. Consequently, a low adhesion energy is expected for the hydroxylated interface [245]. A similar behaviour was found for titanium and silver on α-alumina [98, 250]. The oxygen terminated interface in turn exhibits an increased adhesion energy for platinum [122, 245]. If the hydroxylated surface would undergo a (catalytically enhanced) transition to an oxidized interface, an originally hydroxylated surface would explain the flat particle morphology under UHV annealing conditions.
Originally, a clean α-$Al_2O_3(0001)$ surface in UHV is terminated by an inwardly relaxed, single Al layer and upon exposure to air or water the surface will be covered with hydroxyl groups – see Table 2.1 in Chapter 2 and references therein. Consequently, a hydroxylated surface would explain the flat morphology of the particles – assuming a transition from an hydroxylated interface to an oxidized interface. Despite, as mentioned in Section 2.2.5 studies showed that desorption of hydroxyl groups starts upon annealing above 30 °C [99] and the clean surface is re-established at about 230 °C [99] to 500-600 °C [103, 131]. For sample 26, platinum was deposited at 830 °C, so temperature was even higher[15] – making the single Al-termination the most likely one for the alumina substrate used.

[15]More importantly, the substrate was exposed to this elevated temperature for a decent time before annealing to keep any temperature gradients as low as possible.

XPS-studies by *Farrow et al.* did not reveal modifications of the platinum and oxygen electronic states at the interface upon deposition of platinum [221]. Furthermore, calculations indicate no significant charge transfer between platinum and the alumina substrate [245, 251, 252]. Before annealing in air, the ratio of height to diameter is about 0.2. Figure 3.24 shows a DFT-calculation by *P. Pleßow*[16] relating the adhesion free surface energy[17] for different surface terminations of the alumina substrate to the chemical potential of hydrogen. As the adhesion free energy is linked to the ratio of height to diameter via the Wulff-Kaishev theorem 2.13, the particle height-to-width is displayed, too. Blue, green and red curves display the dependency of the hydrogen chemical potential for the (1×1) Al-terminated surface (here, indicated as *AlO*), the hydroxylated surface (*OH*), and an oxidized (*ox*) interface, respectively. Here, the latter interface is formed via the reaction Al-OH + Pt $\rightarrow$ Al-O-Pt + $\frac{1}{2}H_2$. The condition during growth is marked by a vertical dotted line on the left-hand side of the graph. Additionally, the ratio of height to width determined before annealing in air would correspond to roughly -270 meV/Å^2 and is according to the calculation only accessible to an oxidized interface. The formation of this interface is based on the assumption of a hydroxylated surface when depositing platinum – unlikely in the present case –, but it is unclear if this interface could be formed by segregation of oxygen at elevated temperatures, too. An EELS-study on γ-alumina assumed superficial oxygen to be arranging in close vicinity towards platinum [247]. Generally, there are few (experimental) studies on this interface. A first-principles/DFT calculation supported HRTEM-study by *Ophus et al.* claim the alumina surface to be oxygen terminated at the interface, but surface relaxations are not considered and the overall conclusion is based on a comparison of the structural models gained from DFT with the HRTEM-data. However, a HRTEM-study for a sample annealed at 900 °C comes to the same

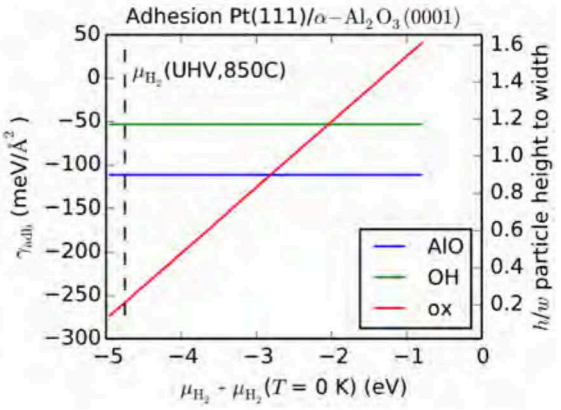

Figure 3.24.: Adhesion of Pt(111) on different surfaces/interfaces of α-Al_2O_3 as a function of the hydrogen chemical potential. Figure through private communication, usage granted by P. Pleßow, see footnote 16.

[16] Private communication – Dr. Philipp Pleßow, Institut für Katalyseforschung und -technologie (IKFT), Hermann-von-Helmholtz-Platz 1, 76344 Eggenstein-Leopoldshafen.

[17] In this work denoted as E_{adh}.

conclusion [226], despite having the same drawbacks as the study mentioned before. In conclusion, the stoichiometry and especially the formation of the interface are not fully understood. Additionally, it is unclear how the single Al-termination would undergo a transition towards a termination with higher adhesion free energy – as the predicted O_3-AlAl-terminated interface.

The study by Jan-Christian Schober [237] showed that especially below a temperature of 500 °C growth of platinum particles is kinetically limited. The fact that also at 1200 °C particles rather grow laterally than in height could mean that also at such elevated temperatures growth is still kinetically limited and the increased mobility of platinum adatoms on the surface is still not sufficient to fully overcome the Ehrlich-Schwöbel-barriers [253, 254] at the borders of platinum islands. This would imply that growth of 3D-particles in UHV would only be enabled by an enhanced deposition rate if tunneling downward of step edges was unfavourable, too. Platinum islands created by de-wetting of platinum thin films at 650 °C remain flat, too [236], thus the growth mode is not limited by the amount of material present when initiating growth of island or nanoparticles. Furthermore, AFM-images correlating the same region of interest before and after annealing (shown above) prove the more or less complete rearrangement of deposited material on the alumina surface, so the underlying mechanism cannot be explained with Ostwald-ripening alone. The formation of 3D-particles upon annealing in air, however, could be explained via formation of metastable, but highly mobile platinum oxides PtO_x which may overcome potential barriers at island borders [182, 183]. The formation of such volatile PtO_x species was recently reported on ceria surfaces [255]. Such platinum oxides are reported to have a low adhesion on alumina surfaces [256], but may re-disperse on or sinter to platinum islands as the Pt-Pt bond is far stronger [257]. Likely, the transition from strongly truncated Wulff shape towards a more ideal Wulff shape with low truncation takes place via a combination of Ostwald-ripening, and rearrangement/sintering of platinum through metastable platinum oxides.

In conclusion, the transition from platinum particles on α-$Al_2O_3(0001)$ with a low height to diameter – representing particles with a strongly truncated Wulffshape – that can be generated by growth and annealing in UHV towards particles with a broad height and diameter distribution after annealing in air was demonstrated. Upon annealing in air, an extensive redistribution of deposited material takes place allowing more 3D-like shapes and H/D ratios between 0.1 and 1 over a broad range

of size. Particles suitable for single-particle X-ray diffraction, which yet requires a diameter of about 100 nm, are found only after annealing in air. Though, it is unclear what exactly drives the transition and redistribution of platinum. Whereas the growth in UHV is suspected to be kinetically limited, upon annealing in air, volatile PtO_x species possibly overcome the potential barriers at step edges, thus enabling 3D-growth. Additionally, the exact structure of the interface remains uncertain. Further experiments are yet to reveal the mechanisms driving the transition. Exemplarily, a XPS study examining the sample before and after high-temperature annealing and exposure to oxygen would provide further insight in the surface states of platinum atoms and might reveal the presence of PtO_x species. Additionally, a sample series for different annealing temperatures in oxygen atmosphere would further elucidate the redispersion mechanism. The role of the interface could be probed by growing particles on an O-terminated alumina (0001) substrate.

Chapter 4.

Ensemble measurements on PtRh particles under operando conditions

As mentioned in Section 2.3, one possibility to prolong the lifetime of a catalyst (here: supported platinum nanoparticles) is to add a certain amount of a second noble metal (here: rhodium) to circumvent catalyst degeneration via particle sintering. Accordingly, this chapter is denoted to an ensemble study of alumina supported platinum-rhodium nanoparticles under operando conditions – here: carbon monoxide oxidation at elevated temperatures and near-ambient pressure.
Firstly, a brief overview will be given, stating possible structural changes of the particles expected to be occurring during the experiment. Afterwards, the sample and the setup used will be introduced. Eventually, data of the experiment will be presented and analysed.

4.1. Catalytically induced structural changes of supported PtRh particles

As presented in Section 2.3 and especially Figure 2.16, the reaction environment can inflict structural changes in noble metal (alloy) particles upon ongoing reactions. Based on studies from other works, following changes in the nanoparticles' structure are expected: sintering, wetting, segregation, and formation of surface oxides. Other effects might be occurring, too, but were not the focus of this work.

As the CO oxidation process is exothermal (about 3 eV per produced CO_2 molecule [204]), additional heat is introduced to the catalyst system. One possible cause might be sintering of particles, expressed through either particle diffusion or (non-classical) Ostwald-ripening [258] which describes dissolving of small particles via inter-particle

diffusion – see also Figure 2.10 in Section 2.2.3. Studies found the intra-particle diffusion to be dominating the sintering process of platinum [258, 259]. Further, it was shown that the sintering process of platinum particles can be damped by addition of rhodium [14, 203, 204, 260–262] – see below. Whereas some authors argue that the damping of the sintering process is related to the higher melting point of rhodium compared to platinum[1] [203], when relating observed particle heights to underlying processes and taking the results from the previous chapter and the comparably large average particle size in this study into account, it seems more reasonable to argue in terms of surface energies. Again, a particle's size and shape are related to the surface energies of occurring facets and the binding towards the support. When adding rhodium to platinum, both the binding energy towards the substrate and the lattice mismatch are altered [122, 204], giving rise to a different height to diameter ratio [41, 204]. During CO oxidation upon the supported bimetallic particles, changes in particle height might be enabled by the heat provided from the oxidation process. Figure 4.1 from reference [204] shows XRR measurements (a-c) and corresponding extracted electron density profiles with associated coverages (d-f) of alumina supported Pt, $Pt_{0.5}Rh_{0.5}$, and Rh particles before (black) and during CO oxidation (orange). Platinum particles are found to undergo a relatively large increase in height accompanied by a significant decrease in coverage. The average lateral diameter stays more or less constant (not shown here). The changes in height and coverage are damped for particles containing rhodium or purely composed of rhodium. Sintering is reported for small particles with sizes of few nanometres. As the diameter of larger particles stays about unchanged upon reaction, the sintering process is accompanied by intra-particle mass transport or wetting. A correlation of the findings with surface energies, adhesion energies, and chemical affinity is not straight-forward and was not fully conducted. The assumption in the publication is that CO oxidation provides enough heat for platinum particles to overcome their kinetically stabilized truncated Wulff-shape.

Segregation is an effect observed in many bimetallic nanoparticle systems, such as PdPt [197], PdRh [14, 263], and especially PtRh [264]. Due to different surface energies of the metals, the total energy of particles is reduced if the metal with lower surface energy constitutes the surface. *Tao et al.* investigated depth profiles and corresponding composition of bimetallic nanoparticles [14, 264]. Figure 4.2 shows the composition profile of Rh_xPt_{1-x} as-synthesized nanoparticles at room temperature and in vacuum determined via XPS. By tuning the energy of the impinging X-ray

[1] Here: Pt(Rh) on barium hexa-aluminate, particle size around few tens of nanometres.

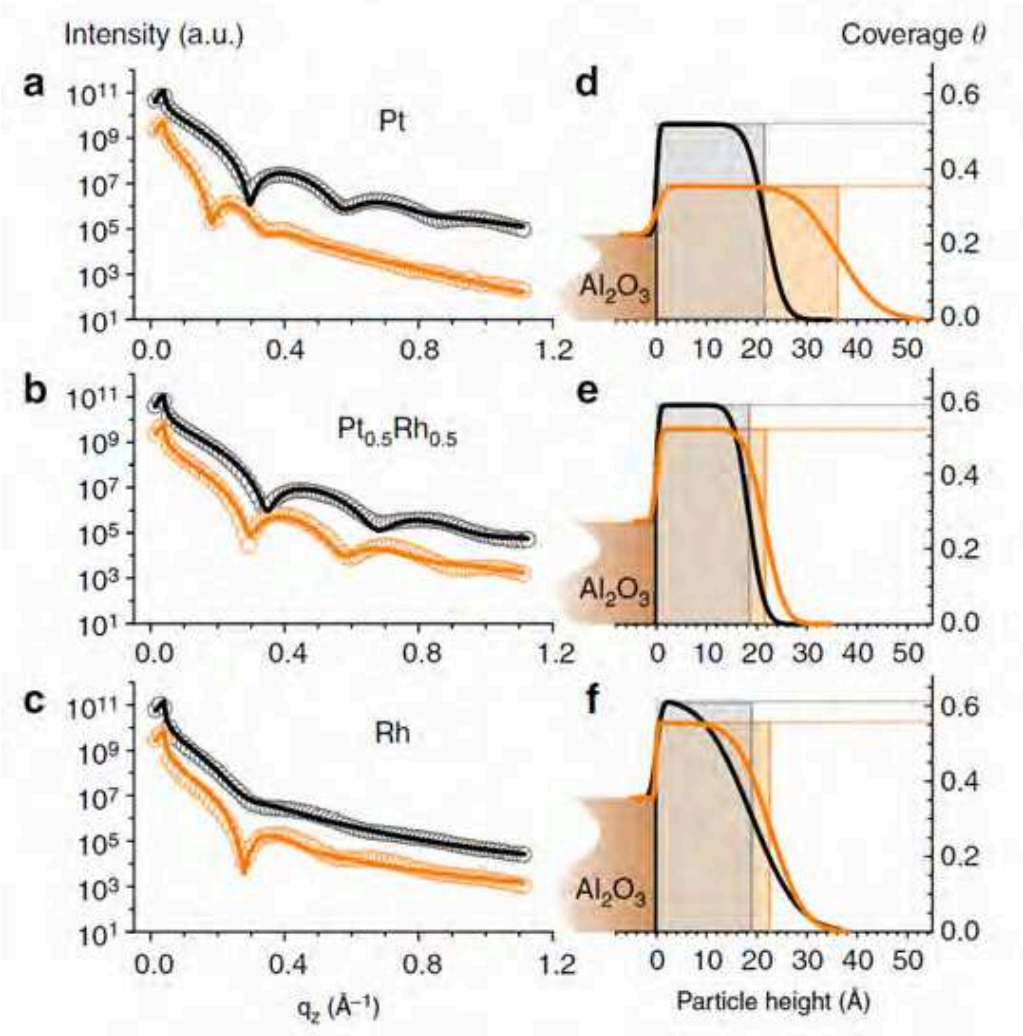

Figure 4.1.: X-ray reflectivity curves (a-c) and corresponding extracted height profiles and coverages (d-f) of Pt, $Pt_{0.5}Rh_{0.5}$, and Rh nanoparticles on α-alumina before (black) and during CO oxidation. In plots a-c, data points are represented by circles and corresponding fits by a solid line. Taken from [204].

beam, the information depth is adjusted. Particles were synthesized using one-step colloidal chemistry [264] on silicon wafers as substrates. Plots (a)-(c) indicate no strong segregation profile, but an overall rather homogeneous alloy. Despite, a small concentration gradient is visible, with the rhodium concentration increasing towards the surface for all investigated compositions. Generally, both calculations and experiments conducted by other authors indicate a different behaviour[2] [265–271]. The general observation and conclusion for surfaces in vacuum is, that in bimetallic Pt_xRh_{1-x} particles platinum segregates towards the surface and constitutes (at least) the topmost superficial layer. Some authors conclude a sub-surface depletion or even oscillatory composition of platinum due to the segregation towards the topmost layer [272, 273]. The segregation is caused by the lower surface energy of platinum compared to rhodium [268] and by energetic differences of the monometallic (Pt-Pt or Rh-Rh) and bimetallic bonds [78, 274–276]. Differences of the results concluded in the study of *Tao et al.* above might arise due to the lack of sensitivity to only one atomic layer. Additionally, the studies mentioned above exhibit manifold ways to fabricate the particles on different supports and hence, properties of the nanoparticles will differ from each other[3].

The segregation profile is found to be sensitive to the environmental conditions of the nanoparticles, as depicted in Figure 4.3. Here, samples from Figure 4.2 were exposed to reducing (H_2) and oxidizing (NO) conditions – see caption of Figure 4.3 for further info. Shown are the atomic fractions of both platinum and rhodium as determined by ambient pressure XPS. The finding is that the near-surface fraction of rhodium can be reversibly increased and decreased by exposure to either oxidizing or reducing conditions. This behaviour is confirmed for CO oxidation on PtRh particles [265, 268, 277]. In the latter case, the segregation of rhodium towards the surface is driven by its high affinity to oxygen [201].

The segregation of rhodium also enables the formation of superficial rhodium oxides upon oxidizing or overstoichiometric conditions. By performing SXRD scans, *Hejral et al.* found the formation of a O-Rh-O trilayer on $MgAl_2O_4$ supported $Pt_{0.33}Rh_{0.67}$ nanoparticles upon CO oxidation at 650 K [277]. The (001)-oriented particles exhibited a size of about ten nanometers. Under stoichiometric conditions, the formation of the trilayer on (001)-type facets was observed. On the (111)-type side facets, the oxide layers were observable for overstoichiometric (i.e. oxygen-rich) conditions.

[2] This example was chosen to emphasize both the ongoing debate on the surface structure and the high demand for measurement techniques sensitive to the surficial atomic structure.

[3] Especially in terms of crystallinity, homogeneity of the elemental distribution, size, shape, support interactions etc..

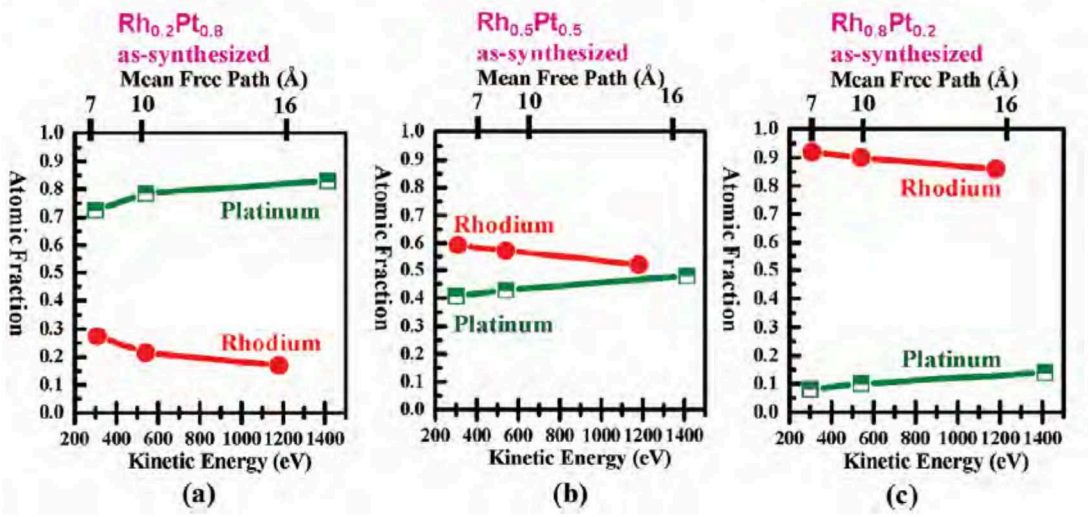

Figure 4.2.: Energy dependent XPS measurements on (a) $Rh_{0.2}Pt_{0.8}$, (b) $Rh_{0.5}Pt_{0.5}$, and $Rh_{0.8}Pt_{0.2}$ nanoparticles at room temperature in vacuum. Shown is the atom fraction of the respective element versus the kinetic energy or mean free path. Taken from [264].

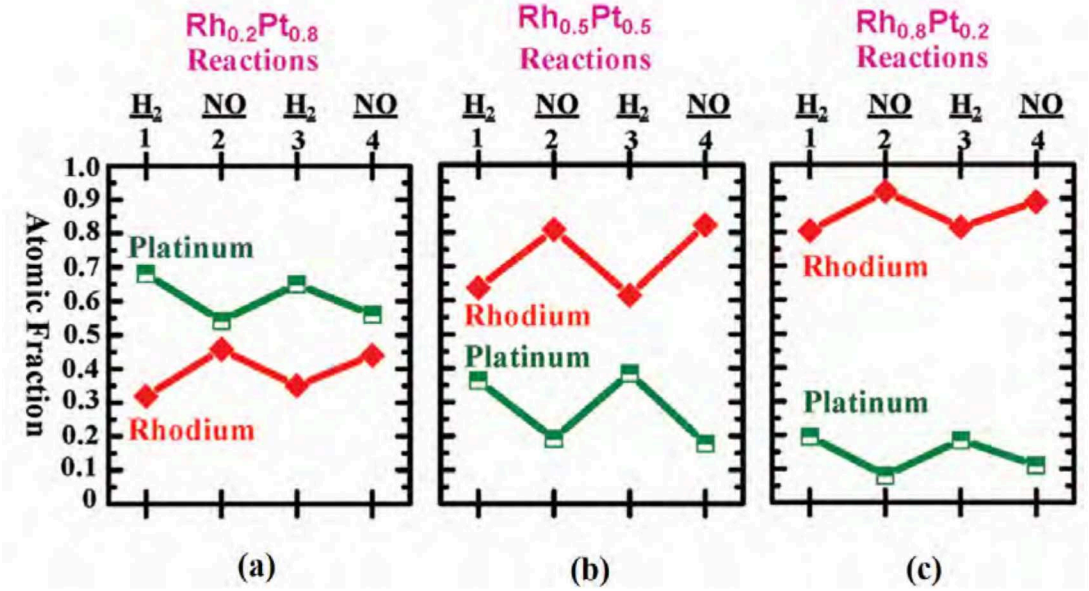

Figure 4.3.: Ambient pressure XPS measurements on (a) $Rh_{0.2}Pt_{0.8}$, (b) $Rh_{0.5}Pt_{0.5}$, and $Rh_{0.8}Pt_{0.2}$ nanoparticles during catalytic reactions. Shown are atomic fractions of the respective elements upon exposure to oxidizing (NO) and reducing (H_2) conditions at 300 °C and 100 mTorr, respectively. Fractions obtained using 645 eV for Rh 3d and 380 eV for Pt 4f, photoelectrons had a mean free path of about 7 Å. Taken from [264] and adapted.

Besides, the authors correlate the formation of the trilayers with an increased CO_2 production rate.

4.2. Sample details

The sample growth applied for this specific study resembles the recipe described in Section 3.3.1. Accordingly, the sample utilized (here: sample 6) for the catalytic experiment features flat particles with a low ratio of height to diameter. Exact growth parameters can be found under sample 6 in Table A.1 in the Appendix.
The (0001)-oriented α-Al_2O_3 substrate was pre-cleaned as stated in Section 2.2.6. Subsequently, the substrate was transferred to an UHV chamber (see Section 2.5.1). After further cleaning procedures (see Section 2.2.6), sample 6 was heated up to 830 °C, and platinum and rhodium were co-deposited on the surface with a flux calibrated ratio of 85:15 (Pt:Rh). Due to the co-deposition mode and the high temperature during deposition of the noble metals, the particles are expected to exhibit a homogeneous, alloy-like distribution of the two elements inside the particles rather than a core-shell morphology or another spatially inhomogeneous distribution. Subsequently, SEM images were taken, see next paragraph and Figure 4.4. Afterwards, the sample was transferred back into the UHV chamber and annealed at 10^{-8} mbar background pressure and 1100 °C for 10 minutes. Again, further details are given in Section 2.2.6.
Figure 4.4 shows an area in the middle of the sample before and after annealing in high vacuum at 1100 °C. Again, dark areas correspond to the alumina substrate and bright areas to the alloy particles. These SEM images extend the findings made in Section 3.3.1 from pure platinum particles to PtRh alloy particles (with low rhodium content). After the annealing step, particles are significantly larger in diameter and the overall coverage slightly decreases – most likely correlated with a slight increase in particle height. The latter assumption is not supported by further data as neither AFM, nor X-ray measurements were conducted for the sample right after deposition of the metals. Table 4.1 shows results from the quantitative analysis of the two SEM images of Figure 4.4, supporting the qualitative findings made by eye. Info on the analysis of SEM images is given in Section B.2. EDX measurements on the sample surface confirm the ratio of platinum and rhodium (data not shown).
Generally, the diameter of the particles on sample 6 is about double in size compared to the pure platinum particles on sample 26 before it was annealed in air. Also, the coverage is slightly higher – averaging over several different areas on the sample and

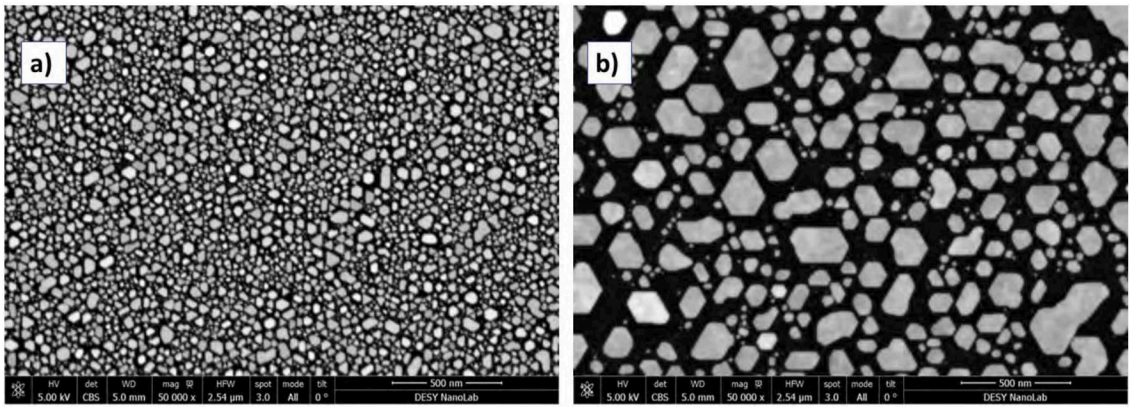

Figure 4.4.: SEM pictures of sample 6 after a) deposition of the metal particles and b) further annealing in high vacuum and 1100 °C.

Parameter	Before annealing	After annealing
Average diameter [nm]	32	80
Number of particles	2487	304
Coverage [%]	37.3	33.3

Table 4.1.: Overview of particle characteristics of sample 6 before annealing in high vacuum and 1100 °C and afterwards. Analysis includes only the two images shown in Figure 4.4.

not only those in Figure 4.4. An elaborate comparison of the growth of pure platinum particles with the alloy particles' growth is not part of this thesis, as a systematic study with corresponding data allowing an in-depth analysis of the influence of rhodium on the alloy particles' growth behaviour was not conducted. Instead, possible morphological changes induced by catalytic reactions were of interest. The setup used for this study will be introduced in the following.

4.3. Experimental setup for operando SXRD on nanoparticles

To characterize in situ morphological changes of the supported nanoparticles under reaction conditions, both a stable sample environment and a suitable characterization method are to be applied. The combination of a small catalysis reactor including a gas supply setup and X-ray scattering represents an excellent match-up for these requirements. Figure 4.5 shows an image of the catalysis chamber with associated gas setup – see Section 2.5.2 – implemented at the six-circle diffractometer – see Section 2.5.3. The image shows 1) first pair of detector slits, 2) gas connections upstream

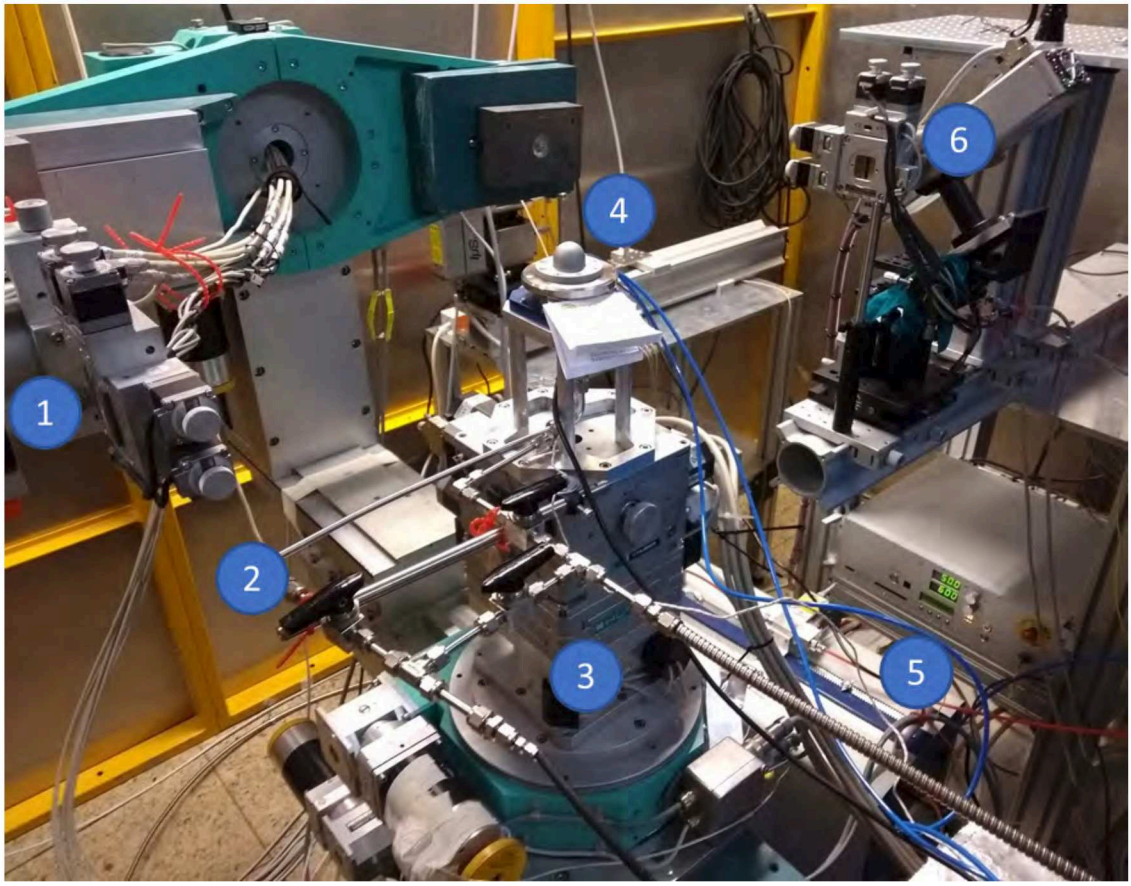

Figure 4.5.: Picture of a part of the experimental setup used: catalysis chamber mounted on a six-circle diffractometer stage. 1) detector slits, 2) gas tubing of the reactor, 3) diffractometer stage, 4) catalysis chamber with beryllium dome (blue tubing: water cooling; black tube: thermocouple), 5) T100 residual gas analyser, and 6) X-ray source and optics.

and downstream the catalysis chamber, 3) diffractometer stage with the catalysis chamber mounted, 4) the catalysis chamber itself with the beryllium dome installed, 5) the residual gas analyser downstream the reactor, and 6) the X-ray source (Cu K-α with $\lambda = 1.54\,\text{Å}$). Not visible in the image is the gas supply setup itself, which is placed outside the X-ray hutch shown in Figure 4.5. Also outside the hutch are the water cooling for the catalysis chamber and the control computer for the gas flow setup and the RGA. This arrangement allows for switching and monitoring the gas environment during X-ray measurements. Prior to using this setup for studies, the complete gas system is checked for any leaks using an external helium bottle and the RGA installed in the gas system. Afterwards, an argon flow is set for several hours to clean the gas lines from water and other remains – see Section 2.5.2 for further measures taken for purging. After insertion of the sample, the setup is flushed with argon, again. Before heating up to the final reaction temperature, any metal oxide remains on the nanoparticles are removed using diluted hydrogen in the argon carrier gas at a sample temperature of 200 °C.
A drawback and source of systematic errors is the way the gas lines are connected to the catalysis reactor, as upon necessary movement of the diffractometer cradle they exert torque on the chamber, causing inherent misalignment – see discussion of experimental results in the following section.

4.4. Morphological changes of PtRh nanoparticles upon catalytic reaction conditions

Using the setup described in the previous section, two catalytic experiments were conducted on sample 6. As described in Section 4.1, aim of the experiments was to detect and quantify changes of the morphology and composition of the nanoparticles during the catalytically enhanced CO oxidation. As the diffractometer is especially suitable for detecting changes of the size of nanoparticles and the overall coverage of the surface with nanoparticles, the first experiment was dedicated to observing reversible shape changes. Environmental details are depicted in Table 4.2 in the first four rows. Starting from an inert environment in the first step, carbon monoxide was added to the argon carrier gas in the second step. Afterwards, a stoichiometric mixture of carbon monoxide and oxygen diluted in argon was used as environment, followed by solely carbon monoxide in argon. Total flow and total pressure were kept constant at 50 $\frac{\text{ml}}{\text{min}}$ and 0.1 bar, respectively, throughout the experiment. During each step, XRR and different XRD scans were undertaken. Unfortunately, a power

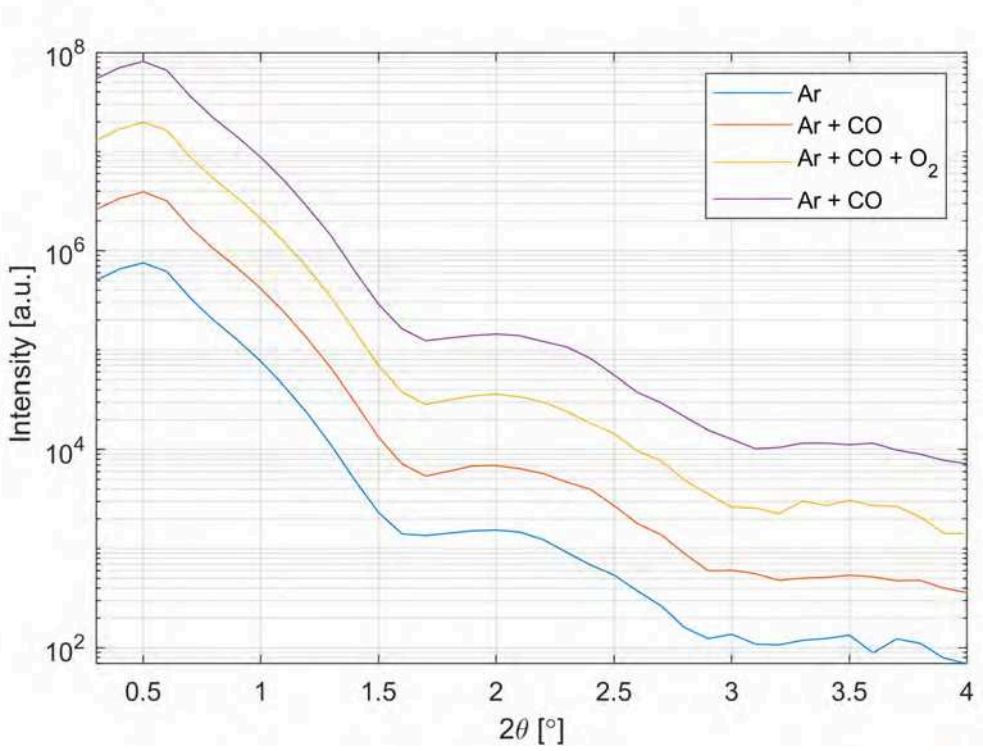

Figure 4.6.: X-ray reflectivity curves gained from the first catalytic experiment on sample 6 – see environmental conditions in Table 4.2. For clarity, curves are shifted in intensity.

cut in the laboratory during the last step caused a massive data loss and terminated the experiment. The only complete dataset is depicted in Figure 4.6 which shows XRR scans for the respective gas environment. The exact flow conditions are given in Table 4.2. The XRR scans are very similar to each other, indicating that any changes in height of the particles and overall surface coverage are negligible. This conclusion is supported by high resolution SEM images that were taken before and after the first experiment. Figure 4.8 shows the same area on the surface before (a) and after (b) the first experiment. Though changes in height are not detectable using SEM, no indication of material transport (sintering or coalescence) is found that would have enabled a shape transformation. Exemplarily, Figure 4.7 shows the XRR scan (filled circles) with FEWLAY fit (straight line) of step 4 (argon and CO) on the left and the corresponding electron density profile on the right. The electron density profile is given in 2δ values, see Section 2.4.3. The most relevant fitting parameters are given in the plot of the layer profile on the right of Figure 4.7 and overall fitting yielded an effective layer thickness $d_{eff} = d_1\delta_1 + d_2\delta_2 = 2.3\,\mathrm{nm}$ (with maximum height $d_1 + d_2 = 6.0\,\mathrm{nm}$) and a pseudo-coverage $\bar{\delta} = \frac{d_1\delta_1 + d_2\delta_2}{d_1 + d_2}$ of about 38.0 % (coverage determined from SEM images about 33.0 %)[4]. The electron density profile indicates an overall uniform layer profile where particles have about the same height. As mentioned above, the XRR scans during the previous steps do not indicate significant changes throughout the experiment. Any RGA data was lost due to the power cut and thus cannot be provided.

As the first catalytic experiment neither provided complete datasets (except for XRR), nor significant changes in particle morphology, a second experiment was conducted almost two months after the first experiment. During the time between the two experiments, the sample was kept in a small plastic box in air. The temperature during the second experiment was increased from 370 °C to 450 °C and overstoichiometric oxygen ratios were added to the experiment's steps – see last six steps in Table 4.2. Figure 4.9 shows the partial pressure of selected gases as recorded during the second experiment by the residual gas analyser in the exhaust gas line downstream the reactor[5]. Starting from only argon carrier gas in step one, the total gas flow was changed towards stoichiometric and overstoichiometric CO oxidation ($4\,\frac{\mathrm{ml}}{\mathrm{min}}$ O_2 versus $4\,\frac{\mathrm{ml}}{\mathrm{min}}$ CO) conditions for the second and third step, followed by reducing conditions in absence of oxygen in the fourth step. For the fifth step, an

[4]Here, indices 1 and 2 refer to the first and second layer of the electron density profile on the right of Figure 4.7.

[5]Info on the layout of the gas setup is given in Figures 2.26 and C.10. See corresponding Sections 2.5.2 and C.4, too.

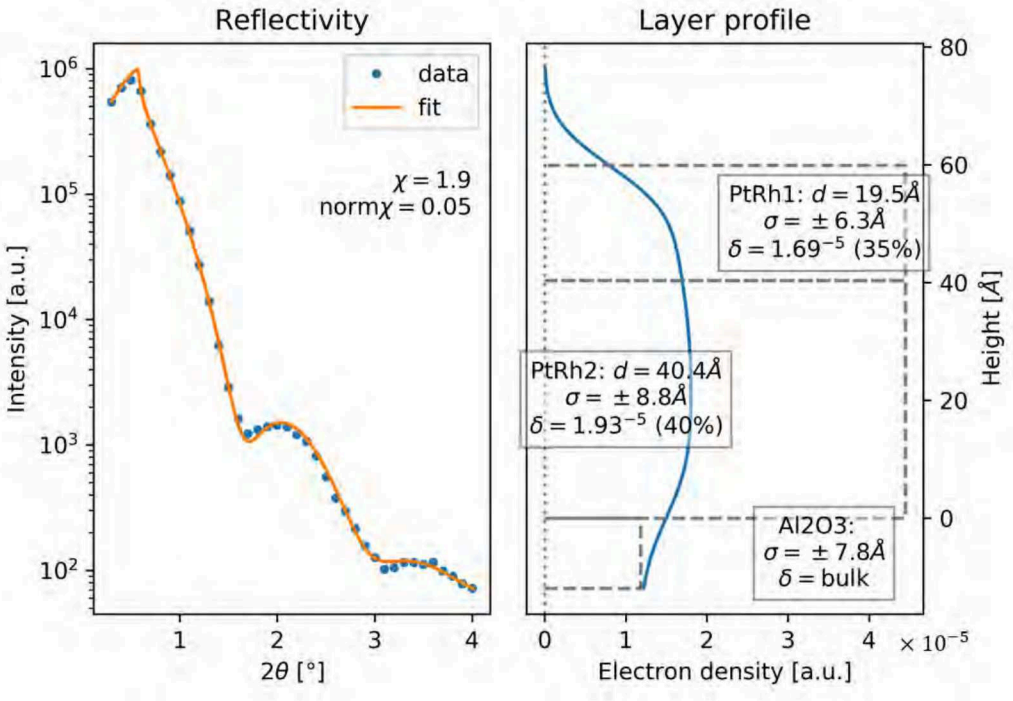

Figure 4.7.: XRR scan with corresponding fit (left) and fitting result (right) of the last step of the first catalytic experiment (at 370 °C). The electron density profile on the right is expressed through 2δ-units, values in brackets denote $\frac{\delta}{\delta_{th}}$ of the corresponding layer, δ_{th} referring to the theoretical bulk value. Fitting was carried out using the Fewlay software, see Section 2.4.3.

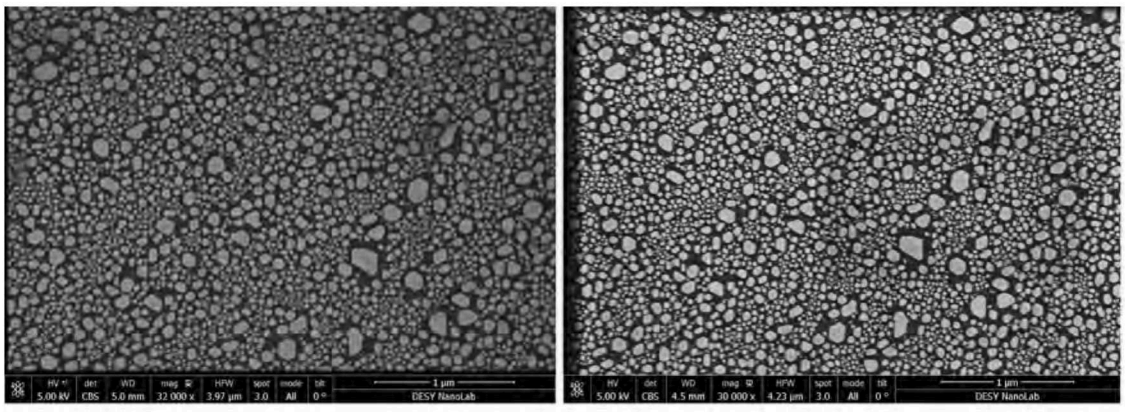

Figure 4.8.: High resolution SEM images of the same area of interest on sample 6 before (a) and after (b) the first catalytic experiment (at 370 °C). Image a) was taken at a slightly larger magnification. Differences in contrast arise due to the imaging process.

Step number	Ar $[\frac{\text{ml}}{\text{min}}]$	CO $[\frac{\text{ml}}{\text{min}}]$	O_2 $[\frac{\text{ml}}{\text{min}}]$	Temperature [°C]
1	50	0	0	370
2	46	4	0	370
3	44	4	2	370
4	46	4	0	370
1	50	0	0	450
2	44	4	2	450
3	42	4	4	450
4	46	4	0	450
5	44	2	4	450
6	46	4	0	450

Table 4.2.: Environmental details during the catalytically enhanced CO oxidation experiments. Entries in first four rows denote the first experiment. Consecutive entries correspond to the second experiment. Total flow was always kept at 50 $\frac{\text{ml}}{\text{min}}$ with a total pressure in the reactor of 0.1 bar.

overstoichiometric ratio of 4 $\frac{\text{ml}}{\text{min}}$ O_2 and 2 $\frac{\text{ml}}{\text{min}}$ CO was chosen, again followed by CO only. For each gas dosing step a certain flow of argon carrier gas was set to keep the total gas flow constantly at 50 $\frac{\text{ml}}{\text{min}}$, compare Table 4.2. In steps two, three, and four, the set CO flow was 4 $\frac{\text{ml}}{\text{min}}$. In the transitions from step one to two and step two to three, an increasing oxygen partial pressure correlates with decreasing CO partial pressure and increasing detected CO_2 signal, hence indicating CO_2 production. Further catalytic tests proved that the detected rise of the CO_2 signal under the environmental conditions examined is related to the alloy particles and not solely the substrate (or reactor), see Section C.5. Partial pressures varying during a gas dosing step as visible in the CO signal in step three are possibly related to the RGA-chamber pressure or contaminants inside it, the sensitivity of the RGA itself, or fluctuation of the supply gas pressure.

Figure 4.10 shows a comparison of the same surface area on sample 6 after the catalytic experiments conducted at 370 °C (a) and 450 °C (b) sample temperature, displaying significant morphological changes. Exemplarily, the orange rectangle marks the very same particles before and after the experiment. Figure 4.11 shows these areas as a zoom-in. In the surface projection shown by SEM the particle in the centre of Figure 4.11 (a) and (b) was shrinking during the second experiment. Apparently, the catalytic experiment conducted at 450 °C caused the larger particles with diameter in the ten nanometers range to significantly decrease in diameter. Considerably smaller particles were shrinking in diameter, too, as can be guessed from Figure 4.11. Generally, the observation is that the larger the original diameter

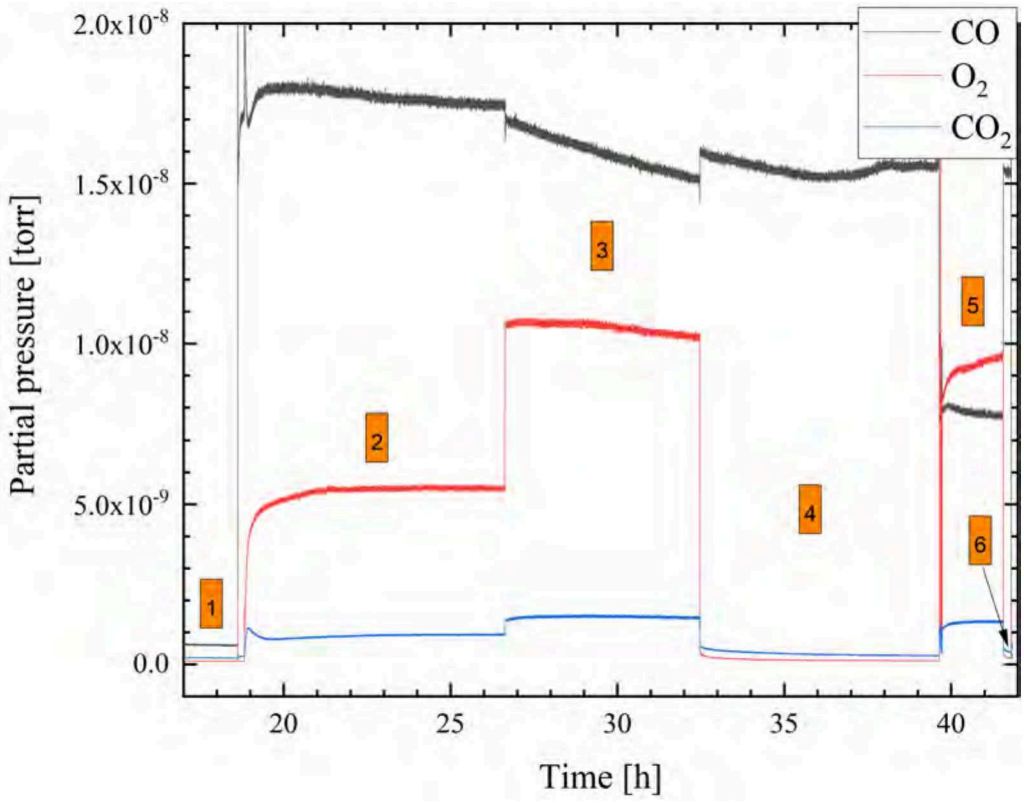

Figure 4.9.: Partial pressure versus time scan during the second catalytic experiment (at 450 °C) recorded from the LPM T100 RGA positioned directly downstream the reactor (compare Figure 2.26). Highlighted numbers refer to the gas dosing steps in Table 4.2. For simplicity, only the signals of CO, O_2, and CO_2 are depicted. The full dataset is presented in Figure C.15 in the Appendix.

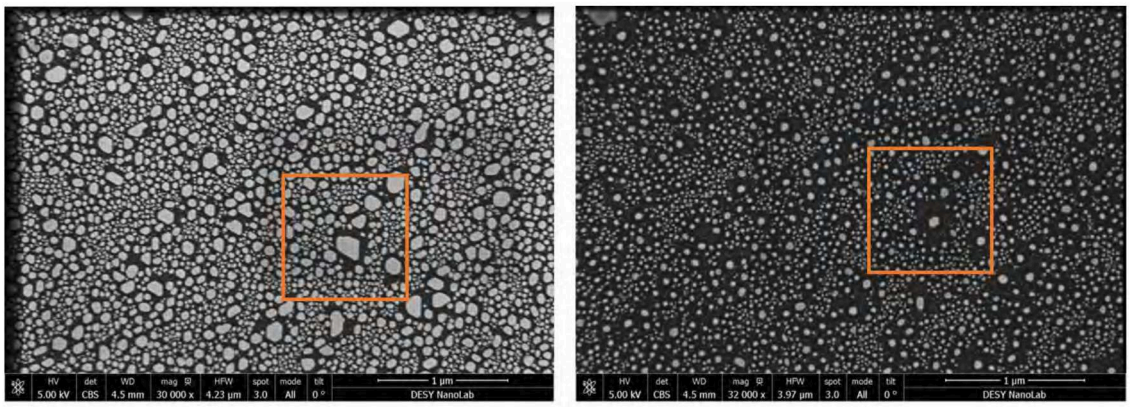

Figure 4.10.: SEM images of the same surface area on sample 6 before (a) and after (b) the second catalytic experiment. The orange box marks the very same spot on the surface. A zoom-in of both the orange area for both SEM images is provided in Figure 4.11. Note that the magnification is slightly different for the images.

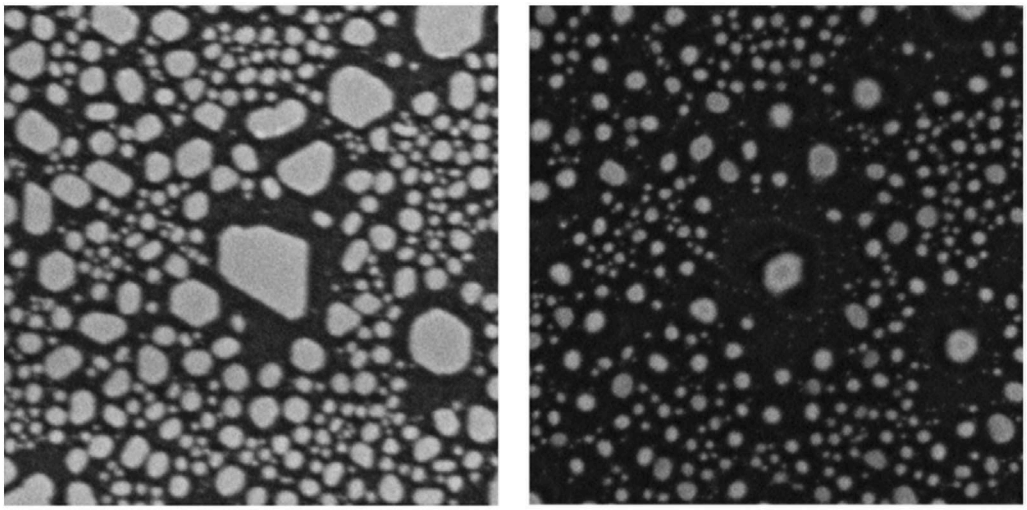

Figure 4.11.: Zoom-in of areas marked in orange in Figure 4.10. Corresponding SEM-images were taken after the catalytic experiments at 370 °C (a) and after 450 °C (b), respectively. The centred particle in (a) exhibits a lateral dimension of 180 nm along the horizontal plane of the image.

of the respective particle was, the larger was the decrease in diameter. Moreover, particles did not collapse into two or more new core particles. Contrary, it seems that particles decreased in diameter via a shrinking mechanism, instead of subdivision into more particles. More importantly, after the second experiment both small and large particles have a more roundish shape closer to the equilibrium shape, abolishing elongated shapes and large, extended facets. Further, it appears that upon shape transition large particles leave behind a pattern with their original shape – similar to coffee rings. These patterns are visible in AFM measurements, too – compare Figure 4.12). According to AFM analysis, these wall-like features exhibit heights of between 1 and 3 nm.

An analysis of both images in Figure 4.10 yields a drastic deviation in surface coverage and average particle size before and after the second catalytic experiment. Upon the CO oxidation experiment, the surface coverage decreased from about 39 % to 22 % with the average lateral particle extend decreasing from 1000 nm^2 to 377 nm^2. AFM measurements were not undertaken before any of the catalytic experiments, but measurements on samples grown with the same parameters (see samples 23 and 24 in Table A.1 in the Appendix) indicate an average initial particle height of about 4 nm (data not show). After the second catalytic experiment however, AFM measurements on sample 6 yielded an average particle height of about 14 nm, having

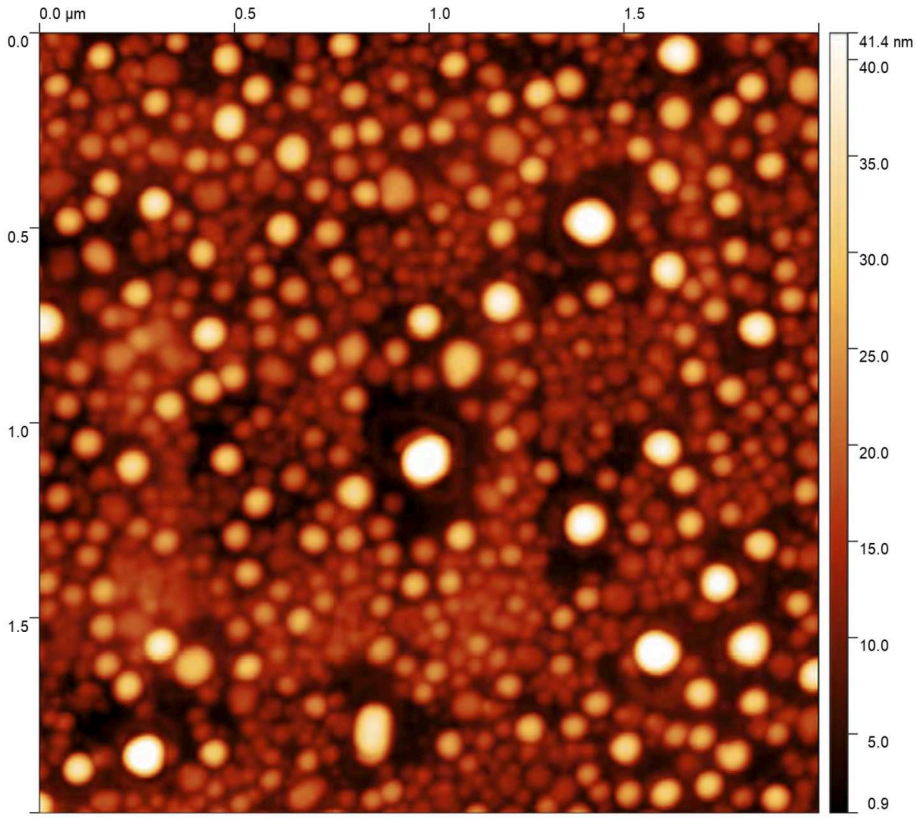

Figure 4.12.: AFM micrograph of highlighted area in Figure 4.10. Image was taken after the experiment at 450 °C. To emphasize ring-like features in the image, the height scale was cut below 0.9 nm and above 41.4 nm.

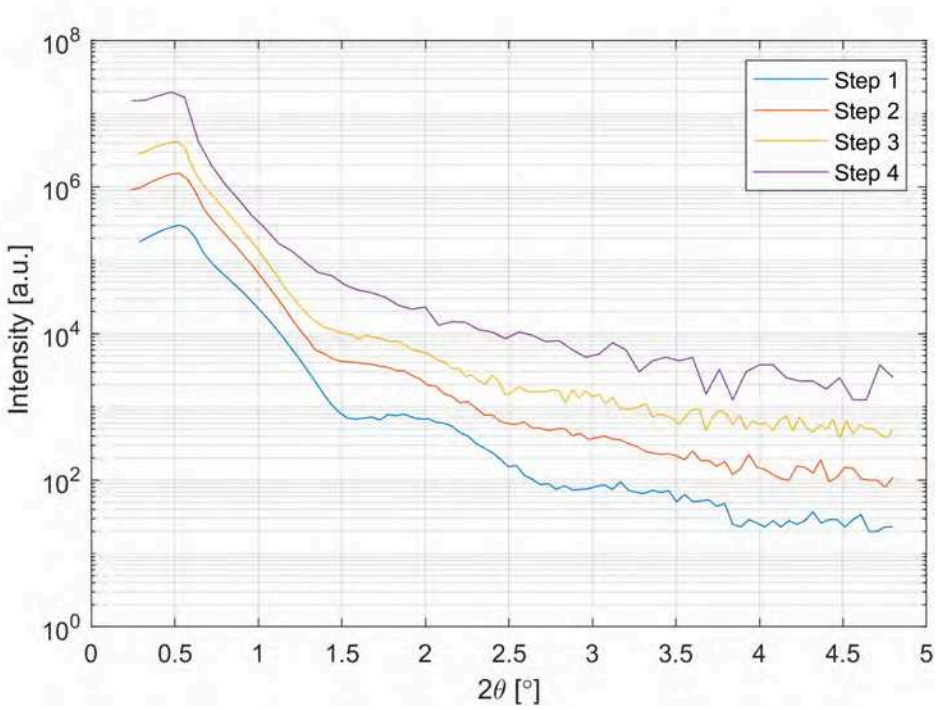

Figure 4.13.: X-ray reflectivity curves during the first four steps of the second catalytic experiment, see Table 4.2. The steps are (1) carrier gas argon only, (2) stoichiometric ratio of CO and O_2, (3) overstoichiometric ratio of O_2 to CO, and (4) CO in carrier gas. For clarity, curves are shifted in intensity.

drastically increased[6]. These results indicate a massive morphological transformation of the particles. Particles that exhibit ring-like features surrounding the core particle obtained heights of 30 to 60 nm during the experiment at 450 °C. However, contrary to platinum particles on sample 26 (see Chapter 3), which was annealed in air at 1200 °C, the alloy particles were not subject to a complete reorganisation of deposited material by surface diffusion processes. All particles stayed at about the same position and no indications of Ostwald-rippening, coalescence, or particle diffusion in general could be found. Instead, an intra-particle mass transport mechanism seems to having dominated the transformation process, enabling the transition from an energetically unfavourable flat, disc-like morphology towards a more Wulff-like, three-dimensional equilibrium shape.

Each gas dosing step during the experiment at 450 °C was accompanied by several X-ray diffraction scans probing both layer and particle properties. Figure 4.13 shows

[6]AFM measurements were undertaken only in the area shown in Figure 4.10. Accordingly, statistical statements given here might not be valid for the hole sample area. Still, SEM images made on various spots of sample 6 indicate that the particle morphology described here does not differ significantly from other areas of the sample.

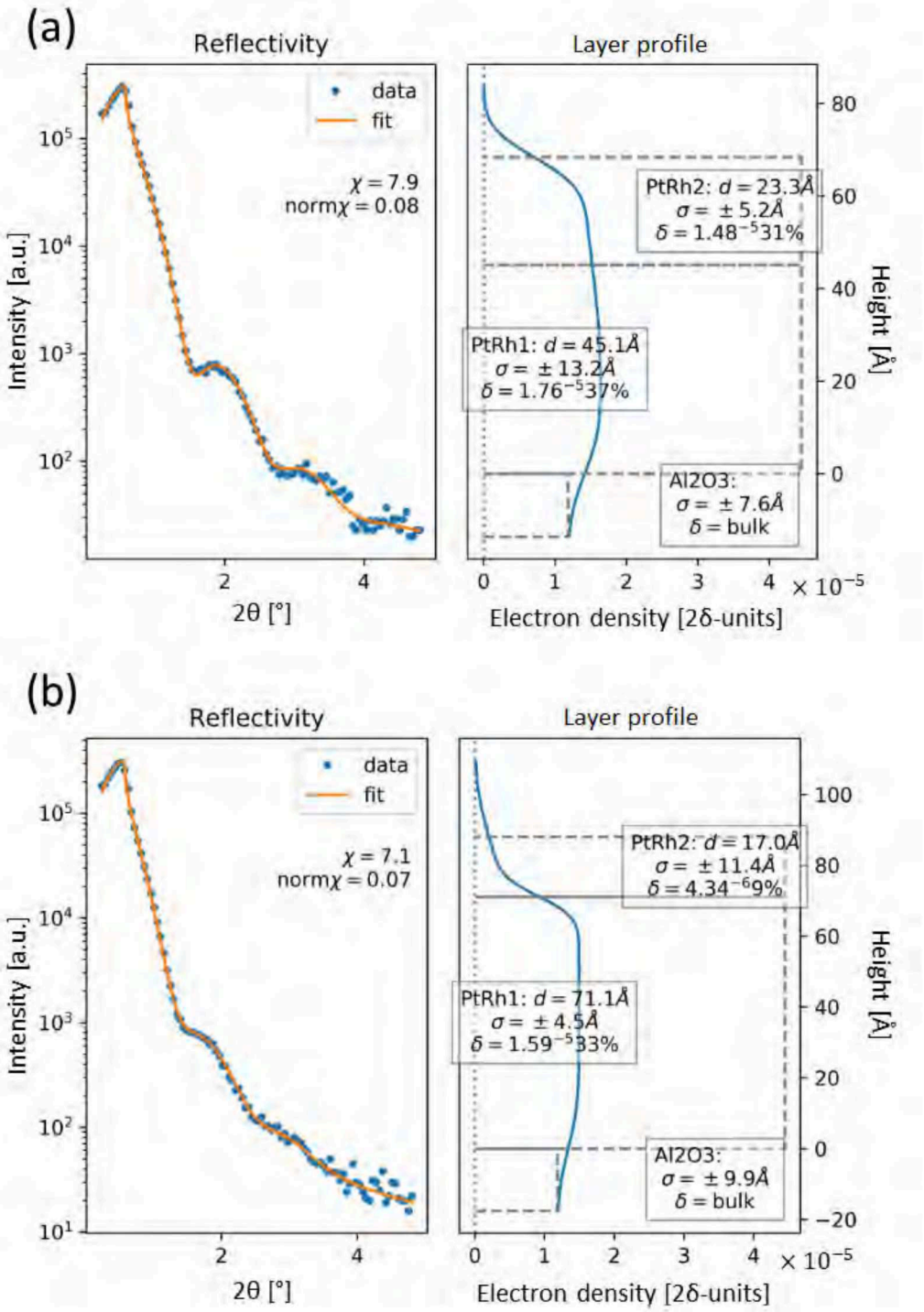

Figure 4.14.: XRR curve with corresponding Fewlay fit (left) and resulting electron density layer profile (right) of steps 1 (a) and 2 (b) of the second catalytic experiment on sample 6. The thickness of the substrate is assumed to be semi-infinite.

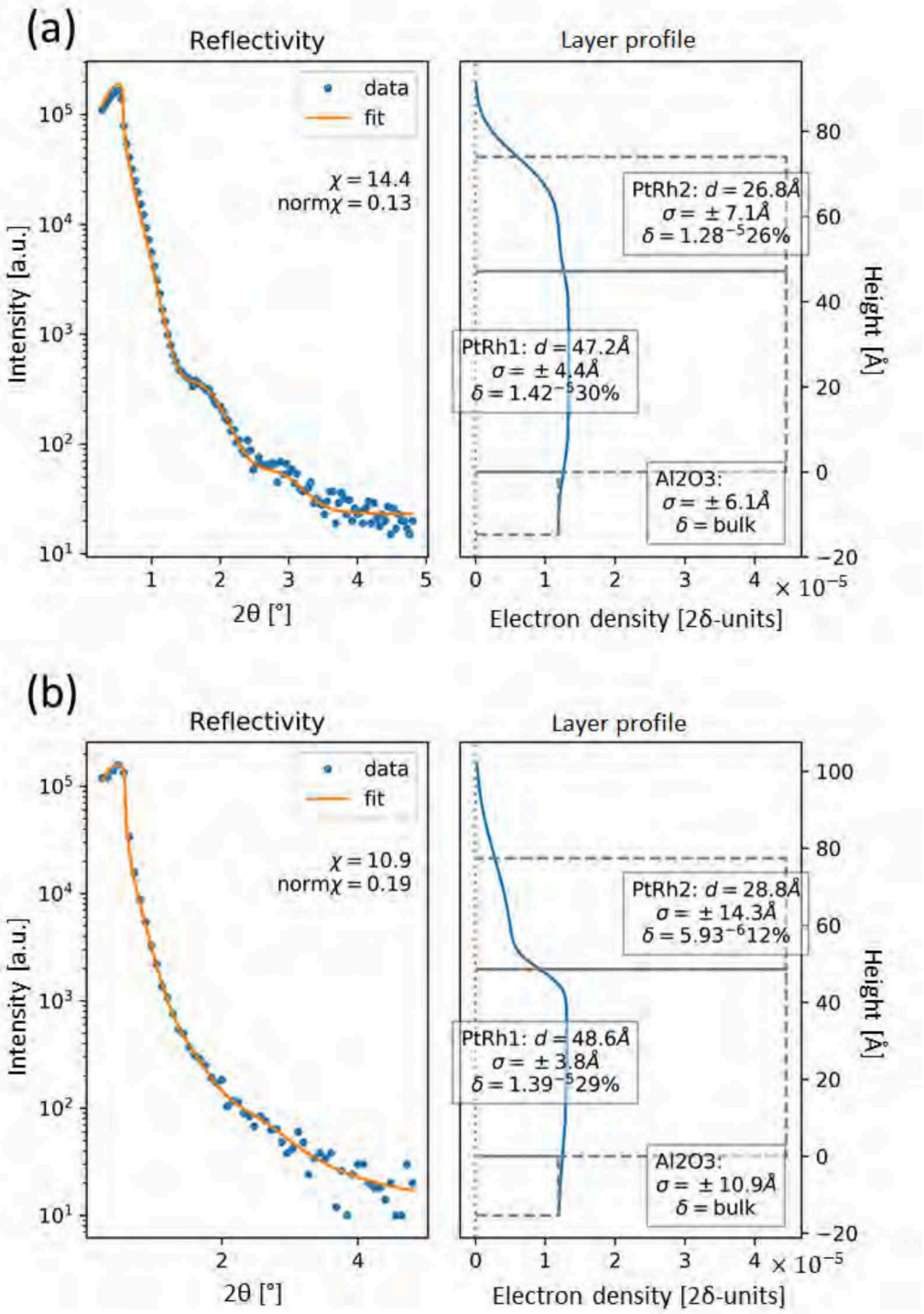

Figure 4.15.: XRR curve with corresponding Fewlay fit (left) and resulting electron density layer profile (right) of steps 1 (a) and 2 (b) of the second catalytic experiment on sample 6. The thickness of the substrate is assumed to be semi-infinite.

X-ray reflectivity scans during the first four steps of the experiment (see Table 4.2). Qualitatively spoken, the two oscillations visible at the beginning of the second catalytic experiment vanished more and more during the course of the experiment. At the same time, these maxima shift towards smaller reflection angles. Overall, this indicates an increasing average layer height with at the same time decreasing electron density of the layers, as the oxygen partial pressure increases. Analogous to the XRR examination of sample 26 in the previous chapter, decreasing (in-plane) coherence may be caused by both decreasing surface coverage and broadening of the particle height distribution. Data fitting done using the Fewlay software [216] supports these assumptions – see fits and corresponding fitting parameters in Figures 4.14 and 4.15. The pseudo-coverage $\bar{\delta}$ decreased continually with increasing oxygen partial pressure from 35 % at step one to 23 % in step four after overstoichiometric conditions. At the same time, the maximum layer height increased from 68 nm to 77 nm, while the effective thickness $d_{eff} = d_1\delta_1 + d_2\delta_2$ decreased from 24 nm to 17 nm. The electron density profiles in Figures 4.14 and 4.15 indicate a broadening of the particle height distribution, because the maximum layer height increased while the effective layer height decreased at the same time. This is attended by increasing values of the respective layers' roughness values σ. Generally, XRR-scans were conducted right after switching the gas flow to the next conditions – so, at the beginning of each step. Consequently, the XRR-scans were probing the sample surface from both the previous and recent step if underlying mass transfer mechanisms happened on a time scale of several minutes. This systematic error was known prior to the experiment, but had to be accepted due to time issues. Nonetheless, the results of the XRR-scan analysis fits the picture yielded from SEM and AFM data. Time issues were also the reason for that XRR-scans were only conducted for the first four steps of the experiment – together with XRD scans, probing particle properties. Figure 4.16 shows L_S scans for the PtRh alloy particles. Here, the coordinates of a platinum surface cell have been used - see Section 2.4.1. As the surface coordinates have been chosen with respect to pure platinum particles, the centres of the PtRh Bragg peaks at $(101)_S$ and $(102)_S$ are slightly shifted towards higher momentum transfer due to the small rhodium content shifting the lattice constant towards smaller values. The peak at about $L_S = 1.6$ corresponds to a $(11\bar{2}3)$ Al_2O_3 substrate peak. Generally, this graph confirms the crystallographic relation already found for the similar alumina supported platinum sample (sample 26) examined in the previous chapter, which is particles having their [111]-axis aligned parallel to the substrate's [0001]-axis, both ABC- and CBA-stacking occurring, and alignment of the particle [110] in-plane axis

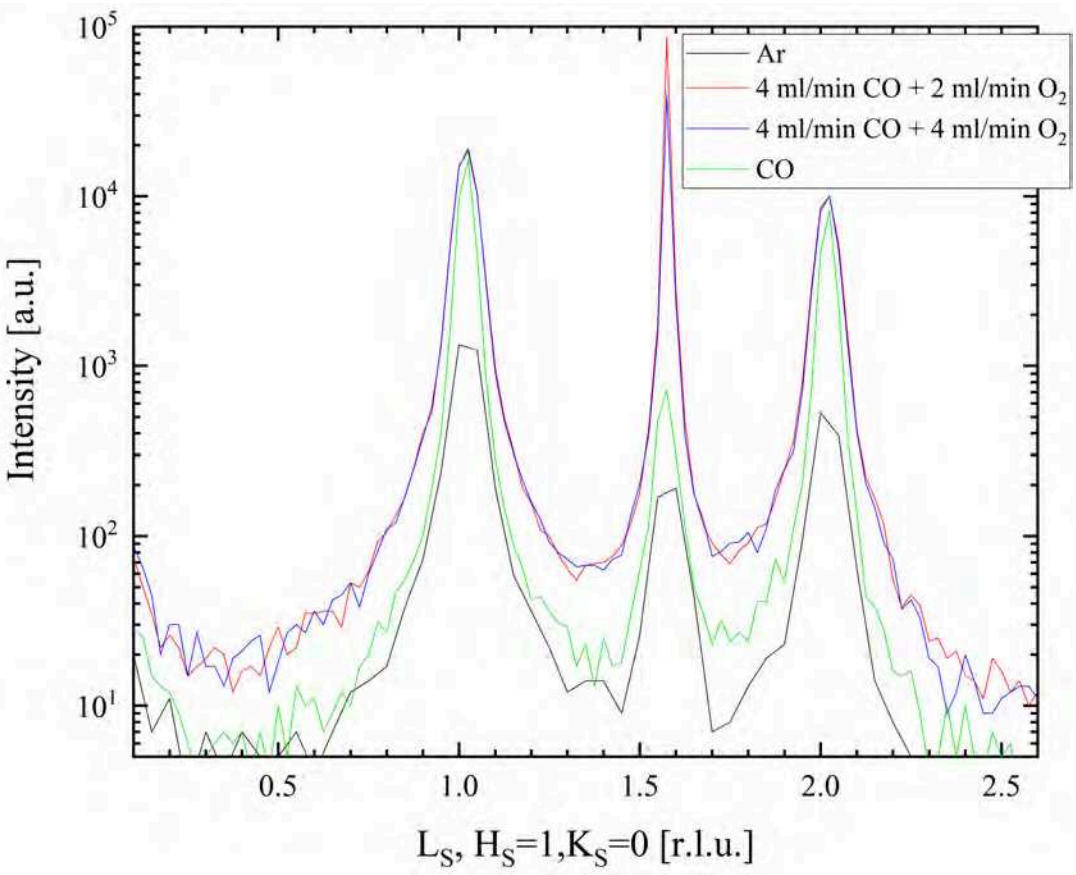

Figure 4.16.: X-ray diffraction scan along the $(1,0)_S$ surface rod of PtRh nanoparticles overlaying with an alumina surface rod. Shown are scans during step one to four, compare Table 4.2. The peak at about $L_S = 1.6$ corresponds to a substrate peak.

	Step 1	Step 2	Step 3	Step 4	After experiment
d_{Bragg} [nm]	9.1	10.6	11.1	16.0	
d_{AFM} [nm]					14
d_{eff} [nm]	2.4	2.5	2.1	1.8	
d_{tot} [nm]	6.8	8.8	7.4	7.7	
Coverage [%]	39				22
$\bar{\delta}$ [%]	35.0	28.4	28.6	22.7	
Average particle size [nm^2]	1000				377

Table 4.3.: Particle and layer properties throughout the second catalytic experiment on sample 6. Values for the coverage and average particle size determined by SEM before the experiment were filled in the cell for step 1 for simplicity.

with the substrate's [11$\bar{2}$0] axis. Fitting both PtRh Bragg-peaks with Pseudo-Voigt functions reveals a progressively increasing average height of the scattering particles – again, note that the scattered signal of Bragg peaks originates mainly from scattering on large particles (see Section 2.4). Results are displayed in Table 4.3. Additional H_S scans were conducted (data not shown), but for all conditions the particle diameter was too large to be probed by Bragg scattering using this setup[7]. Figure 4.16 further indicates a major issue which is alignment with respect to the X-ray measurements, caused by the arrangement of the reactor and the supply gas lines. All scans were done with the same integration time, though the collected intensity especially for the substrate signal deviates drastically (almost three orders of magnitude). Accordingly, values given here have to be interpreted with caution.

As mentioned above, the formation of a $c(2 \times 8)$ or a $p(9 \times 9)$ rhodium surface oxide is expected for such a catalytic experiment [277]. Reciprocal space maps recorded for steps one to five (not shown here) did not contain signals that could be identified with scattering from rhodium oxide formations on the top facets of (111)-oriented particles. Reasons may be manifold. The main reason might be that the reciprocal space maps did not exactly cover the area, where Rh_2O_3 peaks are expected. Theoretically, in-plane peaks are expected at about $H_S = 0.9$ with $K_S = L_S = 0$, see reference [41]. The reciprocal space maps did only cover the range above $L_S = 0.1$. Principally, the Bragg peak signal could have been broad and intense enough to be detected at $L_S = 0.1$. More importantly, the corresponding surface rod should be detectable in the range covered by the reciprocal space map. Possibly, the intensity of the beam was not high enough to enable detecting scattered signal of few rhodium oxide layers. Also, as mentioned above, the experiment suffered from misalignment which

[7]More precisely, the results for all conditions met very similar values where the resolution limit of the setup is to be expected.

might have prevented detecting rhodium oxide formation. In other experiments, the formation of rhodium oxide layers on PtRh nanoparticles was detected on (111)-facets in overstoichiometric oxygen partial pressures for particles with 67 % rhodium content [41, 277]. In addition to the reasons already given, the rhodium content of the particle might have been too low to allow for the formation of superficial rhodium oxide under the environmental conditions given in this experiment.

Table 4.3 displays the parameters determined throughout the catalytic experiment conducted at 450 °C. In the previous chapter, drastic changes in particle morphology were observed, too, and after annealing in air, morphology-related parameters determined by various instruments deviated a lot due to the non-uniform particle size and height distribution. Likewise, the height and coverage of sample 6 deviated increasingly as the second experiment progressed. Again, the cause is the non-unimodal particle shape distribution. The underlying mechanism accountable for the intra-particle mass transport cannot be determined from the measurements undertaken so far. The fact, that the particles' morphology persisted throughout the first catalytic experiment, but changed significantly during the second experiment indicates are somewhat strong correlation to the temperature. In the previous chapter, the platinum particles' shape is assumed to be kinetically stabilized upon annealing in UHV, exhibiting a highly truncated Wulff-shape. In this annealing study of sample 26, the equilibrium shape becomes accessible not through high annealing temperature solely, but both upon access to oxygen and high temperatures, allowing mobile atoms or metastable platinum oxide compounds to overcome potential barriers at the edges of particles. In the light of these findings, heat-driven Ostwald-ripening as sole, dominant sintering and mass transport process is unfavourable for morphology transformation upon the catalytic CO oxidation conditions applied for the studies here – at least for the large particles investigated in this study.
Brought up above, but barely covered, is the overall effect of time on the experiment. The first catalytic experiment lasted about 13 h, the second more than 40 h. Other authors have shown that the overall time of exposure does impact annealing experiments of alumina supported platinum particles [236] mostly in relation to sintering [258, 259, 278]. Experiments conducted in catalytic environments done by our group suggest mass transport mechanisms other than sintering[8].
Again analogous to the study in the previous chapter, the influence of the substrate on the morphology transformation is unclear. As the sample has been exposed to

[8]Data to be published by T. F. Keller, C. Seitz, A. Stierle, among others.

air before both catalytic experiments, the surface is somewhat contaminated with water, hydroxyl groups, and likely carbon-containing aggregates. Prior to the first catalytic experiment, no further cleaning step was undertaken. However, prior to the second catalytic experiment, the sample was exposed to 2 $\frac{\text{ml}}{\text{min}}$ hydrogen in 48 $\frac{\text{ml}}{\text{min}}$ argon at 0.1 bar total pressure and 200 °C sample temperature. Generally, under both circumstances any carbon contaminates should have been removed by either the H_2 dosing or the catalytic reaction [279]. Though, the alumina substrate and the particles might by covered with hydroxyl groups or even be OH-terminated during the experiment due to the exposure to air and possible water remains in the gas supply system. During growth of the particles, the alumina substrate most likely is Al-terminated, already featuring the lowest adhesion energy to PtRh nanoparticles – neglecting the OH-terminated surface, see Figure 3.24. According to the Wulff-Kaishev theorem, increasing height of the particles could only be caused by a transition of the metal/substrate interface towards a hydroxylated interface featuring the lowest adhesion energy. The oxidized interface exhibits a higher adhesion energy, making flat particles with a highly truncated Wulff shape more favourable (see discussion in Section 3.4). It is unclear whether the CO oxidation environment during the experiments conducted here are able to allow for a surface termination transition triggered by a possible water contamination (see Figure C.15) and a resulting hydroxylation of the surface.
Focussing especially on large particles – see Figure 4.10 – it seems as if the mass transfer mechanism causes particles with a high surface to volume ratio to collapse and reorganize atoms sitting on large facets, whereas smaller particles (and the outer remains of the large particles) are self stabilized, hence preserving their original shape. It could be assumed that if Ehrlich-Schwöbel-barriers [253, 254] are limiting the 3D growth of the particles, the CO-oxidation environment enables dissolving atoms from large facets – here top-facets – and agglomerating them to a 3D particle in the centre and coffee-ring-like remains of the original particle. Towards smaller particle size, this intra-particle mass transport mechanism could be damped by additionally stabilizing long-range interactions of the side facets. Further, the small particles may exhibit morphologies closer to the equilibrium shape.

All in all, this chapter demonstrated the feasibility and power of an in-situ study combining on-line mass spectrometry and X-ray diffraction as probing tool with the advantage of direct imaging tools like SEM and AFM. Two CO oxidation experiments were conducted at 370 °C and 450 °C, and accompanied by various characterization

methods. The experiment at 370 °C did not reveal any detectable morphological changes of particles exhibiting a highly truncated Wulff shape. The subsequent experiment at 450 °C however, demonstrated significant morphological changes of the alumina supported alloy nanoparticles during CO oxidation, with an intra-particle mass transport mechanism enabling a morphological transition of large particles with diameters of few hundred nanometers towards their equilibrium shape. In turn, small particles with diameters significantly smaller than 100 nm underwent the same mass transfer mechanism with minor changes in diameter as determined using SEM. Data gained from the various characterization methods did not indicate any influence of sintering mechanisms during the transformation of the particles.

Future experiments have to provide insight in the role of the alumina surface and especially the interface to the particles, as transitions of the alumina surface termination cannot be excluded. Further, the formation of rhodium oxides on the (111) top facets of the nanoparticles has not been observed, unexpectedly. Possibly, SXRD studies during CO oxidation on comparable samples exhibiting a concentration gradient of platinum and rhodium would give new insight in the role of the rhodium content for the formation of the surface oxide.

In total, the stability of small particles during the experiments conducted emphasizes the relevance of supported PtRh alloy nanoparticles with equilibrium shape for industrial catalytic applications.

Chapter 5.

CXDI on a single PtRh nanoparticle

So far in this work, X-ray diffractive and refractive methods were used as powerful tools enabling on-line, non-destructive, atomic scale characterization of samples in enclosed reactors. If such techniques are utilized for the characterization of (supported) nanoparticles, experiments will generally yield ensemble properties of the system studied due to the beam characteristics of common laboratory sources. However, the development of modern third generation synchrotron sources with outstanding beam properties enabled an in-depth, atomically precise characterization of single nanoparticles with sizes in the range of hundred nanometers and below [280]. Further, single-particle X-ray diffraction with proper data analysis does offer atomically precise information on the surficial composition of bimetallic nanoparticles and accompanying strain and displacement states – making it a promising tool for catalytic studies in general.

To pursue the operando study presented in the previous chapter, a combined study of single alumina or STO supported PtRh nanoparticles during CO oxidation is presented here, utilizing both single-particle XRD and on-line mass spectrometry. For this purpose, samples used were pre-characterized using SEM and suitable nanoparticles were preselected for the CXDI diffraction experiment. To maintain general feasibility of this challenging experiment, the CXDI study needed to be conducted in a forward scattering geometry, obtaining specular signal only. This offers the advantage that the scattered signal is independent from the sample's in-plane rotation and thus allowed for moving the reactor as little as possible. In this measurement geometry, the specular signals of alumina and the PtRh particles were possibly overlapping for the (111)-oriented particles selected for the experiment, hence impeding gaining meaningful data from the CXDI study. Accordingly, datasets recorded for the single particle on alumina were discarded. Instead, this chapter focusses on the experiment on a single $Pt_{60}Rh_{40}$ particle with Nb-doped $SrTiO_3$ as

support. Due to difficulties with the localization program at the beamline endstation, a non-precharacterized particle close to the deposited markers was selected for the CXDI study during the experiment. Section 5.1 briefly addresses the existing particle morphologies on the STO supported sample used. Furthermore, the section presents a brief overview over growth of platinum(/rhodium) particles on STO as found in literature. Note, that this chapter focusses on the scattering experiment and not on the average morphology and corresponding epitaxial relationship of particles and the substrate[1]. Having introduced the sample, the setup utilized for the challenging in situ CXDI study at endstation ID01 at ESRF is presented in Section 5.2. Subsequently, Section 5.3 briefly addresses the coherent X-ray diffraction imaging (CXDI) technique. Eventually, the experiment and results from data analysis are presented in Section 5.4.
Note that most of the study and results presented here are the result of team effort and the close collaboration with the research group of Ivan Vartaniants[2]. A corresponding publication will be released soon [281]. Details on contributions are given throughout this chapter.

5.1. Details on the sample

Contrary to the studies presented in the previous two chapters, for this single-particle imaging experiment Nb-doped $SrTiO_3$ was chosen as a support due to experimental reasons (see above). Accordingly, growth of Pt(Rh) on STO is briefly discussed in the following.
Growth of platinum particles on $SrTiO_3$ substrates has been studied by various groups. In the temperature regime below 200-300 °C, layer properties resemble those of platinum on alumina surfaces, as superficial diffusion of platinum is suppressed by its low mobility [282]. For temperatures of about 800 °C during growth or during annealing after growth, both MBE and ALD experiments find epitaxial growth of platinum crystallites on TiO_2-terminated $SrTiO_3(001)$ with $[001]_{Pt}||[001]_{STO}$ and $[111]_{Pt}||[111]_{STO}$, see [282, 283]. Films with thicknesses of about 50 nm deposited at temperatures of up to 750 °C reproduce this epitaxial relationship for higher temperatures [284]. Depending on the amount of deposited material, these studies

[1] Information on ensemble crystalline and epitaxial properties as determined by SXRD and XRR are given in Section C.1 in the Appendix for the sample after exposure to catalytic conditions only.
[2] Deutsches Elektronen-Synchrotron, Notkestraße 85, 22607 Hamburg.

detected particles with average lateral sizes of 3-5 nm (MBE) and 12-15 nm (ALD). However, in both studies particles with lateral extension of 80 nm and larger are present on the surface after annealing (ALD) or after deposition at 800 °C (MBE), already at low amount of deposited material (about 1 ML). Another MBE growth study conducted at 850 °C confirmed findings above, but additionally found (111)-oriented platinum particles for 2 ML coverage [285]. SXRD experiments conducted in our group found (100), (110), and (111)-oriented particles with manifold epitaxial relationships to the substrates for particles deposited on STO(001) at 800 °C and subsequent postannealing in air for 10 min at 1100 °C – see supplementary material to [146]. A high postannealing temperature has been chosen to allow for the particles to obtain their Wulff shape in thermodynamic equilibrium.

For growth of the sample in the present study (see sample 13 in Table A.1 in the Appendix), the postannealing step in air has been replaced with postannealing in UHV for 1 h at 1200 °C to prevent the rhodium content from oxidizing. Furthermore, the particle material is now PtRh instead of pure platinum. Particles were grown in co-deposition at 830 °C in the ratio $Pt_{60}Rh_{40}$. The ratio has been chosen as such to both minimize the lattice mismatch (minimum along [100]-type directions would be $Pt_{85}Rh_{15}$) and at the same time have a high rhodium content to possibly allow for the formation of rhodium surface oxide – compare Section 4.4.
Prior to the CXDI experiment, the sample has been characterized employing both AFM and SEM. Figures 5.1 and 5.2 depict exemplary areas of the sample's surface after postannealing. Judged from SEM images, the growth mode on sample 13 is bimodal. Sample 13 is mostly covered with small particles as can be seen in Figure 5.1 which is exemplarily for most of the surface. The surface coverage in this area[3] is about 18 %, the average lateral size of the particles is about 18 nm^2 with a narrow size distribution, and the average height about 1.5 nm (AFM data not shown) with a narrow height distribution. Figure 5.2, however, shows a bimodal growth mode: on the left of the image, the particle growth mode is as indicated in Figure 5.1. The immanent transition towards a slightly darker background on the right of the image likely indicates a step edge. According to AFM measurements, the step height ranges from about 2.2 nm to 2.7 nm. In the darker area, the particle density is drastically decreased by 75 %. Small particles exhibit dimensions as indicated above, but are less likely to occur. In contrast to areas indicated in Figure 5.1,

[3]For a more exact determination of parameters, a zoomed-in image of this area has been chosen for analysis.

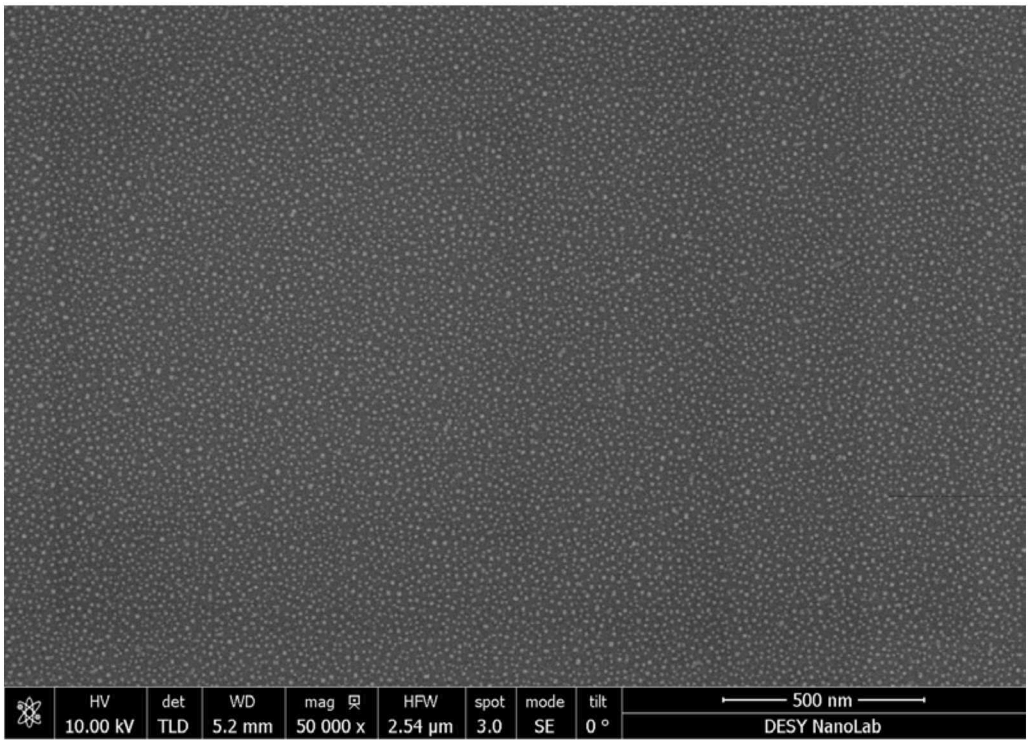

Figure 5.1.: Exemplary SEM image of the surface of sample 13 before the CO oxidation experiment. Round, bright spots indicate alloy particles. Vertical stripes in the image arose from the image capturing procedure.

darker areas are accompanied by – in comparison – very large particles (indicated as bright particles in Figure 5.2) which feature a broad lateral size distribution ranging from tens of nanometers to micrometers. These particles are significantly higher (up to several hundreds of nanometers) and even their facets can be guessed in the SEM image. Judging from the orientation of the facets, these particles exhibit preferred in-plane orientations with the substrate. It is possible that in these two morphologically different areas the surface termination deviates or the surface is reconstructed differently – compare [135, 141, 142]. Due to lack of time prior to the demanding CXDI experiment, no SXRD studies have been conducted on the sample before exposure to catalytic conditions during the CXDI experiment. Nonetheless, after the experiment both SXRD and XRR were preformed to probe the epitaxial relationship of the particles and the STO substrate, as presented in Section C.1 in the Appendix.

Figure 5.3 shows the particle selected during the CXDI experiment. Again, areas of high and low particle density are visible. Despite the contrast of the image, single (tilted) facets can be vaguely discerned with a top facet in the centre of the large

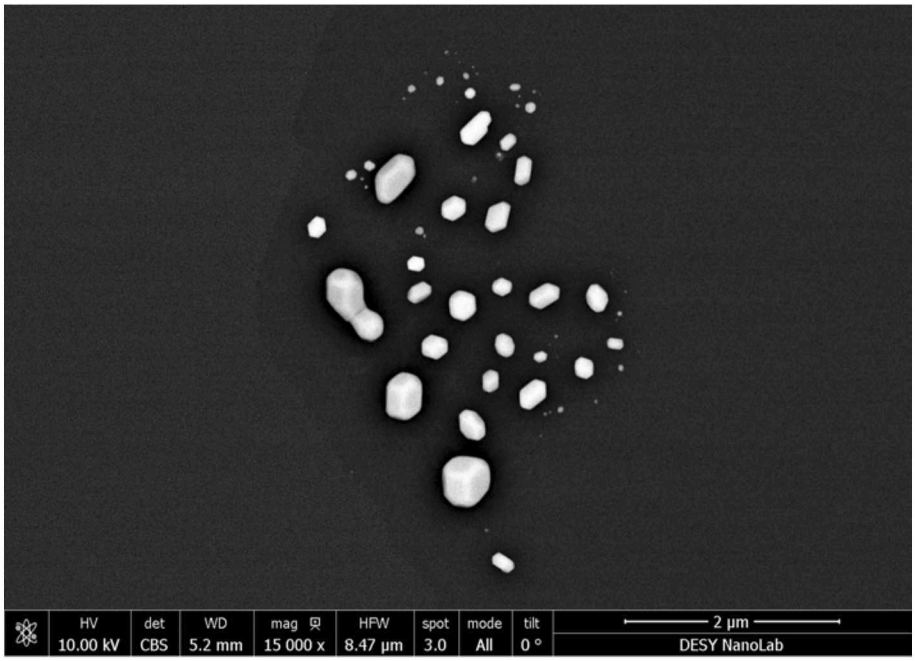

Figure 5.2.: SEM image of rare large particles on the surface of sample 13. Image was taken before CO oxidation experiment.

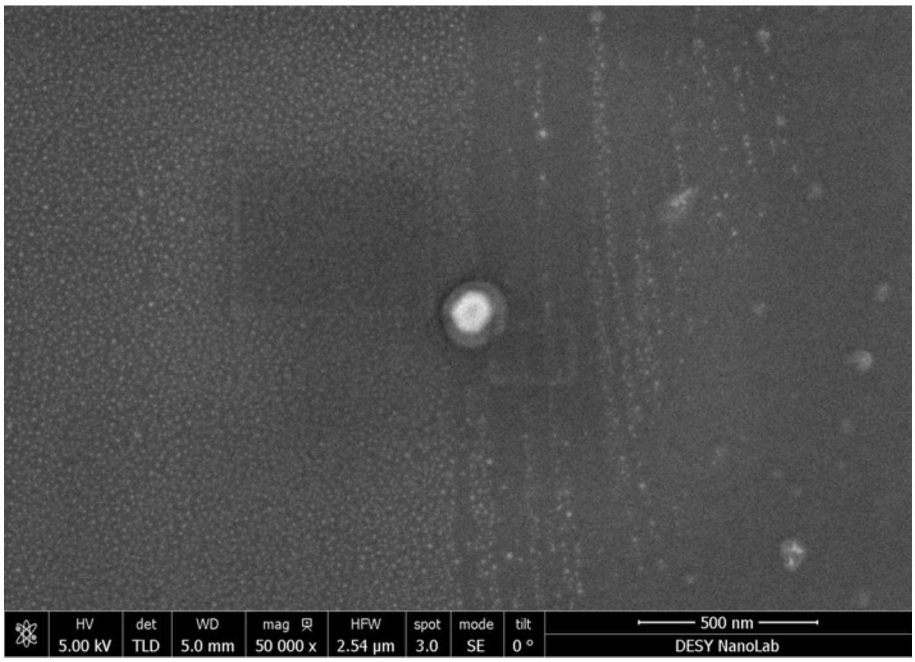

Figure 5.3.: SEM image of the single PtRh particle from the CXDI study after the experiment. Rectangular shades originate from image capturing processes in the SEM system.

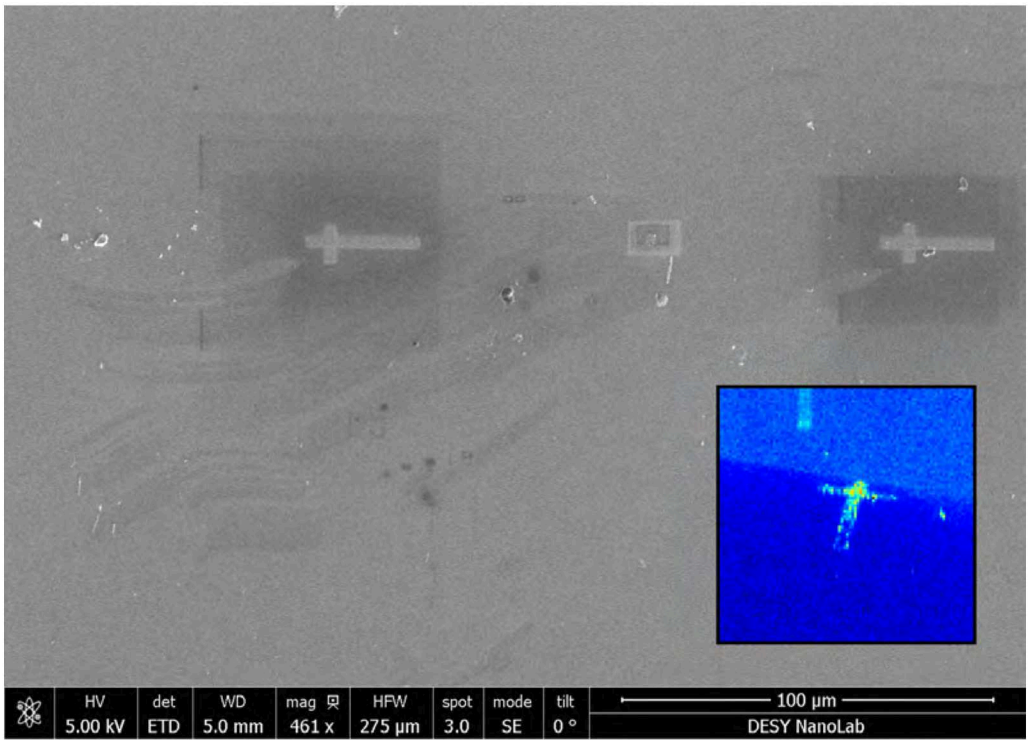

Figure 5.4.: SEM image illustrating cross-shaped markers deposited using FIB and a platinum-containing precursor gas. These markers enable positioning and selecting a suitable region of interest for the nano-focussed synchrotron beam. Rectangular features arose from image capturing precess in the SEM system. The inset on the bottom right shows a K-MAP of a platinum cross-shaped marker at the border of the substrate.

particle in the centre of the image. The shape of the particle alone does already suggest a (111)-orientation with the [111]-axis aligned with the substrate's surface normal.

To enable characterization of the single alloy particle with multiple methods and instruments, markers are needed on the substrate to define positions. Figure 5.4 shows an SEM image of Platinum markers deposited on well-defined spots on the substrate using Focussed Ion Beam (FIB) and a platinum-containing precursor gas which allowed for tracking the position of the preselected nanoparticles at both the beamline's end station in Grenoble and the SEM system in Hamburg. In the middle between the two crosses, an area with a preselected particle is situated. However, due to difficulties using the program tracking the positions, it was decided to study a suitable particle found with the K-MAP mapping technique (see Section 5.2) during the experiment. This particle was later tracked back with SEM.

5.2. Setup layout at end station ESRF ID01

The experiments presented in the following were conducted at the ID01 end station at the *European Synchrotron Radiation Facility* (ESRF), Grenoble (France). Figure 5.5 shows a picture of the setup employed. The X-ray beam is guided through the beamline and corresponding optics (1), and is focussed on a $(400 \times 400)\,\mathrm{nm}^2$ spot using KB-mirrors (a.o.). An optical microscope allows for identification of markers on the sample's surface and to set up a coordinate system to find regions of interest on the sample. As for the experiment presented in the previous chapter, the SXRD catalysis reactor (3) with accompanying gas flow system was used to provide a well-defined gas environment. Analogous, the LPM T100 residual gas analyser with a mass spectrometer was positioned down-stream from the reactor. Throughout the experiment, the total gas flow was kept at $50\,\frac{\mathrm{ml}}{\mathrm{min}}$ at a total reactor pressure of 100 mbar, the temperature was about 700 K. The reactor was mounted on a hexapod with a piezo stage, enabling nm-precise positioning of the sample. The hexapod is mounted on the diffractometer cradle. The reactor is supplied with cooling water (5) and gas (6). The Eiger2M detector with 1030×2164 pixels, a pixel size of $75\,\mu\mathrm{m} \times 75\,\mu\mathrm{m}$ and fly-tube (8) are mounted on the diffractometer arm (7). The distance between sample and detector was 0.85 m.
The energy of the beam was 9 keV ($\lambda = 1.378\,\text{Å}$) with a size of about $(400 \times 400)\,\mathrm{nm}^2$, resulting in a footprint of 1.3 µm along the beam at an incidence angle of $\theta = 17.87\,^\circ$. The coherent flux of the beam was in the order of $10^9\,\frac{\mathrm{photons}}{\mathrm{s}}$. To support re-positioning of the sample and identification of regions of interest, the scanning X-ray protocol *K-MAP* was implemented [286, 287]: at a certain diffraction angle (here: (111) Bragg peak of Pt), the sample surface was scanned by translation of the piezo stage and structures such as the deposited platinum markers could be identified.

5.3. Coherent X-ray diffraction imaging

Principally, the correlation between a spatial electron density distribution and the amplitude distribution of X-rays scattered on these electrons has been used implicitly to obtain size information on nanoparticles in this work so far. Basically, this correlation fundamentally even allows for the exact spatial distribution of the electron density and hence the 3D shape of a single object to be retrieved. However, in X-ray scattering experiments, the key quantity obtained is the intensity $I \propto |A(\boldsymbol{Q})|^2 \propto |\int \rho(\boldsymbol{r}) \mathrm{e}^{-\mathrm{i}\boldsymbol{Q}\cdot\boldsymbol{r}} \mathrm{d}\boldsymbol{r}|^2$, compare Section 2.4. The latter relation implies

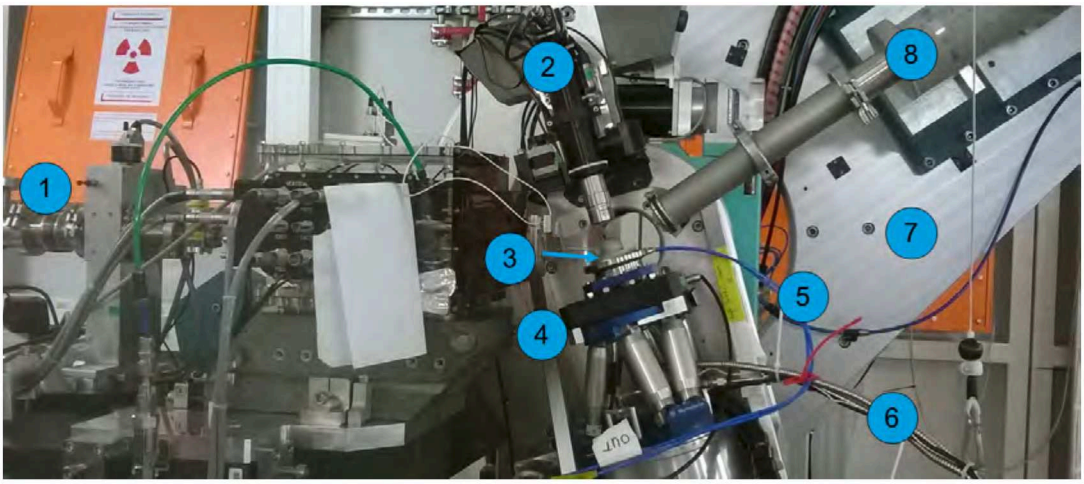

Figure 5.5.: Experimental setup at ESRF ID01: (1) beamline and optics, (2) optical microscope, (3) SXRD catalysis reactor with beryllium dome, (4) hexapod with piezo stage, (5) water cooling tubes, (6) gas supply lines, (7) diffractometer arm, and (8) evacuated fly-tube in front of detector (detector not shown).

that the phase and hence the relationship between scattered waves is lost during the measurement – the so-called *phase problem* – which prevents retrieving the real space shape of the object scattered on [205, 288]. In the seventies and eighties, algorithms were proposed to circumvent this fundamental issue [289, 290]: By cycling Fast Fourier Transforms (FFT) and Inverse Fast Fourier Transforms (iFFT) of an intensity amplitude distribution with an initially randomized phase the original phase and hence the real space image (real space reconstruction) can be calculated. Figure 5.6 shows a simplified sketch of the algorithm applied to a diffraction pattern $I(\boldsymbol{Q})$ – in the present case of a single particle. The starting point is the amplitude distribution as square root of the diffraction pattern's intensity distribution with an additional phase factor. For the first step, the phase will be set randomized. Inverse Fourier transformation via iFFT yields an estimate of the electron density profile $\rho'(\boldsymbol{r})$ which in turn can be refined by applying further size information on the original particle from SEM or AFM measurements[4]. Transforming back to reciprocal space leads to an amplitude distribution $A(\boldsymbol{Q})$ which gets replaced by the original amplitude distribution $A'(\boldsymbol{Q})$. For the next cycle the phase factor gained from the last cycle is kept for further refinement. Cycling through this algorithm results in an approximation of the originally lost phase and the direct space electron density distribution of the particle, see [205] for instructive examples. Principally, the imaging technique does not rely on the utilization of lenses, thus further promoting

[4]Further constraints to the estimate might be positive, real numbers [205]. The prime of $\rho'(\boldsymbol{r})$ does not refer to the derivative of $\rho(\boldsymbol{r})$, see Figure 5.6 to avoid confusion.

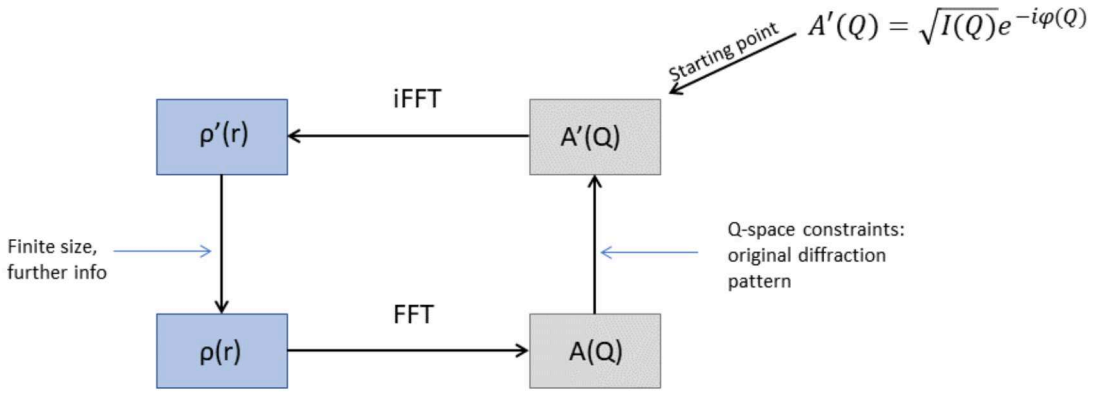

Figure 5.6.: Sketch of a phase retrieval algorithm. The starting point of the first iteration is the square root of the original diffraction pattern with a randomized phase $\phi(\boldsymbol{Q}) = \boldsymbol{Q} \cdot \boldsymbol{r}$. Cycling Fourier transforms and implementing constraints leads to the real space electron density distribution $\rho(\boldsymbol{r})$.

the usage of X-rays. More details on the algorithm and corresponding important facets (e.g. oversampling, error reduction algorithms) are described in [288] and [291].

CXDI became a promising tool for the investigation of small objects in the range of several tens of nanometers to few micrometers in recent years only. The reasons for this do not solely lie in the necessary development of algorithms, digital implementation, and corresponding computational infrastructure. The main reason is that early X-ray sources did not provide X-rays with the properties necessary for CXDI experiments. Not until the development of third generation light sources (ESRF, APS, SPring-8, PETRA III among others), the key properties – coherence and intensity – became available to researchers. Obtaining a real space electron density distribution as inverse Fourier transform of the amplitude scattered in the far-field of an object of finite size relies not only on the proper retrieval of the corresponding phase factors, but also on the incident beam being coherent across the volume of the sample to allow for the wavefronts to constructively interfere [205]. Coherence in this context refers to wavefronts exhibiting a certain, fixed phase relation and is obtained by monochromatic, quasi-unidirectional beams. An incoherent beam would cause the contrast of the diffraction pattern to be decreased significantly. Longitudinal and transverse coherence are illustrated in Figure 5.7, where the coherence length is defined as the distance after which two wavefronts exhibit a phase shift of π. Crucial for the scattering experiment itself is that the beam exhibits coherent properties across the volume of the probed sample, i.e. the longitudinal and tranverse coherence lengths have to be larger than the probed particle's extent. Technically, this is

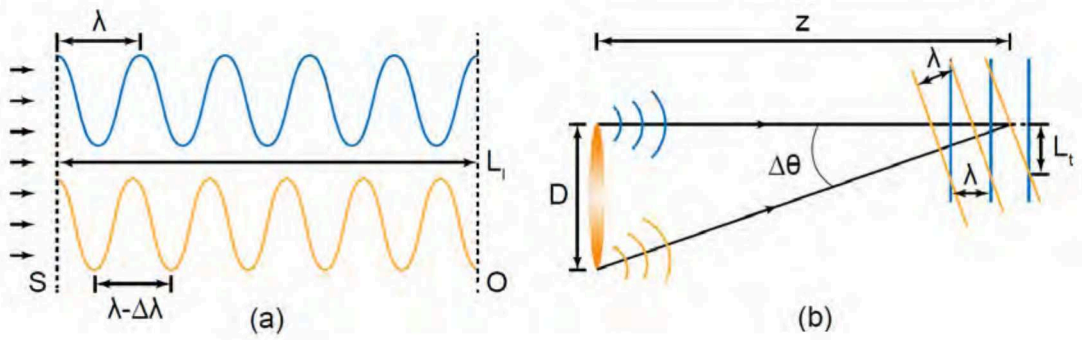

Figure 5.7.: Definition of longitudinal and transverse coherence lengths L_l and L_t. (a) After propagating from point S to point O, two waves with a difference in wavelength of $\Delta\lambda$ exhibit a phase difference of 180 °. The distance between S and O is called longitudinal coherence length L_l. (b) Two wavefronts emitted with an angular difference of $\Delta\theta$ by a source of size D coincide at a distance z from the source. Here, the angular difference leads to a phase shift along the wavefront. At a distance L_t along the wavefront, the phase difference is 180 °. Sketch taken from [32].

achieved by using 2D detectors, suitable, nano-focussing X-ray optics (monochromators, KB-mirrors [292], Fresnel zone plates [293, 294], refractive X-ray lenses [295] etc.) and a significant distance from sample to source (typically about 100 m in the case of third generation light sources). Today, CXDI experiments are not only limited to synchrotrons only. Modern X-ray Free-Electron Lasers (XFEL) provide X-rays with even better beam properties [296–298]. Whereas diffraction experiments at synchrotrons usually are considered to be non-destructive to samples (depending on both the sample and beam intensity), XFEL pulses are so intense the probed area of the sample or the particle (or molecule etc.) usually is destroyed after a single or few pulses without damping the beam intensity [299, 300]. However, the resulting coulomb explosion is significantly slower than the scattering process and hence does not hinder a scattering experiment [299, 301].

As CXDI is naturally not limited to crystalline materials, typical applications of CXDI cover a broad range: imaging of biological samples like proteins and nanocrystals [302], imaging of semiconductor nano-rods [303], mapping of facets and defects of nanoscale objects [304], in situ annealing study of colloidal structures [305], tracking gas-induced segregation in PtRh nanoparticles [306], and observing catalytically induced shape changes [146]. Similar to the latter example, this work emphasizes CXDI as a useful tool for in situ studies, as demonstrated in the following section.

Step number	Ar [$\frac{\text{ml}}{\text{min}}$]	CO [$\frac{\text{ml}}{\text{min}}$]	O_2 [$\frac{\text{ml}}{\text{min}}$]	Temperature [°C]
1	50	0	0	425
2	42	8	0	425
3	38	8	4	425
4	42	8	0	425

Table 5.1.: Gas flow composition and temperature during the catalytically enhanced CO oxidation experiment. Total flow was kept at 50 $\frac{\text{ml}}{\text{min}}$ throughout the experiment with a total pressure in the reactor of 0.1 bar.

5.4. CXDI of a single alloy particle during a catalytic reaction

Chapter 4 showed that a catalytic environment may inflict drastic structural and morphologic changes on (alloy) nanoparticles despite those being a catalyst material participating only passively in corresponding chemical reactions. Nevertheless, the studies presented in this work so far did not provide atomically resolved insight into the superficial structure of the particles and possible accompanying changes induced by e.g. segregation, strain, or reconstruction. Performing single-particle diffraction during a catalytic reaction does provide this crucial data on the chosen model system, correlating the atomic structure of the single nanoparticle's facets with the surrounding catalytic environment.

Similar environmental conditions as in the study presented in Chapter 4 were chosen for the experiment, see Table 5.1. The gas composition was changed slightly and the overall time of the experiment was considerably shorter (8 h here vs. about 25 h for the ensemble study presented in Chapter 4). Additionally, the temperature was changed to 425 °C. The total pressure was kept constant at 0.1 bar throughout the experiment with a total gas flow of 50 $\frac{\text{ml}}{\text{min}}$. Prior to the first CO dosing step, the sample was exposed to 2 $\frac{\text{ml}}{\text{min}}$ H_2 in 48 $\frac{\text{ml}}{\text{min}}$ Ar at 425 °C for 25 min. Figure 5.8 shows the partial pressure signals of the most relevant gases as detected by the T100 residual gas analyser (RGA) positioned downstream the reactor for the gas dosing steps indicated in Table 5.1. Clearly, when dosing CO and O_2, the CO_2 production increases significantly[5] and the sample is catalytically active. A small increase in the CO_2 signal when dosing only Ar and CO is associated to CO_2 remains in the CO gas.

[5] A test experiment confirmed that the increase in CO_2 production is correlated to presence of the alloy particles and neither the STO nor the reactor surface itself are significantly catalytically active within the parameters chosen for this experiment (compare Section C.5).

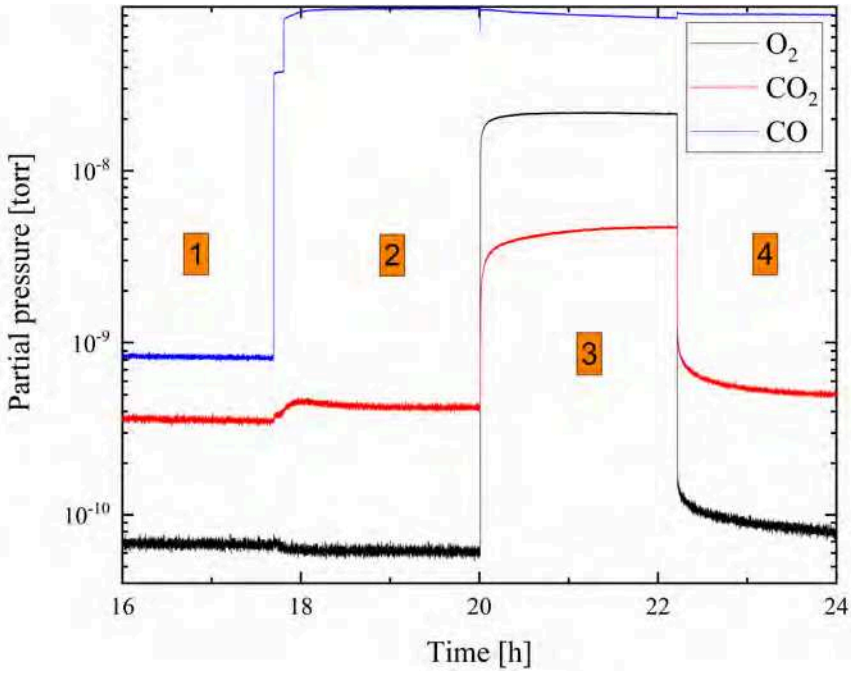

Figure 5.8.: Partial pressure versus time as recorded by the residual gas analyser positioned directly downstream the reactor. For simplicity, only the signals of CO, CO_2, and O_2 are displayed. Highlighted numbers refer to gas dosing steps specified in Table 5.1.

Note, that the whole sample is exposed to the gas and the corresponding catalytic activity is the activity of the whole sample and not solely that of the single particle.

Employing the setup described in Section 5.2, diffraction datasets in specular geometry[6] have been collected for the gas dosing steps specified in Table 5.1. The scattering geometry is sketched in Figure 5.9. To record a complete sample of a Bragg peak in a 3D section of reciprocal space, the particle was centred using the piezo-stage and cradle of the diffractometer and a step-wise rocking scan with $\pm 1\,^\circ$ in η (compare Figure 5.9) was performed. During each step, the nanoparticle was repositioned with respect to the beam using the piezo-stage. Subsequently, 2D diffraction patterns were recorded with an integration time of 5 s (datasets for steps 1 and 4) or 7.5 s. The step size in η was $0.02\,^\circ$.

The centre of the diffracted signal by the particle is found at a diffraction angle of $\theta_B = 17.873\,^\circ$ which corresponds to the Bragg angle of {111}-planes at about 425 °C, hence the particle is (111)-oriented. Assuming that a platinum-rhodium alloy does not exhibit a miscibility gap (following *Maisel et al.* [82]), the exact elemental composition of the particle can be calculated from the Bragg angle and *Vegard's law*

[6] In this geometry, incident and exit angle fulfil the relation $\alpha_i = \alpha_f = \theta_B$ and the scattering vector $\boldsymbol{Q}$ is aligned parallel to the surface normal.

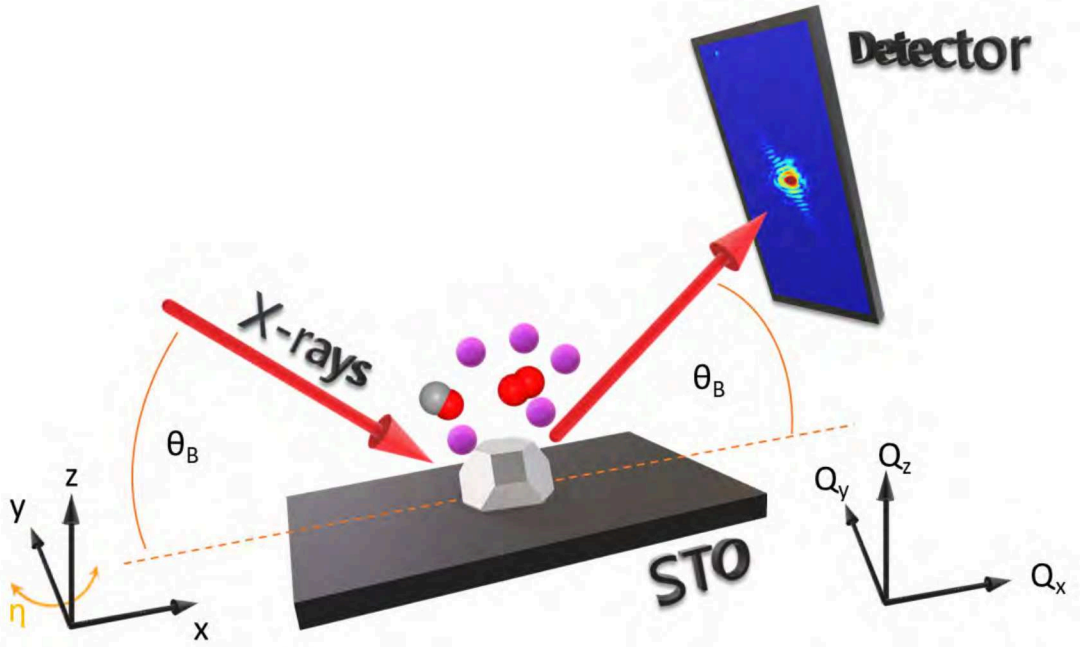

Figure 5.9.: Sketch of the specular scattering geometry at ID01 with corresponding coordinate grids. η denotes a rotation around the y-axis. Purple spheres represent argon atoms, red spheres oxygen, dark grey spheres carbon.

[83, 84]: the distance between {111}-planes is $d_{111} = \frac{a_{\text{alloy}}}{\sqrt{3}}$. Using this, the alloy's lattice constant a_{alloy} can be deduced using Bragg's law:

$$a_{\text{alloy}} = \frac{\sqrt{3}\lambda}{2\sin\theta_B}. \tag{5.1}$$

Using Vegard's law $a_{\text{alloy}} = x \cdot a_{Pt} + (1-x) \cdot a_{Rh}$, with x denoting the concentration of platinum, the composition of the particle is calculated to be $Pt_{58.4}Rh_{41.6}$. Corresponding lattice constants a_{Pt} and a_{Rh} were estimated from temperature dependent measurements of the lattice constants for platinum and rhodium presented in [80] and [79], respectively. Assuming a temperature uncertainty of $\pm 50\,\text{K}$, the error on the composition is $\pm 3\,\%$. EDX measurements carried out by our group confirmed this composition, see supplemental material to [281].

The diffraction dataset gained is a stack of 2D diffraction patterns which has to be properly transformed for further data analysis. The coordinate system is chosen to be fixed on the substrate's surface as indicated in Figure 5.9 where during the rocking scan $\alpha_i + \alpha_f = 2\theta_B$ is fulfilled. Technically, to obtain the evenly gridded 3D cut-out of reciprocal space, $\boldsymbol{k}_f$ is expressed through proper rotation matrices and

the intensity distribution on the detector $\boldsymbol{P}$:

$$\boldsymbol{Q} = \boldsymbol{k}_f - \boldsymbol{k}_i = (M_z M_y)\,\boldsymbol{P} - \boldsymbol{k}_i. \tag{5.2}$$

Here, M_z and M_y are rotation matrices around the z and y axes, respectively, and $\boldsymbol{P}$ is the intensity recorded in each pixel dependent on its position on the detector. The components of $\boldsymbol{P}$ can be calculated geometrically from the detector's pixel size, the known distance of sample and detector, and the modulus of $\boldsymbol{k}_f$. The resulting dataset consists of curved slices in Q-space and hence has been linearly interpolated[7] to fit a regular grid. Figure 5.10 shows the obtained 3D (111) Bragg peak intensity distribution as isosurface of the logarithmic intensity at 25 % of the maximum value. Both a 3D-view (a) and a top-view (b) are depicted. For displaying purposes, the isosurface has been treated with a smoothing algorithm. Crucial for further data analysis and for the feasibility of CXDI is that the substrate's CTR clearly visible in Figure 5.10 (a) as straight line along Q_z is separated from the particle's Bragg peak. This can be seen more clearly in (b), where the Bragg peak's centre is at 0 and the substrate's CTR at (-0.006 -0.04) nm^{-1}, indicated by an orange arrow. Most importantly, the CTR is not overlapping the Bragg peak. This is caused by a small tilt between the particle's and the substrate's surface normals. An overlap would have complicated any further data analysis. In Figure 5.10 (b), the Bragg peak exhibits streaks in a six-fold manner, indicated by three planes I-III. These correspond to the low-index facets arranged in a six-fold symmetry which can be guessed from the SEM image in Figure 5.3. From Figure 5.10 (a) it can be guessed that these facet signals exhibit a component along Q_z, too, hence the 3D intensity distribution indicates high symmetrical properties of the object scattered on. Though, discrepancies along high-symmetry planes I-III indicate that the particle exhibits a deviation from the ideal truncated octahedral shape as will be discussed in the following section.

5.4.1. Reconstructed 3D particle

From the properly prepared 3D intensity distribution the electron density distribution can be retrieved by phase retrieval algorithms as described in Section 5.3. For the dataset here this was done by Y. Y. Kim and L. Gelisio[8]. Additionally, they analysed

[7] The data treatment has been done using *Matlab* with help of Y. Y. Kim. Technically, the interpolation here is carried out with the outdated *TriScatteredInterp* function instead of the *scatteredInterpolant* function for performance reasons.

[8] Deutsches Elektronen-Synchrotron, Notkestraße 85, 22607 Hamburg.

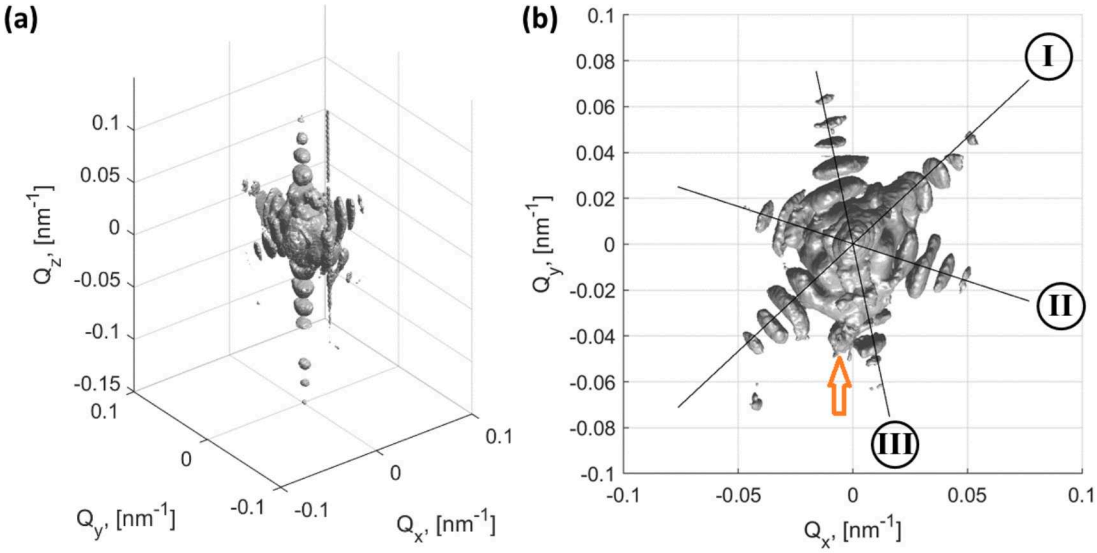

Figure 5.10.: Isovalue surfaces of the processed intensity distribution of the diffraction dataset during step (1), compare Table 5.1. (a) shows a 3D isometric view, (b) a 3D top-view of the dataset. Both isosurfaces are displayed as logarithmic intensity at 25 % of the maximum logarithmic value. High-symmetry directions of the particle are indicated by planes I-III in (b). The orange arrow in (b) indicates the position of the substrate's CTR directed along Q_z.

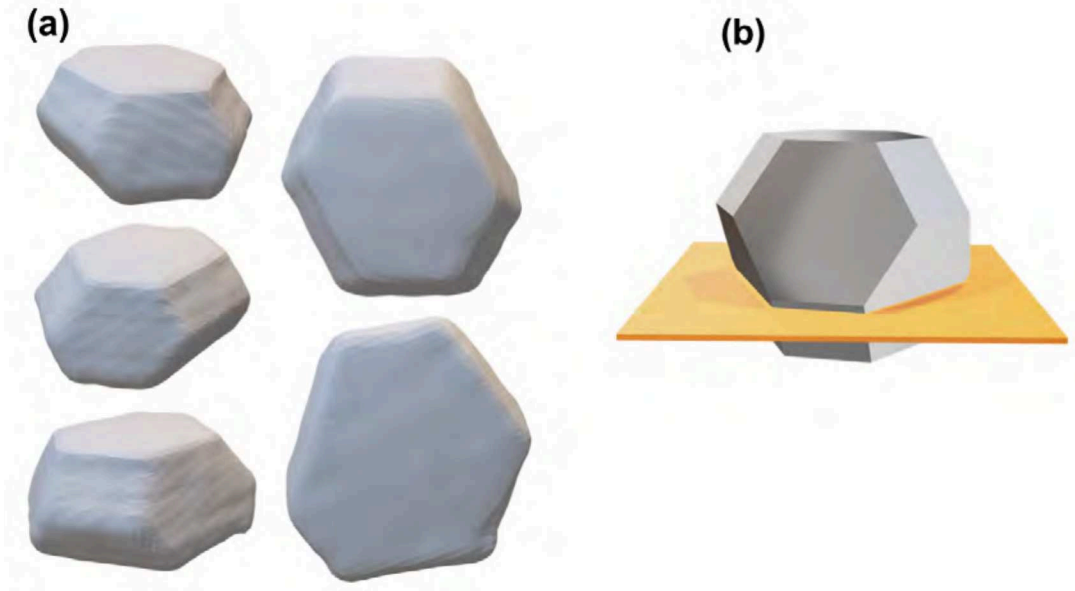

Figure 5.11.: Comparison of reconstructed particle in argon atmosphere (step 1) and corresponding ideal model: (a) isosurface of the electron density $|\rho(\boldsymbol{r})|$ at 55 % of the maximum value. 3D side-views are depicted on the left. On the right are top-view (top) and a view from the bottom (bottom). (b) shows a model of an ideal truncated octahedron cut perpendicular to the [111] growth direction.

displacement and strain of the particle and facets [281], as will be briefly discussed below.

Figure 5.11 (a) shows different perspectives of an isosurface of the particle's electron density distribution $|\rho(\boldsymbol{r})|$ at 55 % of its maximum value. The corresponding dataset was recorded in gas dosing step 1 (compare Table 5.1), i.e. pure argon atmosphere. Compared to an idealized truncated octahedron (idealized Wulff shape) as displayed in Figure 5.11 (b), the particle is cut along the [111] growth direction (indicated by the orange plane) and elongated in in-plane direction. Overall, the particle's shape is close to the theoretical, ideal Wulff-Kaishev construction, compare Figures 2.6 and 2.7. Dents, blisters, and further surface roughness could be attributed to the phase retrieval algorithm or parasitic scattering limiting the phase retrieval process. Upon a closer look, the bottom part of the particle seems more rough than the top facet, which could, too, be attributed to the reasons just given or the tilt and mismatch towards the substrate. The angles between the top facet and side facets fit those of low-index facets (111) and (100). Note, that the spatial resolution of the reconstructed particle is limited due to the limited range in Q of the corresponding recorded diffraction patterns. Depending on the gas dosing step, the spatial resolution of the reconstructed particle was between 10 nm and 20 nm – see supplemental material to [281] for details. The reconstructed particle is 95 nm wide and 120 nm long (at 425 °C) – very similar to dimensions as estimated from SEM imaging (see Figure 5.3). The height is estimated to be about 55 nm. From the position of the minima in between the Laue fringes of the Bragg peak along Q_z, the height of the particle is approximated to be about 54 nm, whereas the 253 atomic layers utilized for fitting the L_S signal of the particle (see Section 5.4.2) correspond to about 56.8 nm. These values agree well with a height of about 56 nm determined via AFM, see Figure 5.12. Note, that any lateral information on the particle gained through AFM will be the particle diameter folded with the tip size and consequently lateral information is significantly overestimated. The FWHM of the Bragg peak yields a particle height of about 60 nm which is probably larger due to the beam size. Cuts through the 3D electron density distribution (data not shown) reveal a homogeneous distribution without artefacts which would have indicated stacking of planes other than {111} planes along z. Epitaxially, the [110] in-plane axis of the particle is aligned with the substrate's [110]-direction, see supplemental material to [281]. Considering the diameter of the particle in the range of about 100 nm, this experimental result alone demonstrates impressively the power of CXDI applied to in situ, operando studies.

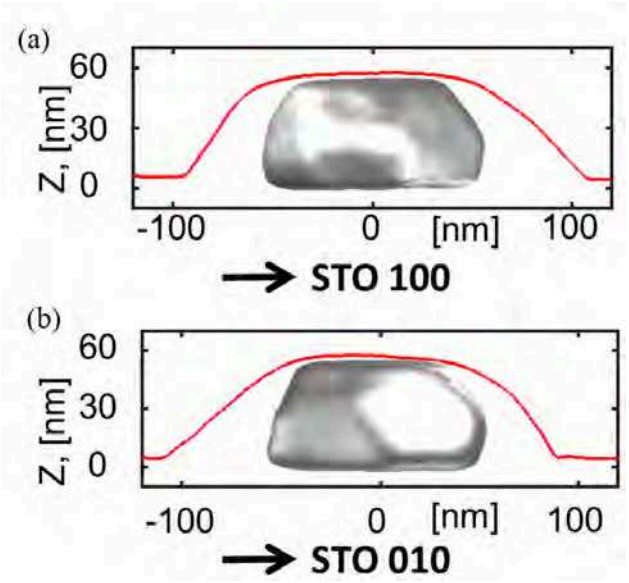

Figure 5.12.: Overlay of the reconstructed particle (side-view) and AFM measurements along (a) STO [100] and (b) STO [010] directions. The red curve shows the AFM measurements. Taken from supplemental material of [281].

In Section 4.4 it was demonstrated how drastic morphological changes of nanoparticles upon CO oxidation conditions can be. The first two rows of Figure 5.13 show top and bottom-view of the reconstructed particle throughout the gas dosing steps. If taking solely the isosurface of the particle into account, no significant changes are visible, indicating that the particle acquired its most stable state in thermodynamic equilibrium. Minor deviations of the isosurface and superficial patterns in different gas dosing steps might be attributed to the limited real space resolution or the phase retrieval process, see above. Here, the surface of the particle is defined as a cut of the electron density distribution at 55 % of its maximum value. However, by analysing the phase information, Y. Y. Kim and L. Gelisio[9] further gained displacement and strain[10] fields in the particle and on its surface. Here, this will be discussed only briefly, an elaborate discussion is presented in [281]. In addition to the real space reconstruction, rows three and four of Figure 5.13 show the superficial displacement component U_z along the z-axis projected on the isosurface (row three) and the interface (row four). Additionally, the figure shows the z-component ε_{zz} of the superficial strain field projected on the isosurface in rows five (surface) and six (interface), respectively. As the momentum transfer vector is aligned parallel to the surface normal (see sketch of the scattering geometry in Figure 5.9), only the

[9]See [281] for further contributors.
[10]Compare Section 2.1.2.

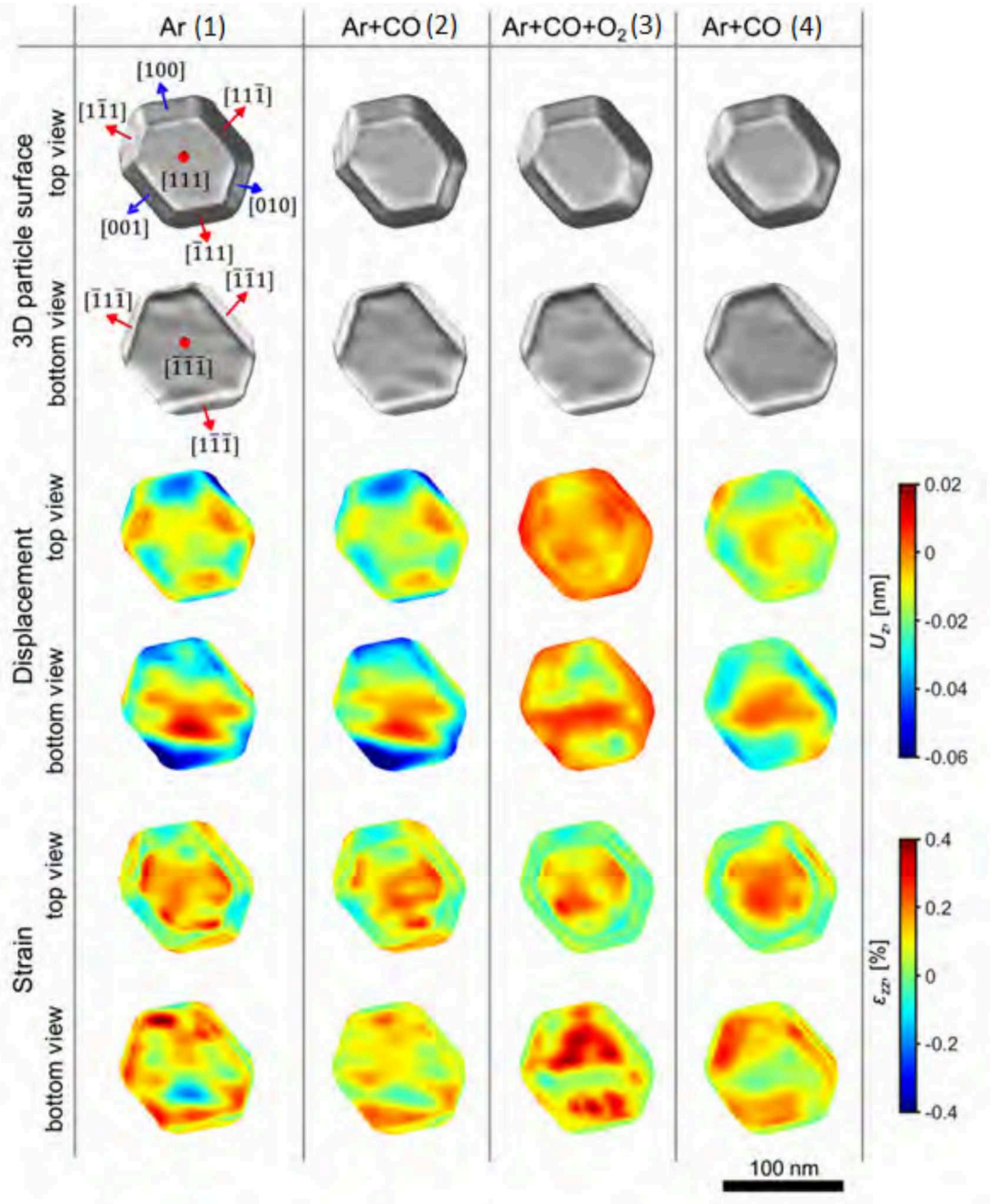

Figure 5.13.: Isosurface of the particle's electron density $|\rho(\boldsymbol{r})|$ at 55 % of its maximum value, superficial displacement U_z, and superficial strain ε_{zz} for the respective gas dosing steps (compare steps 1-4 in Table 5.1). Displacement and strain values are projected onto the isosurface. Taken from supplemental material to [281].

z-components of both displacement and strain could be recovered through phase retrieval. Both displacement and strain were calculated by averaging over voxels of the size $(3 \times 3 \times 2)\,\mathrm{nm}^3$. As the absolute offset to the phases is arbitrary, the centre of mass of the reconstructed electron density is set to zero as reference. So, all displacement and strain values refer to this zero position. Note the different zero-values of the colour bars of displacement and strain. Importantly, both the displacement and the strain field are overlays of the overall changing displacement of atoms with the elemental composition, as Rh exhibits a 3.2 % smaller atomic radius. So, segregation profiles in the alloy particle cause additional intrinsic anisotropic displacement and strain. The displacement values during both gas dosing step 1 (Ar) and step 2 (Ar + CO) are rather similar. The three edges between the (111) top facet and (111)-type side facets exhibit no significant displacement relative to the particle's bulk values. The rest of the particle's top atomic layers appears to be displaced negatively as compared to the bulk. On the bottom of the particle, the displacement values differ significantly across the bottom facet, likely due to the small tilt between particle and substrate and a resulting varying distance between the bottom facet and the substrate and hence spatially varying interfacial forces between particle and substrate, together with interfacial lattice mismatch. In CO oxidizing conditions, the displacement on the particle's surface and interface change significantly from rather negative displacement (especially of the top facet) to an overall relaxation of the top atomic layers (compare zero-position of the colour scale). During subsequent reducing conditions (step 4), the changes from step 2 to step 3 are not fully reverted indicating that the gas dosing cycle is not fully reversible. Likewise, for gas dosing steps 1 and 2, the superficial strain fields are rather similar. In step 2, the strain values are decreased compared to pure Argon dosing. Generally, carbon monoxide dosing does not significantly inflict strain to the surface due to the low interaction of CO and the surface under these environmental conditions – compare Section 2.3. Upon CO oxidation condition (step 3) and subsequent switching to reducing conditions (step 4), the strain values of the (111) top facet seem not to change significantly, whereas the (111)-type side facets undergo inward relaxation under oxidizing conditions which does not fully revert under reducing conditions in step 4. Strain values averaged across each respective facet support these observations, compare Figure C.9 in the Appendix. Accompanying DFT calculations of surface energies considering segregation and adsorption, and corresponding strain profiles lead to the intrinsic segregation profiles of the facets [281]. Under argon and reducing conditions, the DFT calculations confirm a platinum surface termination

of the particle on both (111) and (100)-type facets, in line with findings by other authors [86, 267, 271]. However, the higher affinity of rhodium towards oxygen might cause a rhodium enrichment on the surface upon CO oxidation, as the surface energy of a rhodium terminated particle decreases for an oxygen covered surface compared to platinum termination [277, 307]. The strain relieve on all particle facets during CO oxidation conditions points toward a superficial rhodium enrichment. DFT calculations together with the experimental findings favour a 100 % rhodium termination of (100)-type side facets and the top facet. (111)-type side facets might exhibit a concentration of 50:50 [281]. Further, *Kim et al.* exclude the formation of a rhodium oxide layer (O-Rh-O trilayer, see Section 4.4) under oxidizing conditions in step 3. Overall, the energetically favoured platinum termination is not re-established in subsequent reducing conditions of step 4. Throughout all gas dosing steps, the bottom facet exhibits a far broader strain value distribution which likely originates from interfacial lattice mismatch, see [281] for an elaborate discussion.
As indicated above, the spatial resolution of the reconstructed electron density is limited and the strain values offer limited information on the atomic scale composition of the surface. Accordingly, the recorded scattered signal is analysed further in the following section.

5.4.2. Analysis of line scans along L_S

The phase retrieval and reconstruction of the particle's electron density during the CO oxidation experiment delivered an impressive insight into the particle's shape and the correlated strain field, together with an outlook on future experimental tools for in situ, operando studies. Nonetheless, a SXRD experiment offers more valuable information on the atomically resolved surface composition.
Figure 5.14 shows cutting planes along Q_z and high-symmetry planes I-III in Figure 5.10 (b) for each gas dosing step – compare Table 5.1 for details. The respective images are cuts[11] through reciprocal space showing the colour-coded intensity on logarithmic scale. Additionally, the theoretical position of (111) and (100)-type facet signals are indicated as grey straight and grey dotted lines, respectively. Disruptions with zero intensity perpendicular to the Q_z-axis at about $Q_z = -0.7\,\mathrm{nm}^{-1}$, at $0.35\,\mathrm{nm}^{-1}$, and at about $1.1\,\mathrm{nm}^{-1}$ arise due to dead areas in between detector chips. Additionally, the misalignment of the particle's L_S signal[12] and the Q_z-axis

[11] The intensity distribution of the cuts was calculated by applying the *interp2* function implemented in *Matlab* to the regularly gridded 3D dataset gained from the original diffraction dataset.
[12] Compare Section 2.4.1.

defined by the surface normal promotes the tilt of the particle with respect towards the substrate's surface as already indicated by the divergence of the substrate's CTR and the Bragg peak position – compare Figure 5.10. In all cuts, signals that can be associated with (111)-type facets are clearly visible with accompanying Laue-fringes, whereas scattered signal from (100)-type facets is weak and diffuse. In regard to the real space image reconstructed through CXDI in Figure 5.11, this can be associated with the size of the respective facets, as the (111)-type facets are comparably large and the (100)-type facets small. Especially (100)-type facets at the bottom of the particle appear non-existent in the real space reconstruction.

Especially in contrast to the real space reconstructed images in Figure 5.13, the reciprocal space cuts exhibit significant differences throughout the gas dosing steps. Neglecting the L_S rod for the moment, the facet signal (in terms of intensity of the Laue fringes) increases when changing from Ar to reducing conditions (Ar + CO, step 2) for all cuts I-III. Remarkably, facet signal by (100)-type facets is very faint and diffuse and signal arising from (111)-type facets seems to be shifted along Q_z. This changes when switching to stoichiometric CO oxidation conditions step 3: in all cuts, (111)-type signal is shifted towards the theoretically expected position and especially for (100)-type signal, fringes are significantly more pronounced and less diffuse. Exemplarily, the diffuse signal in cut (I) at negative Q_{inplane} values for $Q_z = 0.2\,\mathrm{nm}^{-1}$ changes from a diffuse, dot-like structure in step 2 to distinguishable fringes in step 3. Upon returning to reducing conditions in step 4, the Bragg peak undergoes a somewhat reversible process back to an intensity distribution which is an intermediate between the distributions of steps 2 and 3. Facet signal appears to be more pronounced and well-ordered as in step 2, but is decreased compared to CO oxidation conditions of step 3. However, assigning features of the Bragg peak intensity distribution to certain, small features of the particle proves hard and not feasible in the frame of this thesis. Yet, Figure 5.14 emphasizes the sensitivity of X-rays towards features on the nanoscale and the power of single-particle scattering using coherent X-ray diffraction.

Exemplarily, Figure 5.15 shows a comparison of plane II in the theoretical scattering pattern by the reconstructed particle (a) and the experimental data (b), both in argon atmosphere (gas dosing step 1). The theoretical scattering pattern is displayed as the modulus squared of the Fourier-transformed electron density $|[\mathrm{FFT}(\rho(\boldsymbol{r}))]|^2$. For both images (a) and (b), the colour bar displays the intensity in logarithmic scale in arbitrary units. Similar to Figure 5.14, the theoretical position of facet signals is indicated with grey straight or dotted lines. Notably, the theoretical pattern does

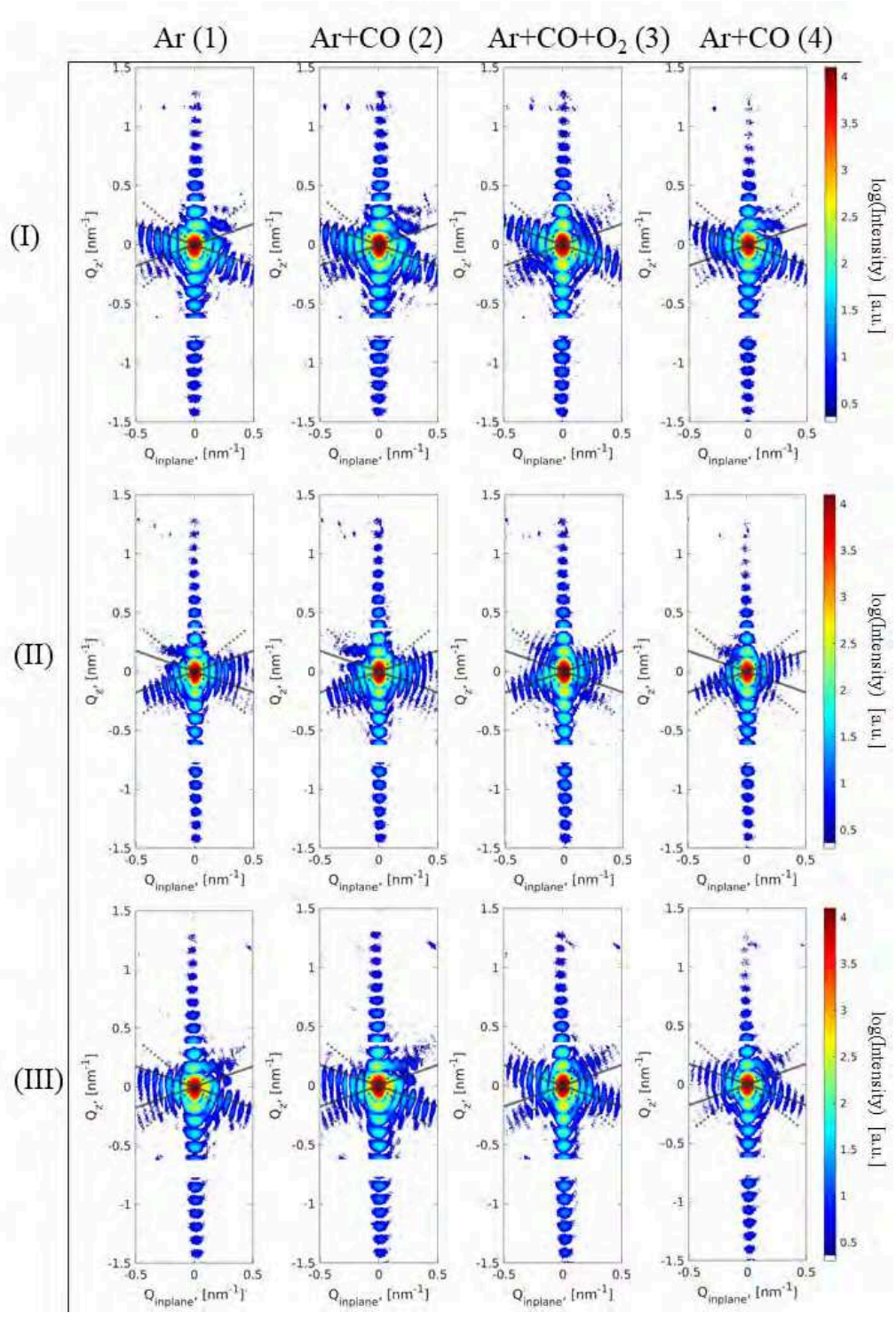

Figure 5.14.: Cuts along high-symmetry planes of the (111) Bragg peak in Figure 5.10. Roman numbers refer to planes indicated in 5.10 (b), Arabic numbers for the gas dosing steps refer to Table 5.1. Dotted grey lines indicate theoretical directions of (100)-type facet signal, straight grey lines indicate theoretical directions of (111)-type facet signal.

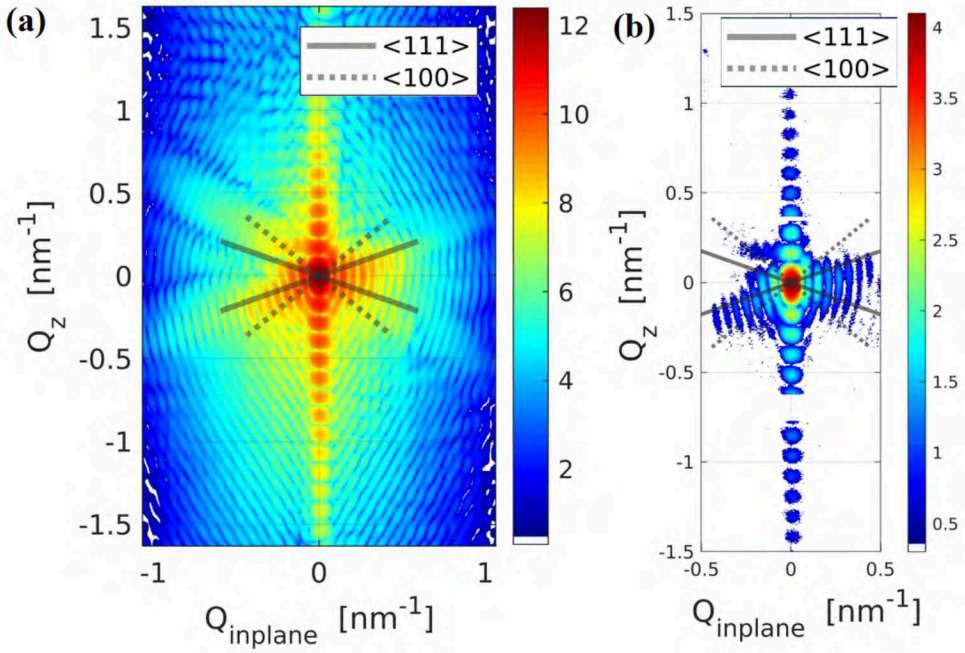

Figure 5.15.: Comparison of plane II of the (111) Bragg peak of the particle in argon atmosphere, compare Figure 5.10 (b). Here, (a) shows plane II through the theoretical diffraction pattern of the reconstructed particle as $|[\mathrm{FFT}(\rho(\boldsymbol{r}))]|^2$ and (b) shows the equivalent cut II through reciprocal space as recorded during the experiment. The colour bar is logarithmic intensity in arbitrary units.

reproduce distinctive features of the original diffraction pattern, such as the (111) facet signal shifted towards negative Q_z-values and the feature at $Q_z = 0.2\,\mathrm{nm}^{-1}$ and negative in-plane values. Very similar to the pattern evolution in Figure 5.14, these features vanish upon exposure to CO oxidation conditions (corresponding data not shown here). Consequently and in addition to Section 5.4.1, these features are attributed to the changing strain states of the particle.

However, the Bragg peak investigated here was recorded in a specular scattering geometry (compare sketch of the scattering geometry in Figure 5.9) and hence further analysis of the 3D intensity data set was focussed on the particle's L_S rod signal, i.e. the intensity parallel to the surface normal of the particle. To gain this, the L_S rod intensity was extracted from plane III in Figure 5.14 by applying the *improfile* function (bicubic interpolation along a line in gridded 2D data)[13] in *Matlab* and considering the tilt of the particle's L_S rod to the substrate's surface normal, compare Figure C.8 in the Appendix. Figure 5.16 shows the extracted intensities for the four gas dosing steps in surface coordinates. All curves have been normalized to $I_{max} = 1$ and shifted with respect to each other for clarity. Areas in the plot with straight slope (e.g. at around $L_S = 2.925\,\mathrm{r.l.u.}$) are sections where the intensity is zero[14], as these are positions of the detector's dead areas between detector chips. Overall, the progression of the plots is very similar. The Bragg peak's centre is set to $L_S = 3\,\mathrm{r.l.u.}$ and accompanying Laue fringes are visible. As described in Section 2.4.2, the Laue fringes' maxima compose the enveloping CTR. The envelope is asymmetric, its slope being more steep towards increasing L_S values for $L_S > 3\,\mathrm{r.l.u.}$ which is true for all curves. As the deviations between the curves are overall small, they cannot be clearly correlated to e.g. a changing segregation profile or strain state of the particle. Equally, differences could be correlated to small variations in setup alignment (thermal drift of the particle, repositioning in between gas dosing steps), beginning decomposition of the particle, data treatment (choice of slices/endpoints and interpolation steps) or temporal fluctuations of the beam. Due to these uncertainties, further analysis was focussed on the dataset recorded during argon dosing.
To analyse the L_S rod, the program *Rod* was applied [209]. This program basically calculates structure factors of a given (surface) structure. For the calculation, it employs several parameters (among others):

[13] Note, that in the course of the data treatment, the dataset was already undergoing two linear interpolations and consequently, the error on the intensity is increased.
[14] In these datasets, data points with zero intensity have been removed and consequently, the straight line is just a connection between data points.

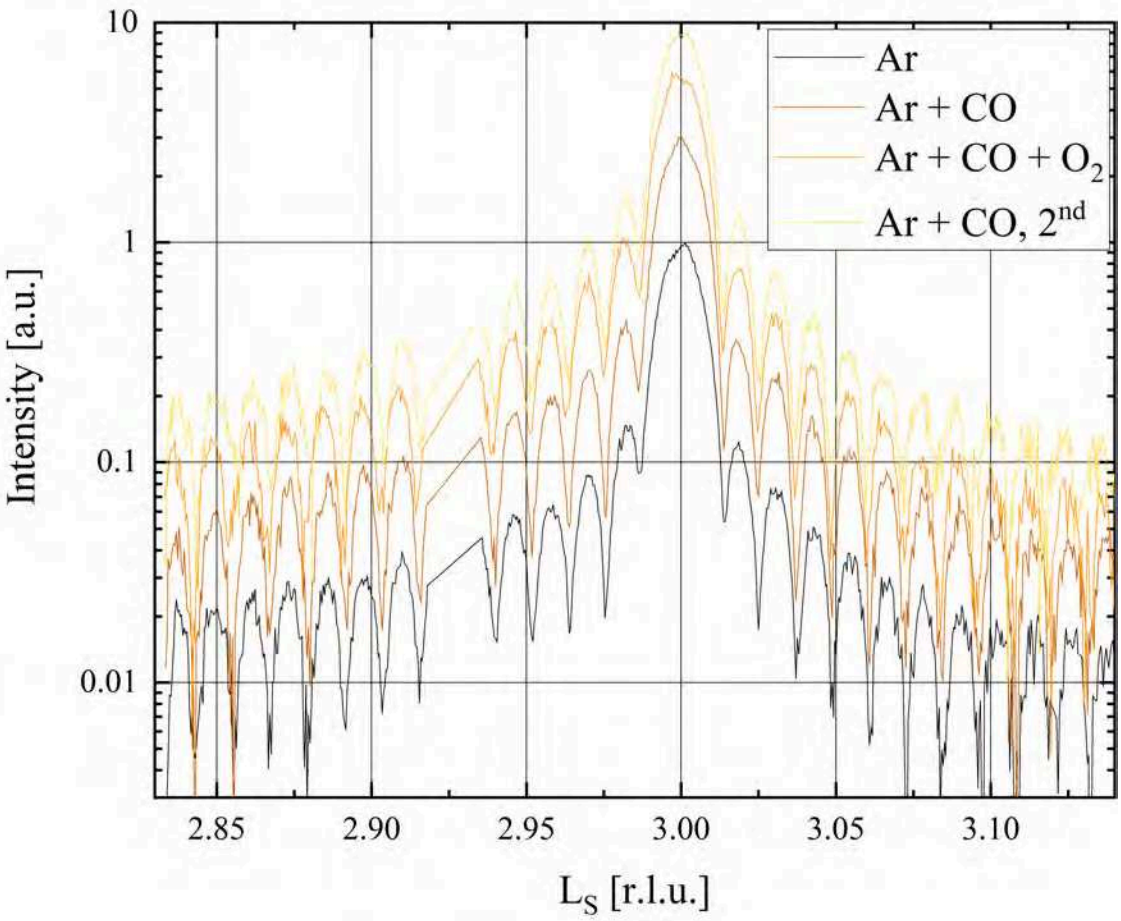

Figure 5.16.: Intensity along the particle's L_S rod for gas dosing steps 1-4. Intensity was normalized and shifted for clarity.

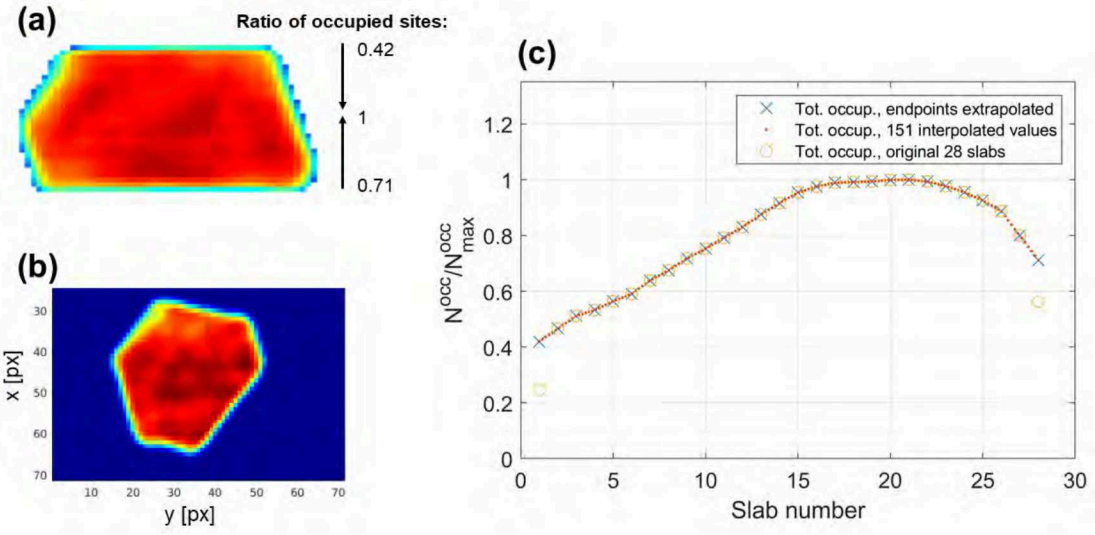

Figure 5.17.: Illustration of occupancy values: (a) x-z and (b) y-x profiles through the 3D electron density distribution of the reconstructed particle, and (c) normalized total occupancy N^{occ} values per slab for further processing in *Rod* surface files to represent the 3D electronic density distribution of the reconstructed particle. Low slab numbers in (c) correspond to the surface, high numbers to the interface. The slab with the highest lateral extension is set to a normalized occupancy value of 1. See text for explanation.

- A (surface) unit cell given in surface coordinates,
- elemental composition,
- occupancy, denoting by which fraction specific positions in the lattice are occupied by the specified element, and
- displacement, denoting by which amount specific positions in the lattice are displaced with regard to the defined structure.

The structure generated in *Rod* is generally composed out of a surface unit cell and a bulk unit cell[15]. The surface cell is duplicated in-plane quasi infinitely and has a given number of atomic planes along z-direction, whereas the bulk cell is duplicated to compose a semi-infinite substrate. For modelling the L_S signal gained from the experimental data, only a surface cell was generated, as the bulk signal does not overlay the particle's Bragg peak in this case. By fitting the absolute intensity of the theoretical diffraction signal (basically the structure factor squared) to the diffraction signal gained from the experiment, the constructed structure in *Rod* is simulated to match limited particle size. Note, that the shape of the intensity distribution of the

[15]Further models for molecules and fluids e.g. can be implemented.

L_S rod does solely depend on the particle's structure along z, which is important for this chapter – compare Section 2.4.2. The absolute intensity however, is irrelevant here. As the atomic structure along z does significantly alter the diffracted signal, the number of contributing scatterers per layer might be a relevant factor to be implemented. This is modelled by an occupancy parameter indicating the number of scatterers per layer N^{occ} normalized by the maximum number of scatterers per layer N^{occ}_{max}. From the distance between Bragg fringes a particle height of about 56 nm can be derived (see Section 5.4.1), which corresponds to 251 atomic layers. The reconstructed 3D electron density distribution however, exhibits 28 slabs along z (i.e. about 9 atoms per slab), which is illustrated in Figure 5.17 (a). It shows a x-z profile through the centre of the reconstructed electron density distribution and the limited resolution is visible. The slab with the highest number of occupied sites – so, the slab with the highest lateral extension – is depicted in Figure 5.17 (b) as profile through the particle's centre along y and x. The threshold for a pixel to be counted as belonging to the particle was 70 % of the maximum electron density per pixel. As a model with several slabs at the surface each with a height of about 2 nm would significantly alter the simulated diffraction signal, the occupancy values were interpolated resulting in a finer step size in the model along z, see Figure 5.17 (c). Further, to implement a mostly homogeneous distribution of platinum and rhodium within the particle, two overlaying unit cells with identical atomic positions are generated, where only the associated occupancy parameters n^{occ} differ. Generally, the relation $N^{occ}/N^{occ}_{max} = n^{occ}_{Pt} + n^{occ}_{Rh}$ holds. To circumvent a blurred-out surface and interface region, the occupancy values for the first and the last slab (i.e. the first and last 9 atomic layers) are extrapolated from the two neighbouring slabs inside the particle, see both the curves indicated with dots and circles in Figure 5.17 (c). Hence, an atomically sharp surface/interface is simulated[16]. The *Rod* version *1.6 standard* employed for this thesis allows for a maximum of 301 occupancy values. The ideal model would employ 502 occupancy values, as it is would need occupancy values for 251 platinum layers and 251 rhodium layers. Yet, tests have shown that inside the particle a layer-resolved occupancy parameter does not significantly alter the fitting result: generated structure factors for 150, 200, 250, and 300 employed occupancy values are quasi identical (tested for a platinum only model, data not shown). An advantage of the chosen model with two overlaying structure models with own occupancy parameters is that segregation profiles can be implemented easily by adapting the elemental ratio of the occupancy values.

[16]See brief discussion of Figure C.18 below.

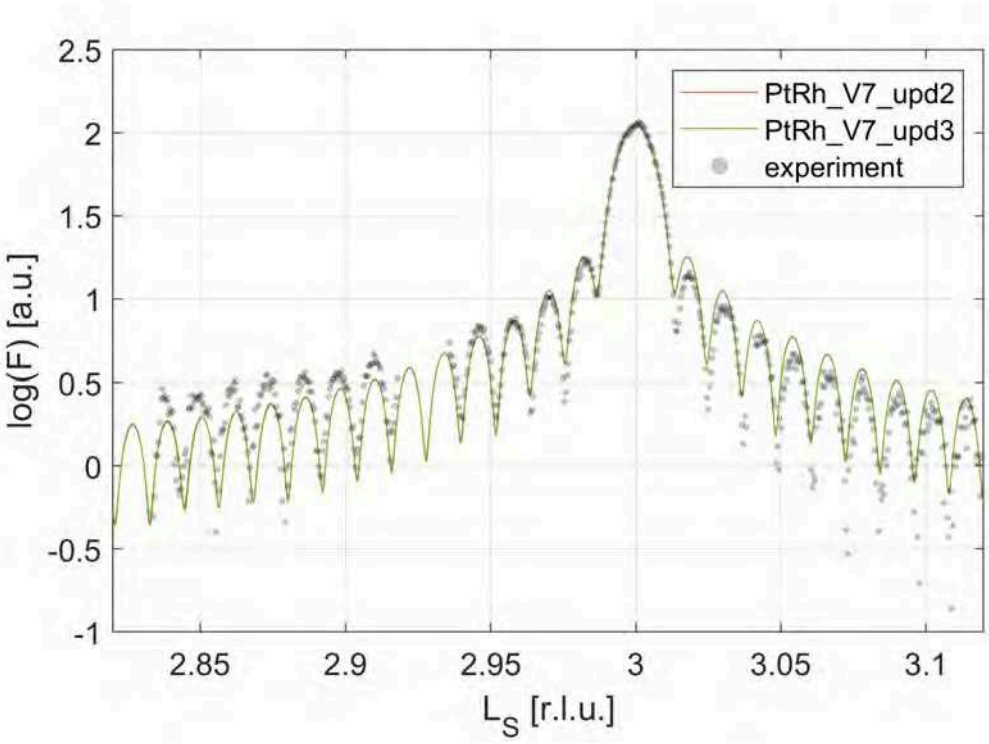

Figure 5.18.: Structure factors F from two models without segregation in topmost four layers (*upd2*, red straight line) and with segregation (*upd3*, green straight line), and experiment ($F = \sqrt{I}$, grey circles). See text for explanation.

In total, about 280 models with different particle shapes, segregation profiles, displaced layers at surface and interface e.g. were tested. Mostly, fitting was not undertaken, as the algorithm tended to find solutions for the structure factor with unreasonable or unphysical structures. This is partially due to the minima of the Laue fringes being not possible to be properly fitted with the models generated, for unknown reason. Further, larger gaps without data points (e.g. around $L_S = 2.92$ r.l.u.) enabled convergence of unphysical structures, as there are no data points to prevent the fitting algorithm from diverging from a proper solution. Possibly, fitting the envelope could have yielded better fitting results. In the following, model names are shortened from e.g. *PtRh_V7_upd1* to *upd1*.

Figure C.18 in the Appendix exemplarily shows a comparison of a bulk model *upd152* (with a height of about 56 nm) and two models (*upd1* and *upd2*) with the particle's electron density profile implemented in the occupancy parameters, whereas model *upd2* additionally exhibits an extrapolated surface. Especially for the first Laue-fringes next to the Bragg peak the bulk model deviates significantly from the data from the experiment. Additionally, an extrapolated surface significantly

improves the calculated structure factor with respect to the experiment. This justifies the implementation of both the particle's electron density profile in the occupancy parameters and the implementation of extrapolated surfaces for models presented in the following.

A first result of the tested models is that the structure factor is not significantly altered upon implementation of segregation profiles – at least in the recorded range of data. Figure 5.18 shows structure factors of two models *upd2* (red) and *upd3* (green) generated using *Rod* together with the L_S rod as $\sqrt{I}$ from the experiment (grey circles, dataset step 1 with argon atmosphere). As stated above, the two models were generated with occupancy parameters resembling the shape of the particle. In model *upd2*, the elemental composition is $Pt_{58}Rh_{42}$ for all layers. Model *upd3* is identical with exception of the first four layers, where a concentration profile as determined in the publication by *Yuge et al.* is implemented [85]: 97 %, 25 %, 65 %, and 45 % Pt concentration from topmost layer to fourth layer. No displaced layers are implemented. The structure factors from the two models do not deviate significantly from each other, hence the difference in electron density of the two elements is too low to display significant changes of the L_S rod within the range of L_S covered by the experiment. Differences become significant only in the region between Bragg peaks where the L_S rods display maximum sensitivity to changes in the surface area, compare Figure C.16 in the Appendix. There, the two models *upd2* and *upd3* are displayed till $L_S = 4.5$ [r.l.u.]. Apart, both models already fit the experimental data quite well. The asymmetry in intensity starting from the first Laue fringes next to the Bragg peak's centre at $L_S = 3$ [r.l.u.] is covered only partially from these two models. Remarkably, some Laue fringes of the models fit the data almost perfectly in both position (L_S) and value (structure factor), but others differ significantly – in either position and value, pointing towards a more complex underlying structure. Furthermore, deviations could be related to fluctuations during the experiment (beam intensity, stage etc.). To further adapt the models to the data, displaced layers were added in the next step.

To illustrate the effect of few displaced atomic layers on the structure factor, Figure 5.19 shows the data obtained during gas dosing step 1 (argon only) of the experiment (grey dots) together with three different models generated with *Rod*: model *upd2* (no displacement, straight red line), *upd37* (exponentially decreasing expansion, green straight line), and *upd57* (exponentially decreasing contraction, purple straight line). For the latter two models, five exponentially displaced layers were implemented at the top facet of the particle, where the topmost layer is displaced most and displacement

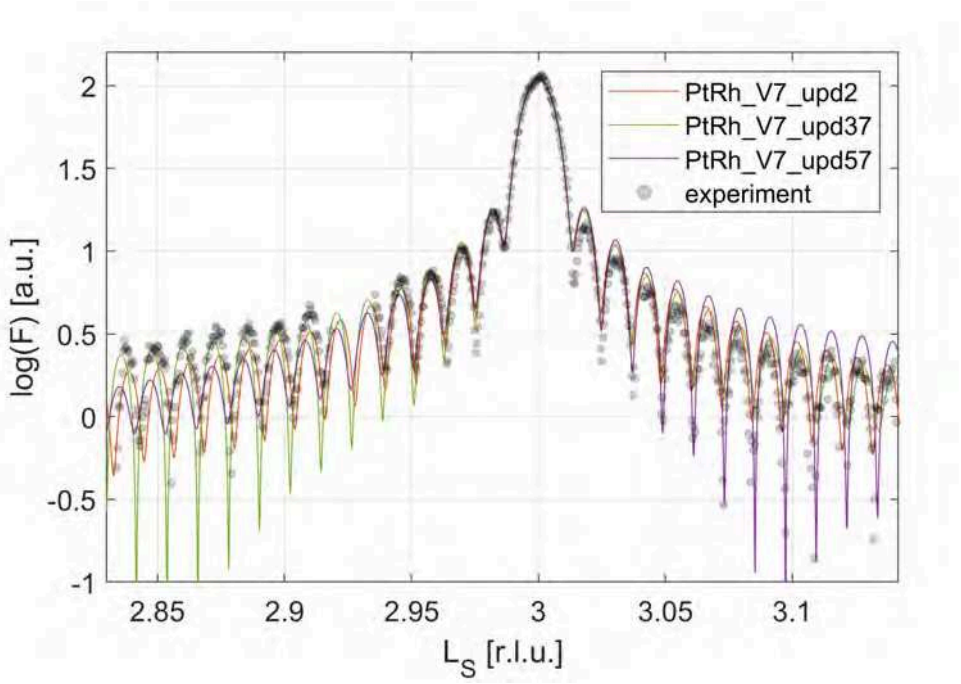

Figure 5.19.: Structure factors F from three models with varying displacement profiles of top five layers: no displacement (*upd2*, red straight line), +0.1 maximum displacement (*upd37*, green straight line), and -0.06 maximum displacement (*upd57*, purple straight line). Data from experiment ($F = \sqrt{I}$, grey circles) is added for comparison. See text for further explanation.

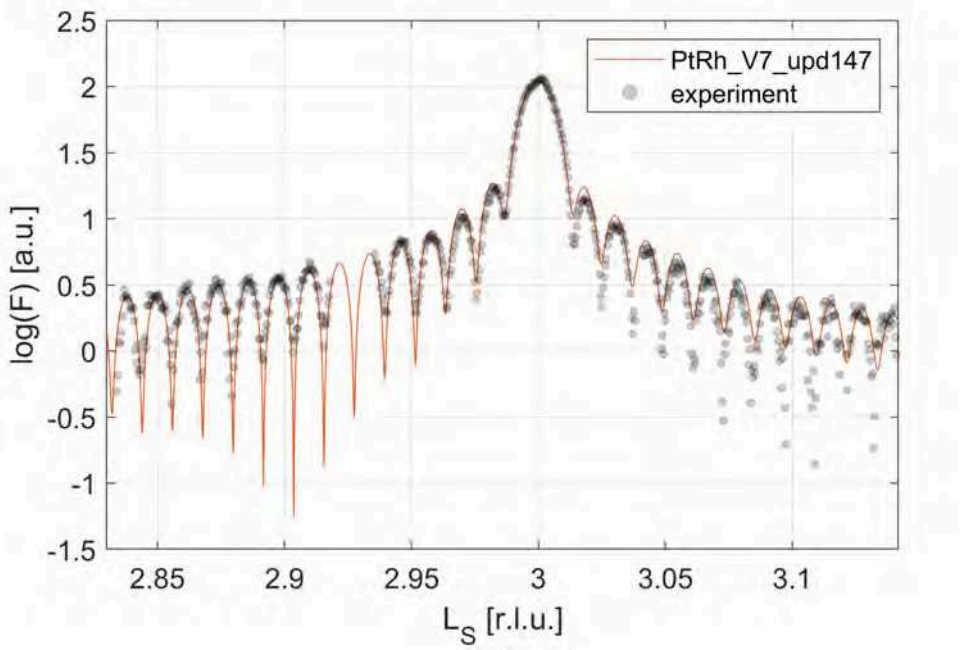

Figure 5.20.: Structure factors F from the best model obtained (red straight line) and data ($F = \sqrt{I}$) recorded in argon (gas dosing step 1), see text for further explanation.

values for subsequent layers decrease exponentially with the sixth layer exhibiting no displacement[17]. For model *upd37*, the first layer is outwardly displaced 0.1 times the size of the chosen unit cell along z (here: $a_3 = 6.7349\,\text{Å}$), which in turn holds three atomic layers. Accordingly, the value 0.1 corresponds to 30 % displacement with respect to the distance between two atomic layers. The average value for 5 layers is about 16.5 %. Similarly, for model *upd57* the first layer is the most contracted (-18 %), with the average over 5 layers being about -10.0 %. As depicted in Figure 5.19, displacement slightly changes the position of the Laue fringes further away from the Bragg peak as the number of coherently scattering atomic layers is decreased. Further, positive displacement (model *upd37*) slightly increases the intensity of the Laue fringes below the Bragg peak at 3 r.l.u. compared to model *upd2* without displacement and decreases it above the Bragg peak. Contrary, contracted layers (model *upd57*) slightly decrease the intensity below the Bragg peak and increase it above it compared to the model without displacement. Further, the intensity of the local minima varies significantly. Similar behaviour was investigated for displacement of the bottom facet at the interface towards the substrate. However, this behaviour is systematic only upon small changes of displacement and strongly depends on the structure of the surface, and consequently a large number of different structures had do be studied to find the best solution.

By combining displacement profiles at top and bottom facet, many models were found which fits the maxima of the Laue fringes very well. Exemplarily, Figure 5.20 shows model *upd147* exhibiting an excellent overlap with the envelope of the data gained from the experiment (step 1 in argon). For this model, the originally 251 atomic layers were replaced with 253 to compensate for the shift of the Laue fringes due to displacement. For this model, no displaced layers at the bottom interface were implemented as this would always lead to more deviation from the original data. For the top facet, four layers with displacement values 0.04, 0.04, 0.04, and 0.03 from the top towards the bulk were configured. Here, 0.04 corresponds to about 0.27 Å, i.e. about 12 % expansion compared to the original position of the respective atomic layer, see Figure 5.21. Note, that the values are given with respect to the non-displaced, original position of each single layer and are accumulated for the *Rod* model[18]. So, basically model *upd147* represents a surface structure where the

[17] As stated here, *exponentially decreasing* refers to a displacement profile where the utmost layer is displaced more than the second layer (etc.). The modulus of displacement is decreasing towards the bulk. Importantly, the exponential values are set for the distance between two layers. Consequently, the absolute displacement values with regard to each atomic layer's original position accumulate towards the surface.

[18] Displacement of the fourth layer inherently displaces the third layer, hence the displacement

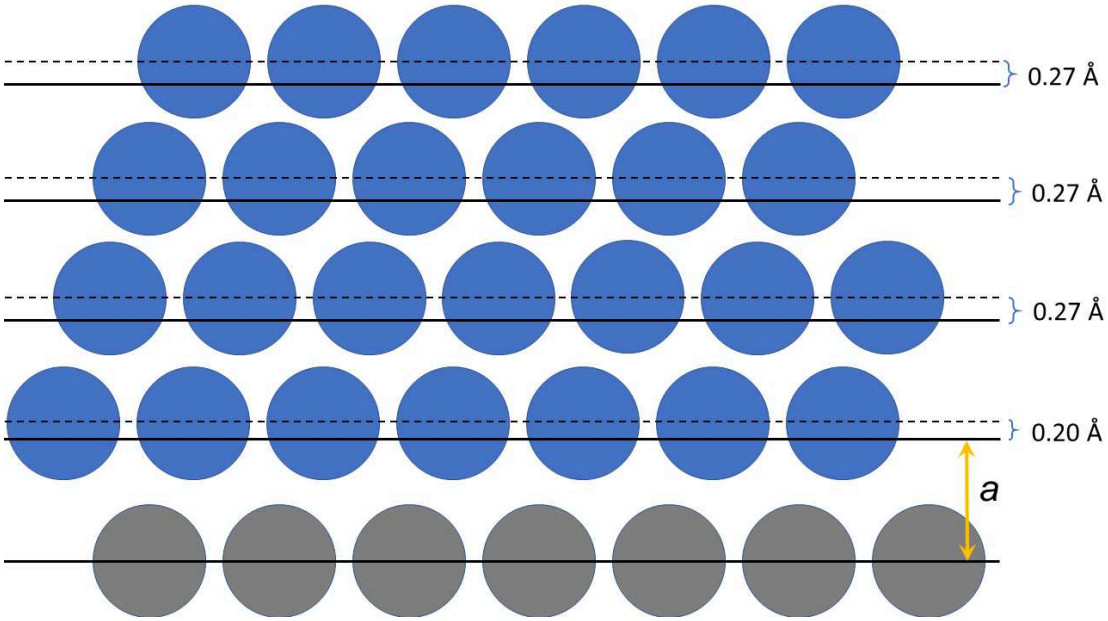

Figure 5.21.: Schematic sketch of the surface profile in *Rod* model 147. Straight black lines denote original atomic positions with $a = a_3/3$, dotted black lines denote the displaced position of the atomic layers.

surface is lifted from the particle, as the three topmost layers maintain their relative distance, compare Figure 5.21.

Notably, none of the 280 different models generated was able to properly describe the different intensities of the first Laue fringes right below and above the Bragg peak which exhibit different intensities. Additionally, the strongly varying intensity of the local minima could not be modulated. Possibly, the implemented model representing the electron density distribution still deviates from the real particle. Moreover, the data recorded during the experiment is limited to the Q-space right around the Bragg peak, where the surface contribution to the recorded diffraction signal is rather small. A comparison to displacement values in Figure 5.13 emphasizes the problem that the displacement likely varies across the facets, hampering a comparison. Additionally, the displacement values given in the figure are averaged across the first 9 atomic layers, hence the detailed structure of the surface is not known. Models with 9 displaced atomic layers (optionally for both top and bottom facet) did non coincide as good with the data from the experiment as models with fewer displaced layers. Generally, the implemented displacement in model *upd147* deviates from the displacement from the reconstructed particle in Figure 5.13 where an overall negative displacement is determined for the nine atomic layers of both top and bottom facet

values have to be accumulated for all layers above the first displaced layer.

(step 1). Structure factors from models with negative displacement for either top facet, bottom facet, or both facets generally did not coincide as good with the data from the experiment as those structure factors from models with exclusively positive displacement (tested using about 60 different models, data not shown). Another general observation is that models with a top layer displaced by the same amount as that in model *upd147* but an exponentially decreasing profile for the subsequent layers do not agree as good with the data as models with an abrupt step between bulk and displaced surface area (like *upd147*). Exemplarily, Figure C.17 in the Appendix shows structure factors for model *upd147* and a model with exponentially decreasing displacement for the top four layers.

The core result of modelling the structure factor using *Rod* is that the most probable structure exhibits few displaced layers (four to five), each of which are displaced at least 0.2 Å (i.e. about 9 %) from their original position, respectively. Thus, a model is favoured where only the fourth or fifth atomic layer is significantly displaced, whereas the layers above maintain their relative distance to each other.

Generally, outward relaxation of few atomic layers at the top of the particle is in line with findings by other authors, despite the fact that the surface structure of Pt(111) is still under debate, compare [308, 309]. If outward relaxation is predicted, the displacement is found to be of few percent – in contrast to findings obtained here. The high amount of displacement could indicate a surface reconstruction which is not in line with SXRD studies by other authors who do not find surface reconstructions of Pt(111) for similar conditions of the experiment presented here [310, 311].

Further tests have shown that small modulations in intensity of the data might be possible to modulate with alternating displacements, where e.g. the sign switches for subsequent layers. Strain analysis and DFT calculations from *Kim et al.* (see discussion of Figure 5.13) suggest that the displacement profile likely is not a uniformly continuous, exponentially decreasing profile, as they find the sign of the strain to be switching at the second layer [281]. However, such profiles are hard to obtain without proper fitting due to the given numbers of parameters, here. Consequently, this was not investigated any further in this work. As partially discussed already, the recorded range of the data does only allow for a very limited insight in the displacement at the surfaces of the particle and especially in the segregation profile. From the three models with different displacements depicted in Figure 5.19, it can be derived that small changes in displacement of few layers have a direct impact on the structure factor. The L_S rod data employed here is the result of several averaging and extraction steps which cause an inherently large error on the intensity which is

increasing with distance from the Bragg peak. Hence, the data treatment and the choice of endpoints for the line profiles have a direct impact on the analysis presented here. Additionally, the electron density profile employed for a proper modulation of the particle's shape does significantly influence the structure factor generated using *Rod*. Accordingly, deviations from surface structures as presented in other publications might be attributed to these influences. The weight of these arguments can be decreased in future experiments by covering the data range (Q-space) in between Bragg peaks. As the validity of the most favourable structure obtained is expected to be limited and treated with care, further investigation of the datasets for gas dosing steps 2, 3, and 4 was not conducted, especially as the differences along L_S between these datasets are very small, see Figure 5.16 and discussion.

In conclusion, this chapter demonstrates the feasibility and power of operando single-particle X-ray diffraction under catalytic reaction conditions. Not only does CXDI offer recovering a real space image of the specimen investigated during a catalytic experiment, additional displacement and strain analysis holds information of both the surface and subsurface structure. Further *Rod* analysis delivers atomically precise information of the surface of the particle. Future experiments may cover different areas in reciprocal space to additionally probe in-plane information of the structures investigated and to get experimental evidence on the superficial segregation in bimetallic nanoparticles – and the formation of rhodium oxide on the surface, which is yet to be found in single-particle studies (more likely for particles with increased rhodium content). Further, the continuous development of synchrotron radiation sources and FELs enables CXDI studies on even smaller particles, thus emphasizing the role of (single-particle) XRD and accompanying analysis methods like phase retrieval especially in the field of (heterogeneous) catalysis.

Chapter 6.

Conclusion and outlook

In conclusion, this work aimed to confirm the important role of platinum and rhodium nanoparticles in the field of heterogeneous catalysis and deliver new, unreported in-situ insight in a catalyst model system. Reflecting the dominant role of both platinum and rhodium in industry-scale catalytic applications, these two materials were selected for a systematic, in-depth growth study with prior focus on platinum. As main support for the particles (0001)-terminated α-Al_2O_3 was chosen. The major aim was to demonstrate the feasibility and associated possibilities of single-particle XRD and ensemble XRD during a catalytic reaction. Not only by selecting a single PtRh particle as model system and performing single-particle XRD, the influence of catalytic reaction conditions on the catalyst itself could be demonstrated. Especially the ensemble XRD study revealed a huge impact of the environment on the catalyst material.

In a first step, the model system had to be generated using MBE. As the typical morphology of alumina supported platinum particles reported in literature was too small to apply single-particle diffraction for the corresponding analysis, the growth of platinum particles on alumina was investigated systematically. Two resulting morphologies were selected for further catalytic investigations: flat particles for ensemble XRD and a 3D particle for single-particle XRD. Deposition of 10 nm platinum in UHV at 830 °C and subsequent annealing at 1100 °C in UHV for 10 min yields the epitaxially grown, hexagonally shaped, (111)-oriented particles with a flat, rather unimodal morphology with an average height of 4 nm and an average diameter of about 20 nm. The surface coverage of the sample with these flat particles is about 40 %. Despite the high temperatures, the particles do not obtain their most favourable shape (Wulff shape) as predicted for thermodynamic equilibrium, hence the growth of platinum on alumina is assumed to be kinetically limited even at elevated temperatures. Though platinum is found to be mobile and diffusing on the

alumina surface at temperatures of above 500 °C, potential barriers possibly prevent platinum atoms from diffusing from the substrate onto particles above heights of 4 nm. 3D particles were generated by subsequent exposure of the sample to annealing in air at 1200 °C for few seconds which drastically changes the observed average morphology. Now, a growth mode with a broad size and diameter distribution is observed with many small particles and few very large particles. In contrast to annealing in UHV where on average the ratio of height to diameter was at about 0.2, the ratio now varies considerably between 0.06 and 0.82. SEM images of the same areas of the sample before and after annealing in air reveal the total rearrangement of deposited material on the substrate. This is accompanied by the average surface coverage decreasing from about 40 % to 7 %, while at the same time the average particle area increased by 7 times. After annealing in air, (001)-oriented particles are observed in addition to the (111)-oriented particles which have been demonstrated upon annealing in UHV. Importantly, after annealing in air some particles exhibit a macroscopic 3D shape close to the ideal truncated Wulff shape and suitable for CXDI studies. The transformation is attributed to the formation of volatile, metastable PtO_x species forming at elevated temperatures and access to oxygen, which overcome kinetic barriers at particle borders, thus enabling 3D growth. An extensive influence of the substrate on the transformation seems unlikely, but cannot clearly be ruled out.

In the next step, a sample with alumina supported $Pt_{85}Rh_{15}$ nanoparticles was created following the recipe stated above for particles with a flat morphology. The addition of rhodium did non significantly alter the morphology of the particles. Purpose of this sample was to monitor changes of the particle morphology by ensemble XRD upon exposure to catalytic CO oxidation reaction conditions. Two experiments were conducted (at 370 °C with a stoichiometric ratio of O_2 and CO, and at 450 °C with an over-stoichiometric ratio) using a catalysis reactor with a beryllium dome which is nearly transparent to X-rays, enabling operando, in-situ characterization of the nanoparticles. The gas environment was controlled and monitored using a gas flow system with a mass spectrometer installed downstream of the reactor. The experiments were conducted at 0.1 bar pressure inside the reactor and 50 $\frac{\text{ml}}{\text{min}}$ gas flow with argon as carrier gas. While the first experiment at 370 °C did not induce any significant changes on the nanoparticles, the second experiment at 450 °C revealed intra-particle mass transport for particles with large diameters which enables a transformation from a highly truncated Wulff shape, more towards a particle shape to be expected in thermodynamic equilibrium – the height increased, the diameter

decreased. Small particles were subject to this transformation, too, but did not undergo changes in morphology that were as drastic. The transformation of the particle morphology was found to be non-reversible. A sintering mechanisms widely discussed in literature for nanoparticles with diameters below 10 nm was not detected. Additionally, the formation of a superficial rhodium oxide on the (111) top facets of the particles was not observed. Likely, required criteria for the formation of rhodium oxide were not met, though it is possible that the experimental setup was not suitable for detecting the superficial rhodium oxide. In future experiments, a significantly increased rhodium content may enable observing rhodium oxide formation under oxidizing conditions.

Having proven the feasibility of operando, in-situ studies combining X-ray diffraction methods and online gas spectrometry, the final step was to conduct a single-particle diffraction experiment with synchrotron radiation. Similar to the previous catalytic study, a catalysis reactor with a beryllium dome, a gas flow system, and a mass spectrometer installed downstream of the reactor were employed. Again, the CO oxidation experiment was conducted at 0.1 bar and 50 $\frac{\text{ml}}{\text{min}}$ gas flow. The temperature was at 425 °C. Following the recipe found for 3D particle growth, the first dataset was recorded on alumina supported PtRh nanoparticles. The recorded Bragg peak was overlapping the substrate's diffraction signal, hence a dataset recorded similarly on a STO supported $Pt_{60}Rh_{40}$ backup sample was chosen for further analysis. Together with collaborating research groups, the 3D electron density distribution of the (111)-oriented particle was recovered for each respective gas dosing step via phase retrieval. Although significant shape changes were not recorded, phase retrieval allowed for gaining information on the displacement and strain fields, displaying partially reversible surface strain relief under oxidizing conditions. Analysis of the particle's L_S rod was carried out by structure factor modelling using the program *Rod* on the dataset recorded in argon only. The model showing most consistency with the dataset favours large outward displacement of the top 4-5 layers with at least 9 % expansion in the fourth or fifth layer. Again, the formation of a superficial rhodium oxide layer was not recorded which, together with the absence of significant changes of morphology, might be attributed to unknown influences by the substrate, experimental conditions unfavourable of rhodium oxide formation, limited resolution, low intensity of the beam, or the rhodium content of the sample being too low. Nonetheless, the challenging experiment yielded outstanding results which have not been reported with similar quality.

The ongoing development of X-ray sources (synchrotrons, FELs) will enable unmet

opportunities in the near future. Highly collimated beams with increased brilliance will enable catalytic studies as reported here on nanoparticles with decreased size, further meeting criteria as found in industry-scale applications. Especially in combination with thin substrates, transmission experiments become favourable which overcome the previous problem that prior to a single-particle diffraction experiment the in-plane and out-of plane orientation of the particle have to be known. Additionally, it offers the opportunities that the footprint of the beam will be its focus size (contrary to SXRD) and that a significant portion of reciprocal space can be recorded with ease. By these means, CXDI and corresponding data analysis will become a major tool of fundamental understanding in heterogeneous catalysis, revealing the role of superficial oxides on bimetallic particles and obtaining new insight the catalyst's role in reaction dynamics, thus enabling to tailor a catalyst's activity, selectivity, and lifetime.

Bibliography

[1] A. L. Lehninger, D. L. Nelson, and M. M. Cox. *Lehninger principles of biochemistry*. 3rd ed. New York: Worth Publishers, 2000. ISBN: 978-1-57259-153-0 978-0-7167-3867-1 (cit. on p. 1).

[2] B. Lindström and L. J. Pettersson. "A Brief History of Catalysis". In: *CATTECH* 7.4 (2003), pp. 130–138. ISSN: 13846566. DOI: 10.1023/A:1025001809516 (cit. on p. 1).

[3] S. Vannuzzi. *Science and Technology Roadmap on Catalysis for Europe*. White Paper. URL https://http://gecats.org/gecats_media/Science+and+Technology+Roadmap+on+Catalysis+for+Europe+2016.pdf. Accessed 23 June 2021. European Cluster on Catalysis, ERIC aisbl, October 2016, p. 128 (cit. on p. 1).

[4] Grand View Research Inc. *Catalyst Market Size & Share, Industry Report, 2020-2027*. White Paper. URL https://www.grandviewresearch.com/industry-analysis/catalyst-market. Accessed 23 June 2021. Grand View Research Inc, 2020, p. 115 (cit. on p. 1).

[5] C. H. F. Peden et al. "Kinetics of carbon monoxide oxidation by oxygen or nitric oxide on rhodium(111) and rhodium(100) single crystals". In: *The Journal of Physical Chemistry* 92.6 (1988), pp. 1563–1567. ISSN: 0022-3654. DOI: 10.1021/j100317a038 (cit. on pp. 1, 36).

[6] M. D. Ackermann et al. "Structure and Reactivity of Surface Oxides on Pt(110) during Catalytic CO Oxidation". In: *Physical Review Letters* 95.25 (2005), p. 255505. DOI: 10.1103/PhysRevLett.95.255505 (cit. on pp. 1, 36).

[7] E. M. C. Alayon et al. "On highly active partially oxidized platinum in carbon monoxide oxidation over supported platinum catalysts". In: *Journal of Catalysis* 263.2 (2009), pp. 228–238. ISSN: 0021-9517. DOI: 10.1016/j.jcat.2009.02.010 (cit. on pp. 1, 36).

[8] A. Boubnov et al. “Structure–activity relationships of Pt/Al2O3 catalysts for CO and NO oxidation at diesel exhaust conditions”. In: *Applied Catalysis B: Environmental* 126 (2012), pp. 315–325. ISSN: 0926-3373. DOI: 10.1016/j.apcatb.2012.07.029 (cit. on pp. 1, 37).

[9] M. Chen, Y. Zheng, and H. Wan. “Kinetics and Active Surfaces for CO Oxidation on Pt-Group Metals Under Oxygen Rich Conditions”. In: *Topics in Catalysis* 56.15 (2013), pp. 1299–1313. ISSN: 1572-9028. DOI: 10.1007/s11244-013-0140-0 (cit. on p. 2).

[10] L. Li et al. “Surface Tension Effects on the Reactivity of Metal Nanoparticles”. In: *The Journal of Physical Chemistry Letters* 6.19 (2015), pp. 3797–3801. DOI: 10.1021/acs.jpclett.5b01746 (cit. on p. 2).

[11] G. Hofmann et al. “Aging of a Pt/Al_2O_3 exhaust gas catalyst monitored by quasi in situ X-ray micro computed tomography”. In: *RSC Advances* 5.9 (2014), pp. 6893–6905. ISSN: 2046-2069. DOI: 10.1039/C4RA14007A (cit. on p. 2).

[12] Q. Xu et al. “The Sintering of Supported Pd Automotive Catalysts”. In: *ChemCatChem* 3.6 (2011), pp. 1004–1014. ISSN: 1867-3899. DOI: 10.1002/cctc.201000392 (cit. on p. 2).

[13] K. F. Kalz et al. “Future Challenges in Heterogeneous Catalysis: Understanding Catalysts under Dynamic Reaction Conditions”. In: *ChemCatChem* 9.1 (2017), pp. 17–29. ISSN: 18673880. DOI: 10.1002/cctc.201600996 (cit. on pp. 2, 37, 38).

[14] F. F. Tao et al. “Action of bimetallic nanocatalysts under reaction conditions and during catalysis: evolution of chemistry from high vacuum conditions to reaction conditions”. In: *Chemical Society Reviews* 41.24 (2012), pp. 7980–7993. ISSN: 1460-4744. DOI: 10.1039/C2CS35185D (cit. on pp. 2, 94).

[15] J. Frenken and I. Groot, eds. *Operando Research in Heterogeneous Catalysis*. Vol. 114. Springer Series in Chemical Physics. Cham: Springer International Publishing, 2017. ISBN: 978-3-319-44437-6 978-3-319-44439-0. DOI: 10.1007/978-3-319-44439-0 (cit. on pp. 2, 3).

[16] R. Gross and A. Marx. *Festkörperphysik*. Berlin, Boston: De Gruyter, 2018. ISBN: 978-3-11-055918-7. DOI: 10.1515/9783110559187 (cit. on pp. 5, 10, 11).

[17] H. Ibach. *Physics of Surfaces and Interfaces*. Springer Berlin Heidelberg, 2006. ISBN: 978-3-540-34709-5. DOI: 10.1007/3-540-34710-0 (cit. on pp. 5, 9, 10).

[18] I. V. Markov. *Crystal growth for beginners: fundamentals of nucleation, crystal growth and epitaxy*. 2nd ed. Singapore ; River Edge, N.J: World Scientific, 2003. ISBN: 978-981-238-245-0 (cit. on pp. 5, 13, 14, 16, 19, 24).

[19] H. Lüth. *Solid surfaces, interfaces and thin films*. 6. ed. Graduate texts in physics. OCLC: 903755941. Cham: Springer, 2015. ISBN: 978-3-319-10756-1 978-3-319-10755-4 (cit. on pp. 5–7, 9–13, 22).

[20] C. Kittel. *Introduction to solid state physics*. 8th ed. Hoboken, NJ: Wiley, 2005. ISBN: 978-0-471-41526-8 (cit. on p. 5).

[21] M. C. Desjonquères and D. Spanjaard. "Introduction to the atomic structure of surfaces: A theoretical point of view". In: *Stress and Strain in Epitaxy*. Ed. by M. Hanbücken and J.-P. Deville. Amsterdam: Elsevier, 2001, pp. 63–98. ISBN: 978-0-444-50865-2. DOI: 10.1016/B978-044450865-2/50004-0 (cit. on pp. 5, 7, 16).

[22] Chemical Rubber Company and D. R. Lide, eds. *CRC handbook of chemistry and physics: a ready-reference book of chemical and physical data*. 84th ed. OCLC: 249116497. Boca Raton: CRC Press, 2003. ISBN: 978-0-8493-0484-2 (cit. on pp. 5, 27).

[23] A. Zangwill. *Physics at surfaces*. Cambridge [Cambridgeshire] ; New York: Cambridge University Press, 1988. ISBN: 978-0-521-32147-1 978-0-521-34752-5 (cit. on p. 6).

[24] H. Ibach. "The role of surface stress in reconstruction, epitaxial growth and stabilization of mesoscopic structures". In: *Surface Science Reports* 29.5-6 (1997), pp. 195–263. ISSN: 01675729. DOI: 10.1016/S0167-5729(97)00010-1 (cit. on pp. 6, 9, 10).

[25] D. J. Bottomley and T. Ogino. "Alternative to the Shuttleworth formulation of solid surface stress". In: *Physical Review B* 63.16 (2001). ISSN: 0163-1829, 1095-3795. DOI: 10.1103/PhysRevB.63.165412 (cit. on p. 6).

[26] R. C. Cammarata. "Chapter 1: Generalized Thermodynamics of Surfaces with Applications to Small Solid Systems". In: *Solid State Physics*. Vol. 61. Elsevier, 2009, pp. 1–75. ISBN: 978-0-12-374292-6. DOI: 10.1016/S0081-1947(09)00001-0 (cit. on p. 6).

[27] W. Nolting. *Grundkurs Theoretische Physik 4/2*. Springer-Lehrbuch. Berlin, Heidelberg: Springer Berlin Heidelberg, 2016. ISBN: 978-3-662-49032-7 978-3-662-49033-4. DOI: 10.1007/978-3-662-49033-4 (cit. on p. 6).

[28] Y. Saitō. *Statistical physics of crystal growth*. River Edge, N.J: World Scientific, 1996. ISBN: 978-981-02-2834-7 (cit. on pp. 6, 13).

[29] P. Müller and R. Kern. "Some elastic effects in crystal growth". In: *Stress and Strain in Epitaxy*. Ed. by M. Hanbücken and J.-P. Deville. Amsterdam: Elsevier, 2001, pp. 3–61. ISBN: 978-0-444-50865-2. DOI: 10.1016/B978-044450865-2/50003-9 (cit. on pp. 7, 9, 16, 20).

[30] J. W. Gibbs. *The scientific papers of J. Willard Gibbs: in two volumes*. Vol. 1. New York and Bombay: Longmans, Green, and CO., 1906 (cit. on p. 7).

[31] G. Cao. *Nanostructures & nanomaterials: synthesis, properties & applications*. OCLC: ocn212610774. London ; Hackensack, NJ: Imperial College Press, 2004. ISBN: 978-1-86094-415-4 978-1-86094-480-2 (cit. on pp. 7, 13, 16, 19, 20, 37).

[32] D. Dzhigaev. "Characterization of nanowires by coherent x-ray diffractive imaging and ptychography". PhD thesis. University of Hamburg, 2017 (cit. on pp. 8, 10, 128).

[33] C. Malgrange, C. Ricolleau, and M. Schlenker. *Symmetry and Physical Properties of Crystals*. Dordrecht: Springer Netherlands, 2014. ISBN: 978-94-017-8992-9 978-94-017-8993-6. DOI: 10.1007/978-94-017-8993-6 (cit. on pp. 9, 10).

[34] R. Hentschke. *Classical Mechanics*. Undergraduate Lecture Notes in Physics. Cham: Springer International Publishing, 2017. ISBN: 978-3-319-48709-0 978-3-319-48710-6. DOI: 10.1007/978-3-319-48710-6 (cit. on p. 10).

[35] A. Maceri. *Theory of Elasticity*. Berlin, Heidelberg: Springer Berlin Heidelberg, 2010. ISBN: 978-3-642-11391-8 978-3-642-11392-5. DOI: 10.1007/978-3-642-11392-5 (cit. on p. 10).

[36] M. Reza Eslami et al. *Theory of Elasticity and Thermal Stresses: Explanations, Problems and Solutions*. Vol. 197. Solid Mechanics and Its Applications. Dordrecht: Springer Netherlands, 2013. ISBN: 978-94-007-6355-5 978-94-007-6356-2. DOI: 10.1007/978-94-007-6356-2 (cit. on p. 10).

[37] H.-J. Butt and M. Kappl. *Surface and Interfacial Forces 2e*. Weinheim, Germany: Wiley-VCH Verlag GmbH & Co. KGaA, 2018. ISBN: 978-3-527-80435-1 978-3-527-34165-8. DOI: 10.1002/9783527804351 (cit. on pp. 10–12).

[38] A. Dangwal Pandey et al. "Single orientation graphene synthesized on iridium thin films grown by molecular beam epitaxy". In: *Journal of Applied Physics* 120.7 (2016), p. 075304. ISSN: 0021-8979. DOI: 10.1063/1.4960804 (cit. on p. 10).

[39] N. Seriani and F. Mittendorfer. "Platinum-group and noble metals under oxidizing conditions". In: *Journal of Physics: Condensed Matter* 20.18 (2008), p. 184023. ISSN: 0953-8984, 1361-648X. DOI: 10.1088/0953-8984/20/18/184023 (cit. on pp. 10, 12).

[40] E. A. Wood. "Vocabulary of Surface Crystallography". In: *Journal of Applied Physics* 35.4 (1964), pp. 1306–1312. ISSN: 0021-8979, 1089-7550. DOI: 10.1063/1.1713610 (cit. on p. 11).

[41] U. Hejral. "Operando Characterization of Supported Alloy Nanoparticles during Catalytic CO Oxidation by Surface Sensitive X-Ray Diffraction". PhD thesis. University of Hamburg, 2015 (cit. on pp. 12, 14, 23, 35, 36, 38, 50, 52, 53, 94, 114, 115).

[42] A. W. Adamson. *Physical chemistry of surfaces*. 5th ed. New York: Wiley, 1990. ISBN: 978-0-471-61019-9 (cit. on p. 13).

[43] M. Hÿtch. "Measurement of displacement and strain by high-resolution transmission electron microscopy". In: *Stress and Strain in Epitaxy*. Elsevier, 2001, pp. 201–219. ISBN: 978-0-444-50865-2. DOI: 10.1016/B978-044450865-2/50010-6 (cit. on p. 12).

[44] B. Gilles. "Strain measurement in ultra-thin films using RHEED and X-ray techniques". In: *Stress and Strain in Epitaxy*. Elsevier, 2001, pp. 173–200. ISBN: 978-0-444-50865-2. DOI: 10.1016/B978-044450865-2/50009-X (cit. on p. 12).

[45] D. Sander. "Stress measurements of atomic layers and at surfaces". In: *Stress and Strain in Epitaxy*. Elsevier, 2001, pp. 221–242. ISBN: 978-0-444-50865-2. DOI: 10.1016/B978-044450865-2/50011-8 (cit. on p. 12).

[46] F. Bechstedt. *Principles of Surface Physics*. OCLC: 725022955. Berlin, Heidelberg: Springer Berlin Heidelberg, 2003. ISBN: 978-3-642-55466-7 (cit. on p. 12).

[47] G. Y. V. Wulff. "Zur Frage der Geschwindigkeit des Wachstums und der Auflösung von Krystallflächen". In: *Zeitschrift für Krystallographie und Mineralogie* 34 (1901), pp. 449–530 (cit. on p. 13).

[48] P. M. Ajayan and L. D. Marks. "Quasimelting and phases of small particles". In: *Physical Review Letters* 60.7 (1988), pp. 585–587. DOI: 10.1103/PhysRevLett.60.585 (cit. on p. 14).

[49] T. Kizuka and N. Tanaka. "Atomic process of epitaxial growth of gold on magnesium oxide studied by cross-sectional time-resolved high-resolution electron microscopy". In: *Physical Review B* 56.16 (1997), R10079–R10088. DOI: 10.1103/PhysRevB.56.R10079 (cit. on p. 14).

[50] L. D. Marks. "Surface structure and energetics of multiply twinned particles". In: *Philosophical Magazine A* 49.1 (1984), pp. 81–93. ISSN: 0141-8610. DOI: 10.1080/01418618408233431 (cit. on p. 14).

[51] F. Calvo. "Chapter 9 - Melting and structural transitions". In: *Frontiers of Nanoscience*. Ed. by S. T. Bromley and S. M. Woodley. Vol. 12. Computational Modelling of Nanoparticles. Elsevier, 2018, pp. 295–331. DOI: 10.1016/B978-0-08-102232-0.00009-9 (cit. on p. 14).

[52] R. Ferrando. "Chapter 6 - Stress-driven structural transitions in bimetallic nanoparticles". In: *Frontiers of Nanoscience*. Ed. by S. T. Bromley and S. M. Woodley. Vol. 12. Computational Modelling of Nanoparticles. Elsevier, 2018, pp. 189–204. DOI: 10.1016/B978-0-08-102232-0.00006-3 (cit. on p. 14).

[53] K. H. Hansen et al. "Palladium Nanocrystals on Al_2O_3: Structure and Adhesion Energy". In: *Physical Review Letters* 83.20 (1999), pp. 4120–4123. DOI: 10.1103/PhysRevLett.83.4120 (cit. on pp. 14, 15).

[54] Z. Zhang, L. Li, and J. C. Yang. "Adhesion of Pt Nanoparticles Supported on γ-Al_2O_3 Single Crystal". In: *The Journal of Physical Chemistry C* 117.41 (2013), pp. 21407–21412. ISSN: 1932-7447. DOI: 10.1021/jp407798b (cit. on p. 14).

[55] M. Methfessel, D. Hennig, and M. Scheffler. “Trends of the surface relaxations, surface energies, and work functions of the 4d transition metals”. In: *Physical Review B* 46.8 (1992), pp. 4816–4829. DOI: 10.1103/PhysRevB.46.4816 (cit. on p. 15).

[56] P. Müller and R. Kern. “Equilibrium nano-shape changes induced by epitaxial stress (generalised Wulf–Kaishew theorem)”. In: *Surface Science* 457.1 (2000), pp. 229–253. ISSN: 0039-6028. DOI: 10.1016/S0039-6028(00)00371-X (cit. on p. 16).

[57] J. E. Ayers. *Heteroepitaxy of semiconductors: theory, growth, and characterization*. OCLC: ocm70878051. Boca Raton: CRC Press, 2007. ISBN: 978-0-8493-7195-0 (cit. on pp. 16, 17, 20, 21, 24).

[58] H. Graoui, S. Giorgio, and C. R. Enry. “Effect of the interface structure on the high-temperature morphology of supported metal clusters”. In: *Philosophical Magazine B* 81.11 (2001), pp. 1649–1658. ISSN: 1364-2812. DOI: 10.1080/13642810108223109 (cit. on p. 16).

[59] C. R. Henry. “Morphology of supported nanoparticles”. In: *Progress in Surface Science* 80.3-4 (2005), pp. 92–116. ISSN: 00796816. DOI: 10.1016/j.progsurf.2005.09.004 (cit. on p. 16).

[60] J. J. Métois and J. C. Heyraud. “SEM studies of equilibrium forms: Roughening transition and surface melting of indium and lead crystals”. In: *Ultramicroscopy* 31.1 (1989), pp. 73–79. ISSN: 0304-3991. DOI: 10.1016/0304-3991(89)90036-3 (cit. on p. 16).

[61] T. K. Sau and A. L. Rogach. “Nonspherical Noble Metal Nanoparticles: Colloid-Chemical Synthesis and Morphology Control”. In: *Advanced Materials* 22.16 (2010), pp. 1781–1804. ISSN: 1521-4095. DOI: 10.1002/adma.200901271 (cit. on pp. 16–18).

[62] P. Sautet. “Stress, strain and chemical reactivity”. In: *Stress and Strain in Epitaxy*. Elsevier, 2001, pp. 155–171. ISBN: 978-0-444-50865-2. DOI: 10.1016/B978-044450865-2/50008-8 (cit. on pp. 16, 37).

[63] H. Stillrich et al. “Magnetic anisotropy and spin reorientation in Co/Pt multilayers: Influence of preparation”. In: *Journal of Magnetism and Magnetic Materials*. Proceedings of the Joint European Magnetic Symposia 322.9 (2010), pp. 1353–1356. ISSN: 0304-8853. DOI: 10.1016/j.jmmm.2009.09.039 (cit. on p. 17).

[64] K.-S. Choi. “Shape control of inorganic materials via electrodeposition”. In: *Dalton Transactions* 0.40 (2008), pp. 5432–5438. DOI: 10.1039/B807848C (cit. on pp. 17, 18).

[65] J. A. Venables and G. D. T. Spiller. “Nucleation and Growth of Thin Films”. In: *Surface Mobilities on Solid Materials: Fundamental Concepts and Applications*. Ed. by V. T. Binh. NATO Advanced Science Institutes Series. Boston, MA: Springer US, 1983, pp. 341–404. ISBN: 978-1-4684-4343-1. DOI: 10.1007/978-1-4684-4343-1_16 (cit. on p. 20).

[66] C. T. Campbell. “Ultrathin metal films and particles on oxide surfaces: structural, electronic and chemisorptive properties”. In: *Surface Science Reports* 27.1 (1997), pp. 1–111. ISSN: 0167-5729. DOI: 10.1016/S0167-5729(96)00011-8 (cit. on pp. 21, 22).

[67] O. Benamara et al. “Growth of platinum ultrathin films on Al_2O_3(0001)”. In: *Surface Science* 605.21-22 (2011), pp. 1906–1912. ISSN: 00396028. DOI: 10.1016/j.susc.2011.07.002 (cit. on pp. 21, 62–64).

[68] M. A. Herman and H. Sitter. *Molecular Beam Epitaxy: Fundamentals and Current Status*. 2., nd ed. 1996. Springer Series in Materials Science 7. OCLC: 864586547. Berlin: Springer Berlin, 2013. ISBN: 978-3-642-80062-7 (cit. on pp. 21, 22).

[69] J. R. Arthur. “Molecular beam epitaxy”. In: *Surface Science* 500.1 (2002), pp. 189–217. ISSN: 0039-6028. DOI: 10.1016/S0039-6028(01)01525-4 (cit. on p. 21).

[70] N. N. Ledentsov. *Growth processes and surface phase equilibria in molecular beam epitaxy*. Springer tracts in modern physics v. 156. Berlin; New York: Springer, 1999. ISBN: 978-3-540-65794-1 (cit. on pp. 22, 24).

[71] M. Bäumer and H.-J. Freund. “Metal deposits on well-ordered oxide films”. In: *Progress in Surface Science* 61.7-8 (1999), pp. 127–198. ISSN: 00796816. DOI: 10.1016/S0079-6816(99)00012-X (cit. on pp. 22, 27).

[72] C. R. Henry. “Surface studies of supported model catalysts”. In: *Surface Science Reports* 31.7-8 (1998), pp. 231–325. ISSN: 01675729. DOI: 10.1016/S0167-5729(98)00002-8 (cit. on p. 22).

[73] A.-L. Barabási and H. E. Stanley. *Fractal concepts in surface growth*. New York, NY, USA: Press Syndicate of the University of Cambridge, 1995. ISBN: 978-0-521-48308-7 978-0-521-48318-6 (cit. on pp. 22–24).

[74] S. V. Ivanov, P. S. Kop'ev, and N. N. Ledentsov. "Thermodynamic analysis of segregation effects in MBE of AIII-BV compounds". In: *Journal of Crystal Growth* 111.1 (1991), pp. 151–161. ISSN: 0022-0248. DOI: 10.1016/0022-0248(91)90963-6 (cit. on p. 24).

[75] J. J. Harris et al. "Kinetic limitations to surface segregation during MBE growth of III–V compounds: Sn in GaAs". In: *Applied Physics A* 33.2 (1984), pp. 87–92. ISSN: 1432-0630. DOI: 10.1007/BF00617613 (cit. on p. 24).

[76] S. V. Ivanov, P. S. Kop'ev, and N. N. Ledentsov. "Thermodynamic analysis of segregation effects in molecular beam epitaxy". In: *Journal of Crystal Growth* 104.2 (1990), pp. 345–354. ISSN: 0022-0248. DOI: 10.1016/0022-0248(90)90134-7 (cit. on p. 24).

[77] R. Heckingbottom. "The Application of Thermodynamics to Molecular Beam Epitaxy". In: *Molecular Beam Epitaxy and Heterostructures*. Ed. by L. L. Chang and K. Ploog. NATO ASI Series. Dordrecht: Springer Netherlands, 1985, pp. 71–104. ISBN: 978-94-009-5073-3. DOI: 10.1007/978-94-009-5073-3_3 (cit. on p. 24).

[78] M. Dalmiglio et al. "Oxidation of Supported PtRh Particles: Size and Morphology Effects". In: *The Journal of Physical Chemistry C* 114.40 (2010), pp. 16885–16891. ISSN: 1932-7447. DOI: 10.1021/jp910370r (cit. on pp. 24, 96).

[79] J. W. Arblaster. "Crystallographic Properties of Rhodium". In: *Platinum Metals Review* 41.4 (1997), pp. 184–189 (cit. on pp. 24, 131).

[80] J. W. Arblaster. "Crystallographic Properties of Platinum". In: *Platinum Metals Review* 41.1 (1997), pp. 12–21 (cit. on pp. 24, 131).

[81] W. G. Moffatt, ed. *The handbook of binary phase diagrams*. Schenectady, NY: Genium Publ, 1984. ISBN: 978-0-931690-00-6 (cit. on p. 24).

[82] S. Maisel, T. Kerscher, and S. Müller. "No miscibility gap in Pt–Rh binary alloys: A first-principles study". In: *Acta Materialia* 60.3 (2012), pp. 1093–1098. ISSN: 13596454. DOI: 10.1016/j.actamat.2011.10.020 (cit. on pp. 24, 130).

[83] L. Vegard. "Die Konstitution der Mischkristalle und die Raumfüllung der Atome". In: *Zeitschrift für Physik* 5.1 (1921), pp. 17–26. ISSN: 0044-3328. DOI: 10.1007/BF01349680 (cit. on pp. 24, 131).

[84] L. Vegard. “XV. Die Röntgenstrahlen im Dienste der Erforschung der Materie”. In: *Zeitschrift für Kristallographie - Crystalline Materials* 67.1-6 (1928), pp. 239–259. ISSN: 2196-7105. DOI: 10.1524/zkri.1928.67.1.239 (cit. on pp. 24, 131).

[85] K. Yuge. “Concentration effects on segregation behavior of Pt-Rh nanoparticles”. In: *Physical Review B* 84.8 (2011). ISSN: 1098-0121, 1550-235X. DOI: 10.1103/PhysRevB.84.085451 (cit. on pp. 24, 147).

[86] K. Yuge et al. “First-principles study of bulk ordering and surface segregation in Pt-Rh binary alloys”. In: *Physical Review B* 74.17 (2006). ISSN: 1098-0121, 1550-235X. DOI: 10.1103/PhysRevB.74.174202 (cit. on pp. 24, 138).

[87] K. Momma and F. Izumi. “*VESTA 3* for three-dimensional visualization of crystal, volumetric and morphology data”. In: *Journal of Applied Crystallography* 44.6 (2011), pp. 1272–1276. ISSN: 0021-8898. DOI: 10.1107/S0021889811038970 (cit. on p. 25).

[88] J. Toofan and P. R. Watson. “The termination of the α-Al_2O_3 (0001) surface: a LEED crystallography determination”. In: *Surface Science* 401.2 (1998), pp. 162–172. ISSN: 0039-6028. DOI: 10.1016/S0039-6028(97)01031-5 (cit. on pp. 26, 28).

[89] J. Ahn and J. W. Rabalais. “Composition and structure of the Al_2O_3{0001}-(1 × 1) surface”. In: *Surface Science* 388.1 (1997), pp. 121–131. ISSN: 0039-6028. DOI: 10.1016/S0039-6028(97)00383-X (cit. on pp. 26, 28).

[90] P. Guénard et al. “Determination of the α-Al_2O_3(0001) Surface Relaxation and Termination by Measurements of Crystal Truncation Rods”. In: *Surface Review and Letters* 05.01 (1998), pp. 321–324. ISSN: 0218-625X. DOI: 10.1142/S0218625X98000591 (cit. on pp. 26, 88).

[91] E. A. Soares et al. “Structure of the α–Al_2O_3(0001) surface from low-energy electron diffraction: Al termination and evidence for anomalously large thermal vibrations”. In: *Physical Review B* 65.19 (2002), p. 195405. DOI: 10.1103/PhysRevB.65.195405 (cit. on p. 26).

[92] T. Suzuki et al. “Structure of α-Al_2O_3(0001) surface and Ti deposited on α-Al_2O_3(0001) substrate: CAICISS and RHEED study”. In: *Surface Science* 437.3 (1999), pp. 289–298. ISSN: 0039-6028. DOI: 10.1016/S0039-6028(99)00706-2 (cit. on pp. 26, 28).

[93] I. Vilfan and T. Deutsch. "Structure determination of the $(3\sqrt{3} \times 3\sqrt{3})$ reconstructed α-$Al_2O_3(0\,0\,0\,1)$". In: *Surface Science* (2002), pp. L215–L221 (cit. on pp. 26, 28).

[94] G. Renaud et al. "Atomic Structure of the α - $Al_2O_3(0001)$ $(\sqrt{31} \times \sqrt{31})R\pm9°$ Reconstruction". In: *Physical Review Letters* 73.13 (1994), pp. 1825–1828. ISSN: 0031-9007. DOI: 10.1103/PhysRevLett.73.1825 (cit. on pp. 26, 28).

[95] M. Gautier et al. "α-$Al_2O_3(0001)$ Surfaces: Atomic and Electronic Structure". In: *Journal of the American Ceramic Society* 77.2 (1994), pp. 323–334. ISSN: 1551-2916. DOI: 10.1111/j.1151-2916.1994.tb06999.x (cit. on pp. 26, 28).

[96] C. Barth and M. Reichling. "Imaging the atomic arrangements on the high-temperature reconstructed α-$Al_2O_3(0001)$ surface". In: *Nature* 414.6859 (2001), pp. 54–57. ISSN: 1476-4687. DOI: 10.1038/35102031 (cit. on pp. 26, 28).

[97] V. Coustet and J. Jupille. "High-resolution electron-energy-loss spectroscopy of isolated hydroxyl groups on α-$Al_2O_3(0001)$". In: *Surface Science*. Proceedings of the European Conference on Surface Science 307-309 (1994), pp. 1161–1165. ISSN: 0039-6028. DOI: 10.1016/0039-6028(94)91557-1 (cit. on pp. 26, 28).

[98] R. Lazzari and J. Jupille. "Wetting and interfacial chemistry of metallic films on the hydroxylated α-$Al_2O_3(0001)$ surface". In: *Physical Review B* 71.4 (2005), p. 045409. DOI: 10.1103/PhysRevB.71.045409 (cit. on pp. 26, 29, 89).

[99] C. E. Nelson et al. "Desorption of H_2O from a hydroxylated single-crystal α-$Al_2O_3(0001)$ surface". In: *Surface Science* 416.3 (1998), pp. 341–353. ISSN: 0039-6028. DOI: 10.1016/S0039-6028(98)00439-7 (cit. on pp. 26–29, 89).

[100] J. W. Elam et al. "Adsorption of H_2O on a Single-Crystal α-$Al_2O_3(0001)$ Surface". In: *The Journal of Physical Chemistry B* 102.36 (1998), pp. 7008–7015. ISSN: 1520-6106. DOI: 10.1021/jp981070j (cit. on pp. 26–29).

[101] P. J. Eng et al. "Structure of the Hydrated α-Al_2O_3 (0001) Surface". In: *Science* 288.5468 (2000), pp. 1029–1033. ISSN: 0036-8075, 1095-9203. DOI: 10.1126/science.288.5468.1029 (cit. on pp. 26, 28, 29, 62, 88, 89).

[102] S. A. Chambers et al. "Laminar Growth of Ultrathin Metal Films on Metal Oxides: Co on Hydroxylated α-$Al_2O_3(0001)$". In: *Science* 297.5582 (2002), pp. 827–831. ISSN: 0036-8075, 1095-9203. DOI: 10.1126/science.1073404 (cit. on pp. 26, 89).

[103] Q. Fu, T. Wagner, and M. Rühle. "Hydroxylated α-Al_2O_3 (0001) surfaces and metal/α-Al_2O_3 (0001) interfaces". In: *Surface Science* 600.21 (2006), pp. 4870–4877. ISSN: 0039-6028. DOI: 10.1016/j.susc.2006.08.008 (cit. on pp. 26, 28, 29, 89).

[104] J. A. Kelber et al. "Copper wetting of α-Al_2O_3(0001): theory and experiment". In: *Surface Science* 446.1 (2000), pp. 76–88. ISSN: 0039-6028. DOI: 10.1016/S0039-6028(99)01089-4 (cit. on pp. 26, 89).

[105] C. Niu et al. "Cu interactions with α-Al_2O_3(0001): effects of surface hydroxyl groups versus dehydroxylation by Ar-ion sputtering". In: *Surface Science* 465.1 (2000), pp. 163–176. ISSN: 0039-6028. DOI: 10.1016/S0039-6028(00)00728-7 (cit. on pp. 26, 89).

[106] P. Liu et al. "Reaction of water vapor with α-Al_2O_3(0001) and α-Fe_2O_3(0001) surfaces: synchrotron X-ray photoemission studies and thermodynamic calculations". In: *Surface Science* 417.1 (1998), pp. 53–65. ISSN: 0039-6028. DOI: 10.1016/S0039-6028(98)00661-X (cit. on pp. 26, 28, 29).

[107] T. M. French and G. A. Somorjai. "Composition and surface structure of the (0001) face of α-alumina by low-energy electron diffraction". In: *The Journal of Physical Chemistry* 74.12 (1970), pp. 2489–2495. ISSN: 0022-3654, 1541-5740. DOI: 10.1021/j100706a014 (cit. on pp. 26, 28, 89).

[108] T. Akatsu et al. "Morphology and microstructure of the Ar^+-ion sputtered (0001) α-Al_2O_3 surface". In: *Applied Surface Science* 165.2 (2000), pp. 159–165. ISSN: 0169-4332. DOI: 10.1016/S0169-4332(00)00376-7 (cit. on p. 26).

[109] M. Gautier et al. "Modifications of α-Al_2O_3(0001) surfaces induced by thermal treatments or ion bombardment". In: *Surface Science* 250.1 (1991), pp. 71–80. ISSN: 0039-6028. DOI: 10.1016/0039-6028(91)90710-A (cit. on pp. 26, 28).

[110] M. Vermeersch et al. "The aluminium/sapphire interface formation at high temperature: an AES and LEED study". In: *Surface Science* 323.1 (1995), pp. 175–187. ISSN: 0039-6028. DOI: 10.1016/0039-6028(94)00643-1 (cit. on p. 26).

[111] M. Vermeersch et al. "The Al/Al_2O_3 interface formation as studied by electron spectroscopies". In: *Surface Science* 235.1 (1990), pp. 5–14. ISSN: 0039-6028. DOI: 10.1016/0039-6028(90)90101-D (cit. on p. 26).

[112] G. Renaud. "Oxide surfaces and metal/oxide interfaces studied by grazing incidence X-ray scattering". In: *Surface Science Reports* 32.1 (1998), pp. 5–90. ISSN: 0167-5729. DOI: 10.1016/S0167-5729(98)00005-3 (cit. on pp. 26, 28).

[113] Q. Fu and T. Wagner. "Interaction of nanostructured metal overlayers with oxide surfaces". In: *Surface Science Reports* 62.11 (2007), pp. 431–498. ISSN: 01675729. DOI: 10.1016/j.surfrep.2007.07.001 (cit. on pp. 26–28, 89).

[114] M. Haruta. "Size- and support-dependency in the catalysis of gold". In: *Catalysis Today*. Copper, Silver and Gold in Catalysis 36.1 (1997), pp. 153–166. ISSN: 0920-5861. DOI: 10.1016/S0920-5861(96)00208-8 (cit. on pp. 27, 37).

[115] J. Maier. *Physical chemistry of ionic materials: ions and electrons in solids*. OCLC: ocm48932877. Chichester ; Hoboken, NJ: Wiley, 2004. ISBN: 978-0-471-99991-1 978-0-470-87076-1 (cit. on p. 27).

[116] Q. Fu et al. "Metal-Oxide Interfacial Reactions: Encapsulation of Pd on TiO_2 (110)". In: *The Journal of Physical Chemistry B* 109.2 (2005), pp. 944–951. ISSN: 1520-6106. DOI: 10.1021/jp046091u (cit. on p. 27).

[117] E. Bus, J. T. Miller, and J. A. van Bokhoven. "Hydrogen Chemisorption on Al_2O_3-Supported Gold Catalysts". In: *The Journal of Physical Chemistry B* 109.30 (2005), pp. 14581–14587. ISSN: 1520-6106. DOI: 10.1021/jp051660z (cit. on p. 27).

[118] G. Ertl. "Reactions at Surfaces: From Atoms to Complexity (Nobel Lecture)". In: *Angewandte Chemie International Edition* 47.19 (2008), pp. 3524–3535. ISSN: 1521-3773. DOI: https://doi.org/10.1002/anie.200800480 (cit. on pp. 27, 35, 37, 38).

[119] K. Wefers and C. Misra. *Oxides and Hydroxides of Aluminum*. Tech. rep. 19. Alcoa Laboratories, Aluminum Company of America, 1987, p. 100 (cit. on p. 27).

[120] I. Levin and D. Brandon. "Metastable Alumina Polymorphs: Crystal Structures and Transition Sequences". In: *Journal of the American Ceramic Society* 81.8 (1998), pp. 1995–2012. ISSN: 1551-2916. DOI: 10.1111/j.1151-2916.1998.tb02581.x (cit. on p. 27).

[121] J. M. McHale et al. “Surface Energies and Thermodynamic Phase Stability in Nanocrystalline Aluminas”. In: *Science* 277.5327 (1997), pp. 788–791. ISSN: 0036-8075, 1095-9203. DOI: 10.1126/science.277.5327.788 (cit. on pp. 27, 28, 64).

[122] H.-T. Li et al. “Interfacial Stoichiometry and Adhesion at Metal/α-Al_2O_3 Interfaces”. In: *Journal of the American Ceramic Society* 94.s1 (2011), s154–s159. ISSN: 1551-2916. DOI: 10.1111/j.1551-2916.2011.04405.x (cit. on pp. 27, 28, 89, 94).

[123] M. D. Groner et al. “Low-Temperature Al_2O_3 Atomic Layer Deposition”. In: *Chemistry of Materials* 16.4 (2004), pp. 639–645. ISSN: 0897-4756. DOI: 10.1021/cm0304546 (cit. on p. 27).

[124] W. Y. Ching and Y.-N. Xu. “First-Principles Calculation of Electronic, Optical, and Structural Properties of α-Al_2O_3”. In: *Journal of the American Ceramic Society* 77.2 (1994), pp. 404–411. ISSN: 1551-2916. DOI: 10.1111/j.1151-2916.1994.tb07008.x (cit. on p. 27).

[125] X.-G. Wang, A. Chaka, and M. Scheffler. “Effect of the Environment on α-Al_2O_3 (0001) Surface Structures”. In: *Physical Review Letters* 84.16 (2000), pp. 3650–3653. DOI: 10.1103/PhysRevLett.84.3650 (cit. on pp. 28, 29).

[126] J. Guo, D. E. Ellis, and D. J. Lam. “Electronic structure and energetics of sapphire (0001) and $(1\bar{1}02)$ surfaces”. In: *Physical Review B* 45.23 (1992), pp. 13647–13656. DOI: 10.1103/PhysRevB.45.13647 (cit. on p. 28).

[127] I. Manassidis and M. J. Gillan. “Structure and Energetics of Alumina Surfaces Calculated from First Principles”. In: *Journal of the American Ceramic Society* 77.2 (1994), pp. 335–338. ISSN: 1551-2916. DOI: 10.1111/j.1151-2916.1994.tb07000.x (cit. on p. 28).

[128] W. C. Mackrodt et al. “The morphology of α-Al_2O_3 and α-Fe_2O_3: The importance of surface relaxation”. In: *Journal of Crystal Growth* 80.2 (1987), pp. 441–446. ISSN: 0022-0248. DOI: 10.1016/0022-0248(87)90093-5 (cit. on p. 28).

[129] V. E. Henrich and P. A. Cox. *The surface science of metal oxides*. Cambridge ; New York: Cambridge University Press, 1994. ISBN: 978-0-521-44389-0 (cit. on pp. 28, 30).

[130] K. C. Hass et al. “The Chemistry of Water on Alumina Surfaces: Reaction Dynamics from First Principles”. In: *Science* 282.5387 (1998), pp. 265–268. ISSN: 0036-8075, 1095-9203. DOI: 10.1126/science.282.5387.265 (cit. on pp. 28, 29).

[131] Z. Łodziana, J. K. Nørskov, and P. Stoltze. “The stability of the hydroxylated (0001) surface of α-Al_2O_3”. In: *The Journal of Chemical Physics* 118.24 (2003), pp. 11179–11188. ISSN: 0021-9606. DOI: 10.1063/1.1574798 (cit. on pp. 28, 29, 89).

[132] J. M. McHale, A. Navrotsky, and A. J. Perrotta. “Effects of Increased Surface Area and Chemisorbed H_2O on the Relative Stability of Nanocrystalline γ-Al_2O_3 and α-Al_2O_3”. In: *The Journal of Physical Chemistry B* 101.4 (1997), pp. 603–613. ISSN: 1520-6106. DOI: 10.1021/jp9627584 (cit. on p. 28).

[133] D. H. Lee and R. A. Condrate. “An FTIR spectral investigation of the structural species found on alumina surfaces”. In: *Materials Letters* 23.4 (1995), pp. 241–246. ISSN: 0167-577X. DOI: 10.1016/0167-577X(95)00039-9 (cit. on p. 29).

[134] B. A. Hendriksen, D. R. Pearce, and R. Rudham. “Heats of adsorption of water on α- and γ-alumina”. In: *Journal of Catalysis* 24.1 (1972), pp. 82–87. ISSN: 0021-9517. DOI: 10.1016/0021-9517(72)90010-3 (cit. on p. 29).

[135] N. Bickel et al. “Structure determination of the $SrTiO_3$(100) surface”. In: *Vacuum* 41.1-3 (1990), pp. 46–48 (cit. on pp. 28–30, 122).

[136] J. G. Chen, J. E. Crowell, and J. T. Yates. “Assignment of a surface vibrational mode by chemical means: Modification of the lattice modes of Al_2O_3 by a surface reaction with H2O”. In: *The Journal of Chemical Physics* 84.10 (1986), pp. 5906–5909. ISSN: 0021-9606. DOI: 10.1063/1.449902 (cit. on p. 29).

[137] M. A. Schildbach and A. V. Hamza. “Clean and water-covered sapphire ($1\bar{1}02$) surfaces: structure and laser-induced desorption”. In: *Surface Science* 282.3 (1993), pp. 306–322. ISSN: 0039-6028. DOI: 10.1016/0039-6028(93)90936-E (cit. on p. 29).

[138] M. Schmidbauer, A. Kwasniewski, and J. Schwarzkopf. “High-precision absolute lattice parameter determination of $SrTiO_3$, $DyScO_3$ and $NdGaO_3$ single crystals”. In: *Acta Crystallographica Section B: Structural Science* 68.1 (2012), pp. 8–14. ISSN: 0108-7681. DOI: 10.1107/S0108768111046738 (cit. on p. 29).

[139] J. Brunen and J. Zegenhagen. "Investigation of the $SrTiO_3$ (110) surface by means of LEED, scanning tunneling microscopy and Auger spectroscopy". In: *Surface Science* 389.1-3 (1997), pp. 349–365. ISSN: 00396028. DOI: 10.1016/S0039-6028(97)00450-0 (cit. on p. 30).

[140] D. S. Deak. "Strontium titanate surfaces". In: *Materials Science and Technology* 23.2 (2007), pp. 127–136. ISSN: 0267-0836, 1743-2847. DOI: 10.1179/174328407X154383 (cit. on p. 30).

[141] R. Herger et al. "Surface of Strontium Titanate". In: *Physical Review Letters* 98.7 (2007), p. 076102. DOI: 10.1103/PhysRevLett.98.076102 (cit. on pp. 30, 122).

[142] N. Erdman et al. "The structure and chemistry of the TiO_2-rich surface of $SrTiO_3$(001)". In: *Nature* 419.6902 (2002), pp. 55–58. ISSN: 1476-4687. DOI: 10.1038/nature01010 (cit. on pp. 30, 122).

[143] K. Nassau and A. E. Miller. "Strontium titanate: An index to the literature on properties and the growth of single crystals". In: *Journal of Crystal Growth* 91.3 (1988), pp. 373–381. ISSN: 0022-0248. DOI: 10.1016/0022-0248(88)90254-0 (cit. on p. 30).

[144] C. Rodenbücher et al. "Homogeneity and variation of donor doping in Verneuil-grown $SrTiO_3$:Nb single crystals". In: *Scientific Reports* 6.1 (2016). ISSN: 2045-2322. DOI: 10.1038/srep32250 (cit. on p. 31).

[145] Y. Tateno et al. "Growth of $SrTiO_3$ Single Crystals with a Diameter of about 30 mm by the Verneuil Method". In: *Crystal Growth & Design* 19.2 (2019), pp. 604–612. ISSN: 1528-7483, 1528-7505. DOI: 10.1021/acs.cgd.8b01004 (cit. on p. 31).

[146] M. Abuìn et al. "Coherent X-ray Imaging of CO-Adsorption-Induced Structural Changes in Pt Nanoparticles: Implications for Catalysis". In: *ACS Applied Nano Materials* 2.8 (2019), pp. 4818–4824. DOI: 10.1021/acsanm.9b00764 (cit. on pp. 31, 121, 128, 195).

[147] G. Koster et al. "Quasi-ideal strontium titanate crystal surfaces through formation of strontium hydroxide". In: *Applied Physics Letters* 73.20 (1998), pp. 2920–2922. ISSN: 0003-6951. DOI: 10.1063/1.122630 (cit. on p. 31).

[148] G. Ertl and H. Freund. "Catalysis and Surface Science". In: *Physics Today* 52.1 (1999), pp. 32–38. ISSN: 0031-9228, 1945-0699. DOI: 10.1063/1.882569 (cit. on p. 33).

[149] I. Langmuir. "Part II.—"Heterogeneous reactions". Chemical reactions on surfaces". In: *Transactions of the Faraday Society* 17.0 (1922), pp. 607–620. ISSN: 0014-7672. DOI: 10.1039/TF9221700607 (cit. on p. 33).

[150] T. Engel and G. Ertl. "Elementary Steps in the Catalytic Oxidation of Carbon Monoxide on Platinum Metals". In: *Advances in Catalysis*. Ed. by D. D. Eley, H. Pines, and P. B. Weez. Vol. 28. Academic Press, 1979, pp. 1–78. DOI: 10.1016/S0360-0564(08)60133-9 (cit. on pp. 34, 35).

[151] B. Hammer, Y. Morikawa, and J. K. Nørskov. "CO Chemisorption at Metal Surfaces and Overlayers". In: *Physical Review Letters* 76.12 (1996), pp. 2141–2144. DOI: 10.1103/PhysRevLett.76.2141 (cit. on p. 34).

[152] B. Hammer, L. B. Hansen, and J. K. Nørskov. "Improved adsorption energetics within density-functional theory using revised Perdew-Burke-Ernzerhof functionals". In: *Physical Review B* 59.11 (1999), pp. 7413–7421. DOI: 10.1103/PhysRevB.59.7413 (cit. on p. 34).

[153] D. Kulginov et al. "CO_2 sticking on Pt(111): The role of kinetic energy and internal degrees of freedom". In: *Journal of Vacuum Science & Technology A* 13.3 (1995), pp. 1511–1516. ISSN: 0734-2101. DOI: 10.1116/1.579717 (cit. on p. 34).

[154] H. Bonzel, ed. *Adsorbed Layers on Surfaces. Part 5: Adsorption of molecules on metal, semiconductor and oxide surfaces*. Vol. 42A5. Landolt-Börnstein - Group III Condensed Matter. Springer Berlin Heidelberg, 2006. ISBN: 978-3-540-25848-3. DOI: 10.1007/b104235 (cit. on p. 34).

[155] D. D. Eley and E. K. Rideal. "Parahydrogen Conversion on Tungsten". In: *Nature* 146.3699 (1940), pp. 401–402. ISSN: 1476-4687. DOI: 10.1038/146401d0 (cit. on p. 34).

[156] P. Mars and D. W. van Krevelen. "Oxidations carried out by means of vanadium oxide catalysts". In: *Chemical Engineering Science*. The Proceedings of the Conference on Oxidation Processes 3 (1954), pp. 41–59. ISSN: 0009-2509. DOI: 10.1016/S0009-2509(54)80005-4 (cit. on p. 34).

[157] I. Chorkendorff and J. W. Niemantsverdriet. *Concepts of Modern Catalysis and Kinetics*. 1st ed. Wiley, 2003. ISBN: 978-3-527-30574-2 978-3-527-60265-0. DOI: 10.1002/3527602658 (cit. on pp. 34, 35, 37, 38).

[158] K. Christmann. *Introduction to Surface Physical Chemistry*. Ed. by Deutsche Bunsen-Gesellschaft für Physikalische Chemie et al. Vol. 1. Topics in Physical Chemistry. Heidelberg: Steinkopff, 1991. ISBN: 978-3-7985-0858-3 978-3-662-08009-2. DOI: 10.1007/978-3-662-08009-2 (cit. on p. 34).

[159] G. L. Haller. "New catalytic concepts from new materials: understanding catalysis from a fundamental perspective, past, present, and future". In: *Journal of Catalysis*. 40th Anniversary Commemorative Issue 216.1 (2003), pp. 12–22. ISSN: 0021-9517. DOI: 10.1016/S0021-9517(02)00122-7 (cit. on p. 34).

[160] P. Sabatier. *La catalyse en chimie organique*. Vol. 3. Encyclopédie de science chimique appliquée. Ch. Béranger, 1913 (cit. on p. 34).

[161] J. Cheng and P. Hu. "Utilization of the Three-Dimensional Volcano Surface To Understand the Chemistry of Multiphase Systems in Heterogeneous Catalysis". In: *Journal of the American Chemical Society* 130.33 (2008), pp. 10868–10869. ISSN: 0002-7863. DOI: 10.1021/ja803555g (cit. on p. 34).

[162] T. Bligaard et al. "The Brønsted–Evans–Polanyi relation and the volcano curve in heterogeneous catalysis". In: *Journal of Catalysis* 224.1 (2004), pp. 206–217. ISSN: 0021-9517. DOI: 10.1016/j.jcat.2004.02.034 (cit. on p. 34).

[163] M. Salmeron and R. Schlögl. "Ambient pressure photoelectron spectroscopy: A new tool for surface science and nanotechnology". In: *Surface Science Reports* 63.4 (2008), pp. 169–199. ISSN: 0167-5729. DOI: 10.1016/j.surfrep.2008.01.001 (cit. on p. 34).

[164] A. Stierle, J. Gustafson, and E. Lundgren. "Surface-Sensitive X-ray Diffraction Across the Pressure Gap". In: *Operando Research in Heterogeneous Catalysis*. Ed. by J. Frenken and I. Groot. Springer Series in Chemical Physics. Cham: Springer International Publishing, 2017, pp. 59–87. ISBN: 978-3-319-44439-0. DOI: 10.1007/978-3-319-44439-0_3 (cit. on p. 34).

[165] S. Krick Calderón et al. "CO oxidation on Pt(111) at near ambient pressures". In: *The Journal of Chemical Physics* 144.4 (2016), p. 044706. ISSN: 0021-9606. DOI: 10.1063/1.4940318 (cit. on pp. 34, 36).

[166] X. Su et al. "High-Pressure CO Oxidation on Pt(111) Monitored with Infrared-Visible Sum Frequency Generation (SFG)". In: *Journal of the American*

Chemical Society 119.17 (1997), pp. 3994–4000. ISSN: 0002-7863. DOI: 10.1021/ja9638723 (cit. on pp. 35, 36).

[167] F. Gao et al. "CO Oxidation on Pt-Group Metals from Ultrahigh Vacuum to Near Atmospheric Pressures. 2. Palladium and Platinum". In: *The Journal of Physical Chemistry C* 113.1 (2009), pp. 174–181. ISSN: 1932-7447, 1932-7455. DOI: 10.1021/jp8077985 (cit. on pp. 35, 36).

[168] R. L. Palmer and J. N. Smith. "Molecular beam study of CO oxidation on a (111) platinum surface". In: *The Journal of Chemical Physics* 60.4 (1974), pp. 1453–1463. ISSN: 0021-9606. DOI: 10.1063/1.1681219 (cit. on p. 35).

[169] T. Matsushima. "Kinetic studies on the CO oxidation over platinum by means of carbon 13 tracer". In: *Surface Science* 79.1 (1979), pp. 63–75. ISSN: 0039-6028. DOI: 10.1016/0039-6028(79)90026-8 (cit. on p. 35).

[170] C. T. Campbell et al. "Model oxide-supported metal catalysts: energetics, particle thicknesses, chemisorption and catalytic properties". In: *Topics in Catalysis* 14.1 (2000), pp. 43–51. ISSN: 1572-9028. DOI: 10.1023/A:1009002915667 (cit. on p. 35).

[171] M. Kinne et al. "Kinetics of the CO oxidation reaction on Pt(111) studied by in situ high-resolution x-ray photoelectron spectroscopy". In: *The Journal of Chemical Physics* 120.15 (2004), pp. 7113–7122. ISSN: 0021-9606. DOI: 10.1063/1.1669378 (cit. on p. 35).

[172] J. L. Gland and E. B. Kollin. "Carbon monoxide oxidation on the Pt(111) surface: Temperature programmed reaction of coadsorbed atomic oxygen and carbon monoxide". In: *The Journal of Chemical Physics* 78.2 (1983), pp. 963–974. ISSN: 0021-9606. DOI: 10.1063/1.444801 (cit. on p. 35).

[173] M. Xu, J. Liu, and F. Zaera. "Kinetic evidence for the dependence of surface reaction rates on the distribution of reactants on the surface". In: *The Journal of Chemical Physics* 104.21 (1996), pp. 8825–8828. ISSN: 0021-9606. DOI: 10.1063/1.471606 (cit. on p. 35).

[174] A. Urakawa et al. "Simultaneous in situ monitoring of surface and gas species and surface properties by modulation excitation polarization-modulation infrared reflection-absorption spectroscopy: CO oxidation over Pt film". In: *The Journal of Chemical Physics* 124.5 (2006), p. 054717. ISSN: 0021-9606. DOI: 10.1063/1.2159484 (cit. on p. 35).

[175] F. Zaera, J. Liu, and M. Xu. "Isothermal study of the kinetics of carbon monoxide oxidation on Pt(111): Rate dependence on surface coverages". In: *The Journal of Chemical Physics* 106.10 (1997), pp. 4204–4215. ISSN: 0021-9606. DOI: 10.1063/1.473126 (cit. on p. 35).

[176] J. Wintterlin et al. "Atomic and Macroscopic Reaction Rates of a Surface-Catalyzed Reaction". In: *Science* 278.5345 (1997), pp. 1931–1934. ISSN: 0036-8075, 1095-9203. DOI: 10.1126/science.278.5345.1931 (cit. on p. 35).

[177] S. Völkening and J. Wintterlin. "CO oxidation on Pt(111)—Scanning tunneling microscopy experiments and Monte Carlo simulations". In: *The Journal of Chemical Physics* 114.14 (2001), pp. 6382–6395. ISSN: 0021-9606. DOI: 10.1063/1.1343836 (cit. on p. 35).

[178] S. Akhter and J. M. White. "The effect of oxygen islanding on Co and H2 oxidation on Pt(111)". In: *Surface Science* 171.3 (1986), pp. 527–542. ISSN: 0039-6028. DOI: 10.1016/0039-6028(86)91058-7 (cit. on p. 35).

[179] C. Klünker et al. "CO stretching vibrations on Pt(111) and Pt(110) studied by sumfrequency generation". In: *Surface Science* 360.1 (1996), pp. 104–111. ISSN: 0039-6028. DOI: 10.1016/0039-6028(96)00638-3 (cit. on pp. 35, 37).

[180] W. X. Li et al. "Oxidation of Pt(110)". In: *Physical Review Letters* 93.14 (2004), p. 146104. DOI: 10.1103/PhysRevLett.93.146104 (cit. on p. 35).

[181] E. Lundgren et al. "Surface oxides on close-packed surfaces of late transition metals". In: *Journal of Physics: Condensed Matter* 18.30 (2006), R481–R499. ISSN: 0953-8984. DOI: 10.1088/0953-8984/18/30/R01 (cit. on p. 35).

[182] C. Ellinger et al. "Atmospheric pressure oxidation of Pt(111)". In: *Journal of Physics: Condensed Matter* 20.18 (2008), p. 184013. ISSN: 0953-8984. DOI: 10.1088/0953-8984/20/18/184013 (cit. on pp. 35, 91).

[183] D. J. Miller et al. "Oxidation of Pt(111) under Near-Ambient Conditions". In: *Physical Review Letters* 107.19 (2011), p. 195502. DOI: 10.1103/PhysRevLett.107.195502 (cit. on pp. 35, 36, 91).

[184] A. Farkas et al. "High Pressure Carbon Monoxide Oxidation over Platinum (111)". In: *The Journal of Physical Chemistry C* 117.19 (2013), pp. 9932–9942. ISSN: 1932-7447. DOI: 10.1021/jp401867g (cit. on pp. 35, 36).

[185] C.-P. Hwang and C.-T. Yeh. “Platinum-oxide species formed by oxidation of platinum crystallites supported on alumina”. In: *Journal of Molecular Catalysis A: Chemical* 112.2 (1996), pp. 295–302. ISSN: 1381-1169. DOI: 10.1016/1381-1169(96)00127-6 (cit. on p. 36).

[186] J. Neugebohren et al. “Velocity-resolved kinetics of site-specific carbon monoxide oxidation on platinum surfaces”. In: *Nature* 558.7709 (2018), pp. 280–283. ISSN: 1476-4687. DOI: 10.1038/s41586-018-0188-x (cit. on p. 36).

[187] F. Gao et al. “CO Oxidation on Pt-Group Metals from Ultrahigh Vacuum to Near Atmospheric Pressures. 1. Rhodium”. In: *The Journal of Physical Chemistry C* 113.1 (2009), pp. 182–192. ISSN: 1932-7447. DOI: 10.1021/jp8077979 (cit. on p. 36).

[188] S. H. Oh et al. “Comparative kinetic studies of CO-O_2 and CO-NO reactions over single crystal and supported rhodium catalysts”. In: *Journal of Catalysis* 100.2 (1986), pp. 360–376. ISSN: 0021-9517. DOI: 10.1016/0021-9517(86)90103-X (cit. on p. 36).

[189] J. Gustafson et al. “Structure and catalytic reactivity of Rh oxides”. In: *Catalysis Today*. Time-resolved and in-situ study of heterogeneous catalysts and catalytic processes using X-rays: current possibilities and future prospects, European Synchrotron Radiation Facility, Grenoble, France, 5-7 February, 2008 145.3 (2009), pp. 227–235. ISSN: 0920-5861. DOI: 10.1016/j.cattod.2008.11.011 (cit. on p. 36).

[190] J. Gustafson et al. “Catalytic Activity of the Rh Surface Oxide: CO Oxidation over Rh(111) under Realistic Conditions”. In: *The Journal of Physical Chemistry C* 114.10 (2010), pp. 4580–4583. ISSN: 1932-7447. DOI: 10.1021/jp910988b (cit. on p. 36).

[191] J. Gustafson et al. “Sensitivity of catalysis to surface structure: The example of CO oxidation on Rh under realistic conditions”. In: *Physical Review B* 78.4 (2008), p. 045423. DOI: 10.1103/PhysRevB.78.045423 (cit. on p. 36).

[192] R. Westerström et al. “Structure and reactivity of a model catalyst alloy under realistic conditions”. In: *Journal of Physics: Condensed Matter* 20.18 (2008), p. 184018. ISSN: 0953-8984. DOI: 10.1088/0953-8984/20/18/184018 (cit. on p. 36).

[193] W. X. Li and B. Hammer. "Reactivity of a gas/metal/metal-oxide three-phase boundary: CO oxidation at the Pt(111)–c(4×2)-2CO/α-PtO_2 phase boundary". In: *Chemical Physics Letters* 409.1 (2005), pp. 1–7. ISSN: 0009-2614. DOI: 10.1016/j.cplett.2005.04.064 (cit. on p. 36).

[194] J. I. Flege and P. Sutter. "In situ structural imaging of CO oxidation catalysis on oxidized Rh(111)". In: *Physical Review B* 78.15 (2008), p. 153402. DOI: 10.1103/PhysRevB.78.153402 (cit. on p. 36).

[195] B. L. M. Hendriksen and J. W. M. Frenken. "CO Oxidation on Pt(110): Scanning Tunneling Microscopy Inside a High-Pressure Flow Reactor". In: *Physical Review Letters* 89.4 (2002), p. 046101. DOI: 10.1103/PhysRevLett.89.046101 (cit. on p. 36).

[196] L. Olsson and E. Fridell. "The Influence of Pt Oxide Formation and Pt Dispersion on the Reactions $NO_2 \Leftrightarrow NO+1/2\ O_2$ over Pt/Al_2O_3 and $Pt/BaO/Al_2O_3$". In: *Journal of Catalysis* 210.2 (2002), pp. 340–353. ISSN: 0021-9517. DOI: 10.1006/jcat.2002.3698 (cit. on p. 36).

[197] N. M. Martin et al. "Characterization of Surface Structure and Oxidation/Reduction Behavior of Pd–Pt/Al_2O_3 Model Catalysts". In: *The Journal of Physical Chemistry C* 120.49 (2016), pp. 28009–28020. ISSN: 1932-7447. DOI: 10.1021/acs.jpcc.6b09223 (cit. on pp. 36, 94).

[198] Y. Yourdshahyan et al. "Catalytic behavior at the nanoscale: CO adsorption on Al_2O_3-supported Pt clusters". In: ed. by T. Lian and H.-L. Dai. San Diego, CA, 2003, pp. 223–231. DOI: 10.1117/12.508615 (cit. on p. 37).

[199] V. Komanicky et al. "Shape-Dependent Activity of Platinum Array Catalyst". In: *Journal of the American Chemical Society* 131.16 (2009), pp. 5732–5733. ISSN: 0002-7863, 1520-5126. DOI: 10.1021/ja900459w (cit. on p. 37).

[200] T. Nilsson Pingel et al. "Influence of atomic site-specific strain on catalytic activity of supported nanoparticles". In: *Nature Communications* 9.1 (2018). ISSN: 2041-1723. DOI: 10.1038/s41467-018-05055-1 (cit. on p. 37).

[201] J. A. Kurzman, L. M. Misch, and R. Seshadri. "Chemistry of precious metal oxides relevant to heterogeneous catalysis". In: *Dalton Transactions* 42.41 (2013), pp. 14653–14667. ISSN: 1477-9234. DOI: 10.1039/C3DT51818C (cit. on pp. 37, 96).

[202] L. Li et al. “Investigation of Catalytic Finite-Size-Effects of Platinum Metal Clusters”. In: *The Journal of Physical Chemistry Letters* 4.1 (2013), pp. 222–226. DOI: 10.1021/jz3018286 (cit. on p. 37).

[203] A. Cao, R. Lu, and G. Veser. “Stabilizing metal nanoparticles for heterogeneous catalysis”. In: *Physical Chemistry Chemical Physics* 12.41 (2010), pp. 13499–13510. DOI: 10.1039/C0CP00729C (cit. on pp. 38, 94).

[204] U. Hejral et al. “Tracking the shape-dependent sintering of platinum–rhodium model catalysts under operando conditions”. In: *Nature Communications* 7.1 (2016). ISSN: 2041-1723. DOI: 10.1038/ncomms10964 (cit. on pp. 38, 93–95).

[205] J. Als-Nielsen and D. McMorrow. *Elements of Modern X-ray Physics*. 1st ed. Wiley, 2011. ISBN: 978-0-470-97395-0 978-1-119-99836-5. DOI: 10.1002/9781119998365 (cit. on pp. 39–47, 49–52, 126, 127).

[206] B. E. Warren. *X-ray diffraction*. Dover ed. New York: Dover Publications, 1990. ISBN: 978-0-486-66317-3 (cit. on p. 39).

[207] V. G. Levič. *Theory of the electromagnetic field. Theory of relativity*. Theoretical physics Vol. 1. Amsterdam: North-Holland Publ, 1970. ISBN: 978-0-7204-0177-6 (cit. on p. 39).

[208] P. Nolte. “In situ Oxidation Study of Supported Rh and Pd Nanoparticles”. PhD thesis. University of Hamburg, 2009 (cit. on p. 45).

[209] E. Vlieg. “ROD: a program for surface X-ray crystallography”. In: *Journal of Applied Crystallography* 33.2 (2000), pp. 401–405. ISSN: 0021-8898. DOI: 10.1107/S0021889899013655 (cit. on pp. 48, 142).

[210] H. Dosch. “Evanescent absorption in kinematic surface Bragg diffraction”. In: *Physical Review B* 35.5 (1987), pp. 2137–2143. DOI: 10.1103/PhysRevB.35.2137 (cit. on pp. 49, 50).

[211] G. H. Vineyard. “Grazing-incidence diffraction and the distorted-wave approximation for the study of surfaces”. In: *Physical Review B* 26.8 (1982), pp. 4146–4159. DOI: 10.1103/PhysRevB.26.4146 (cit. on p. 49).

[212] R. Feidenhans’l. “Surface structure determination by X-ray diffraction”. In: *Surface Science Reports* 10.3 (1989), pp. 105–188. ISSN: 0167-5729. DOI: 10.1016/0167-5729(89)90002-2 (cit. on p. 49).

[213] L. Spieß et al. *Moderne Röntgenbeugung: Röntgendiffraktometrie für Materialwissenschaftler, Physiker und Chemiker*. Wiesbaden: Springer Fachmedien Wiesbaden, 2019. ISBN: 978-3-8348-1219-3 978-3-8348-8232-5. DOI: 10.1007/978-3-8348-8232-5 (cit. on pp. 50, 51).

[214] L. G. Parratt. "Surface Studies of Solids by Total Reflection of X-Rays". In: *Physical Review* 95.2 (1954), pp. 359–369. DOI: 10.1103/PhysRev.95.359 (cit. on pp. 51, 52).

[215] L. Névot and P. Croce. "Caractérisation des surfaces par réflexion rasante de rayons X. Application à l'étude du polissage de quelques verres silicates". In: *Revue de Physique Appliquée* 15.3 (1980), pp. 761–779. ISSN: 0035-1687. DOI: 10.1051/rphysap:01980001503076100 (cit. on p. 52).

[216] A. Stierle. *FEWLAY: a software for fitting X-ray reflectivity curves*. andreas.stierle@desy.de (cit. on pp. 52, 77, 112).

[217] M. Lohmeier and E. Vlieg. "Angle calculations for a six-circle surface X-ray diffractometer". In: *Journal of Applied Crystallography* 26.5 (1993), pp. 706–716. ISSN: 0021-8898. DOI: 10.1107/S0021889893004868 (cit. on p. 57).

[218] T. Sunaoshi et al. "STEM/SEM, Chemical Analysis, Atomic Resolution and Surface Imaging At $\leq$ 30 kV with No Aberration Correction for Nanomaterials on Graphene Support". In: *Microscopy and Microanalysis* 22.S3 (2016), pp. 604–605. ISSN: 1431-9276, 1435-8115. DOI: 10.1017/S1431927616003871 (cit. on p. 57).

[219] J. I. Goldstein et al. *Scanning Electron Microscopy and X-Ray Microanalysis*. 4th ed. 2018. New York, NY: Springer New York : Imprint: Springer, 2018. ISBN: 978-1-4939-6676-9. DOI: 10.1007/978-1-4939-6676-9 (cit. on p. 59).

[220] E. Meyer, R. Bennewitz, and H. J. Hug. *Scanning Probe Microscopy The Lab on a Tip*. OCLC: 1255226372. Cham: Springer International Publishing AG, 2021. ISBN: 978-3-030-37089-3 (cit. on p. 60).

[221] R. Farrow et al. "Epitaxial growth of Pt on basal-plane sapphire: a seed film for artificially layered magnetic metal structures". In: *Journal of Crystal Growth* 133.1-2 (1993), pp. 47–58. ISSN: 00220248. DOI: 10.1016/0022-0248(93)90102-3 (cit. on pp. 61, 90).

[222] H. Zhou et al. "Investigation of platinum films grown on sapphire (0001) by molecular beam epitaxy". In: *Journal of Crystal Growth* 234.2 (2002), pp. 561–568. ISSN: 0022-0248. DOI: 10.1016/S0022-0248(01)01676-1 (cit. on p. 61).

[223] B. M. Lairson et al. “Epitaxial Pt(001), Pt(110), and Pt(111) films on MgO(001), MgO(110), MgO(111), and Al_2O_3(0001)”. In: *Applied Physics Letters* 61.12 (1992), pp. 1390–1392. ISSN: 0003-6951. DOI: 10.1063/1.107547 (cit. on p. 61).

[224] T. J. Minvielle et al. “Temperature dependence of the epitaxial growth of Pt on basal-plane sapphire”. In: *Surface Science* 366.3 (1996), pp. L755–L759. ISSN: 0039-6028. DOI: 10.1016/0039-6028(96)00941-7 (cit. on p. 61).

[225] T. Tachibana et al. “Heteroepitaxial growth of {111}-oriented diamond films on platinum{111}/sapphire{0001} substrates”. In: *Journal of Crystal Growth* 205.1 (1999), pp. 163–168. ISSN: 0022-0248. DOI: 10.1016/S0022-0248(99)00223-7 (cit. on p. 61).

[226] S. Ramanathan et al. “Microstructural study of epitaxial platinum and Permalloy/platinum films grown on (0001) sapphire”. In: *Philosophical Magazine A* 81.8 (2001), pp. 2073–2094. ISSN: 0141-8610. DOI: 10.1080/01418610108216653 (cit. on pp. 61, 91).

[227] C. Train and V. Mathet. “Morphology and magnetic properties of Pt/Co/Pt/Al_2O_3(0001) structures: influence of the growth temperature”. In: *Surface Science* 412-413 (1998), pp. 495–501. ISSN: 0039-6028. DOI: 10.1016/S0039-6028(98)00474-9 (cit. on p. 61).

[228] S. Roberts and R. J. Gorte. “A comparison of Pt overlayers on α-Al_2O_3(0001), ZnO(0001)Zn, and ZnO(000$\bar{1}$)O”. In: *The Journal of Chemical Physics* 93.7 (1990), pp. 5337–5344. ISSN: 0021-9606. DOI: 10.1063/1.459653 (cit. on p. 61).

[229] Y. Murata et al. “Layer growth of Pt on α-Al_2O_3/Ru(0001)”. In: *Surface Science* 493.1 (2001), pp. 114–119. ISSN: 0039-6028. DOI: 10.1016/S0039-6028(01)01197-9 (cit. on p. 61).

[230] R. Vargas et al. “Epitaxial growth of iridium and platinum films on sapphire by metalorganic chemical vapor deposition”. In: *Applied Physics Letters* 65.9 (1994), pp. 1094–1096. ISSN: 0003-6951. DOI: 10.1063/1.112108 (cit. on p. 61).

[231] A. Nefedov et al. “High-resolution x-ray scattering study of platinum thin films on sapphire”. In: *Journal of Physics: Condensed Matter* 10.4 (1998), pp. 717–730. ISSN: 0953-8984, 1361-648X. DOI: 10.1088/0953-8984/10/4/002 (cit. on p. 62).

[232] C. Gatel, P. Baules, and E. Snoeck. "Morphology of Pt islands grown on MgO(001)". In: *Journal of Crystal Growth* 252.1 (2003), pp. 424–432. ISSN: 0022-0248. DOI: 10.1016/S0022-0248(03)00868-6 (cit. on p. 64).

[233] L. Vitos et al. "The surface energy of metals". In: *Surface Science* 411.1 (1998), pp. 186–202. ISSN: 0039-6028. DOI: 10.1016/S0039-6028(98)00363-X (cit. on p. 64).

[234] D. M. Lipkin, J. N. Israelachvili, and D. R. Clarke. "Estimating the metal-ceramic van der Waals adhesion energy". In: *Philosophical Magazine A* 76.4 (1997), pp. 715–728. ISSN: 0141-8610. DOI: 10.1080/01418619708214205 (cit. on p. 64).

[235] F. R. d. Boer, ed. *Cohesion in metals: transition metal alloys*. 2., corr. print. Cohesion and structure 1. OCLC: 246582949. Amsterdam: North Holland, 1988. ISBN: 978-0-444-87098-8 (cit. on p. 64).

[236] M. Sui et al. "Effects of annealing temperature and duration on the morphological and optical evolution of self-assembled Pt nanostructures on c-plane sapphire". In: *PLOS ONE* 12.5 (2017), e0177048. ISSN: 1932-6203. DOI: 10.1371/journal.pone.0177048 (cit. on pp. 65, 91, 115).

[237] J.-C. Schober. "Temperature Depending Growth and Characterisation of Platinum Nanoparticles on (0001)-α-Al_2O_3". Bachelor's thesis. University of Hamburg, 2017 (cit. on pp. 65–67, 91).

[238] R. D. Long et al. "Charged Defect Quantification in Pt/Al_2O_3/$In_{0.53}Ga_{0.47}As$/InP MOS Capacitors". In: *Journal of The Electrochemical Society* 158.5 (2011), G103. ISSN: 00134651. DOI: 10.1149/1.3545799 (cit. on p. 88).

[239] D. J. Burnett et al. "Defect Enhanced Carbon Monoxide Oxidation at Elevated Oxygen Pressures on a Pt/Al_2O_3 Thin Film". In: *The Journal of Physical Chemistry B* 108.17 (2004), pp. 5314–5323. ISSN: 1520-6106. DOI: 10.1021/jp036012z (cit. on p. 88).

[240] I. Kasatkin et al. "Role of Lattice Strain and Defects in Copper Particles on the Activity of Cu/ZnO/Al_2O_3 Catalysts for Methanol Synthesis". In: *Angewandte Chemie International Edition* 46.38 (2007), pp. 7324–7327. ISSN: 1521-3773. DOI: https://doi.org/10.1002/anie.200702600 (cit. on p. 88).

[241] M. Choi, A. Janotti, and C. G. Van de Walle. "Native point defects and dangling bonds in α-Al_2O_3". In: *Journal of Applied Physics* 113.4 (2013), p. 044501. ISSN: 0021-8979. DOI: 10.1063/1.4784114 (cit. on p. 88).

[242] B. D. Evans, G. J. Pogatshnik, and Y. Chen. "Optical properties of lattice defects in α-Al_2O_3". In: *Nuclear Instruments and Methods in Physics Research Section B: Beam Interactions with Materials and Atoms* 91.1 (1994), pp. 258–262. ISSN: 0168-583X. DOI: 10.1016/0168-583X(94)96227-8 (cit. on p. 88).

[243] A. S. Ivanova et al. "Metal-support interactions in Pt/Al_2O_3 and Pd/Al_2O_3 catalysts for CO oxidation". In: *Applied Catalysis B: Environmental* 97.1 (2010), pp. 57–71. ISSN: 0926-3373. DOI: 10.1016/j.apcatb.2010.03.024 (cit. on p. 88).

[244] A. Fritsch and P. Légaré. "XPS study of the Pt/Al_2O_3 interface". In: *Surface Science Letters* 184.1 (1987), pp. L355–L360. ISSN: 0167-2584. DOI: 10.1016/0167-2584(87)90758-4 (cit. on p. 88).

[245] B. Hinnemann and E. A. Carter. "Adsorption of Al, O, Hf, Y, Pt, and S Atoms on α-Al_2O_3(0001)". In: *The Journal of Physical Chemistry C* 111.19 (2007), pp. 7105–7126. ISSN: 1932-7447. DOI: 10.1021/jp068869c (cit. on pp. 88–90).

[246] C. Zhou et al. "Growth Pathway of Pt Clusters on α-Al_2O_3(0001) Surface". In: *The Journal of Physical Chemistry C* 111.37 (2007), pp. 13786–13793. ISSN: 1932-7447. DOI: 10.1021/jp073131w (cit. on p. 88).

[247] H. O. Ayoola et al. "Probing the Local Bonding at the Pt/γ-Al_2O_3 Interface". In: *The Journal of Physical Chemistry C* 124.18 (2020), pp. 9876–9885. ISSN: 1932-7447. DOI: 10.1021/acs.jpcc.9b12029 (cit. on pp. 88, 90).

[248] J. Libuda et al. "Interaction of rhodium with hydroxylated alumina model substrates". In: *Surface Science* 384.1 (1997), pp. 106–119. ISSN: 0039-6028. DOI: 10.1016/S0039-6028(97)00170-2 (cit. on p. 89).

[249] M. Sterrer and H.-J. Freund. "Towards Realistic Surface Science Models of Heterogeneous Catalysts: Influence of Support Hydroxylation and Catalyst Preparation Method". In: *Catalysis Letters* 143.5 (2013), pp. 375–385. ISSN: 1572-879X. DOI: 10.1007/s10562-013-0987-5 (cit. on p. 89).

[250] M. García-Mota, M. Rieger, and K. Reuter. "Ab initio prediction of the equilibrium shape of supported Ag nanoparticles on α-Al_2O_3(0001)". In: *Journal of Catalysis* 321 (2015), pp. 1–6. ISSN: 0021-9517. DOI: 10.1016/j.jcat.2014.10.009 (cit. on p. 89).

[251] T. R. Ward, P. Alemany, and R. Hoffmann. “Adhesion of rhodium, palladium, and platinum to alumina and the reduction of nitric oxide on the resulting surfaces: a theoretical analysis”. In: *The Journal of Physical Chemistry* 97.29 (1993), pp. 7691–7699. ISSN: 0022-3654, 1541-5740. DOI: 10.1021/j100131a044 (cit. on p. 90).

[252] C. Verdozzi et al. “Sapphire (0001) Surface, Clean and with d-Metal Overlayers”. In: *Physical Review Letters* 82.4 (1999), pp. 799–802. DOI: 10.1103/PhysRevLett.82.799 (cit. on p. 90).

[253] G. Ehrlich and F. G. Hudda. “Atomic View of Surface Self-Diffusion: Tungsten on Tungsten”. In: *The Journal of Chemical Physics* 44.3 (1966), pp. 1039–1049. ISSN: 0021-9606. DOI: 10.1063/1.1726787 (cit. on pp. 91, 116).

[254] R. L. Schwoebel and E. J. Shipsey. “Step Motion on Crystal Surfaces”. In: *Journal of Applied Physics* 37.10 (1966), pp. 3682–3686. ISSN: 0021-8979. DOI: 10.1063/1.1707904 (cit. on pp. 91, 116).

[255] X. Wang, J. A. v. Bokhoven, and D. Palagin. “Atomically dispersed platinum on low index and stepped ceria surfaces: phase diagrams and stability analysis”. In: *Physical Chemistry Chemical Physics* 22.1 (2019), pp. 28–38. ISSN: 1463-9084. DOI: 10.1039/C9CP04973H (cit. on p. 91).

[256] X. Wang, J. A. v. Bokhoven, and D. Palagin. “Ostwald ripening versus single atom trapping: towards understanding platinum particle sintering”. In: *Physical Chemistry Chemical Physics* 19.45 (2017), pp. 30513–30519. ISSN: 1463-9084. DOI: 10.1039/C7CP05887J (cit. on p. 91).

[257] P. N. Plessow and F. Abild-Pedersen. “Sintering of Pt Nanoparticles via Volatile PtO_2: Simulation and Comparison with Experiments”. In: *ACS Catalysis* 6.10 (2016), pp. 7098–7108. DOI: 10.1021/acscatal.6b01646 (cit. on p. 91).

[258] T. W. Hansen et al. “Sintering of Catalytic Nanoparticles: Particle Migration or Ostwald Ripening?” In: *Accounts of Chemical Research* 46.8 (2013), pp. 1720–1730. ISSN: 0001-4842. DOI: 10.1021/ar3002427 (cit. on pp. 93, 94, 115).

[259] S. B. Simonsen et al. “Direct Observations of Oxygen-induced Platinum Nanoparticle Ripening Studied by In Situ TEM”. In: *Journal of the American Chemical Society* 132.23 (2010), pp. 7968–7975. ISSN: 0002-7863. DOI: 10.1021/ja910094r (cit. on pp. 94, 115).

[260] J. Y. Park et al. “Tuning of Catalytic CO Oxidation by Changing Composition of Rh-Pt Bimetallic Nanoparticles”. In: *Nano Letters* 8.2 (2008), pp. 673–677. ISSN: 1530-6984. DOI: 10.1021/nl073195i (cit. on p. 94).

[261] J. H. Sinfelt. “Structure of bimetallic clusters”. In: *Accounts of Chemical Research* 20.4 (1987), pp. 134–139. ISSN: 0001-4842. DOI: 10.1021/ar00136a002 (cit. on p. 94).

[262] N. Toshima and T. Yonezawa. “Bimetallic nanoparticles—novel materials for chemical and physical applications”. In: *New Journal of Chemistry* 22.11 (1998), pp. 1179–1201. ISSN: 1369-9261. DOI: 10.1039/A805753B (cit. on p. 94).

[263] P. Müller et al. “In situ oxidation study of Pd–Rh nanoparticles on $MgAl_2O_4(001)$”. In: *Phys. Chem. Chem. Phys.* 16.27 (2014), pp. 13866–13874. ISSN: 1463-9076, 1463-9084. DOI: 10.1039/C4CP01271B (cit. on p. 94).

[264] F. Tao et al. “Evolution of Structure and Chemistry of Bimetallic Nanoparticle Catalysts under Reaction Conditions”. In: *Journal of the American Chemical Society* 132.25 (2010), pp. 8697–8703. ISSN: 0002-7863, 1520-5126. DOI: 10.1021/ja101502t (cit. on pp. 94, 96, 97).

[265] A. Kalinkin, A. Pashis, and V. Bukhtiyarov. “CO oxidation over the Pt-Rh system. 3. Reaction on a heterophase surface”. In: *Reaction Kinetics and Catalysis Letters* 78.1 (2003), pp. 121–127. ISSN: 1588-2837. DOI: 10.1023/A:1022522118315 (cit. on p. 96).

[266] A. Kalinkin, A. Pashis, and V. Bukhtiyarov. “CO oxidation over the Pt-Rh system. 2. Reaction on an alloy”. In: *Reaction Kinetics and Catalysis Letters* 78.1 (2003), pp. 107–112. ISSN: 1588-2837. DOI: 10.1023/A:1022518017407 (cit. on p. 96).

[267] A. Ruban and H. Skriver. “Calculated surface segregation in transition metal alloys”. In: *Computational Materials Science* 15.2 (1999), pp. 119–143. ISSN: 09270256. DOI: 10.1016/S0927-0256(99)00003-8 (cit. on pp. 96, 138).

[268] J. A. Herron and M. Mavrikakis. “On the composition of bimetallic near-surface alloys in the presence of oxygen and carbon monoxide”. In: *Catalysis Communications* 52 (2014), pp. 65–71. ISSN: 15667367. DOI: 10.1016/j.catcom.2013.10.021 (cit. on p. 96).

[269] M. E. Grass et al. “A Reactive Oxide Overlayer on Rhodium Nanoparticles during CO Oxidation and Its Size Dependence Studied by In Situ Ambient-Pressure X-ray Photoelectron Spectroscopy”. In: *Angewandte Chemie International Edition* 47.46 (2008), pp. 8893–8896. ISSN: 1521-3773. DOI: https://doi.org/10.1002/anie.200803574 (cit. on p. 96).

[270] J. Florencio, D. Ren, and T. T. Tsong. “Absolute composition depth-profiles in surface segregation of Pt-Rh alloys”. In: *Surface Science* 345.3 (1996), pp. L29–L33. ISSN: 00396028. DOI: 10.1016/0039-6028(95)01041-6 (cit. on p. 96).

[271] E. Platzgummer et al. “Temperature-dependent segregation on $Pt_{25}Rh_{75}$(111) and (100)”. In: *Surface Science* 419.2-3 (1999), pp. 236–248. ISSN: 00396028. DOI: 10.1016/S0039-6028(98)00800-0 (cit. on pp. 96, 138).

[272] B. Legrand and G. Tréglia. “Surface segregation in PtRh alloys revisited in the framework of the tight-binding Ising model”. In: *Surface Science* 236.3 (1990), pp. 398–408. ISSN: 00396028. DOI: 10.1016/0039-6028(90)90482-N (cit. on p. 96).

[273] D. M. Ren et al. “Oscillatory compositional depth profiles in surface segregation of a Pt-Rh alloy”. In: *Physical Review B* 47.7 (1993), pp. 3944–3946. ISSN: 0163-1829, 1095-3795. DOI: 10.1103/PhysRevB.47.3944 (cit. on p. 96).

[274] A. M. Schoeb et al. “Driving force for surface segregation in bimetallic catalysts”. In: *Surface Science Letters* 278 (1992), pp. L125–L130. DOI: 10.1016/0039-6028(92)90573-O (cit. on p. 96).

[275] M. Brejnak, J. Kudrnovský, and P. Modrak. “Electronic theory of surface segregation in transition metal alloys”. In: *Surface Science* 307-309 (1994), pp. 821–825. ISSN: 00396028. DOI: 10.1016/0039-6028(94)91498-2 (cit. on p. 96).

[276] M. Brejnak and P. Modrak. “Electronic theory of surface segregation in the coherent potential approximation: The surface segregation in CoNi, IrPt and RhPt”. In: *Surface Science* 280.3 (1993), pp. L285–L290. ISSN: 0039-6028. DOI: 10.1016/0039-6028(93)90676-B (cit. on p. 96).

[277] U. Hejral et al. “Identification of a Catalytically Highly Active Surface Phase for CO Oxidation over PtRh Nanoparticles under Operando Reaction Conditions”. In: *Physical Review Letters* 120.12 (2018). ISSN: 0031-9007, 1079-7114. DOI: 10.1103/PhysRevLett.120.126101 (cit. on pp. 96, 114, 115, 138).

[278] S. R. Challa et al. “Relating Rates of Catalyst Sintering to the Disappearance of Individual Nanoparticles during Ostwald Ripening”. In: *Journal of the American Chemical Society* 133.51 (2011), pp. 20672–20675. ISSN: 0002-7863. DOI: 10.1021/ja208324n (cit. on p. 115).

[279] D. Ferri, T. Bürgi, and A. Baiker. “Pt and Pt/Al_2O_3 Thin Films for Investigation of Catalytic Solid-Liquid Interfaces by ATR-IR Spectroscopy: CO Adsorption, H_2-Induced Reconstruction and Surface-Enhanced Absorption”. In: *The Journal of Physical Chemistry B* 105.16 (2001), pp. 3187–3195. ISSN: 1520-6106. DOI: 10.1021/jp002268i (cit. on p. 116).

[280] K. Giewekemeyer et al. “Experimental 3D coherent diffractive imaging from photon-sparse random projections”. In: *IUCrJ* 6.3 (2019), pp. 357–365. ISSN: 2052-2525. DOI: 10.1107/S2052252519002781 (cit. on p. 119).

[281] Y. Y. Kim et al. “Single Alloy Nanoparticle X-Ray Imaging during a Catalytic Reaction”. In: *arXiv:2103.01573 [cond-mat]* (2021). arXiv: 2103.01573 (cit. on pp. 120, 131, 134–138, 151).

[282] W. Guo, A. B. Posadas, and A. A. Demkov. “Temperature dependence of the morphology and electronic structure of ultrathin platinum on TiO_2-teminated $SrTiO_3$ (001)”. In: *Journal of Vacuum Science & Technology B* 35.6 (2017), p. 061203. ISSN: 2166-2746. DOI: 10.1116/1.4991892 (cit. on p. 120).

[283] Z. Feng et al. “Thermally induced nanoscale structural and morphological changes for atomic-layer-deposited Pt on $SrTiO_3$(001)”. In: *Journal of Applied Physics* 110.10 (2011), p. 102202. ISSN: 0021-8979. DOI: 10.1063/1.3661163 (cit. on p. 120).

[284] M. Kasai and H. Dohi. “Surface structure and electrochemical properties of platinum films grown on $SrTiO_3$(100) substrates”. In: *Surface Science* 666 (2017), pp. 14–22. ISSN: 00396028. DOI: 10.1016/j.susc.2017.08.018 (cit. on p. 120).

[285] A. D. Polli et al. “Growth of platinum on TiO_2- and SrO-terminated $SrTiO_3$ (100)”. In: *Surface Science* 448.2 (2000), pp. 279–289. ISSN: 0039-6028. DOI: 10.1016/S0039-6028(99)01233-9 (cit. on p. 121).

[286] G. A. Chahine et al. “Imaging of strain and lattice orientation by quick scanning X-ray microscopy combined with three-dimensional reciprocal space mapping”. In: *Journal of Applied Crystallography* 47.2 (2014), pp. 762–769. ISSN: 1600-5767. DOI: 10.1107/S1600576714004506 (cit. on p. 125).

[287] S. J. Leake et al. “The Nanodiffraction beamline ID01/ESRF: a microscope for imaging strain and structure”. In: *Journal of Synchrotron Radiation* 26.2 (2019), pp. 571–584. ISSN: 1600-5775. DOI: 10.1107/S160057751900078X (cit. on p. 125).

[288] I. A. Vartanyants and I. K. Robinson. “Partial coherence effects on the imaging of small crystals using coherent x-ray diffraction”. In: *Journal of Physics: Condensed Matter* 13.47 (2001), pp. 10593–10611. ISSN: 0953-8984, 1361-648X. DOI: 10.1088/0953-8984/13/47/305 (cit. on pp. 126, 127).

[289] R. Gerchberg and W. Saxton. “Practical algorithm for determination of phase from image and diffraction plane pictures”. In: *Optik* 35.2 (1972), pp. 237–246 (cit. on p. 126).

[290] J. R. Fienup. “Phase retrieval algorithms: a comparison”. In: *Applied Optics* 21.15 (1982), p. 2758. ISSN: 0003-6935, 1539-4522. DOI: 10.1364/AO.21.002758 (cit. on p. 126).

[291] I. Vartanyants and O. Yefanov. “Coherent X-Ray Diffraction Imaging of Nanostructures”. In: *X-Ray Diffraction*. Ed. by O. Seeck and B. Murphy. Pan Stanford, 2015, pp. 341–384. ISBN: 978-981-4303-59-0 978-981-4303-60-6. DOI: 10.1201/b15674-13 (cit. on p. 127).

[292] P. Kirkpatrick and A. V. Baez. “Formation of Optical Images by X-Rays”. In: *JOSA* 38.9 (1948), pp. 766–774. DOI: 10.1364/JOSA.38.000766 (cit. on p. 128).

[293] B. Niemann, D. Rudolph, and G. Schmahl. “Soft X-ray imaging zone plates with large zone numbers for microscopic and spectroscopic applications”. In: *Optics Communications* 12.2 (1974), pp. 160–163. ISSN: 0030-4018. DOI: 10.1016/0030-4018(74)90381-2 (cit. on p. 128).

[294] C. G. Schroer. “Focusing hard x rays to nanometer dimensions using Fresnel zone plates”. In: *Physical Review B* 74.3 (2006), p. 033405. DOI: 10.1103/PhysRevB.74.033405 (cit. on p. 128).

[295] B. Lengeler et al. “Parabolic refractive X-ray lenses”. In: *Journal of Synchrotron Radiation* 9.3 (2002), pp. 119–124. ISSN: 0909-0495. DOI: 10.1107/S0909049502003436 (cit. on p. 128).

[296] I. A. Vartanyants and A. Singer. “Coherence properties of hard x-ray synchrotron sources and x-ray free-electron lasers”. In: *New Journal of Physics* 12.3 (2010), p. 035004. ISSN: 1367-2630. DOI: 10.1088/1367-2630/12/3/035004 (cit. on p. 128).

[297] A. Mancuso, O. Yefanov, and I. Vartanyants. “Coherent diffractive imaging of biological samples at synchrotron and free electron laser facilities”. In: *Journal of Biotechnology* 149.4 (2010), pp. 229–237. ISSN: 01681656. DOI: 10.1016/j.jbiotec.2010.01.024 (cit. on p. 128).

[298] A. P. Mancuso et al. “Coherent-Pulse 2D Crystallography Using a Free-Electron Laser X-Ray Source”. In: *Physical Review Letters* 102.3 (2009). ISSN: 0031-9007, 1079-7114. DOI: 10.1103/PhysRevLett.102.035502 (cit. on p. 128).

[299] H. N. Chapman et al. “Femtosecond X-ray protein nanocrystallography”. In: *Nature* 470.7332 (2011), pp. 73–77. ISSN: 1476-4687. DOI: 10.1038/nature09750 (cit. on p. 128).

[300] R. Neutze et al. “Potential for biomolecular imaging with femtosecond X-ray pulses”. In: *Nature* 406.6797 (2000), pp. 752–757. ISSN: 0028-0836. DOI: 10.1038/35021099 (cit. on p. 128).

[301] W. H. Massover. “Radiation damage to protein specimens from electron beam imaging and diffraction: a mini-review of anti-damage approaches, with special reference to synchrotron X-ray crystallography”. In: *Journal of Synchrotron Radiation* 14.Pt 1 (2007), pp. 116–127. ISSN: 0909-0495. DOI: 10.1107/S0909049506052307 (cit. on p. 128).

[302] C. Caleman et al. “On the feasibility of nanocrystal imaging using intense and ultrashort X-ray pulses”. In: *ACS nano* 5.1 (2011), pp. 139–146. ISSN: 1936-086X. DOI: 10.1021/nn1020693 (cit. on p. 128).

[303] D. Dzhigaev et al. “Bragg coherent x-ray diffractive imaging of a single indium phosphide nanowire”. In: *Journal of Optics* 18.6 (2016), p. 064007. ISSN: 2040-8978, 2040-8986. DOI: 10.1088/2040-8978/18/6/064007 (cit. on p. 128).

[304] M.-I. Richard et al. “Crystallographic orientation of facets and planar defects in functional nanostructures elucidated by nano-focused coherent diffractive X-ray imaging”. In: *Nanoscale* 10.10 (2018), pp. 4833–4840. ISSN: 2040-3372. DOI: 10.1039/C7NR07990G (cit. on p. 128).

[305] A. V. Zozulya et al. "*In situ* X-ray crystallographic study of the structural evolution of colloidal crystals upon heating". In: *Journal of Applied Crystallography* 46.4 (2013), pp. 903–907. ISSN: 0021-8898. DOI: 10.1107/S0021889813003725 (cit. on p. 128).

[306] T. Kawaguchi et al. "Gas-Induced Segregation in Pt-Rh Alloy Nanoparticles Observed by In Situ Bragg Coherent Diffraction Imaging". In: *Physical Review Letters* 123.24 (2019), p. 246001. DOI: 10.1103/PhysRevLett.123.246001 (cit. on p. 128).

[307] J. Wellendorff et al. "A benchmark database for adsorption bond energies to transition metal surfaces and comparison to selected DFT functionals". In: *Surface Science*. Reactivity Concepts at Surfaces: Coupling Theory with Experiment 640 (2015), pp. 36–44. ISSN: 0039-6028. DOI: 10.1016/j.susc.2015.03.023 (cit. on p. 138).

[308] Z. Crljen et al. "Relaxation and reconstruction on (111) surfaces of Au, Pt, and Cu". In: *Physical Review B* 68.19 (2003), p. 195411. DOI: 10.1103/PhysRevB.68.195411 (cit. on p. 151).

[309] J. Wan et al. "Surface relaxation and stress of fcc metals: Cu, Ag, Au, Ni, Pd, Pt, Al and Pb". In: *Modelling and Simulation in Materials Science and Engineering* 7.2 (1999), pp. 189–206. ISSN: 0965-0393. DOI: 10.1088/0965-0393/7/2/005 (cit. on p. 151).

[310] A. R. Sandy et al. "Reconstruction of the Pt(111) surface". In: *Physical Review Letters* 68.14 (1992), pp. 2192–2195. DOI: 10.1103/PhysRevLett.68.2192 (cit. on p. 151).

[311] G. Grübel et al. "Reconstruction of the Pt(111) surface: X-ray-scattering measurements". In: *Physical Review B* 48.24 (1993), pp. 18119–18139. DOI: 10.1103/PhysRevB.48.18119 (cit. on p. 151).

[312] W. Rasband. *ImageJ*. http://imagej.nih.gov/ij. USA, Accessed 10 July 2021 (cit. on p. 197).

[313] C. A. Schneider, W. S. Rasband, and K. W. Eliceiri. "NIH Image to ImageJ: 25 years of Image Analysis". In: *Nature methods* 9.7 (2012), pp. 671–675. ISSN: 1548-7091 (cit. on p. 197).

[314] P. Klapetek and D. Nečas. *Gwyddion*. http://gwyddion.net/. Accessed 10 July 2021 (cit. on p. 197).

[315] D. Nečas and P. Klapetek. “Gwyddion: an open-source software for SPM data analysis”. In: *Open Physics* 10.1 (2012). ISSN: 2391-5471. DOI: 10.2478/s11534-011-0096-2 (cit. on p. 197).

Appendix A.

Sample details

A.1. List of samples

In the course of the present work, dozens of samples have been grown. The most important samples, that contributed to this work, are listed in Table A.1. Sample names in column *original name* starting with "ID" where grown either by or together with Christoph Seitz. Samples 1 to 5 were grown either by or together with Jan-Christian Schober. Manuel Abuìn Herraez was involved in the growth of most of the samples. For samples 17 and 18, 10 nm Pt were deposited at RT by Miriam Barthelmeß[1] on bare alumina substrates using a Winter Vakuumtechnik[2] HVB 100 electron beam evaporator (deposition rate 0.02 nm/s, pressure $7 \cdot 10^{-7}$ mbar, sample rotation at 10 rpm). After postannealing in the tube furnace, the samples were transferred to the UHV-system and Rh was deposited the usual way. Sample 26 was annealed after deposition in the tube furnace, but reached the maximum temperature only for a few seconds due to wrong programming of the temperature controller. The ramping speed for heating up was set to 1200 K/h and cooling down takes even longer, so the sample was in the temperature range above 1100 °C for at least 10 min. Samples 2 and 21, and samples 4 and 22 are the same samples, respectively. The original samples 2 and 4 were modified later on. Those samples were given different names referring to different stages of preparation to avoid confusion in the main text.

[1] DESY, Notkestraße 85, DE-22607 Hamburg.
[2] Winter Vakuumtechnik, Kreuzwegäcker 24, DE-71711 Steinheim an der Murr.

Sample number	original name	substrate	dep. time [min]	flux Pt/Rh [nA]	dep. temp. [°C]	postannealing	comment
1	Pt5	Al_2O_3	118	19.7/0	530	no	
2	Pt6	Al_2O_3	120	21.1/44.2	630	no	
3	Pt7	Al_2O_3	120	36.01/0	RT	no	
4	Pt8	Al_2O_3	102	37.7/0	830	no	
5	Pt9	Al_2O_3	103	36.7/0	330	no	
6	PtRh1	Al_2O_3	240	18.5/4.2	830	UHV, 1100 °C, 10 min	
7	PtRh2	Al_2O_3	90	18/3.8	830	UHV, 1100 °C, 10 min; UHV, 1150 °C, 150 min	
8	PtRh3	Al_2O_3	50	17.3/3.3	1000	no	
9	PtRh4	Al_2O_3	45	18/3.8	830	UHV, 1100 °C, 30 min; UHV, 1200 °C, 60 min	
10	PtRh5	Al_2O_3	30	20.9/3.6	830	UHV, 1200 °C, 60 min	
11	PtRh7	Al_2O_3	30	19.5/13	830	UHV, 1100-1200 °C, 60 min	
12	PtRh8	Al_2O_3	10/6	19.2/14.5	830	UHV, 1100-1200 °C, 60 min	
13	PtRh10	$SrTiO_3$	30	19.5/13.0	830	UHV, 1200 °C, 60 min	ESRF2017
14	PtRh11	$SrTiO_3$	10/6	19.2/14.5	830	UHV, 1200 °C, 60 min	
15	PtRh12	$SrTiO_3$	55	21.5/0	800	TF, 1100 °C, 10 min	
16	PtRh15	$SrTiO_3$	55	21.5/0	800	no	
17	PtRh16	Al_2O_3	x/140	x/84.17	RT/650	TF, 1200 °C, 10 min	
18	PtRh17	Al_2O_3	x/140	x/84.17	RT/650	TF, 1300 °C, 10 min	ESRF2017
19	PtRh18	Al_2O_3	118/53	21.2/44.9	630/620	TF, 1000 °C, 10 min	APS2018
20	PtRh19	Al_2O_3	116/53	22.7/44.4	630/620	TF, 1000 °C, 10 min	ESRF2018
21	Pt6+Rh	Al_2O_3	120/53	21.1/44.2	630/620	TF, 1000 °C, 10 min	APS2018
22	Pt8 annealed	Al_2O_3	102	37.7/0	830	TF, 1100 °C, 10 min	
23	ID19AlOA5-A	Al_2O_3	218	17.8/4.0	830	UHV, 1100 °C, 10 min	P21 2019
24	ID19AlOA5-B	Al_2O_3	218	17.8/4.0	830	UHV, 1100 °C, 10 min	P23 2019
25	ID19STOA8-B	$SrTiO_3$	29	20.5/14.0	630	UHV, 1200 °C, 60 min	
26	Pt10-A	Al_2O_3	165	27.4/0	830	UHV, 1100 °C, 10 min; TF, 1200 °C, few seconds	
27	Pt10-B	Al_2O_3	165	27.4/0	830	UHV, 1100 °C, 10 min	

Table A.1.: Overview of the most relevant information on the most important samples. Split fields indicate values for Pt and Rh, respectively. Two specifications in the field for deposition time indicate subsequent deposition of the noble metals. TF in *postannealing* is an abbreviation for tube furnace, which means the sample was annealed in air after deposition of noble metals.

A.2. Information on substrates

Samples 1-12 and 17-18 (most likely) were grown using following substrates:

- Manufacturer: SurfaceNet GmbH
- Lot. No.: 7319-17 (7319200717)
- Material: Al2O3
- Orientation: (0001)K(1120) 2 slots
- Size: $10 \times 10\,\mathrm{mm}^2$
- Thickness: 1 mm
- Polishing: 1 epi pol

The sample from publication [146] was grown using following substrate:

- Manufacturer: SurfaceNet GmbH
- Lot. No.: 6280250416
- Material: SrTiO3 0.1 wt% Nb
- Orientation: (001)$\pm$ 0.1 $^\circ$ K(010)
- Size: $10 \times 5\,\mathrm{mm}^2$
- Thickness: 0.5 mm
- Polishing: 1 epi pol

Samples 13-16 were grown using following substrates:

- Manufacturer: SurfaceNet GmbH
- Lot. No.: 7501250917
- Material: SrTiO3 0.7 wt% Nb
- Orientation: (001)$\pm$ 0.1 $^\circ$ K(010)
- Size: $10 \times 5\,\mathrm{mm}^2$
- Thickness: 0.5 mm
- Polishing: 1 epi pol

Appendix B.

Supplementary information on SEM- and AFM-measurements

B.1. Markers for correlation of positions

This section contains Figures B.1, B.2, and B.3, which indicate how areas of interest were tracked in between experiments.

B.2. Image analysis for SEM and AFM-images

SEM-images were analysed using the program *ImageJ*, see [312, 313]. Here, the spatial scale can be set in the desired unit and range within the program. Afterwards, either a colour- or a contrast threshold is set and structures above (or below) the threshold will be counted as particles. All statistics like counting, average area etc. are done by the program. The area of a particle is that of a closed object with colour values above the selected threshold. No further refinement concerning circularity or size selection was undertaken. A problem concerning reproducibility and systematics is that if one looked at several SEM-images, the images would exhibit different image contrasts and brightnesses. Accordingly, this has to be accounted for manually.
AFM-micrographs were analysed with the program *Gwyddion*, see [314, 315]. Images were levelled properly using a three-point method and setting the resulting minimum to zero. Sometimes, further image processing has been undertaken by removing fast-scanning features, as can be seen in figures B.4 and B.7. For the latter image, horizontal line artefacts were removed via the *Remove Scares* tool in Gwyddion. In Figure B.6, the *Mark grains by threshold* was used to mask particles that surpass a height threshold of – here – 3 nm. Statistics then can be applied to this preselected area, yielding a height distribution that basically resembles the distribution without

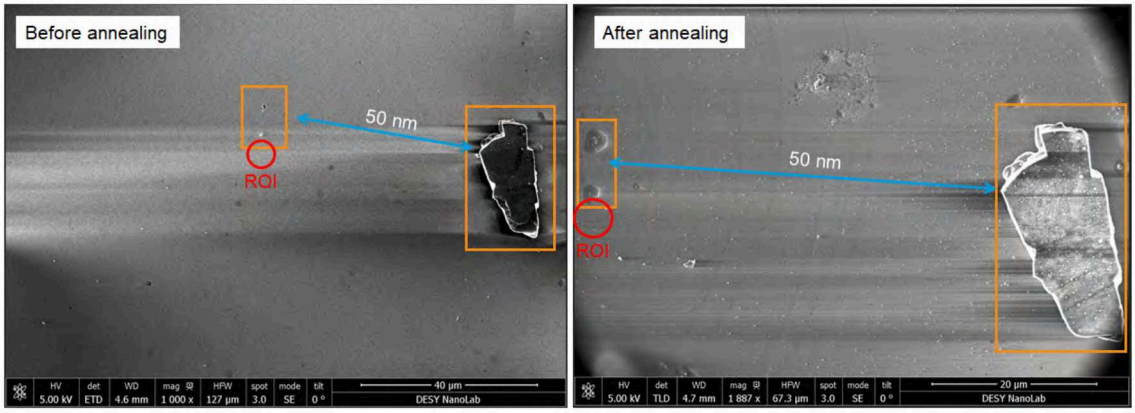

Figure B.1.: Correlation of a specific region of interest (red) on the same sample before (left) and after (right) treatment in a tube furnace. Inhomogeneities like the macroscopic particles marked in orange in the respective images allow for the original region of interest to be tracked back. Images here were taken on sample 26. The distance between the two areas indicated is 50 µm and not 50 nm.

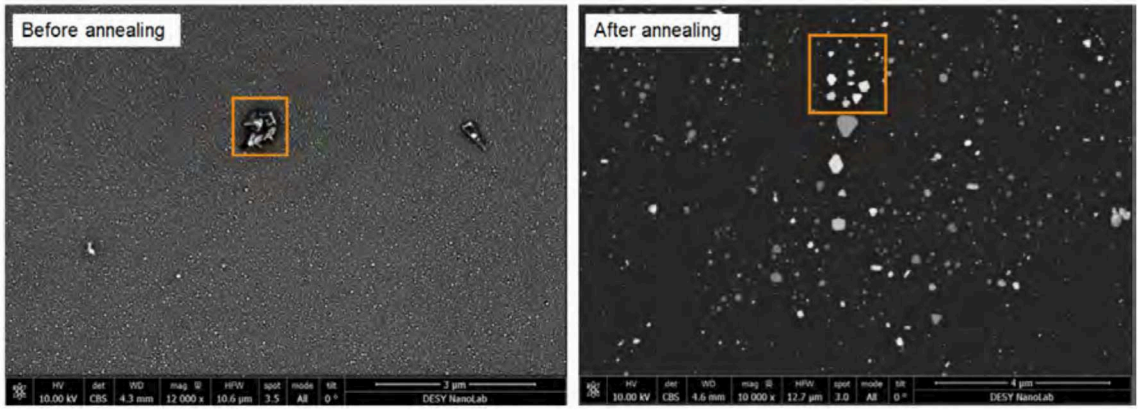

Figure B.2.: Correlation of a specific region of interest (marked red in Figure B.1) on sample 26 before (left) and after (right) treatment in a tube furnace. The orange area marks the position of a macroscopic inhomogeneity to track the area of interest.

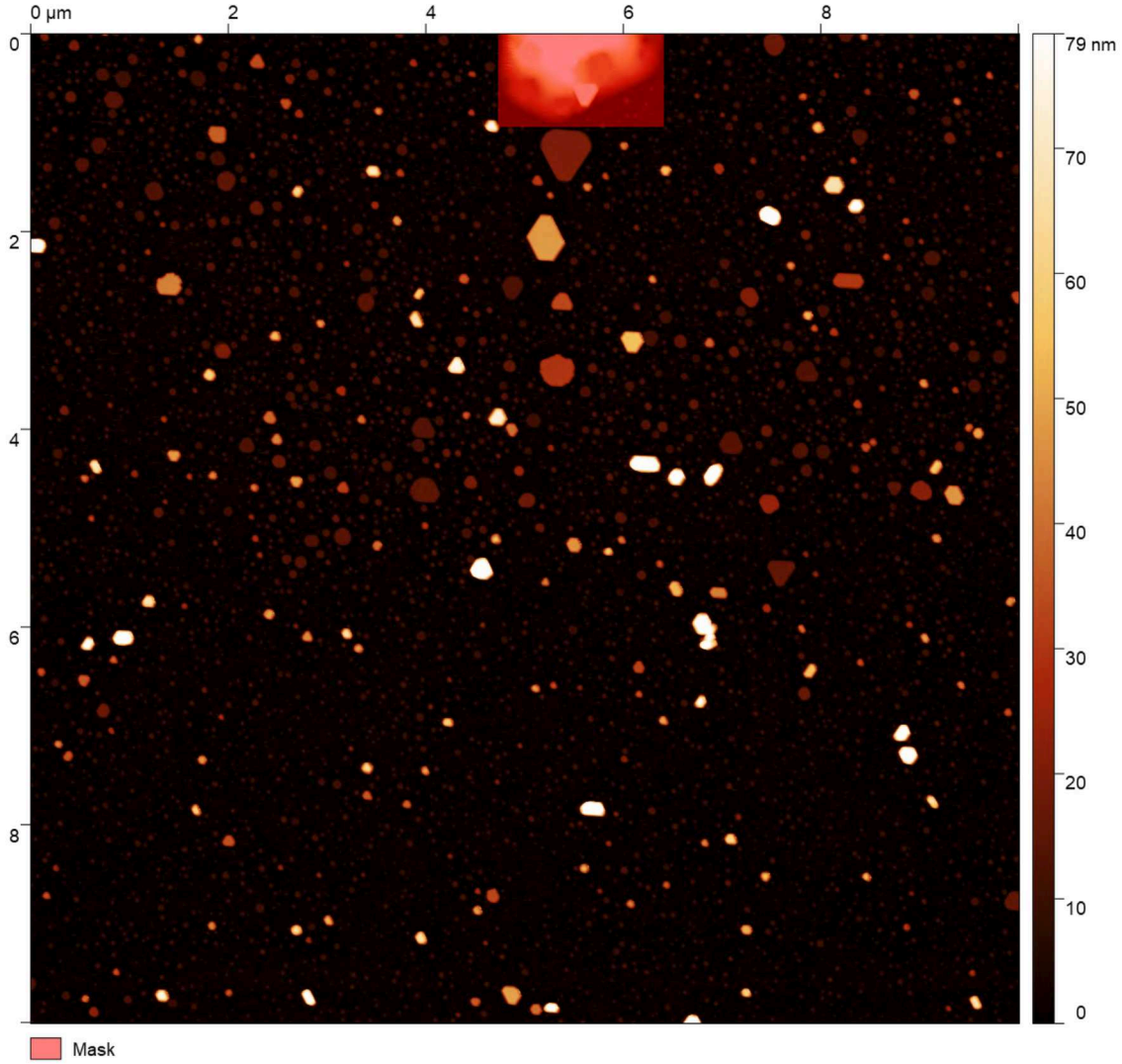

Figure B.3.: AFM micrograph of the area of interest on sample 26. The area marked in red is excluded from particle analysis.

threshold, but above 3 nm – see Figure B.8. The peaks are slightly shifted in height, most likely due to different levelling. The average height of particles above a threshold of 3 nm is about 13.8 nm. All statistics are done by the program itself. Plotting has been done using Matlab.

B.3. Supporting images for AFM and SEM-analysis

This section contains further figures supporting the thesis with complementary information – see Section B.2. The scale of Figures B.4 and B.5 is misleading on an absolute scale, as it is supposed to serve the purpose to identify features of almost negligible height, which would vanish on other scales. To relate the absolute height with the corresponding objects in the image, it is referred to other AFM images in Section 3.3 or other images in the Appendix.

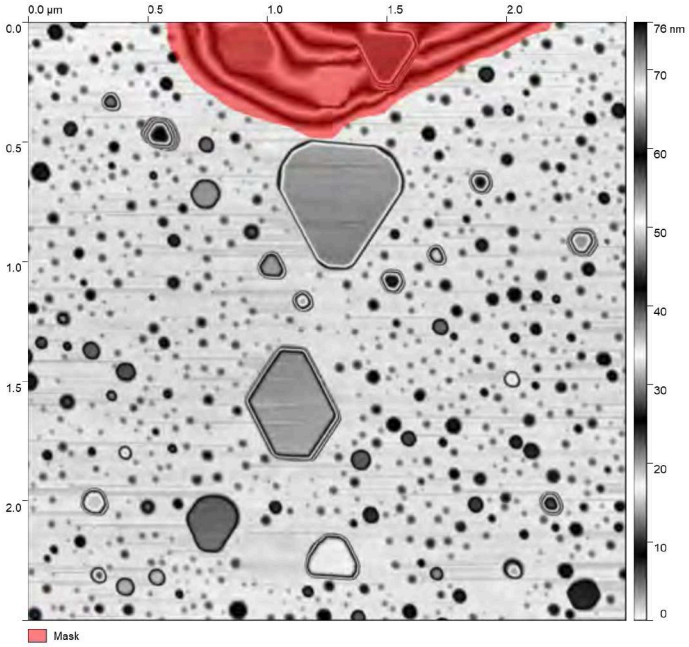

Figure B.4.: AFM-micrograph (height sensor) of the preselected area of interest on sample 26 after annealing in air. The substrate's surface was levelled and set to 0 nm height. No further processing was undertaken. Excluding the masked region (in red), the average height is 4.06 nm. The alternating scale is chosen in a way to highlight horizontal, stripe-like features, not to identify absolute heights of particles.

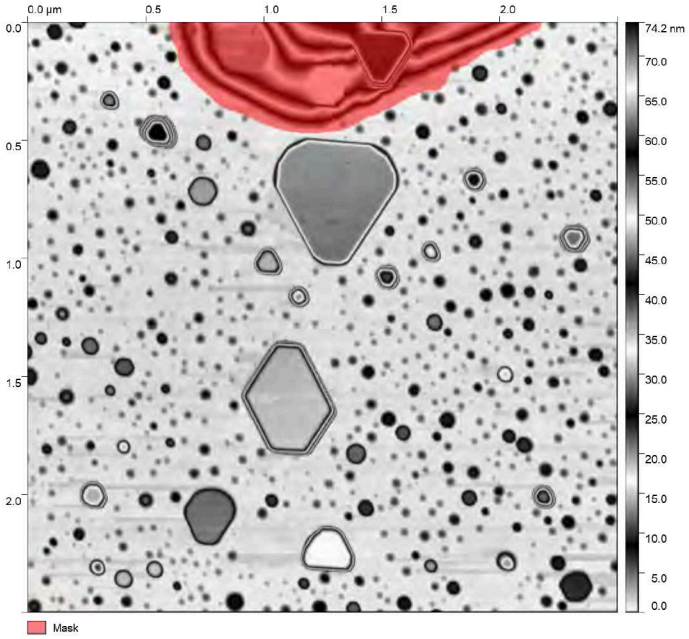

Figure B.5.: AFM-micrograph of the preselected area of interest on sample 26 after annealing in air. The substrate's surface was levelled and set to 0 nm height. Fast-scanning artefacts along the x-axis were partially eliminated using the *Remove Scars* feature in Gwyddion. Excluding the masked region (in red), the average height is 4.04 nm. The scale is chosen in a way to highlight stripe-like features, not to identify absolute heights of particles.

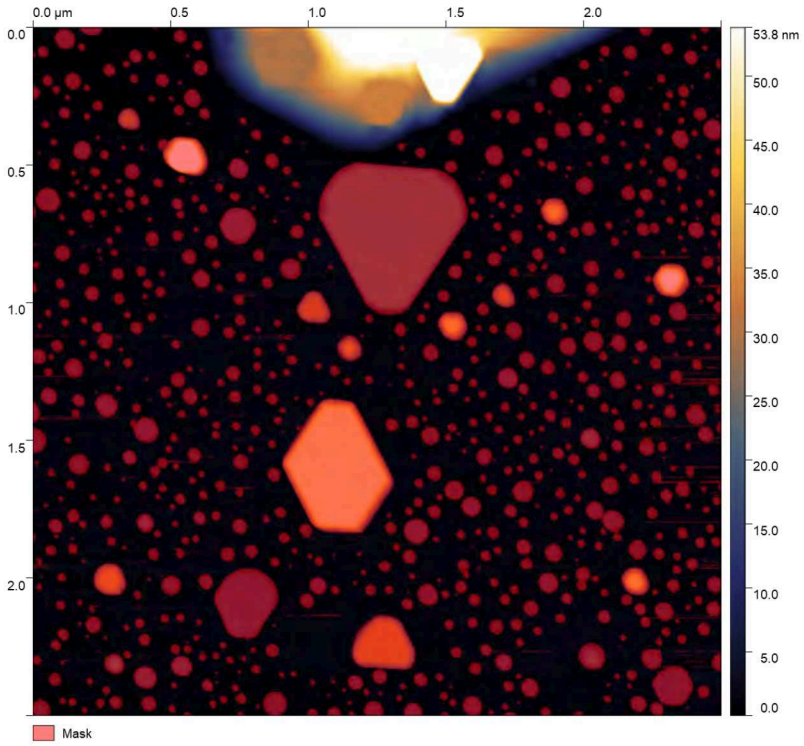

Figure B.6.: Image of the region of interest on sample 26 after annealing. Here, the Gwyddion tool *Mark grains by threshold* was used to preselect particles on the surface for further analysis, the mask is coloured in red.

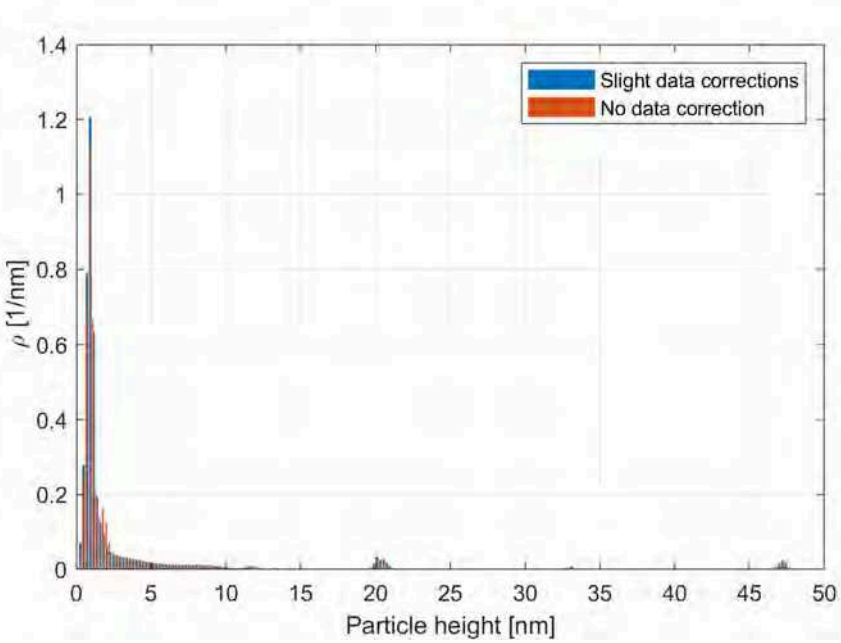

Figure B.7.: Particle height distribution functions for AFM-images B.4 and B.5. The former image was corrected using the *Remove Scars* feature of the program Gwyddion.

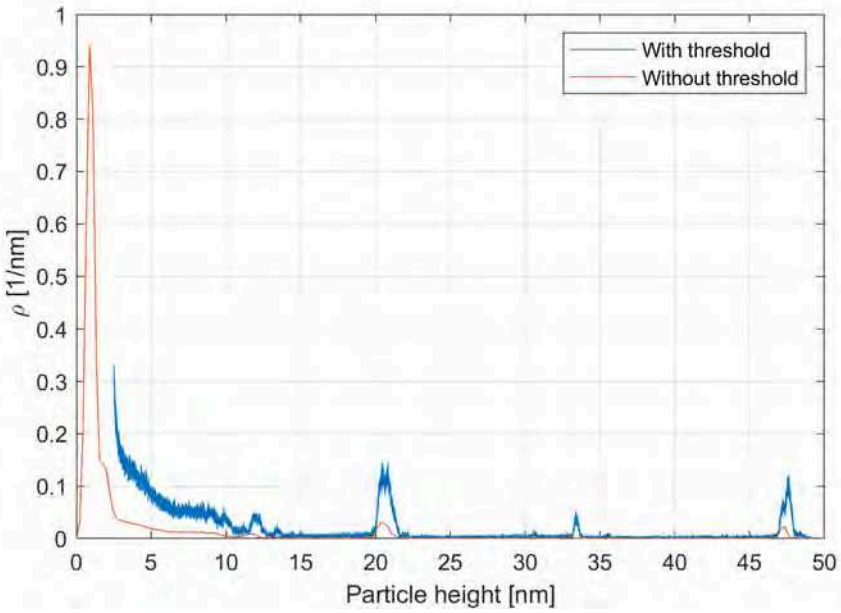

Figure B.8.: Particle height distribution functions for AFM-image B.4. The height distribution is plotted for the image with height threshold set to 3 nm (blue) and without any threshold (orange).

Appendix C.

Supporting X-ray studies and info concerning X-ray measurements

C.1. SXRD ensemble study on sample 13

Following the catalytic CXDI study, the average orientation of the alloy nanoparticles with respect to the STO-susbstrate and the orientation of the substrate's edges were determined using grazing incidence X-ray diffraction. The study was further supported by wide-angle XRR. For this purpose, a six circle diffractometer with a source emitting Cu-Kαradiation were employed – see Section 2.5.3.
Gracing incidence rocking scans around the surface normal with $\alpha_i = \alpha_f = 0.3°$ confirmed the (100)-orientation of the crystal's side edges (data not shown). Figure C.1 shows a wide-angle XRR on sample 13. Clearly, (001) and (002) Bragg peaks are visible and confirm the (001)-orientation of the substrate's surface. The narrow $(002)_{\mathrm{STO}}$ Bragg peak is overlaying a broader signal which might by originating from (002) and (111) oriented particles with varying composition and tilt towards the surface normal, hence the broad peak is asymmetric, broad and hard to assign[1]. To get additional information about the average nanoparticle orientation, mesh-scans in reciprocal space were conducted, see Figure C.2. $\mathrm{H_S}$, $\mathrm{K_S}$, and $\mathrm{L_S}$ are the reciprocal surface coordinates corresponding to the STO simple cubic unit vectors $\boldsymbol{a}$, $\boldsymbol{b}$, $\boldsymbol{c}$ with $|\boldsymbol{a}| = |\boldsymbol{b}| = |\boldsymbol{c}| = a_{\mathrm{STO}} = 3.905\,\text{Å}$ and $\mathrm{H_S}$, $\mathrm{K_S}$ beeing aligned with the $(100)_{\mathrm{STO}}$ and $(010)_{\mathrm{STO}}$ bulk in-plane unit vectors, respectively. $\mathrm{L_S}$ refers to the out-of plane component of the reciprocal lattice. The reflexes circled in orange colour $(101)_{\mathrm{S}}$,

[1]Note, that likely for this measurement the surface normal has been aligned using the substrate's (002) Bragg peak. This causes signals from particles, which might exhibit a significant tilt of their growth direction towards the substrate's orientation, to significantly decrease in intensity when measuring in specular geometry. Accordingly, particle signal might not be visible in this scan.

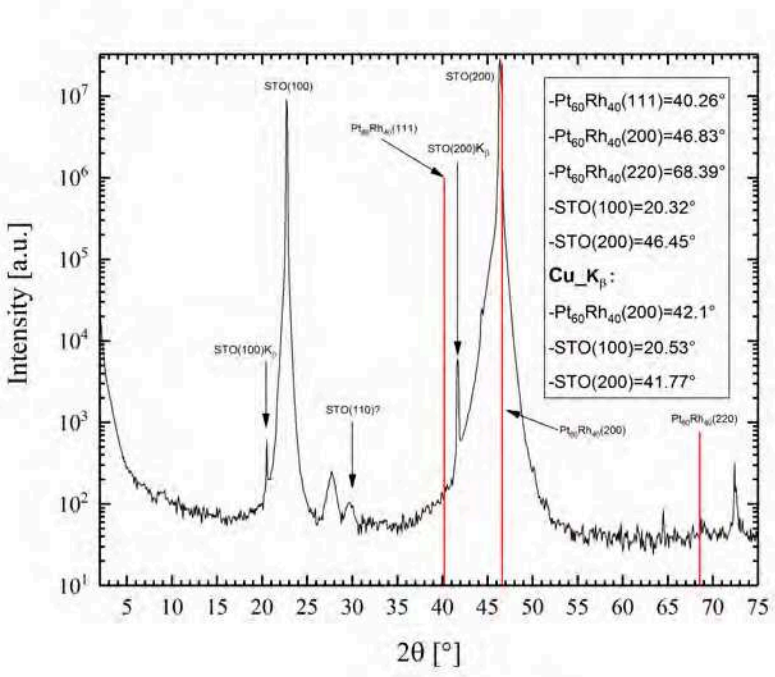

Figure C.1.: Wide-angle XRR on sample 13. Calculated positions of possibly occuring spots are indicated by vertical lines. See text for further info.

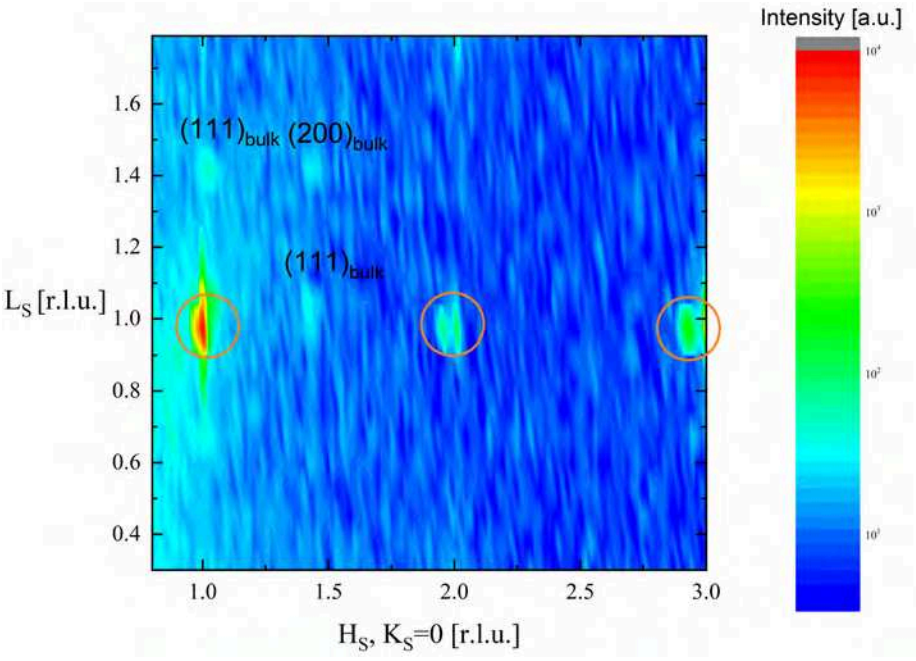

Figure C.2.: Reciprocal space map. Substrate reflexes are highlighted in orange circles.

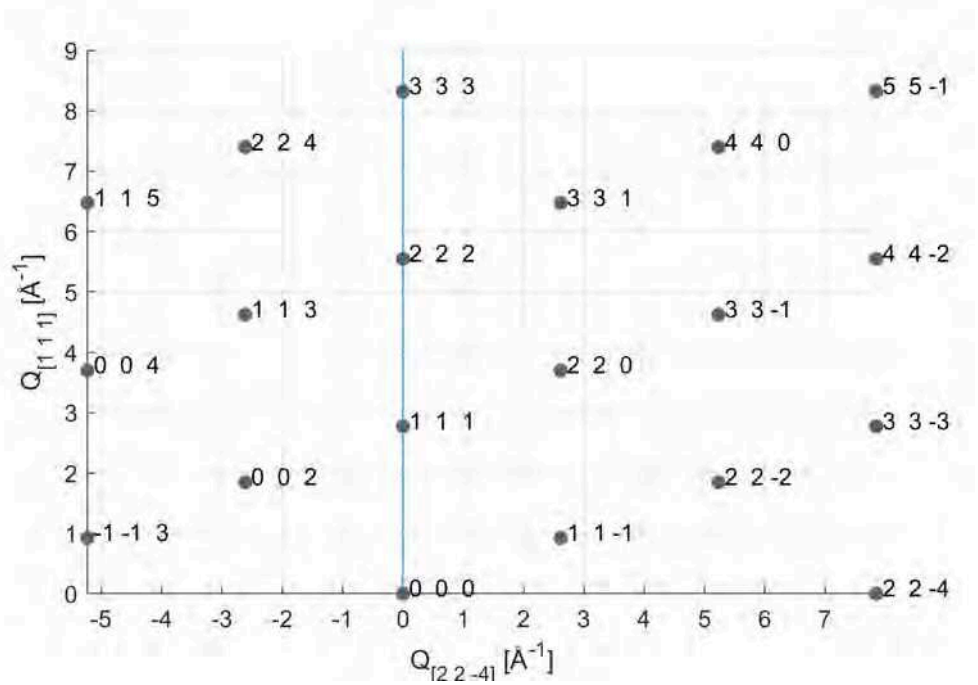

Figure C.3.: Calculated reciprocal space lattice for (111)-oriented particles.

$(201)_S$, and $(301)_S$ originate from the (001)-oriented STO substrate. For all reflexes with the term bulk as index the d-spacing of the Bragg reflex value corresponds to the momentum transfer of the indicated bulk hkl-value. Both the topper $(111)_{bulk}$ and the $(200)_{bulk}$ reflexes arise by scattering on nanoparticles with their (110)-axis in growth direction and their in-plane (110)-axes aligned with the $(100)_{STO}$ or $(010)_{STO}$ direction. The $(111)_{bulk}$ at (1.4, 0, 1.05) originates from (001)-oriented nanoparticles with $[100]_{Pt}||[100]_{STO}$. None of the reflexes fit the theoretical reflexes of (111)-oriented particles as can be deducted from the calculated reciprocal space map in Figure C.3. Additional grazing incidence measurements for (200), (220), and (111) in-plane Bragg-peaks of particles confirm these results (data not shown). To additionally probe the distribution of the nanoparticles' average lattice constants across the sample, in-plane radial scans in reciprocal space have been conducted in the grazing incidence geometry at different spots on the sample surface, see Figure C.4. The strongest peak at $2\theta = 67.8\,^\circ$ corresponds to a (220)-STO substrate reflection which does not vary along the sample. The broader peak towards higher angles corresponds to the nanoparticle's (220)-reflection revealing information about the ratio between Pt and Rh across the sample, compare Figure C.5. Here, the sample is highlighted in blue and the orange circles schematically indicate the areas subsequently illuminated by the X-ray beam. Additionally, the location B roughly equals the location of the single nanoparticle from the CXDI study, see Section 5.4. The composition varies

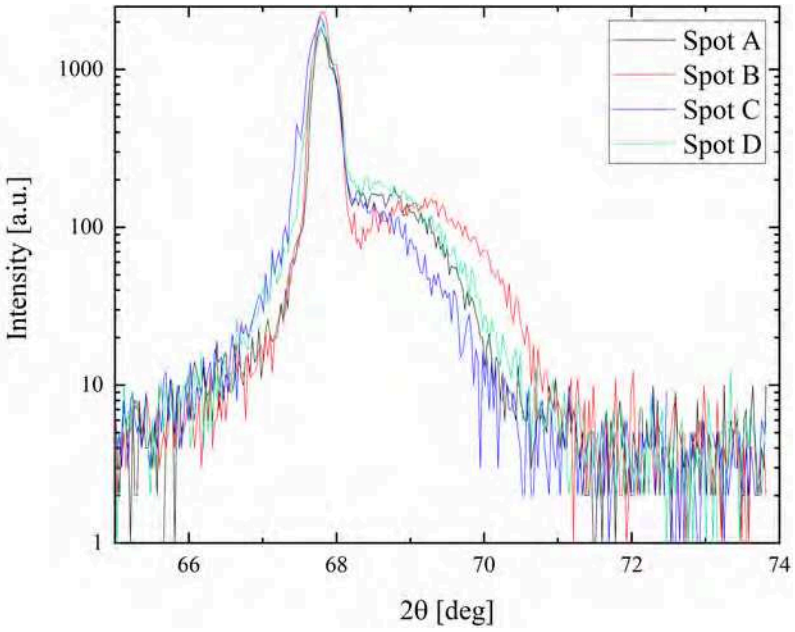

Figure C.4.: In-plane θ-2θ measurement along the (220)-substrate direction at different sample positions (see Figure C.5).

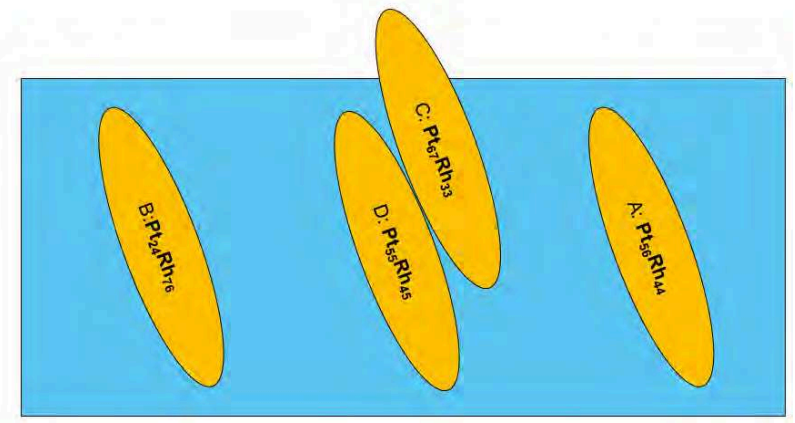

Figure C.5.: Top-view scheme of the different measurement areas for in-plane radial scans on sample 13, compare Figure C.4.

between $Pt_{24}Rh_{76}$ in area B and $Pt_{67}Rh_{33}$ in area C close to the center of the sample. It is remarkable that the average composition in area B – the area of the preselected nanoparticle – actually differs a lot from the composition which has been estimated for the preselected nanoparticle itself, which is $Pt_{58}Rh_{42}$. The underlying growth mechanisms are not well understood, yet. Compare Section 5.1.

C.2. ROIs used with LAMBDA-detector at DESY NanoLab

Size of ROIs (x1,y1,x2,y2), compare Figure C.6:

- lmbdROI1: 761,142,867,163
- lmbdROI2: 802,109,831,193
- lmbdROI3: 803,145,829,162
- lmbdROI4: 756,152,871,200
- lmbdROI5: 724,147,904,158

C.3. Supporting X-ray measurements

Information to Figure C.7:

- Curve was recorded at DESY NanoLab, at a six-circle diffractometer.
- Detector: Lambda300K, ROI for both curves: lmbdROI1 (see Figure C.6).

C.4. Supporting info on gas system and catalytic reactor

Figure C.10 depicts the layout of the interior gas flow system in the LPM gas flow cabinet, see Section 2.5.2. Each gas flow is set and monitored by a mass flow controller (MFC) calibrated for the respective gas. The arrangement of the two mixing valves MIX and MRS allows for the usage of a versatile gas mix. Further, this combination additionally redirecting gases directly to the exhaust valve (MFC shunt) to clean

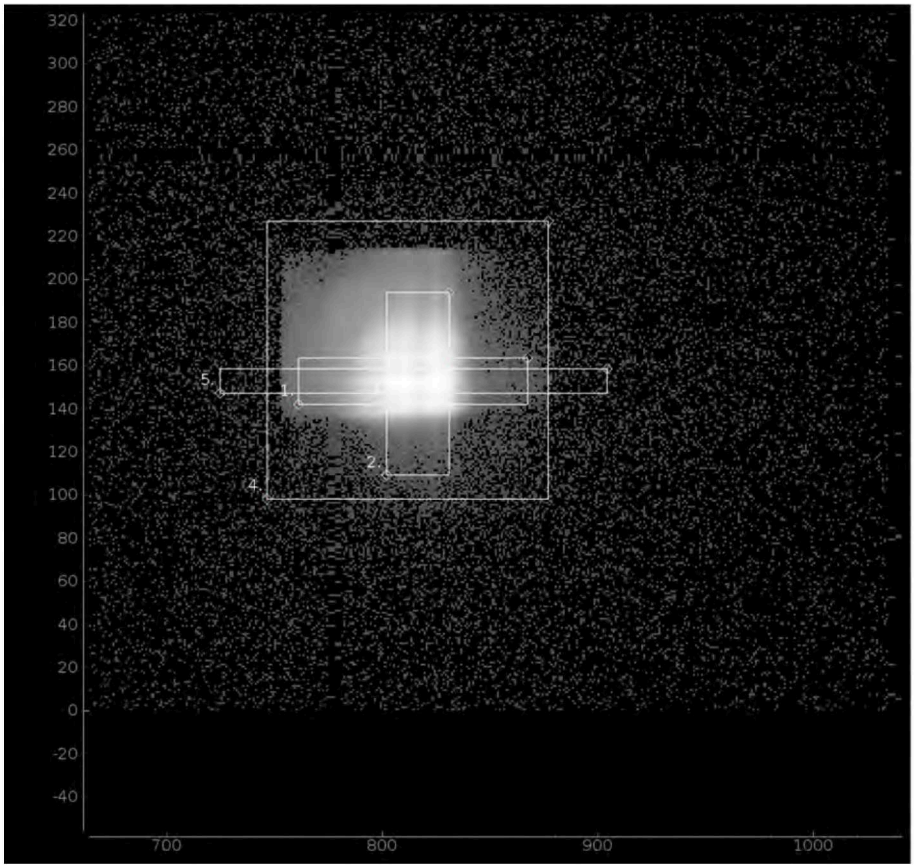

Figure C.6.: Regions of interest used for the LAMBDA detector of the six-circle diffractometer at DESY NanoLab.

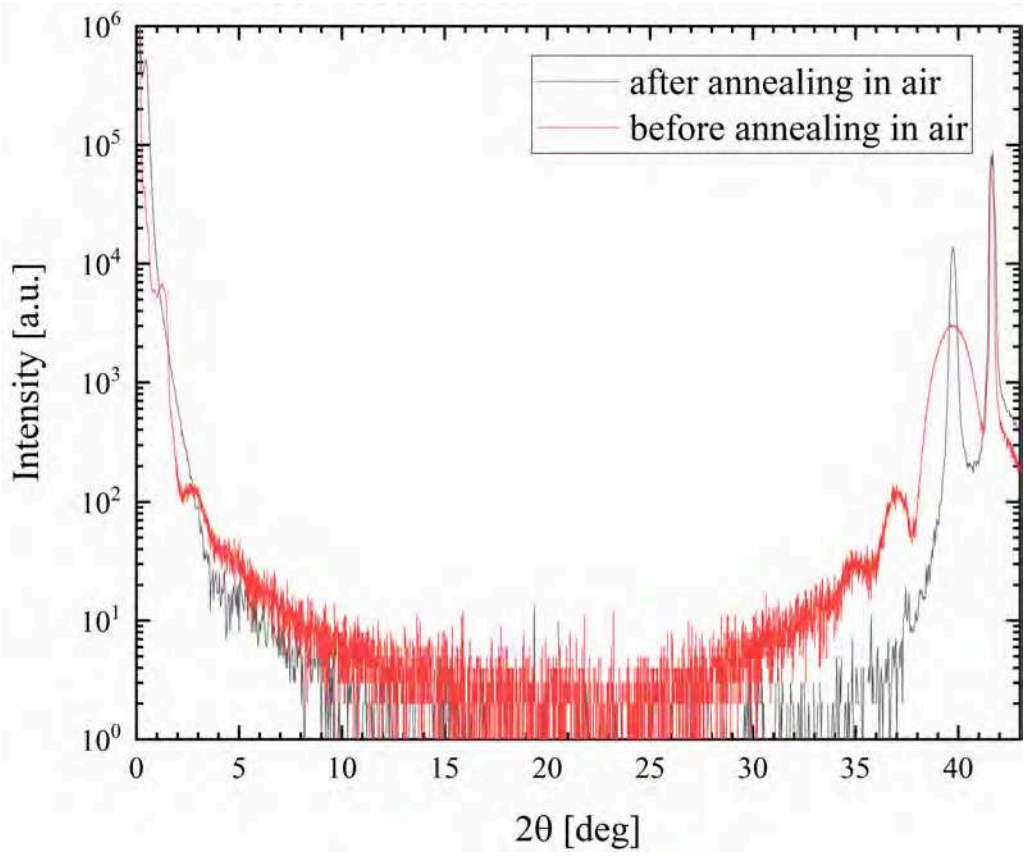

Figure C.7.: Wide-angle XRR curve for **sample 26** before (red) and after annealing in air (black).

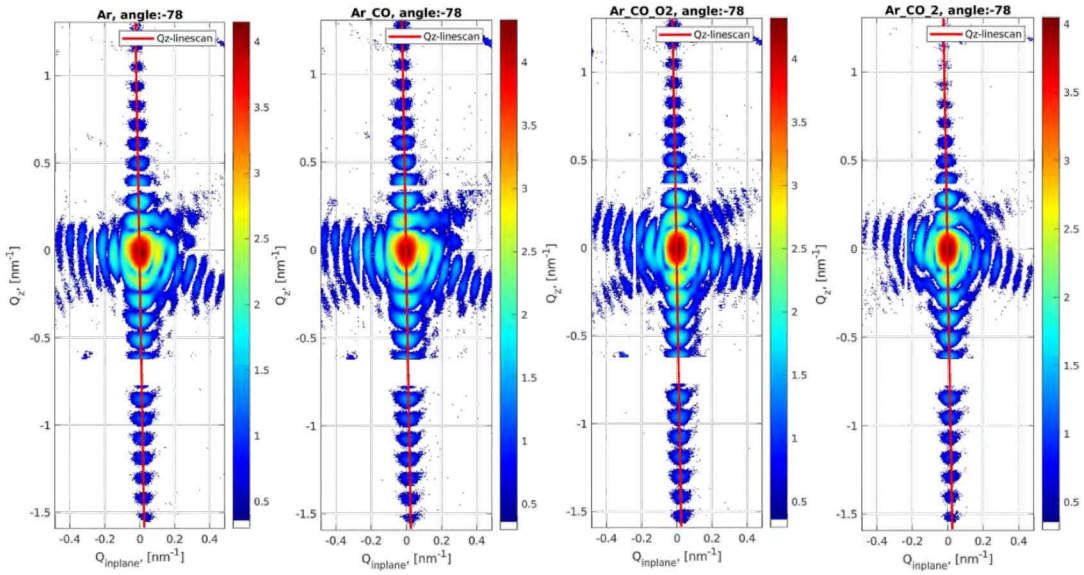

Figure C.8.: High-symmetry plane (III) in the 3D intensity distribution from the CXDI scattering experiment on sample 13 - compare Figure 5.10 and discussion in Section 5.4. Red lines indicate the exact positions of the Q_z line scans.

and dry the interior gas lines. The INJ valve features the option to operate the gas system in a pulsed mode which was not applied for this thesis. The total gas pressure is monitored by the back pressure controller (BPC) in the exhaust gas line coming from the reactor. Apart, a TPD controller enables time-controlled degassing of the valves (up to 70 °C).

The catalytic reactor (catalysis chamber) features a ceramic heating stage. The temperature calibration has been done using type-C thermocouples and is depicted in Figure C.11. The designations of the curves refer to the laboratories where they have been recorded so that corresponding lab book entries may be tracked back. Curve *L044* was recorded using the thermocouple directly attached to an bare alumina substrate, whereas for curve *P21* the thermocouple was attached to the bottom of the heater. Further differences between the curves arise due to different layouts of the read-out wiring (*L044*: capton foil crossing the gasket of the reactor; *P21*: TC directly connected to the TC feed through of the reactor), differences in heating layout (for the *P21* curve a spare heater with a different electrical contact to the feed through has been used), and the atmosphere in the reactor (*L044*: Argon pressure 0.08 bar, 20 $\frac{\text{ml}}{\text{min}}$; *P21*: Argon pressure 0.1 bar, 50 $\frac{\text{ml}}{\text{min}}$). Throughout this thesis, all temperature annotations concerning the catalysis chamber refer to calibration curve *L044*.

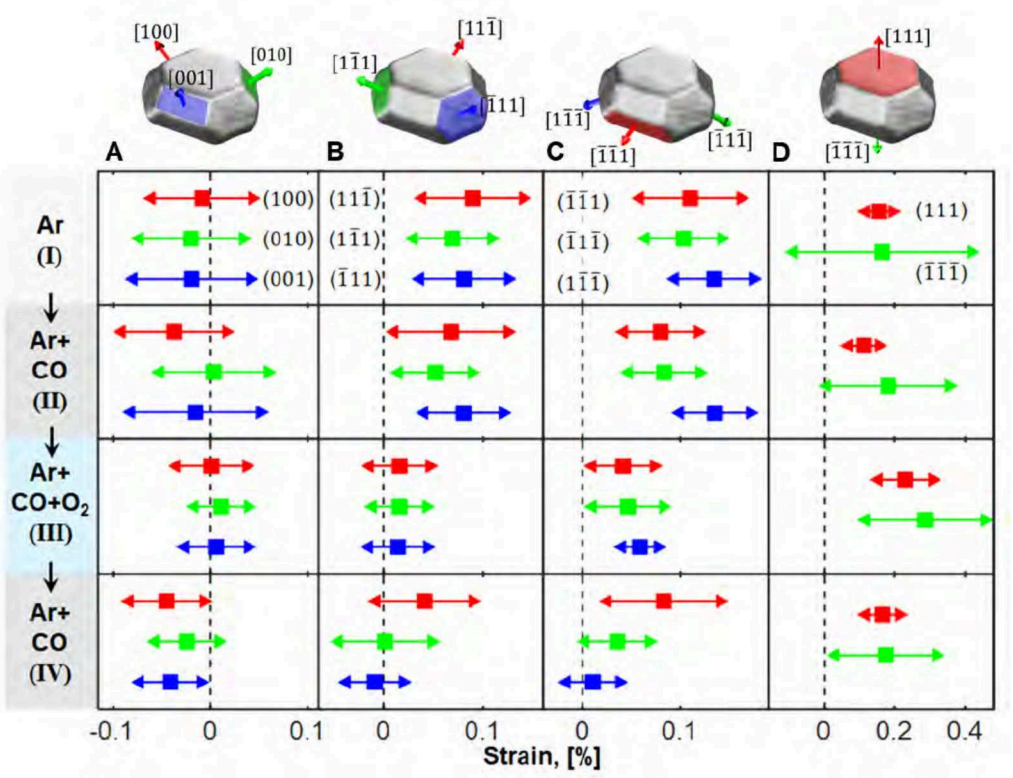

Figure C.9.: Facet resolved strain of the single particle's surface reconstructed from the CXDI experiment (see Section 5.4.1) during gas dosing steps 1-4, see Table 5.1. Corresponding facets are indicated on the top. For the strain values, squares represent the average strain value on the facet and lines with arrows indicate the standard variation.

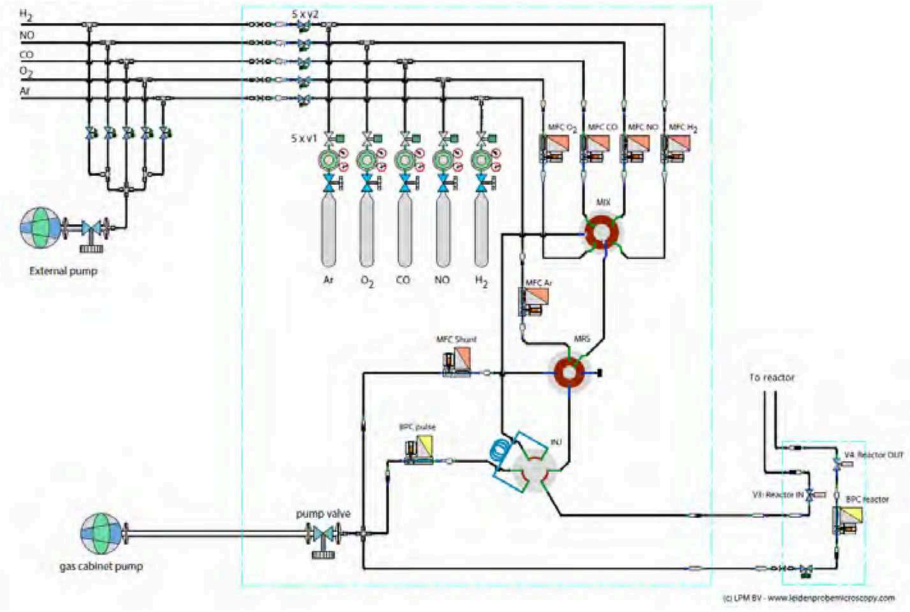

Figure C.10.: Schematic of the mobile gas cabinet setup. Note that NO gas has not been used in this thesis. More info given in text. Original schematic provided by LPM (see footnote 27 in Section 2.5.2), schematic was adapted for simplicity, usage granted by LPM.

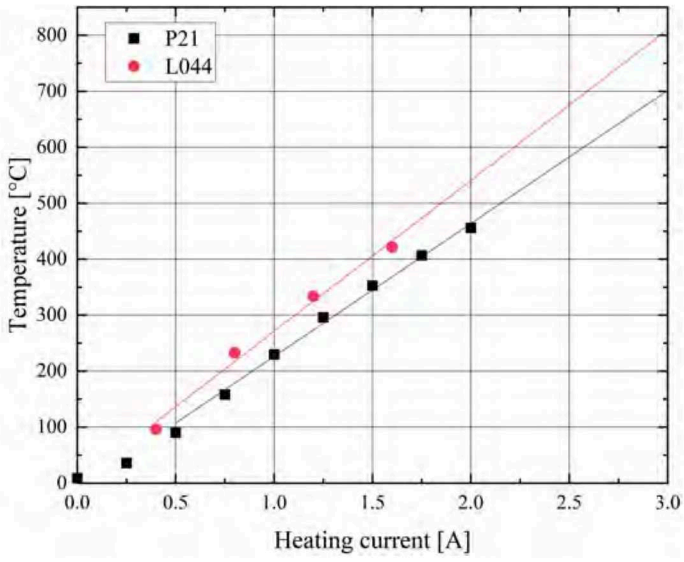

Figure C.11.: Temperature calibration curves of the ceramic heater of the catalysis chamber. The curves show the measured temperature of a thermocouple in dependency of an external driving current and corresponding linear fits. More info given in text.

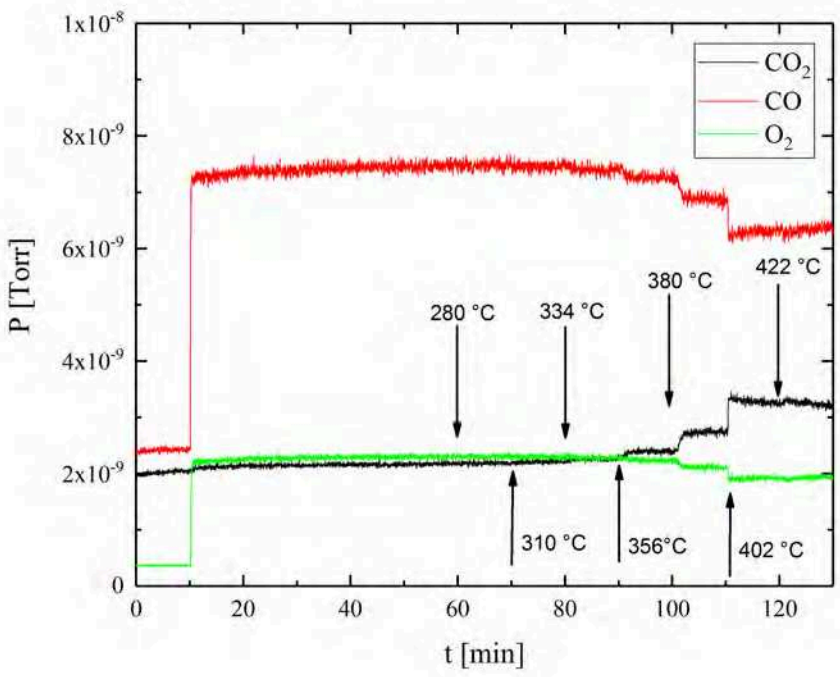

Figure C.12.: Catalytic test of alumina supported PtRh nanoparticles. The partial pressure of CO, O_2, and CO_2 was tracked by the T100 RGA while ramping the temperature of the sample.

C.5. Catalytic test experiments and further RGA data

To characterize the gas setup and to verify the catalytic activity of the fabricated samples a test series was conducted.

A test experiment yielded the optimal temperature for catalytic experiments with the fabricated alumina supported PtRh nanoparticles. Figure C.12 shows a section of pressure versus time curves recorded by a mass spectrometer in the exhaust gas of the catalysis chamber. The temperature was ramped step-wise, while keeping the respective gas flows and the total pressure (0.1 bar) constant. According to this experiment, the largest increase in CO_2 production happens around 420 °C. Higher temperatures do not significantly increase the monitored CO_2 signal (plot not shown, here). Hence, to preserve the sensitive material inside the catalysis chamber, 420 ° was chosen as temperature for the catalytic experiments.

In turn, to test whether the measured CO_2 signals originate from solely CO oxidation on nanoparticles, further tests with test samples (see below) and bare substrates (only shown for STO) were conducted. All tests were conducted with about the

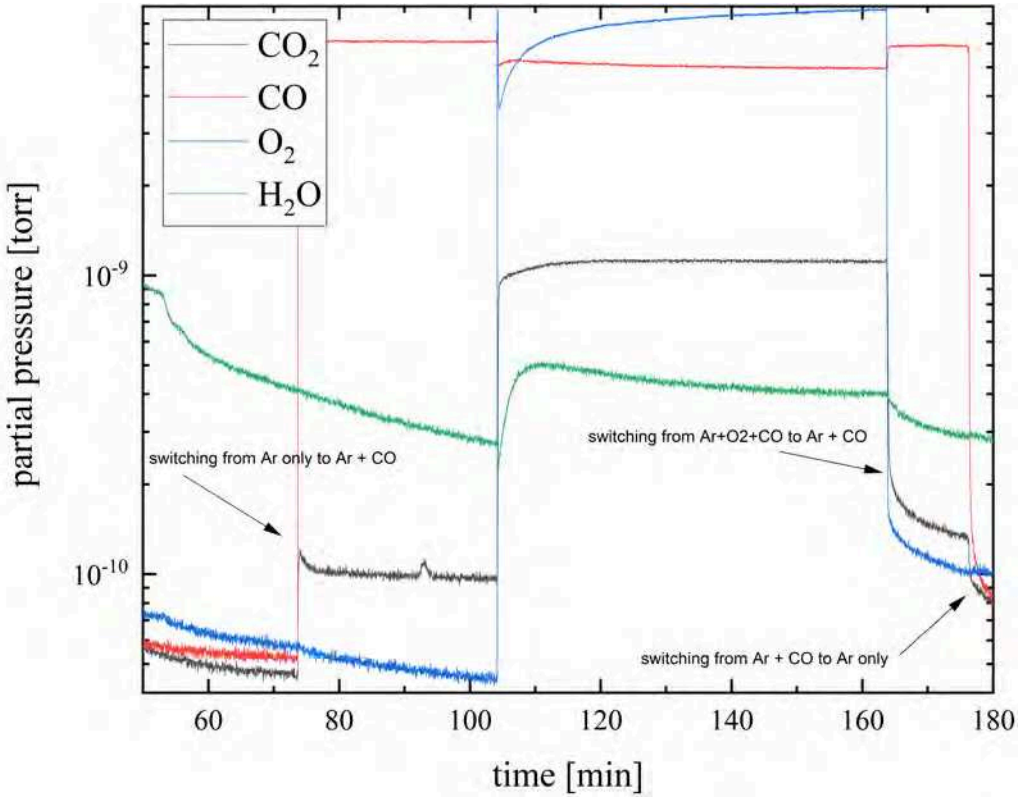

Figure C.13.: Catalytic test on sample 23 ($Pt_{85}Rh_{15}/Al_2O_3$). Depicted is the partial pressure of gas signals collected by the LPM T100 RGA. Test was conducted at 450 °C, 0.1 bar total pressure in the reactor, and a total flow of 50 $\frac{\text{ml}}{\text{min}}$.

same overall gas settings: 50 $\frac{\text{ml}}{\text{min}}$ total flow, 0.1 bar total pressure, Argon as carrier gas, temperature 700 K. Figure C.13 shows a test on an alumina supported PtRh nanoparticle sample (further info in caption of figure). The signals of H_2 and Argon have been removed from the graph for clarity. Clearly, a rise in the CO_2 signal is visible, when increasing the CO partial pressure in absence of oxygen. A similar increase of CO_2 signal is found on the same tests conducted on bare STO and alumina substrates. However, when switching to CO-oxidation reaction conditions, the measured CO_2 increases by an order of magnitude on the alumina supported PtRh test sample. A similar increase is not observed in the tests on the bare substrates (see test for STO in Figure C.14) – even in over-stoichiometric (oxygen-rich) conditions. In Figure C.13, the CO_2 offset when switching from pure Argon to Argon + CO might originate due to CO_2 residuals in the CO gas or CO gas line. Apart, the graph of the H_2O partial pressure shows that there is still water contamination in the system – as already addressed in Section 2.5.2. The rise and fluctuation in the CO_2 signal in Figure C.14 correlates with the CO signal and the overall level of the signal is very low, hence it can be assumed that both the reactor and the bare substrates (data for alumina not shown) are not significantly catalytically active in the frame of the experiments conducted in this work.

Figure C.15 displays supporting information on the second catalytic experiment (at 450 °C) on sample 6. See caption of the image and Chapter 4 for further info.

C.6. Supporting Rod data

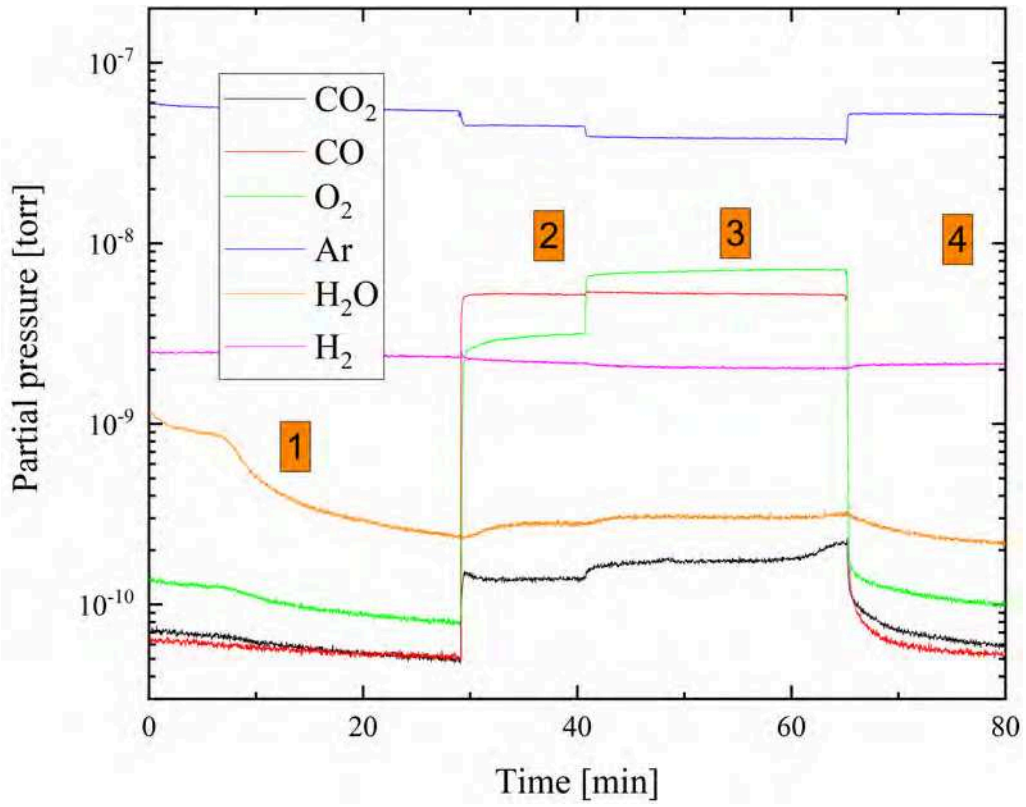

Figure C.14.: Catalytic test on a bare Nb-doted STO substrate. Highlighted numbers indicate following gas dosing steps (total flow 50 $\frac{\text{ml}}{\text{min}}$, total pressure 0.1 bar, temperature 450 °C): (1) Ar only, (2) 4 $\frac{\text{ml}}{\text{min}}$ CO and 4 $\frac{\text{ml}}{\text{min}}$ O_2 with Ar carrier gas, (3) 4 $\frac{\text{ml}}{\text{min}}$ CO and 8 $\frac{\text{ml}}{\text{min}}$ O_2 with Ar carrier gas, and (4) Ar only.

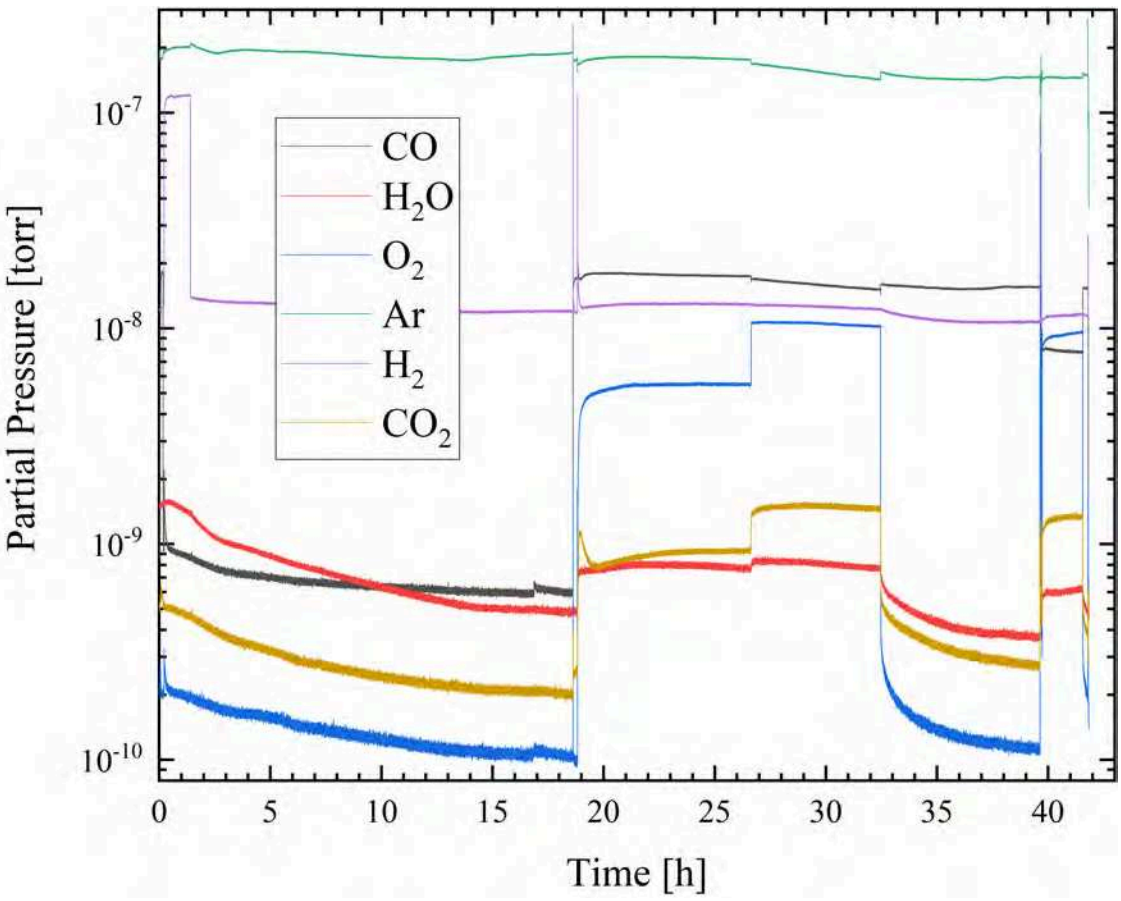

Figure C.15.: RGA data from second catalytic experiment (at 450 °C) on sample 6 – see Chapter 4. Shown is on logarithmic scale the recorded partial pressure of respective gases versus time. The data recorded by the LPM T100 RGA is recorded in the exhaust gas directly downstream the reactor. Total pressure of the reactor was 0.1 bar and the total flow was kept at 50 $\frac{\text{ml}}{\text{min}}$. Info on the gas flow mixture is given in Figure 4.9 and Table 4.2.

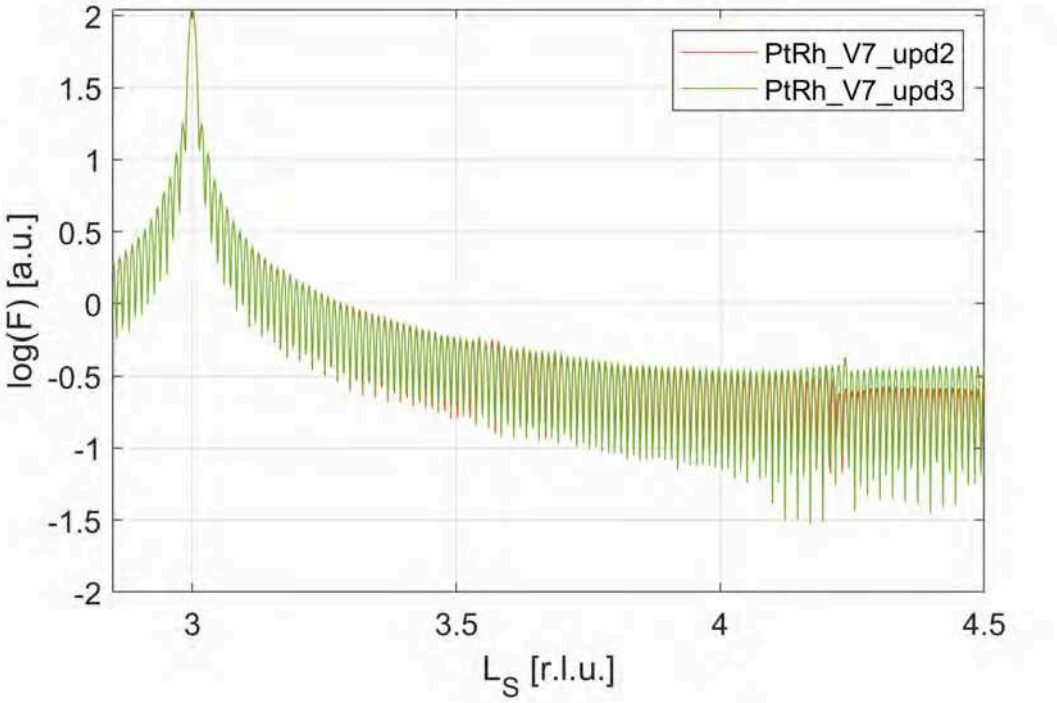

Figure C.16.: Structure factor of models *upd2* (no segregation, red straight line) and *upd3* (segregation in first four layers, green straight line) as generated using *Rod*.

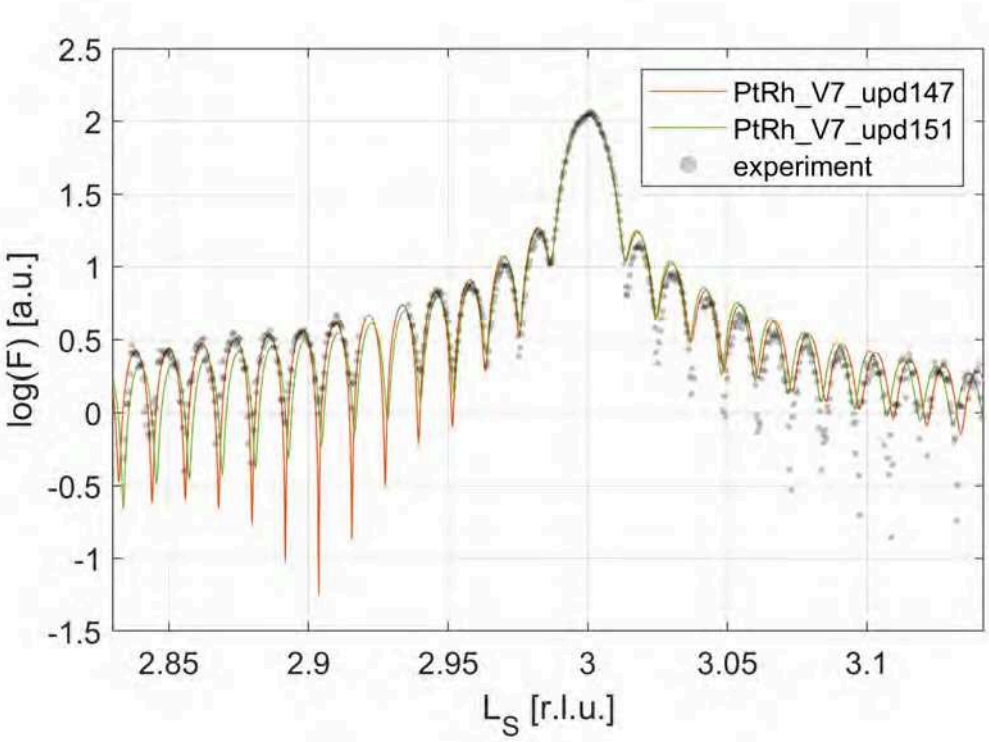

Figure C.17.: Structure factor of models *upd147* and *upd151*, comparing four strongly displaced layers with four exponentially displaced layers, respectively. Displacement values are: 0.27 Å, 0.27 Å, 0.27 Å, and 0.20 Å (*upd147*), and 0.27 Å, 0.06 Å, 0.01 Å, and 0.003 Å (*upd151*). Values are given from topmost layer towards the bulk and refer to each respective layer's ideal (un-displaced) position.

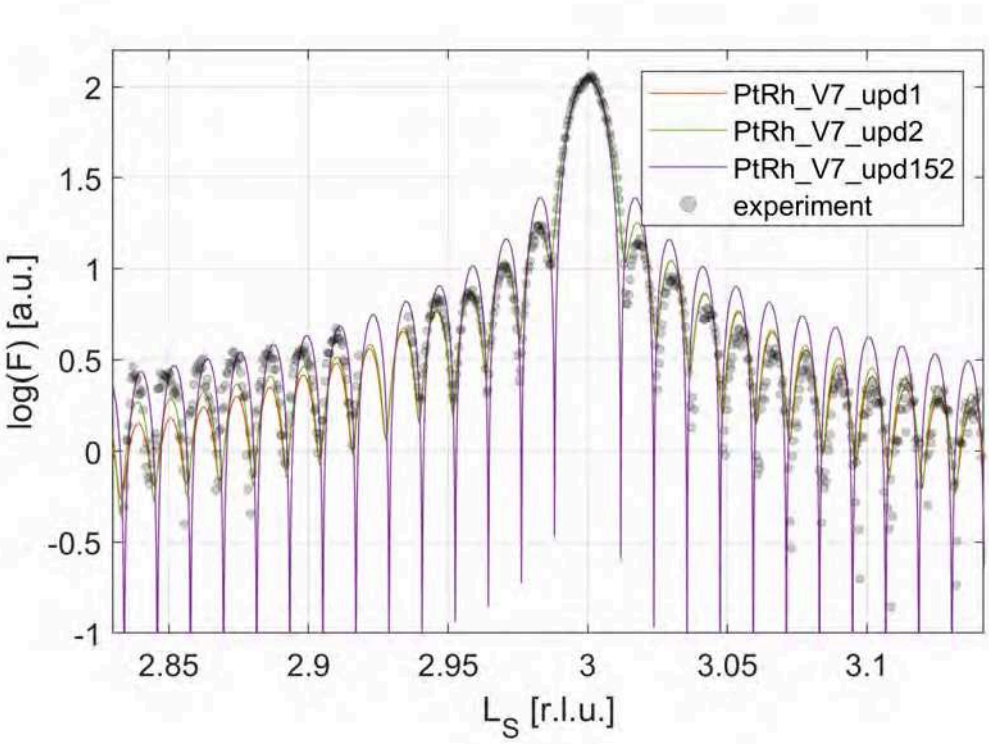

Figure C.18.: Structure factor models without segregation and without displacement. For models *upd1* and *upd2* the occupancy parameters resemble the particle shape, whereas for model *upd2* occupancy parameters of the utmost layers are extrapolated to implement an atomically sharp surface. Model *upd152* is a bulk model with $n_{Pt}^{occ} + n_{Rh}^{occ} = 1$. Compare Section 5.4.2. Grey circles represent data from the experiment in Argon atmosphere.

Acknowledgements

Many people contributed directly or indirectly to the success of this work:

- First of all, I like to thank Andreas Stierle for the opportunity to do my PhD in his group, for proof-reading my thesis, for continuously giving new ideas and input, and for his patience and advice throughout the years. Additional non-work related chats and his insights in hiking in the surroundings of Grenoble were much appreciated.

- Many thanks go to Ivan Vartaniants, not only for the co-supervision of my thesis, but also for his support as mentor and throughout my data analysis.

- I gratefully thank the examination committee for joining my PhD defence talk and contributing to an interesting discussion of my thesis' results.

- Without the support provided at DESY NanoLab my work probably would have been finished in 2050. Many thanks go to Katharina Röper, Satish Kulkarni, Arno Jeromin, Dennis Renner, and especially Simon Geile for their very much appreciated helping hands, help during experiments or providing supporting data and material to my measurements. Further, my colleagues from NanoLab made working at DESY a nice and fun experience and years to remember with joy. Many thanks go to Konstantin Krausert, Dirk Franz, Björn Arndt, Marcus Creutzburg, Pirmin Lakner, the Gleißners, Steffen Tober, Guilherme dalla Lana Semione, Jan-Christian Schober, Elin Grånäs, Simon Chung, Manuel Abuìn, Christoph Seitz, Vedran Vonk, Thomas Keller and all the others for a nice, exciting time in the office, the lab, and outside DESY!

- Many thanks go to Young Yong Kim, Luca Gelisio, Dmitry Dzhigaev, and Sergey Lazarev for their help with CXDI data treatment and data analysis, and a very nice time during lunch breaks.

- I'd like to thank beamline staff of ESRF ID01, APS 34-ID-C, and PETRA P07, P21, P22, and P23 for their close collaboration and help during beamtimes and experiments.

- Mit den wichtigsten Beitrag zu einem der prägensten Schritte meines Lebens lieferten meine Eltern mit ihrer bedingungslosen Unterstützung besonders in der Studienzeit und ihrem Glauben an mich. Ihr seid die Größten!